

ZZ PRODUCTION IN PROTON-PROTON COLLISIONS AT  
 $\sqrt{s} = 13$  TeV IN FOUR-LEPTON EVENTS USING THE  
CMS DETECTOR AT THE CERN LHC

*by*

Nathaniel Woods

A dissertation submitted in partial fulfillment of  
the requirements for the degree of

Doctor of Philosophy  
(Physics)

*at the*  
UNIVERSITY OF WISCONSIN – MADISON  
2017

Defended on X October 2017

Dissertation approved by the following members of the Final Oral Committee:

Wesley Smith · Bjorn Wiik Professor of Physics  
Sridhara Dasu · Professor of Physics  
Matthew Herndon · Professor of Physics  
Someone · Professor of Physics  
Someone · Professor of Something

## Abstract

## Acknowledgements

# Contents

Abstract . . . . .	i
Acknowledgements . . . . .	ii
<b>Contents</b>	iii
<b>List of Figures</b>	viii
<b>List of Tables</b>	xii
<b>1 The Standard Model</b>	1
1.1 Introduction . . . . .	2
1.2 Matter and Forces . . . . .	3
1.3 Electroweak Symmetry Breaking and the Higgs Boson . . . . .	9
1.4 Diboson and Multiboson Physics . . . . .	12
1.4.1 Vector Boson Scattering . . . . .	16
1.5 Limitations and Possible Extensions . . . . .	16
1.5.1 Anomalous Gauge Couplings . . . . .	17
1.6 Proton-Proton Collisions . . . . .	20
1.7 ZZ Measurements in Context . . . . .	22
<b>2 ZZ Phenomenology and Previous Results</b>	24
2.1 Nonresonant ZZ/Z $\gamma^*$ Production and Decay . . . . .	25

2.1.1	Vector Boson Scattering . . . . .	27
2.1.2	Prior Measurements . . . . .	28
2.2	Resonant $ZZ^*/Z\gamma^*$ Production . . . . .	34
2.2.1	$Z$ Boson Decays to Four Leptons . . . . .	34
2.2.2	Higgs Boson Production . . . . .	35
2.2.2.1	Prior Measurements . . . . .	36
2.3	Anomalous Gauge Couplings . . . . .	38
2.3.1	Previous Limits . . . . .	40
2.4	Background Processes . . . . .	41
<b>3</b>	<b>The CMS Experiment and the CERN LHC</b>	<b>43</b>
3.1	The CERN Large Hadron Collider . . . . .	43
3.1.1	Accelerator Chain, Layout, and Detectors . . . . .	45
3.1.2	Operating Parameters . . . . .	48
3.1.2.1	Design . . . . .	49
3.1.2.2	Run I . . . . .	50
3.1.2.3	Run II . . . . .	51
3.2	The Compact Muon Solenoid Detector . . . . .	52
3.2.1	Terminology and Geometry . . . . .	53
3.2.2	Magnet and Inner Tracking System . . . . .	54
3.2.2.1	Pixel Detector . . . . .	57
3.2.2.2	Strip Tracker . . . . .	58
3.2.3	Electromagnetic Calorimeter . . . . .	58
3.2.4	Hadronic Calorimeter . . . . .	60
3.2.5	Muon Spectrometer . . . . .	62
3.2.5.1	Drift Tubes . . . . .	63

3.2.5.2	Cathode Strip Chambers . . . . .	64
3.2.5.3	Resistive Plate Chambers . . . . .	65
3.2.6	Data Acquisition and Trigger . . . . .	66
3.2.6.1	Level-1 Trigger . . . . .	67
3.2.6.2	High-Level Trigger . . . . .	69
3.2.7	Luminosity Determination . . . . .	70
<b>4</b>	<b>Simulation</b>	<b>73</b>
4.1	Monte Carlo Event Generation . . . . .	73
4.1.1	Matrix Element and Hard Process Generation . . . . .	74
4.1.2	Parton Shower, Hadronization, and Underlying Event . . . . .	75
4.1.3	Pileup Simulation . . . . .	77
4.1.4	Samples Used in this Analysis . . . . .	77
4.2	Detector Simulation . . . . .	78
<b>5</b>	<b>Object Reconstruction and Selection</b>	<b>81</b>
5.1	Track Reconstruction and Vertex Identification . . . . .	82
5.2	Particle Flow Reconstruction . . . . .	84
5.2.1	PF Candidates . . . . .	85
5.2.1.1	Muons . . . . .	86
5.2.1.2	Electrons and Prompt Photons . . . . .	87
5.2.1.3	Charged and Neutral Hadrons . . . . .	87
5.2.2	Jets . . . . .	88
5.2.3	Missing Transverse Energy . . . . .	90
5.3	Object Identification and Selection . . . . .	90
5.3.1	Electrons . . . . .	91
5.3.2	Muons . . . . .	93

5.3.3	Final State Photon Radiation . . . . .	94
5.3.4	Jets . . . . .	95
5.3.5	Misidentified Objects . . . . .	95
5.4	ZZ Candidate and Event Selection . . . . .	96
5.4.1	$Z/\gamma^*$ Candidate Selection . . . . .	97
5.4.2	ZZ Candidate Selection . . . . .	98
5.4.3	Dijet and VBS Signal Selection . . . . .	99
<b>6</b>	<b>Analysis Strategy</b>	<b>100</b>
6.1	Background Estimation . . . . .	100
6.2	Systematic Uncertainties . . . . .	103
6.3	Fiducial and Total Cross Section Calculation . . . . .	105
6.3.1	Signal Strength Extraction . . . . .	108
6.3.2	$Z \rightarrow 4\ell$ Branching Fraction . . . . .	108
6.4	Differential Cross Sections . . . . .	109
6.4.1	Unfolding . . . . .	110
6.4.2	Uncertainties . . . . .	111
6.5	VBS Signal Extraction . . . . .	111
6.6	Anomalous Gauge Coupling Searches . . . . .	113
<b>7</b>	<b>Results</b>	<b>115</b>
7.1	Four-Lepton Yield and Distributions . . . . .	116
7.1.1	Full Spectrum . . . . .	116
7.1.2	$Z \rightarrow 4\ell$ Resonance . . . . .	116
7.1.3	Higgs Resonance . . . . .	118
7.1.4	ZZ Production . . . . .	121
7.2	ZZ Fiducial and Total Cross Section . . . . .	122

7.2.1	$Z \rightarrow 4\ell$ Branching Fraction . . . . .	128
7.3	Differential Cross Sections . . . . .	132
7.4	Vector Boson Scattering . . . . .	134
7.5	Anomalous Coupling Limits . . . . .	134
<b>8</b>	<b>Conclusions</b>	<b>152</b>
8.1	Summary . . . . .	152
8.2	Outlook . . . . .	154
<b>Bibliography</b>		<b>156</b>

# List of Figures

1.1	Triple gauge boson coupling vertex . . . . .	13
1.2	Quartic gauge boson coupling vertex . . . . .	13
1.3	Higgs couplings to the gauge bosons . . . . .	14
1.4	Higgs self couplings . . . . .	14
1.5	Tree level Feynman diagrams for diboson production in fermion-anti-fermion collisions . . . . .	15
1.6	Gluon-gluon fusion box diagram for general diboson production . . .	15
1.7	Unitarity violation in vector boson scattering without a Higgs boson	16
1.8	Neutral anomalous gauge coupling vertices . . . . .	18
1.9	Neutral anomalous triple gauge coupling vertex . . . . .	19
1.10	Parton distribution functions . . . . .	21
2.1	Leading order $ZZ \rightarrow 4\ell$ production . . . . .	26
2.2	Next-to-leading order $ZZ \rightarrow 4\ell$ production . . . . .	26
2.3	Gluon-gluon fusion box diagram for $ZZ \rightarrow 4\ell$ production . . . . .	27
2.4	Vector boson scattering diagrams . . . . .	29
2.5	Measured $e^+e^- \rightarrow ZZ$ cross sections from OPAL. . . . .	30
2.6	Measured four-lepton mass spectrum from D0. . . . .	31
2.7	Measured four-lepton mass spectrum from CMS at $\sqrt{s} = 8$ TeV. . . . .	32

2.8	Measured four-lepton mass spectrum from ATLAS at $\sqrt{s} = 8$ TeV. . . . .	33
2.9	Feynman diagram for $Z \rightarrow 4\ell$ production . . . . .	35
2.10	Higgs production mechanisms . . . . .	36
2.11	Higgs boson SM cross section and branching ratio, as a function of $m_H$ .	37
2.12	Enhancements in $p_T^Z$ and $p_T^\mu$ resulting from nonzero aTGCs . . . . .	38
2.13	Lepton angular correlations resulting from nonzero aTGCs . . . . .	39
2.14	Previous two-dimensional aTGC limits from CMS. . . . .	41
2.15	Example background diagrams . . . . .	42
3.1	LHC dipole schematic . . . . .	46
3.2	LHC accelerator and experiment layout . . . . .	47
3.3	Integrated luminosity delivered to CMS in each LHC run period . .	51
3.4	CMS cutout schematic . . . . .	53
3.5	Inner tracker layout . . . . .	56
3.6	Tracker material budget in radiation lengths . . . . .	57
3.7	ECAL geometry . . . . .	59
3.8	HCAL geometry . . . . .	61
3.9	Total material budget in nuclear interaction lengths . . . . .	62
3.10	Muon system geometry . . . . .	63
3.11	Trigger data flow . . . . .	70
4.1	Comparison of data and simulation in $e^+e^-$ events around the $Z$ resonance . . . . .	80
6.1	Misidentification rates for electrons and muons . . . . .	102
7.1	Full four-lepton mass spectrum . . . . .	117
7.2	Mass of all $Z/\gamma^*$ candidates in the full spectrum selection . . . . .	118

7.3	Mass of $Z_1$ candidates in the full spectrum selection . . . . .	119
7.4	Scatter plot of $m_{Z_2}$ vs. $m_{Z_1}$ for data events in the full spectrum selection	120
7.5	Four-lepton mass in the $Z \rightarrow 4\ell$ selection . . . . .	121
7.6	Scatter plot of $m_{Z_2}$ vs. $m_{Z_1}$ for data events in the $Z \rightarrow 4\ell$ selection .	122
7.7	Four-lepton mass spectrum around the Higgs resonance . . . . .	123
7.8	Mass of $Z_1$ candidates in events near the Higgs resonance . . . . .	124
7.9	Mass of $Z_2$ candidates in events near the Higgs resonance . . . . .	125
7.10	Scatter plot of $m_{Z_2}$ vs. $m_{Z_1}$ for data events near the Higgs resonance	126
7.11	Four-lepton mass spectrum for events with both $Z$ candidates on-shell	127
7.12	Mass of all $Z/\gamma^*$ candidates in the on-shell selection . . . . .	128
7.13	Jet multiplicity . . . . .	129
7.14	Transverse momentum of the leading and subleading jets . . . . .	130
7.15	Pseudorapidity of the leading and subleading jets . . . . .	130
7.16	Dijet invariant mass . . . . .	131
7.17	Dijet pseudorapidity separation . . . . .	132
7.18	Total ZZ cross section as a function of center-of-mass energy . . . . .	133
7.19	Normalized differential ZZ cross section as a function of four-lepton invariant mass . . . . .	135
7.20	Normalized differential ZZ cross section as a function of four-lepton system $p_T$ . . . . .	136
7.21	Normalized differential ZZ cross section as a function of Z boson candidate $p_T$ . . . . .	137
7.22	Normalized differential ZZ cross section as a function of leading lepton $p_T$ . . . . .	138
7.23	Normalized differential ZZ cross section as a function of $\Delta R$ between the Z bosons . . . . .	139

7.24	Normalized differential ZZ cross section as a function of $\Delta\phi$ between the Z bosons . . . . .	140
7.25	Normalized differential ZZ cross section as a function of jet multiplicity	141
7.26	Normalized differential ZZ cross section as a function of dijet invariant mass . . . . .	142
7.27	Normalized differential ZZ cross section as a function of dijet pseudorapidity separation . . . . .	143
7.28	Normalized differential ZZ cross sections as functions of leading and subleading jet transverse momentum . . . . .	144
7.29	Normalized differential ZZ cross sections as functions of leading and subleading jet pseudorapidity . . . . .	145
7.30	Normalized differential four-lepton cross section as a function of four-lepton invariant mass with loosened Z mass cuts . . . . .	146
7.31	VBS signal extraction GBDT output . . . . .	147
7.32	ZZ invariant mass distribution with example aTGC working points .	148
7.33	Asymptotic one- and two-dimensional aTGC limits at 95% confidence level . . . . .	149
7.34	One-dimensional aTGC limits as a function of the maximum ZZ invariant mass used in the calculation . . . . .	150
7.35	ZZ invariant mass distribution for dijet events, with example aQGC working points . . . . .	151

# List of Tables

1.1	Particle content of the standard model . . . . .	4
3.1	LHC beam parameters . . . . .	50
6.1	Systematic uncertainties on the total yield . . . . .	105
6.2	Fiducial phase space definitions . . . . .	107
7.1	Expected and observed yields for $Z \rightarrow 4\ell$ production. . . . .	117
7.2	Expected and observed yields for Higgs boson production. . . . .	120
7.3	Expected and observed yields for doubly-resonant ZZ production. . . . .	123

## <sup>0</sup> Chapter 1

### <sup>1</sup> The Standard Model

2 The mission of fundamental particle physics is an audacious one. An exercise in  
3 reductionism taken to its logical extreme, the goal of the field is to find the minimal set  
4 of mathematical precepts that underlie all interactions of matter and energy and from  
5 which everything else in the universe is, in principle, an emergent property. Despite  
6 the loftiness of its goals, the program has been extraordinarily successful, yielding the  
7 standard model (SM), which is elegant in its mathematical formulation yet expansive  
8 and powerful in its predictions, most of which have been verified in exquisite detail.  
9 And yet work remains. One area of particular interest is the physics of the electroweak  
10 interaction, which was the last piece to fall into place. Its final major component,  
11 the existence of the Higgs boson, was definitively confirmed only as recently as 2012  
12 and some details remain hazy or unverified, from an experimental perspective. These  
13 statements will be explained and made more precise here in Chapter 1, which gives  
14 an overview of the SM with a focus on its electroweak sector, and describes some of  
15 the shortcomings that motivate continued searches for new physics even now that it  
16 is complete. Chapter 1 also describes diboson and multiboson processes, interactions  
17 involving multiple instances of the particles underlying electroweak physics, which

18 are valuable tools for understanding how the bosons interact with each other. This  
19 thesis presents several studies of the ZZ diboson process, intended to illuminate the  
20 behavior of the neutral part of electroweak interactions. Details of ZZ physics are  
21 described in Chapter 2, along with a review of previous literature.

22 High-energy particle collisions in a laboratory provide a way to investigate funda-  
23 mental interactions in a controlled setting. CERN’s Large Hadron Collider (LHC),  
24 a proton-proton collider in tunnels running beneath the Swiss-French border near  
25 Geneva, provides collision at record-breaking energies and rates, which can be used  
26 by the Compact Muon Solenoid (CMS) detector to study diboson processes in un-  
27 precedented detail. These apparatus are described in Chapter 3. Accurate simula-  
28 tions of physics and particles’ interactions with the detector are vital to obtaining  
29 valid results; this process is described in Chapter 4. Chapter 5 describes how physics  
30 objects are built from the detector signals, and how those appropriate for analysis are  
31 selected. The strategy for performing the ZZ measurements in question is given in  
32 Chapter 6. New studies of four-lepton events in a sample of proton-proton collision  
33 are presented in Chapter 7.

## 34 **1.1 Introduction**

35 The standard model is a set of several related theories that together describe matter  
36 and its interactions at a fundamental level. The SM is a remarkable theory, making  
37 detailed predictions for a wide range of measurements that have matched data within  
38 the precision of essentially every experiment over roughly four decades. It is arguably  
39 the best-confirmed theory in the history of science despite making some of the boldest,  
40 broadest, and most precise predictions. There are a few known phenomena that the  
41 SM does not cover, and some of its features seem for now to be surprising coincidences

42 (see Section 1.5), but it is generally believed to be self-consistent; future advances will  
43 likely add to it, explain its free parameters, or find some deeper underlying structure,  
44 not contradict it.

45 The following sections give a general overview of the SM and related topics that  
46 serve as background material for the four-lepton processes described in more detail  
47 in subsequent chapters. This includes discussions of the particle content of the SM  
48 and the gauge structure that leads to particle interactions, the spontaneous symmetry  
49 breaking mechanism that leads to the specific structure of the electroweak sector of the  
50 SM, diboson processes, and the SM’s limitations and how they might be addressed.  
51 Some details are also given about the proton-proton interactions used to probe particle  
52 interactions at high energies. More complete information may be found in a number  
53 of texts, including Refs. [1–5]. Everything that follows uses units such that  $c = \hbar = 1$ ,  
54 where  $c$  is the speed of light and  $\hbar$  is the reduced Planck’s constant  $\hbar = h/2\pi$ .

## 55 1.2 Matter and Forces

56 In the SM, matter is made of fermions (particles with half-integer spin; all SM fun-  
57 damental fermions have spin  $\frac{1}{2}$ ) which interact by exchanging gauge bosons (integer  
58 spin; spin 1 for the SM force carriers). Table 1.1 lists the fundamental particles and  
59 some of their properties. With the exception of the neutral bosons, all particles have  
60 a corresponding antiparticle which is the same except that all its quantum numbers  
61 have opposite sign. The fermions come in two categories, leptons and quarks. All  
62 the quarks and half the lepton types carry electric charge and are therefore subject  
63 to interactions through the electromagnetic force, described by quantum electrody-  
64 namics (QED) [2]. In a QED interaction, two charged particles exchange a photon,  
65 which carries the momentum transferred from one to the other. The photon is a

66 spin-1 gauge boson that is massless and electrically neutral itself, explaining why  
 67 electromagnetic forces are long-range.

Table 1.1: The particles of the standard model, and some of their properties. All fermions have a corresponding antiparticle with opposite sign for all quantum numbers. Quarks and leptons are grouped by generation. Note that the listed  $T^3$  (the measured component of the weak isospin, described below) applies only to left-handed fermions; right-handed fermions have  $T^3 = 0$  and do not couple to the  $W^\pm$  (right-handed neutrinos, if they exist, do not couple to the  $Z$  either).

Particle	Mass (GeV)	Charge ( $e$ )	$T^3$	Gauge couplings
Scalar boson (spin 0)				
H	125	0		$W^\pm, Z$
Fermion (spin 1/2)				
u	0.023	+2/3	+1/2	$g, \gamma, Z, W^\pm$
d	0.048	-1/3	-1/2	$g, \gamma, Z, W^\pm$
e	$5.11 \times 10^{-4}$	-1	+1/2	$\gamma, Z, W^\pm$
$\nu_e$	$< 2.2 \times 10^{-9}$	0	-1/2	$Z, W^\pm$
c	1.28	+2/3	+1/2	$g, \gamma, Z, W^\pm$
s	0.95	-1/3	-1/2	$g, \gamma, Z, W^\pm$
$\mu$	0.105	-1	+1/2	$\gamma, Z, W^\pm$
$\nu_\mu$	$< 1.7 \times 10^{-4}$	0	-1/2	$Z, W^\pm$
t	172	+2/3	+1/2	$g, \gamma, Z, W^\pm$
b	4.2	-1/3	-1/2	$g, \gamma, Z, W^\pm$
$\tau$	1.77	-1	+1/2	$\gamma, Z, W^\pm$
$\nu_\tau$	$< 0.018$	0	-1/2	$Z, W^\pm$
Vector boson (spin 1)				
g	0	0	0	$g$
$\gamma$	0	0	0	$W^\pm$
Z	91.2	0	0	$W^\pm$
$W^\pm$	80.4	$\pm 1$	$\pm 1$	$\gamma, Z, W^\pm$

68 There are six types of quarks which fall into three “generations:” up and down  
 69 (u and d, first generation); charm and strange (c and s, second generation); and top

and bottom ( $t$  and  $b$ , third generation)<sup>1</sup>. Quark masses increase with each successive generation. Up-type quarks ( $u, c, t$ ) have electric charge  $+2/3$  (in units of the positron charge  $e$ ) while down-type quarks have  $-1/3$ . Quarks are the building blocks of hadrons, including  $q\bar{q}'$  bound states called mesons and  $qq'q''/\bar{q}\bar{q}'\bar{q}''$  bound states called baryons, of which protons ( $uud$ ) and neutrons ( $udd$ ) are the most familiar. Top quarks are too heavy to form bound states; the toponium ( $t\bar{t}$  meson) weak decay width is larger than the spacing between its energy levels and its mean lifetime is an order of magnitude shorter than its orbital period so no resonance may form [5]. Hadrons are bound by the strong nuclear force, described by the theory of quantum chromodynamics (QCD).

The mediator for the strong force is the gluon, which like the photon is a massless spin-1 gauge boson. The analog of electric charge is “color”, a notion originally introduced [6] as an ad hoc explanation of how identical quarks could exist in the symmetric bound state of a hadron despite the Fermi exclusion principle and later found to be the charge underlying the strong force [1, 7]. Unlike electric charge, there are three types of color charge, typically called red, green, and blue, though these names are arbitrary<sup>2</sup>. The analogy with visible color comes primarily from the heuristic that natural states must be “colorless,” i.e. a hadron may have equal parts color and corresponding anticolor as in a meson, but it may also be “white,” containing red, blue, and green in equal measures as in a baryon. This implies that a color charged object cannot exist on its own, a property known as confinement.

Confinement arises from the structure of QCD interactions and gluons themselves. Among fermions, only quarks interact through the strong force, but gluons also carry color charge and interact with each other. Because gluons self-interact, have no dis-

---

<sup>1</sup>Top and bottom quarks are sometimes called truth and beauty.

<sup>2</sup>Negative color charges, carried by antiquarks, are typically called antired, antigreen and antiblue.

94 tinct antiparticle, and are massless, they can split and radiate infinitely. The resulting  
95 soft gluon interactions around quarks lead to an anti-screening effect that causes the  
96 strength of the strong force to change as a function of the distance between interacting  
97 quarks, with close quarks interacting less strongly as far as a single gluon exchange  
98 is concerned. As quark separation gets larger, the potential energy of strong inter-  
99 actions rises rapidly, until it is energetically favorable for the gluon connecting them  
100 to split into a  $q\bar{q}$  pair that screens them and effectively breaks off the interaction.  
101 A single colored particle will thus cause more colored particles to be produced from  
102 vacuum until only colorless bound states remain, enforcing confinement. This pro-  
103 cess is known as hadronization, and causes single quarks or gluons leaving a hard  
104 scattering interaction to produce “jets” of many hadrons, each carrying a fraction of  
105 the original parton momentum, that enter the detector in a conical shower. This is  
106 why a free quark has never been observed, and is not expected to be found, and why  
107 the strong interaction is short-range even though gluons are massless. It is also why,  
108 for example,  $qq\bar{q}$  bound states are not seen in nature. Conversely, close-range QCD  
109 is relatively feeble, leading to “asymptotic freedom,” the property of partons within  
110 hadrons that they may be considered independent in high-energy collisions, because  
111 their interactions are weak enough that bound state effects may be neglected (see  
112 Section 1.6).

113 Leptons may be electrically charged or neutral, and come in three generations,  
114 each containing one lepton of each type, a charged lepton and a corresponding neu-  
115 trino. In order of charged lepton mass, the generations are the electron and its  
116 neutrino ( $e$  and  $\nu_e$ ), muon and its neutrino ( $\mu$  and  $\nu_\mu$ ), and tau and its neutrino ( $\tau$   
117 and  $\nu_\tau$ ). Taus decay quickly, with a mean lifetime of  $2.9 \times 10^{-13}$  s in their rest frame;  
118 muons also decay, but their lifetime ( $2.2 \mu\text{s}$ ) is long compared to other time scales in-  
119 volved in particle collider experiments, so they are considered stable particles for the

120 purposes of this work. Neutrinos are known to have mass [8–10], and the masses are  
 121 known to be small but they have not been measured. All leptons and quarks interact  
 122 via the weak nuclear force, which is best known for causing the nuclear beta decay  
 123 reaction  $n \rightarrow p + e^- + \bar{\nu}_e$ . Neutrinos are notable for coupling to the rest of the SM only  
 124 through weak interactions, making them difficult to detect in practice. Detectors at  
 125 particle colliders make no attempt to detect neutrinos, and their involvement in the  
 126 process is inferred only through the apparent momentum imbalance resulting from  
 127 the fact that they are missed.

128 The weak force operates through two mechanisms, charged-current and neutral-  
 129 current interactions. Neutral-current interactions proceed through exchange of a Z  
 130 boson, an electrically neutral spin-1 mediator, and are analogous to electromagnetic  
 131 interactions except for two important differences. Unlike the  $\gamma$ , the Z has mass—in  
 132 fact, one of the largest known masses at 91 GeV [11]—giving it longitudinal polariza-  
 133 tion modes [2] and limiting the range of the force because it decays with a halflife on  
 134 the order of  $10^{-25}$  s [11]. Also unlike QED, weak interactions do not respect parity  
 135 ( $P$ ) symmetry. The Z boson couples more strongly to left-handed fermions (those  
 136 with helicity opposite their direction of motion) and right-handed antifermions than  
 137 to their opposite-spin counterparts. The degree of asymmetry varies by fermion type;  
 138 notably, the Z does not couple at all to right-handed neutrinos. Neutral-current inter-  
 139 actions are still symmetric under combined charge conjugation ( $C$ ) and parity ( $CP$ )  
 140 transformations, because processes that are odd under  $P$  are also odd under  $C$ .

141 Charged-current interaction proceed through exchange of an electrically charged  
 142 boson, the  $W^\pm$ , which has a mass around 80 GeV [11]. Leptons couple to  $W^+$  bosons  
 143 in  $\ell^-, \bar{\nu}_\ell$  pairs ( $W^+$  bosons likewise with their antiparticles), causing  $\mu$  and  $\tau$  decays.  
 144 Lepton flavor is conserved in the sense that charged leptons couple to the W only  
 145 in conjunction with the (anti-)neutrino from the same generation, so the total lepton

number  $N_\ell = n_{\ell^-} - n_{\ell^+} + n_{\nu_\ell} - n_{\bar{\nu}_\ell}$ , where  $n_X$  is the number of X particles in existence, is conserved separately for  $\ell \in (\text{e}, \mu, \tau)$ . Flavor conservation does not hold for quarks undergoing charged weak interactions. An up-type quark always couples to the W in conjunction with a down-type quark, as it must to obey conservation of electric and color charge. The pairings are in general described by a unitary  $3 \times 3$  matrix known as the Cabibbo–Kobayashi–Maskawa (CKM) matrix which defines the intergenerational mixing [12, 13]. Flavor-changing currents allow heavy quarks to decay to lighter ones, and are thus responsible for the decay of hadrons that do not contain the  $q\bar{q}$  pair necessary for strong or electromagnetic decays.

Charged-current interactions also do not respect parity symmetry, and in fact are maximally parity violating: the W couples only to left-handed fermions and right-handed antifermions. Because neutrinos interact only through the weak force<sup>3</sup>, and the Z also couples only to left-handed neutrinos, this implies that it is not clear if right-handed neutrinos even exist. If they do, they have no way to interact with other matter and they are not part of the SM. Unlike neutral-current interactions, charged-current interactions violate CP symmetry at a small but measurable rate. CP violation was first observed in neutral kaon mixing before the theory of the weak force was fully worked out [14]. After flavor-changing charged currents were formalized it was realized that CP violation could arise from a complex phase in the CKM matrix, which arises in models with at least three generations of quarks<sup>4</sup> [13]. CP violation was subsequently confirmed by observation in a number of meson decays [15–20].

The quantum number analogous to electric charge and color charge for the weak interaction is the three-component weak isospin  $T^i$ , which is typically defined such that the measured component is  $T^3$ . Left-handed fermions have  $|T| = \frac{1}{2}$ , the W $^\pm$

---

<sup>3</sup>Aside from gravity, presumably, but this interaction is not experimentally accessible and is not covered by the standard model.

<sup>4</sup>At the time, only the first two generations were known, so the observed CP asymmetry was taken as an early indication of the existence of top and bottom quarks.

170 has  $|T| = \pm 1$ , and all other particles have  $|T| = 0$ . Weak isospin is conserved in all  
 171 electromagnetic, strong, and fermion-fermion weak interactions, but is not conserved  
 172 in general because the Higgs boson (see below) carries weak isospin. Electric charge  
 173 is always conserved, and is related to the measured component of the weak isospin  
 174 by the weak hypercharge  $Y$ , which is

$$Y = 2(Q - T^3), \quad (1.1)$$

175 where  $Q$  is the electric charge. This connection between the electromagnetic and  
 176 weak forces, and the parallels between the weak neutral-current interaction and QED  
 177 hint at the intriguing possibility that the two forces could be unified under a single  
 178 theory, but important differences—in particular, boson mass—must be explained.  
 179 The mechanism for this is called electroweak symmetry breaking.

### 180 1.3 Electroweak Symmetry Breaking and the 181 Higgs Boson

182 The structures of the fundamental forces arise from symmetries in the underlying  
 183 fields, specifically gauge invariance of the relevant terms in the SM Lagrangian. Much  
 184 of the phenomenology of QCD, for example, arises from the SU(3) symmetry of  
 185 invariance under local color phase transformations, and the fact that the symmetry  
 186 is non-Abelian (i.e. the transformation operators do not commute). Charges are  
 187 the generators of the relevant symmetry group, the conserved currents of Noether’s  
 188 first theorem [21]. A full treatment of the SM’s symmetry group structure and its  
 189 connections to the theory’s phenomenology is given in a number of books, including  
 190 Refs. [2, 4, 5, 22]. The relevant point here is that the weak force arises from an SU(2)  
 191 symmetry generated by the weak isospin  $T$ , and the electromagnetic force from a

192 U(1) symmetry generated by the electric charge  $Q$ , so a unified electroweak force  
 193 should obey an  $SU(2)_L \times U(1)$  symmetry, where the  $L$  indicates that only left-handed  
 194 fermions transform under the  $SU(2)$  symmetry. The resulting unified electroweak  
 195 theory is known as the Glashow–Weinberg–Salam (GWS) model [23–25].

196 An unbroken  $SU(2)_L \times U(1)$  symmetry implies four massless vector gauge fields:  
 197 a triplet  $W_\mu^i (i \in 1, 2, 3)$  which couple to fields with weak isospin (but only for left-  
 198 handed particles), and a singlet  $B_\mu$  which couples to weak hypercharge currents. This  
 199 looks like the weak and electromagnetic forces discussed above, except that the weak  
 200 gauge fields are massless and all three weak bosons are maximally P-violating. The  
 201 gauge bosons can be given mass if the underlying symmetry is somehow broken in the  
 202 theory’s vacuum state. Symmetry breaking occurs via the Higgs mechanism<sup>5</sup> [26–28],  
 203 which introduces an isospin doublet of complex scalar fields

$$\phi = \begin{pmatrix} \phi^+ \\ \phi^0 \end{pmatrix}, \quad (1.2)$$

204 with a Lagrangian of the form

$$\mathcal{L}_H = (D_\mu \phi)^\dagger (D^\mu \phi) + \mu^2 \phi^\dagger \phi - \lambda^2 (\phi^\dagger \phi)^2 \quad (1.3)$$

205 where  $\mu$  and  $\lambda$  are nonzero real numbers,  $D_\mu$  is the covariant derivative invariant  
 206 under  $SU(2)_L \times U(1)_Y$ ,

$$D_\mu = \partial_\mu + igT_i W_\mu^i + i\frac{g'Y}{2}B_\mu, \quad (1.4)$$

207 and  $g$  and  $g'$  are the  $W_\mu^i$  and  $B_\mu$  coupling strengths. Because the potential in Eq. (1.3)  
 208 is not minimized at 0, for small excitations around the vacuum expectation value

---

<sup>5</sup>The Higgs mechanism is also called the Englert–Brout–Higgs–Guralnik–Hagen–Kibble mechanism to acknowledge more of the theorists who developed it, with Anderson and ’t Hooft sometimes included as well.

209 (VEV)  $v = \frac{\mu}{2\lambda} = 246 \text{ GeV}$ , in appropriately chosen coordinates, the doublet of com-  
 210 plex scalar fields is reduced to

$$\phi = \frac{1}{\sqrt{2}} \begin{pmatrix} 0 \\ v + h(x) \end{pmatrix}. \quad (1.5)$$

211 Substituting Eq. (1.5) into Eq. (1.3) introduces mixing terms between the  $W_\mu^i$ ,  
 212  $B_\mu$ , and  $h$  fields. The new Lagrangian has mass eigenstates

$$\begin{aligned} W_\mu^\pm &= \frac{1}{\sqrt{2}} (W_\mu^1 \mp W_\mu^2) \\ Z_\mu &= \frac{gW_\mu^3 - g'B_\mu}{\sqrt{g^2 + g'^2}} = W_\mu^3 \cos \theta_W - B_\mu \sin \theta_W \\ A_\mu &= \frac{g'W_\mu^3 + gB_\mu}{\sqrt{g^2 + g'^2}} = W_\mu^3 \cos \theta_W + B_\mu \sin \theta_W \end{aligned} \quad (1.6)$$

213 where  $\theta_W$  is the Weinberg electroweak mixing angle

$$\tan \theta_W = \frac{g'}{g}. \quad (1.7)$$

214 The newly defined fields are the gauge fields for the weak and electromagnetic forces,  
 215 and in this basis, the Lagrangian has terms

$$\mathcal{L}_{m_V} = -\frac{v^2 g^2}{4} W_\mu^+ W^{-\mu} - \frac{v^2 (g^2 + g'^2)}{8} Z_\mu Z^\mu, \quad (1.8)$$

216 which imply boson masses

$$\begin{aligned} m_W &= \frac{1}{2} v g \\ m_Z &= \frac{1}{2} v \sqrt{g^2 + g'^2} \end{aligned} \quad (1.9)$$

$$m_A = m_\gamma = 0,$$

217 and

$$\cos \theta_W = \frac{m_W}{m_Z}. \quad (1.10)$$

218 The original Higgs doublet in Eq. (1.2) had four degrees of freedom (two complex  
 219 scalars), of which only one remains in the final Higgs field  $H = h - v$ , which is now

220 a physical field with a corresponding massive scalar boson. The other three became  
 221 the longitudinal polarization modes of the vector bosons.

222 Electroweak symmetry breaking thus explains the observed structure of the elec-  
 223 tromagnetic and weak forces. Three bosons become massive, while one stays mass-  
 224 less. Because the photon is massless, the theory retains the  $U(1)_{EM}$  gauge symmetry  
 225 observed in electromagnetic interactions and electric charge is conserved, while the  
 226  $SU(2)$  symmetry is broken and its generator  $T^i$  is not. The  $W^\pm$  bosons still couple  
 227 only to left-handed fermions, while the  $Z$  couples right- and left-handed fermions but  
 228 not equally. The nonzero VEV even gives a convenient mechanism for generation of  
 229 fermion masses in Yukawa couplings with Lagrangian terms of the form

$$\mathcal{L}_{mf} = \sqrt{2} \frac{m_f}{v} (\bar{f}_L f_R + \bar{f}_R f_L). \quad (1.11)$$

230 It also controls off-diagonal terms in the Lagrangian that cause interactions between  
 231 the electroweak bosons, the primary focus of this research.

## 232 1.4 Diboson and Multiboson Physics

233 In addition to the previously discussed boson mass terms introduced into the SM  
 234 Lagrangian by electroweak symmetry breaking, boson interaction terms appear for  
 235 trilinear gauge boson couplings

$$\begin{aligned} \mathcal{L}_{WWV} = -ig & [ (W_{\mu\nu}^+ W^{-\mu} - W^{+\mu} W_{\mu\nu}) (A^\nu \sin \theta_W - Z^\nu \cos \theta_W) \\ & + W_\nu^- W_\mu^+ (A^{\mu\nu} \sin \theta_W - Z^{\mu\nu} \cos \theta_W) ], \end{aligned} \quad (1.12)$$

236 which results in the vertices shown in fig 1.1; quartic gauge couplings

$$\begin{aligned} \mathcal{L}_{WWVV} = -\frac{g^2}{4} & \left\{ [2W_\mu^+ W^{-\mu} + (A_\mu \sin \theta_W - Z_\mu \cos \theta_W)^2]^2 \right. \\ & - [W_\mu^+ W_\nu^- + W_\nu^+ W_\mu^- \\ & \left. + (A_\mu \sin \theta_W - Z_\mu \cos \theta_W) (A_\nu \sin \theta_W - Z_\nu \cos \theta_W)]^2 \right\}, \end{aligned} \quad (1.13)$$

<sup>237</sup> (Fig. 1.2); Higgs couplings to the massive vector bosons

$$\mathcal{L}_{HV} = \left( g m_W H + \frac{g^2}{4} H^2 \right) \left( W_\mu^+ W^{-\mu} + \frac{Z_\mu Z^\mu}{2 \cos^2 \theta_W} \right), \quad (1.14)$$

<sup>238</sup> (Fig. 1.3); and Higgs self-interactions

$$\mathcal{L}_{HH} = -\frac{g m_H^2}{4 m_W} H^3 - \frac{g^2 m_H^2}{32 m_W^2} H^4, \quad (1.15)$$

<sup>239</sup> (Fig. 1.4).

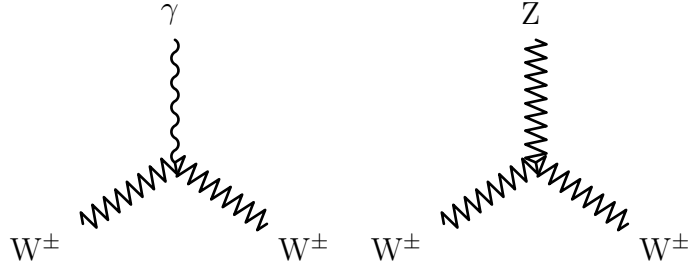


Figure 1.1: Vertex for the trilinear gauge boson couplings allowed at tree level in the SM.

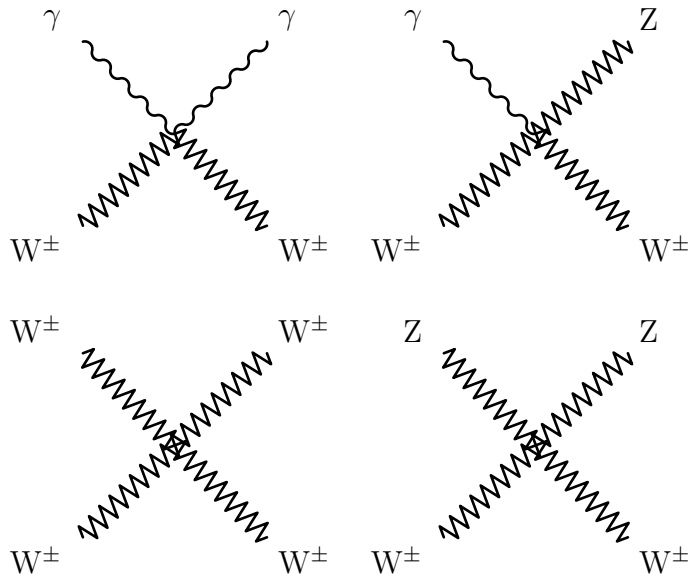


Figure 1.2: Vertices for the quartic gauge boson couplings allowed at tree level in the SM.

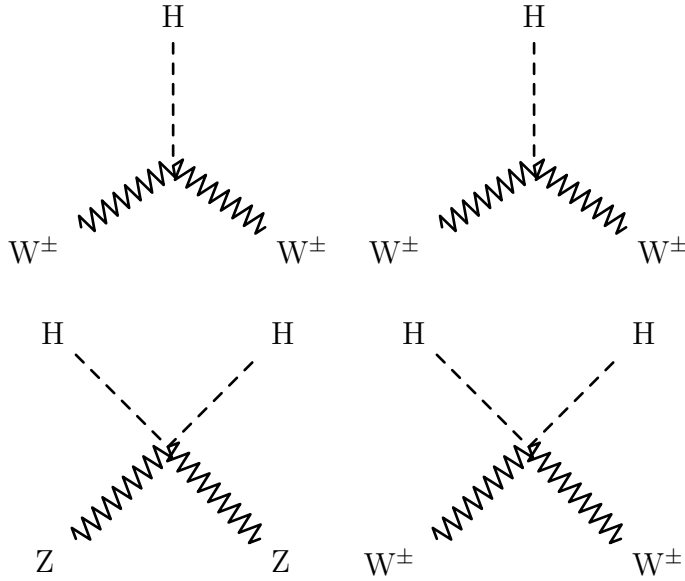


Figure 1.3: Vertices for Higgs boson couplings to gauge bosons allowed at tree level in the SM.

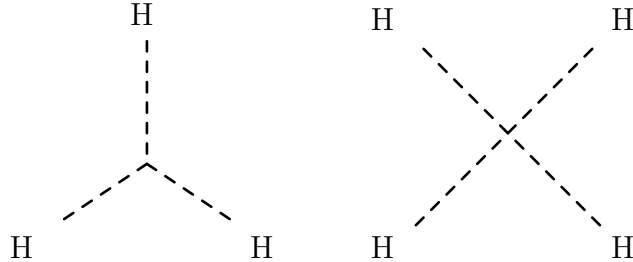


Figure 1.4: Higgs boson trilinear and quartic self-coupling vertices.

240        The structure of the interactions shown in Figs. 1.1–1.4 depends on the details  
 241        of the GWS model and spontaneous symmetry breaking, making multiboson interac-  
 242        tions excellent probes of the SM electroweak and Higgs sectors. One can confirm the  
 243        basic validity of the Higgs mechanism by observation of a Higgs boson, and its inter-  
 244        actions with the massive gauge bosons can be probed in decays to  $ZZ^*$  and  $W^\pm W^{\mp*}$ ,  
 245        which were in fact used in its discovery (see Section 2.2.2.1). The SM makes a num-  
 246        ber of other testable predictions about the behavior of the electroweak bosons, the  
 247        most easily testable of which are the multiboson production cross sections, i.e. the

248 rates at which particle collisions result in final states with two or more electroweak  
 249 gauge bosons. The tree-level diagrams for general diboson production in fermion-  
 250 antifermion collisions ( $f\bar{f} \rightarrow VV$ ) are shown in Fig. 1.5. The cross section for such  
 251 a process will be strongly dependent on the gauge bosons' couplings to fermions, in  
 252 the first diagram in Fig. 1.5, and their couplings to other gauge bosons in the second  
 253 diagram (which does not contribute at all for neutral gauge bosons in the SM). Dibo-  
 254 son production in gg collisions does not occur at tree level but may proceed through  
 255 a quark loop as in the so-called box diagram of Fig. 1.6.

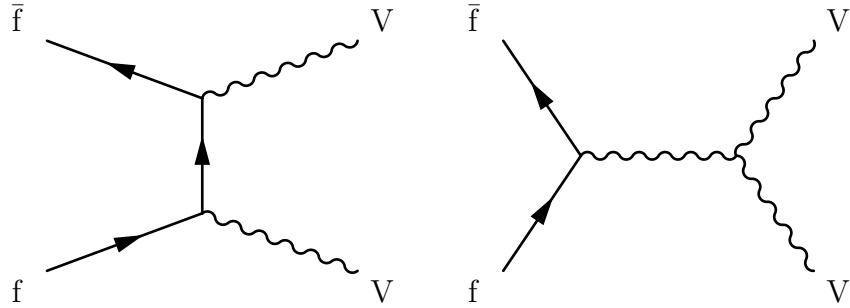


Figure 1.5: Tree-level Feynman diagrams for diboson production in fermion-anti-fermion collisions. The second diagram does not contribute for neutral gauge bosons in the SM.

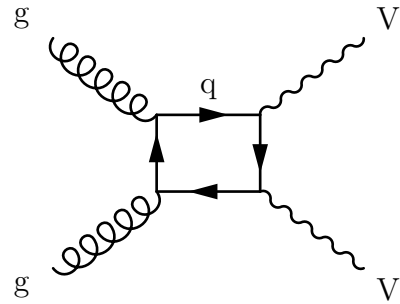


Figure 1.6: Leading order “box” diagram for diboson production through a quark loop in a gluon-gluon fusion event.

### 256 1.4.1 Vector Boson Scattering

257 Quasielastic vector boson scattering (VBS) interactions ( $VV \rightarrow VV$ ) are sensitive  
 258 to a number of features of the SM electroweak sector. If only the vector bosons are  
 259 considered, the scattering amplitude for the process grows quadratically with the  
 260 center-of-mass energy, violating unitarity [29]. Interference from diagrams involving  
 261 the Higgs boson restores unitarity, as shown in Fig. 1.7. The VBS cross section is  
 262 therefore sensitive to both the four-point gauge boson couplings of Fig. 1.2 and the  
 263 structure of the Higgs field, and can be used to distinguish the SM from models  
 264 without a Higgs boson and models with multiple particles that play its role.

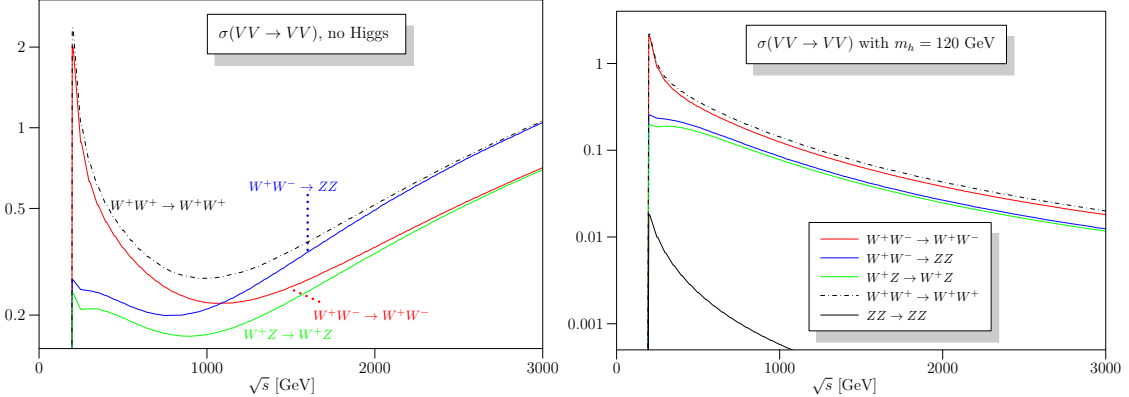


Figure 1.7:  $VV \rightarrow VV$  scattering cross sections as a function of center-of-mass energy for the SM with no Higgs boson (left) and a Higgs boson with  $m_H = 120$  GeV (right), reproduced from Ref. [29]. The model with no Higgs violates unitarity.

### 265 1.5 Limitations and Possible Extensions

266 As noted above, the SM is believed to be fully self-consistent, but it has several notable  
 267 omissions. It makes no mention of gravity, which is too weak to be probed at the  
 268 level of individual particles at energies available in collider experiments. Neutrinos in  
 269 the SM are massless, but they are found experimentally to oscillate between the three

270 flavors in flight, which implies that the flavor eigenstates are not mass eigenstates,  
 271 and thus that they have mass. Dark matter, the unidentified substance that makes up  
 272 roughly 80% of the universe’s gravitationally interacting material [11, 30–32], is also  
 273 not described. Some consider the SM to be “ad hoc” in the sense that the fermion  
 274 masses, and a number of other parameters—19 in all—are completely unconstrained,  
 275 and a more aesthetically satisfying theory would make predictions for all of them. A  
 276 nicer theory would also offer thorough explanations for what seem now like remarkable  
 277 coincidences. For example, the so-called hierarchy problem: it is intuitively surprising  
 278 that the strengths of the fundamental forces vary by many orders of magnitude, and  
 279 do so in such a way that large quantum corrections to the effective Higgs potential  
 280 cancel almost exactly, causing the Higgs boson mass to be nonzero but much smaller  
 281 than the scale of the corrections ( $\mathcal{O}(10^{19} \text{ GeV})$ ) [33–35].

282 A number of theories have been proposed which modify or extend the SM [11,  
 283 32], adding new symmetry groups, unifying the existing ones further, adding new  
 284 particles, etc. A fourth generation of fermions would be a simple extension, but the  
 285 fourth neutrino would have to have a mass more than half the Z boson mass to have  
 286 escaped detection so far, which would be surprising given the small masses of the  
 287 first three [11, 36]. Supersymmetric models, for example, posit a symmetry between  
 288 bosons and fermions, such that each particle would have a “superpartner” with the  
 289 opposite spin statistics which would provide an opposite correction to the effective  
 290 Higgs potential and thus a clean solution to the hierarchy problem [11, 37]. Despite  
 291 extensive searches, no evidence of such models has been found [38].

### 292 **1.5.1 Anomalous Gauge Couplings**

293 Another simple extension to the SM would be a new force, with mediator gauge bosons  
 294 analogous to the W and Z above the masses accessible at existing colliders. Such a

295 force would originate from a previously undiscovered symmetry, which in many models  
 296 could result from a higher symmetry which unifies all the fundamental forces at high  
 297 energy but is broken and effectively reduces to the SM in the low-energy limit [11,  
 298 33, 35, 39]. This, and several other possible extensions to the SM, would appear in  
 299 practice as small deviations from the expected couplings of the gauge bosons. Such  
 300 deviations from standard model interactions are called anomalous gauge couplings  
 301 (aGC), and may involve anomalous trilinear (aTGC) or quartic (aQGC) vertices. Of  
 302 particular interest here are the anomalous neutral couplings, which correspond to  
 303 the vertices shown in Fig. 1.8. These interactions are forbidden in the SM. Their  
 304 existence would increase the cross section for diboson production, and affect the cross  
 305 section for  $ZZ \rightarrow ZZ$  scattering, changing the requirements on the Higgs field needed  
 306 to preserve unitarity.

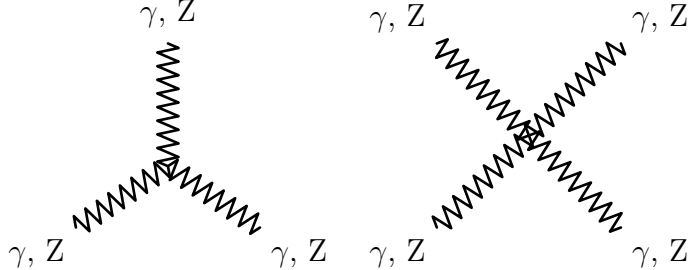


Figure 1.8: Fully-neutral gauge coupling vertices, for aTGCs (left) and aQGCs (right). These are forbidden in the SM.

307 Several theoretical frameworks exist for describing aGCs. For aTGCs, we use the  
 308 effective Lagrangian approach described in Ref. [40–42]. In this parameterization, a  
 309  $ZZV$  coupling (where  $V$  may be  $Z$  or  $\gamma$ ) has a vertex function corresponding to the  
 310 vertex shown in Fig. 1.9 of the form

$$\Gamma_V^{\alpha,\beta,\delta}(q_1, q_2, P) = i \frac{\hat{s} - m_V^2}{m_Z^2} (f_4^V (P^\alpha g^{\delta\beta} + P^\beta g^{\delta\alpha}) + f_5^V \varepsilon^{\delta\alpha\beta\lambda} (q_1 - q_2)_\lambda), \quad (1.16)$$

311 where  $\hat{s}$  is the center of mass energy squared,  $g^{\mu\nu}$  is the Minkowski metric and  $\varepsilon^{\alpha\beta\gamma\delta}$  is  
 312 the fully antisymmetric tensor with  $\varepsilon^{0123} = 1$ . Neutral aTGCs are then described by

313 two parameters  $f_4^{\gamma,Z}$  associated to CP-odd terms and two parameters  $f_5^{\gamma,Z}$  associated  
 314 to CP-even terms.<sup>6</sup> The effective Lagrangians in use here are taken to be low-energy  
 315 approximations invalid at high energy, and are not unitary at high  $\sqrt{\hat{s}}$ . In some  
 316 previous literature (see Section 2.3.1), unitarity is enforced with a generalized dipole  
 317 for factor [42, 43], such that the vertex factor takes an energy dependence,

$$f_i^V(\hat{s}) = \frac{f_{i,0}^V}{(1 + \hat{s}/\Lambda^2)^n}, \quad (1.17)$$

318 where  $\Lambda$  is the energy scale of the new physics process. No such form factor is applied  
 319 in this work, to avoid adding unnecessary model dependence, so  $\Lambda$  is taken to be much  
 320 larger than the energies accessible in the experiment and no form factor is applied.

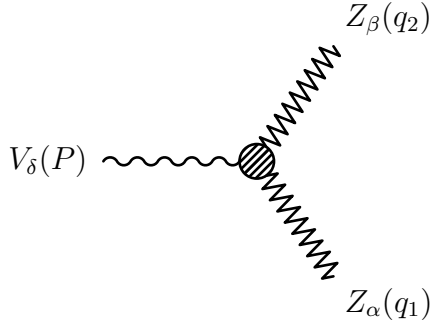


Figure 1.9: An anomalous neutral triple gauge coupling vertex, with momentum labels corresponding to Eq. (1.16).

321 For aQGCs, we adopt an effective field theory approach [44] which parameterizes  
 322 the effects of new physics as a set of field operators [45]. The operators are chosen to  
 323 be dimension-8, because this is the lowest dimension that can yield neutral quartic  
 324 couplings, and the lowest dimension that can produce a theory with aQGCs but no  
 325 aTGCs. Out of the large class of operators which control aQGCs in general, ZZ VBS

---

<sup>6</sup>There are, of course, analogous terms for all anomalous VVV couplings, where V may be any of the electroweak bosons, but only the ZZZ and ZZ $\gamma$  terms are relevant to this work.

326 is sensitive to five,

$$\begin{aligned}\mathcal{L}_{T0} &= \frac{f_{T0}}{\Lambda^4} \text{Tr} [\hat{W}_{\mu\nu} \hat{W}^{\mu\nu}] \times \text{Tr} [\hat{W}_{\alpha\beta} \hat{W}^{\alpha\beta}] \\ \mathcal{L}_{T1} &= \frac{f_{T1}}{\Lambda^4} \text{Tr} [\hat{W}_{\alpha\nu} \hat{W}^{\mu\beta}] \times \text{Tr} [\hat{W}_{\mu\beta} \hat{W}^{\alpha\nu}] \\ \mathcal{L}_{T2} &= \frac{f_{T2}}{\Lambda^4} \text{Tr} [\hat{W}_{\alpha\mu} \hat{W}^{\mu\beta}] \times \text{Tr} [\hat{W}_{\beta\nu} \hat{W}^{\nu\alpha}] \\ \mathcal{L}_{T8} &= \frac{f_{T8}}{\Lambda^4} B_{\mu\nu} B^{\mu\nu} B_{\alpha\beta} B^{\alpha\beta} \\ \mathcal{L}_{T9} &= \frac{f_{T9}}{\Lambda^4} B_{\alpha\mu} B^{\mu\beta} B_{\beta\nu} B^{\nu\alpha},\end{aligned}\tag{1.18}$$

327 where

$$\hat{W}_{\mu\nu} = \sum_j W_{\mu\nu}^j \frac{\sigma^j}{2},\tag{1.19}$$

328 and  $\Lambda \gg \sqrt{s}$  is again the scale of the new physics causing the change in the effective  
329 couplings.

## 330 1.6 Proton-Proton Collisions

331 Our experimental probe of all these interactions is proton-proton collisions. As dis-  
332 cussed above, protons are bound states of three quarks (uud), known as the valence  
333 quarks, held together by virtual gluon exchange. The proton constituents, quarks and  
334 gluons, are collectively called partons. The gluons carry roughly half the total proton  
335 momentum [2]. Because the number of gluons is not conserved, and they self-interact,  
336 the gluon structure of the proton is constantly evolving, and gluons produce virtual  
337  $q\bar{q}$  “sea quark” pairs which annihilate again on time scales of order  $t_{virt} \sim 1/\Delta E$  [3].  
338 A sufficiently energetic color-charged particle colliding with a proton may therefore  
339 interact with any kind of quark or with a gluon, and interesting physics in a pp  
340 collision may be initiated by  $qq$ ,  $q\bar{q}$ ,  $qg$ , or  $gg$  scattering. A particle that scatters  
341 with a proton of energy  $P$  has a probability of interacting with a parton of a given  
342 type with momentum  $xP$  given by the parton distribution function (PDF)  $f(x, Q^2)$ ,

343 where  $x$  is the fraction of the proton momentum carried by the parton and  $Q$  is the  
 344 momentum transfer of the interaction [3]. Heuristically, the PDF is a function of  $Q$   
 345 because it sets the wavelength of the mediating gauge boson and thus the scale on  
 346 which the interaction can resolve constituent partons. PDFs are nonperturbative and  
 347 have not been calculated from theory, so they are built from fits to experimental data  
 348 from fixed-target and symmetric  $e^\pm p$  deep inelastic scattering (DIS) data, and from  
 349 hadron collider data [46]. The most recent PDFs from the NNPDF collaboration [46]  
 350 are shown in Fig 1.10.

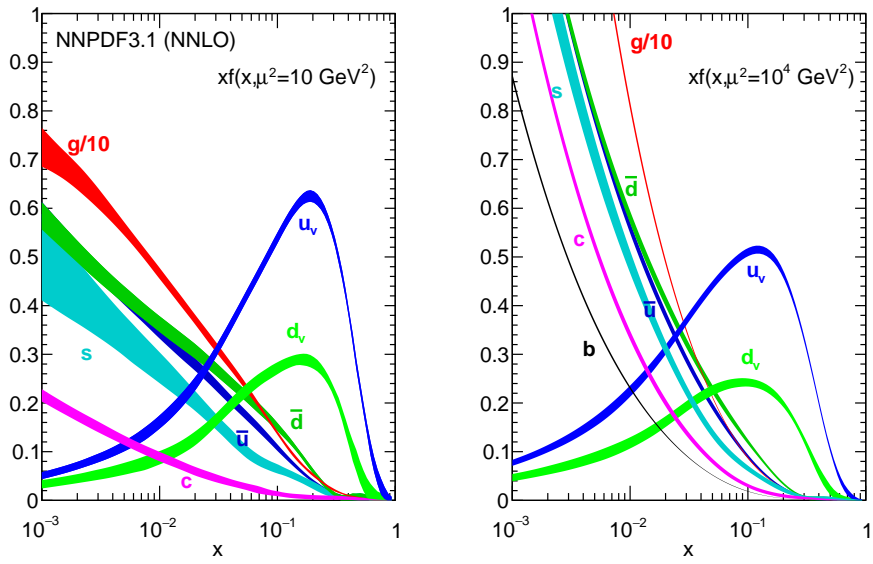


Figure 1.10: Parton distribution functions from NNPDF3.1, reproduced from Ref. [46], which used  $\mu$  for the momentum transfer denoted  $Q$  in the text.

351 As mentioned previously, the rate at which a scattering process occurs is called its  
 352 cross section  $\sigma$ , typically given in barns, a unit of area  $b = 10^{-24} \text{ cm}^2$ . The number  
 353 of collisions is characterized by the luminosity  $\mathcal{L}$  such that the rate of events with  
 354 final state  $X$  will be given by

$$\frac{dN_X}{dt} = \sigma(\text{pp} \rightarrow X) \mathcal{L} \quad (1.20)$$

as described in more detail in Section 3.1. If the initial protons each have momentum  $P$  and collide head on, such that their center-of-mass energy is  $\sqrt{s} = 2P$ , the interacting partons will have total energy  $\sqrt{\hat{s}} = \sqrt{2x_1x_2}P$  where  $x_1$  and  $x_2$  are the fraction of its proton's momentum each incoming parton carried. The cross section is given by

$$\sigma(pp \rightarrow X) = \sum_{p_1, p_2 \in q, \bar{q}, g} C_{p_1, p_2} \int dx_1 dx_2 f_{p_1}(x_1, Q^2) f_{p_2}(x_2, Q^2) \sigma_{\text{ME}}(p_1 + p_2 \rightarrow X), \quad (1.21)$$

where  $\sigma_{\text{ME}}$  is the matrix-level cross section for the bare partons to scatter to final state  $X$  and  $C_{p_1, p_2}$  is a combinatoric factor based on the number of possible color combinations that varies based on the initial state particles  $p_1$  and  $p_2$ . This factorization into perturbative hard process physics and the nonperturbative PDF greatly simplifies calculations.

## 1.7 ZZ Measurements in Context

This is the context for the work described in the following chapters: the SM is incomplete, but it has been tested extensively and no discrepancies have been found (a partial review of studies that did not exclude the SM can be found in Chapter 2). Because the electroweak sector was the last to be confirmed experimentally and is generally best explored at high energies, a number of aspects await detailed confirmation and remain a potential area where new physics might be found. This thesis presents several studies of diboson events with  $\ell^+ \ell^- \ell'^+ \ell'^-$  ( $\ell, \ell' \in e, \mu$ ) final states designed to probe the interactions of the neutral electroweak bosons. In particular, as one can deduce from Eqs. (1.12)–(1.14), ZZ production processes are sensitive to the details of the couplings between the gauge bosons and can therefore be used to investigate the GWS model and the Higgs model and spontaneous symmetry break-

377 ing. Measurements of ZZ production have been made before, but measurements  
378 in a new energy regime and with a very large dataset allow stringent new tests of  
379 the SM and allow the potential observation of previously unseen phenomena within  
380 and beyond it. The results presented here substantially expand our understanding  
381 of ZZ production, with inclusive and differential cross section measurements at the  
382 record-breaking center-of-mass energy of 13 TeV, the most precise measurement of  
383 the  $Z \rightarrow 4\ell$  branching fraction to date, and searches for vector boson scattering and  
384 anomalous neutral gauge couplings.

## **₀ Chapter 2**

# **₁ ZZ Phenomenology and Previous ₂ Results**

₃ Four-lepton final states originate primarily from three physics processes: nonresonant  
 ₄ diboson production, resonant Higgs boson production, and resonant single-Z produc-  
 ₅ tion. Multi-Z triboson production (WZZ and ZZZ) occurs at negligible rates [47, 48].  
 ₆ Single-Z triboson production (WWZ) [48, 49] and t̄tZ production result in final states  
 ₇ with four prompt leptons, but are considered background (see Section 2.4). The three  
 ₈ signal processes can be distinguished by kinematics, but all involve the Z boson.

₉       The Z was first indirectly observed in 1973 when the Gargamelle bubble chamber  
 ₁₀ experiment at CERN recorded an elastic muon antineutrino-electron ( $\bar{\nu}_\mu + e^- \rightarrow$   
 ₁₁  $\bar{\nu}_\mu + e^-$ ) scattering event [50]. Direct observation in leptonic decays came roughly  
 ₁₂ a decade later, from the UA1 experiment, also at CERN [51]. Clean  $e^+e^-$  collisions  
 ₁₃ at LEP and SLAC, where the center-of-mass energy could be adjusted to produce  
 ₁₄ Z bosons copiously, allowed its properties—and a number of other parameters of  
 ₁₅ the electroweak theory—to be measured with per-mille precision or better [52]. Of

16 particular importance to this study, the Z mass is

$$m_Z = 91.1876 \pm 0.0021 \text{ GeV}, \quad (2.1)$$

17 its full width is

$$\Gamma_Z = 2.4952 \pm 0.0023 \text{ GeV}, \quad (2.2)$$

18 its width in leptonic decays is

$$\Gamma_Z(\ell^+\ell^-) = 83.984 \pm 0.086 \text{ MeV}, \quad (2.3)$$

19 and it decays to a pair of charged leptons 3.3658% of the time for each lepton fla-  
20 vor [11].

## 21 **2.1 Nonresonant ZZ/Z $\gamma^*$ Production and Decay**

22 Leading-order ZZ production is q $\bar{q}$ -initiated and proceeds through  $t$ -channel quark  
23 exchange, as shown in Fig. 2.1. At next-to-leading order (NLO; several representa-  
24 tive diagrams are shown in Fig. 2.2), production may have a gluon in the initial state  
25 and may have a quark or gluon in the final state which hadronizes and appears exper-  
26 imentally as a jet [53–55]. Next-to-next-to-leading order (NNLO) adds gluon-gluon  
27 fusion box diagrams (Fig. 2.3), as well as q $\bar{q}$ -initiated production with two loops, one  
28 loop and a final state jet, and two jets [56, 57]. The NNLO corrections are generally  
29 large, outside the scale uncertainties of the NLO calculation, because the gluon-fusion  
30 diagrams contribute only positively to the cross section due to their distinct initial  
31 state, and have a large amplitude—roughly 60% of the total NNLO correction—due  
32 to the high effective gluon luminosity in multi-TeV proton collisions [56]. Because  
33 of the box diagrams’ large contribution, “NLO + gg” simulations are often used, in  
34 which NLO q $\bar{q}$ /qg/ $\bar{q}g \rightarrow ZZ$  and LO gg  $\rightarrow ZZ$  samples are summed even though they  
35 formally contribute at different orders in  $\alpha_s$ .

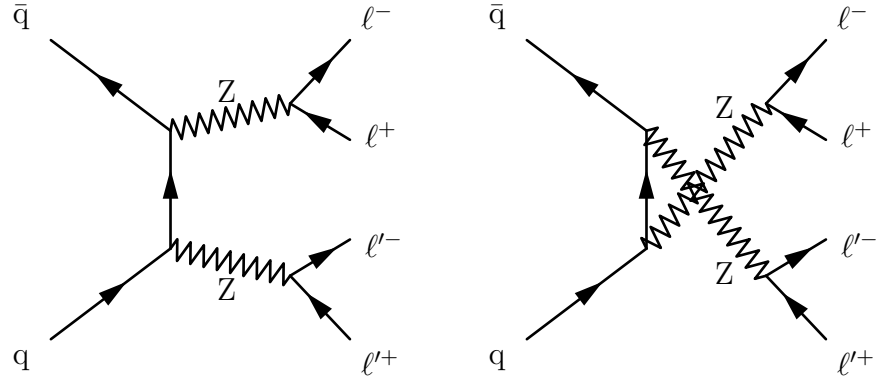


Figure 2.1: Leading order Feynman diagrams for  $ZZ \rightarrow 4\ell$  production in  $pp$  collisions.

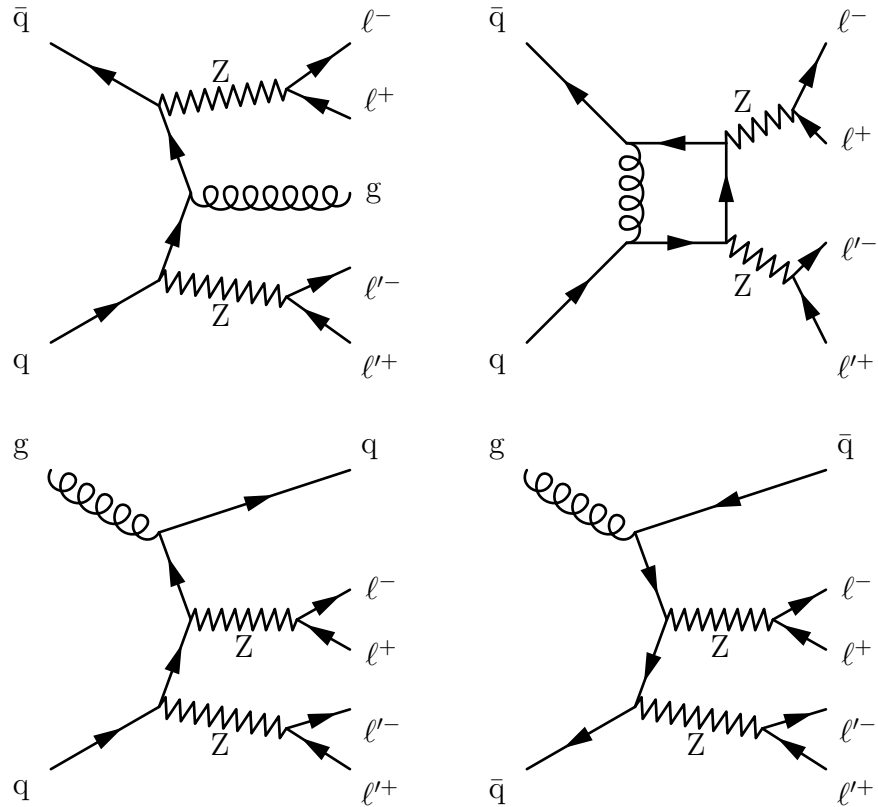


Figure 2.2: Three representative NLO Feynman diagrams for  $ZZ \rightarrow 4\ell$  production in  $pp$  collisions. Clockwise from the top right, the NLO diagrams are examples of one-loop diagrams, real antiquark and quark emission, and real gluon emission.

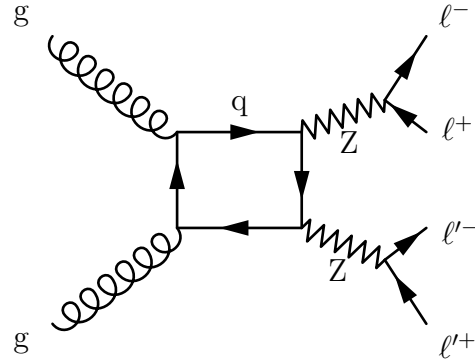


Figure 2.3: A LO box diagram for  $ZZ \rightarrow 4\ell$  production through a quark loop in a gluon-gluon fusion event. This is formally an NNLO diagram for  $ZZ$  production overall, but is often included in NLO calculations because it accounts for a large fraction of the NNLO correction, due to the high effective gluon luminosity in proton collisions at high  $Q^2$ .

36 Production of pairs of on-shell Z bosons<sup>1</sup> turns on sharply at the kinematic thresh-  
 37 old  $\sqrt{\hat{s}} = 2m_Z = 182.4$  GeV, and in proton-proton collisions at  $\sqrt{s} = 13$  TeV, peaks  
 38 around  $m_{ZZ} \approx 200$  GeV before falling steeply at higher invariant masses. Continuum  
 39 production occurs below the kinematic threshold when one or both Z bosons are re-  
 40 placed by a  $Z^*/\gamma^*$  admixture, typically in the form of a  $q\bar{q} \rightarrow Z$  event in which one of  
 41 the incoming quarks emits a virtual photon as initial state radiation (ISR). Events of  
 42 interest in this analysis (see Sections 5.4 and 6.3) generally have one on-shell Z, and  
 43 a  $Z^*/\gamma^*$  at a lower mass. Nonresonant  $Z\gamma^*$  production is generally flat as a function  
 44 of invariant mass between roughly 100 GeV and the doubly resonant threshold.

### 45 2.1.1 Vector Boson Scattering

46 Vector boson scattering proceeds at hadron colliders through the diagrams shown in  
 47 Fig 2.4, resulting in a  $ZZjj$  final state. This fully electroweak (EWK) production

---

<sup>1</sup>Events with two on-shell Z bosons are often called “doubly resonant,” but are a subset of “nonresonant” production in the sense that the  $ZZ$  system is not produced by a resonance. Either term may be used to distinguish “continuum” production from “singly resonant” production from  $Z \rightarrow 4\ell$ ,  $H \rightarrow ZZ^*$ , or a potential new particle which decays to  $ZZ$ .

48 must be distinguished from the background of QCD-initiated ZZ + jets events (see  
 49 Section 2.4). The hallmark of the EWK process is a pair of high energy, high ra-  
 50 pidity jets from the quarks, which retain a high boost along the  $z$ -axis even after  
 51  $W^\pm$  or  $Z$  emission and are thus deflected through a small angle in the lab frame. At  
 52 the same time, the ZZ system is produced with high invariant mass and low boost  
 53 compared to QCD-initiated ZZjj events, in which the ZZ system recoils against the  
 54 jets [58]. Because the hard scattering interaction involves no color exchange or recon-  
 55 nection [58–60], VBS events are much less likely to have less energetic jets between  
 56 the two high-energy quark jets. Useful variables to discriminate between EWK and  
 57 QCD production therefore include the angle between the jets, the jet energies, the  
 58 dijet invariant mass, the ZZ invariant mass and rapidity, and the number of central  
 59 jets (see Section 6.5 for a full list and definitions).

### 60 2.1.2 Prior Measurements

61 Doubly resonant ZZ production was first observed in  $e^+e^-$  collisions at LEP by the  
 62 ALEPH, OPAL, L3, and DELPHI experiments, from 183 GeV, just above the thresh-  
 63 old center-of-mass energy, to the LEP maximum of 209 GeV [61–66]. Because the ZZ  
 64 cross section is very small, these measurements used all possible final states except  
 65 those in which all Z decay products were neutrinos or taus. This was possible because  
 66  $e^+e^-$  collisions do not suffer from the hadronization effect described above, so jets can  
 67 be reliably matched to a hard scattering process, allowing identification of  $Z \rightarrow q\bar{q}$   
 68 decays. The measurements agreed with the SM, but were dominated by statistical  
 69 uncertainties. Example measured cross sections from OPAL are shown in Fig 2.5 [65].

70 Production in hadron collisions was first observed by the CDF and D0 experi-  
 71 ments, in 1.96 TeV  $p\bar{p}$  events at Tevatron [67–71]. In contrast to the LEP measure-  
 72 ments,  $p\bar{p}$  colliders cause too many extraneous jets for the hadronic channels to be

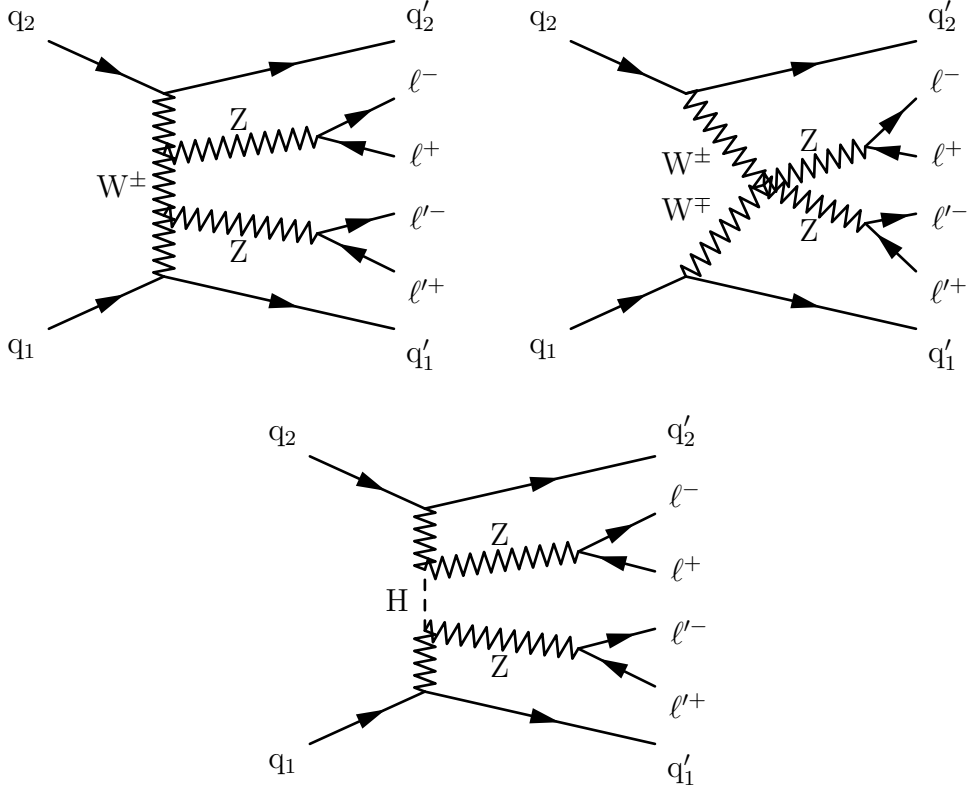


Figure 2.4: The primary ZZ VBS diagrams at hadron colliders. Diagrams also exist with antiquarks and with permutation and crossing of the final state particles. The interaction is only unitary to arbitrarily high energy when all diagrams are considered.

73 seen above the background, so only the  $4\ell$  and  $2\ell 2\nu$  ( $\ell = e, \mu$ ) final states were used.  
 74 These fully leptonic decay modes have small branching fractions on top of the small  
 75 ZZ cross section of around  $1.6 \text{ pb}$  [53], but the total Tevatron dataset of roughly  $6 \text{ fb}^{-1}$   
 76 was large enough for CDF and D0 to find a few dozen events each. Results were again  
 77 fully consistent with the SM but the statistical uncertainties were large, as can be  
 78 seen in the example  $m_{4\ell}$  shown in Fig. 2.6 [70].

79 The first run of the LHC (see Section 3.1) produced large datasets of pp collisions  
 80 at  $\sqrt{s} = 7$  and  $8 \text{ TeV}$ , producing ZZ events with a higher cross section than at  
 81 Tevatron [56] and with a greater integrated luminosity. The measurement channels  
 82 were again the fully leptonic  $4\ell$  and  $2\ell 2\nu$  decays, and the cross sections were measured

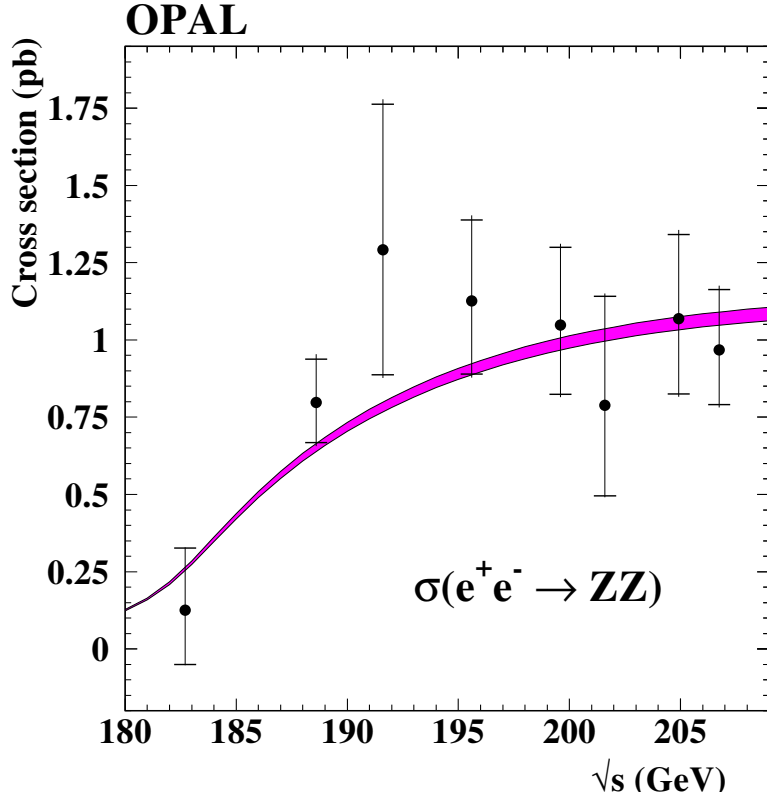


Figure 2.5: Measured  $e^+e^- \rightarrow ZZ$  cross sections from the OPAL experiment, reproduced from Ref. [65]. Points represent the measured values. Vertical bars are the total uncertainty with horizontal bars indicating the statistical uncertainties, which dominate. The band is the SM prediction with a 2% theoretical uncertainty.

at  $\sqrt{s} = 7$  and 8 TeV by both CMS [72–75] and ATLAS [76–78]. With a dataset of roughly  $20\text{ fb}^{-1}$  and signal event counts in the hundreds even for the low-rate  $4\ell$  channel, the 8 TeV measurements had the statistical power to include differential cross sections as functions of kinematic observables for the ZZ system and the associated jets. Statistical uncertainties were still larger than the systematic uncertainties, but they were at the level of 5–10% for the total cross section, compared to 30–50% at Tevatron and 15–150% at LEP depending on the experiment and center-of-mass energy<sup>2</sup>. The four-lepton mass spectra from the CMS and ATLAS ZZ cross section

<sup>2</sup>Most LEP ZZ cross section measurements had statistical uncertainties around 20–40%; see references given in the text for details.

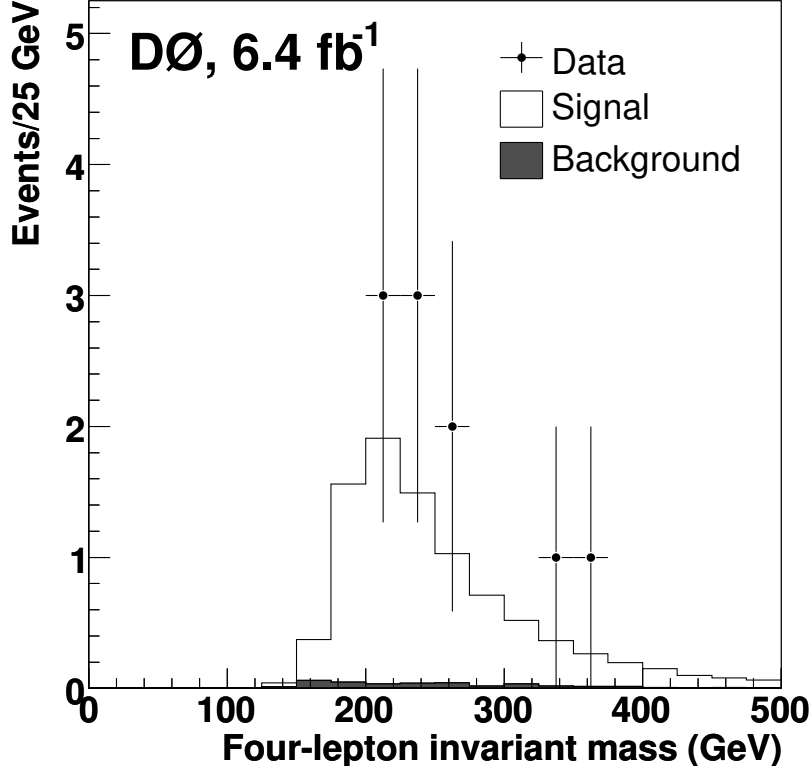


Figure 2.6: Measured  $m_{4\ell}$  distribution from ZZ events collected by D0, reproduced from Ref. [70]. Points represent data with vertical bars showing statistical uncertainties, while the histograms show the SM expectation.

91 measurements at 8 TeV are shown in Figs. 2.7 and 2.8, respectively [73, 77].

92 CMS found that the total ZZ cross sections, defined as the cross sections of all  
93 events with two Z bosons in the mass range 60–120 GeV, to be

$$\begin{aligned}\sigma_{ZZ}(7 \text{ TeV}) &= 6.24^{+0.86} (\text{stat})^{+0.41} (\text{syst}) \pm 0.14 (\text{lumi}) \text{ pb} \\ \sigma_{ZZ}(8 \text{ TeV}) &= 7.7 \pm 0.5 (\text{stat})^{+0.5}_{-0.4} (\text{syst}) \pm 0.4 (\text{theo}) \pm 0.2 (\text{lumi}) \text{ pb},\end{aligned}\tag{2.4}$$

94 when measured with  $4\ell$  final states [73, 76], and

$$\begin{aligned}\sigma_{ZZ}(7 \text{ TeV}) &= 5.1^{+1.5}_{-1.4} (\text{stat})^{+1.4}_{-1.1} (\text{syst}) \pm 0.1 (\text{lumi}) \text{ pb} \\ \sigma_{ZZ}(8 \text{ TeV}) &= 7.2 \pm 0.8 (\text{stat})^{+1.9}_{-1.5} (\text{syst}) \pm 0.2 (\text{lumi}) \text{ pb}\end{aligned}\tag{2.5}$$

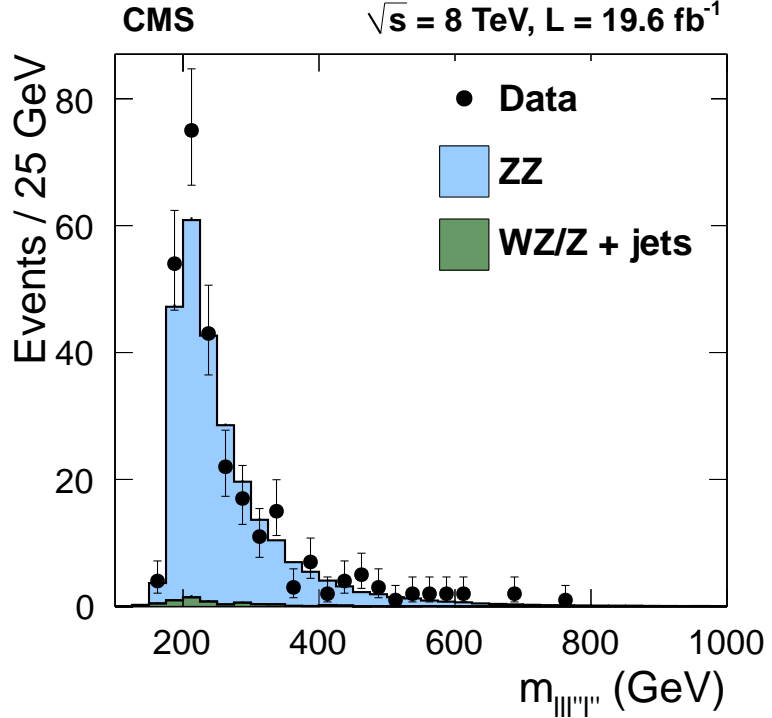


Figure 2.7: Measured  $m_{4\ell}$  distribution from ZZ events collected by CMS at  $\sqrt{s} = 8$  TeV, reproduced from Ref. [77]. Points represent data with vertical bars showing statistical uncertainties, while the histograms show the SM expectation. The grey hatched band represents the total uncertainty on the prediction.

when measured with  $2\ell 2\nu$  final states [74]. ATLAS found

$$\begin{aligned}\sigma_{ZZ}(7 \text{ TeV}) &= 6.7 \pm 0.7 \text{ (stat)}^{+0.4}_{-0.3} \text{ (syst)} \pm 0.3 \text{ (lumi)} \text{ pb} \\ \sigma_{ZZ}(8 \text{ TeV}) &= 7.3 \pm 0.4 \text{ (stat)} \pm 0.3 \text{ (syst)} \pm 0.2 \text{ (lumi)} \text{ pb},\end{aligned}\quad (2.6)$$

using  $4\ell$  final states at 7 TeV [76] and a combination of  $4\ell$  and  $2\ell 2\nu$  events at 8 TeV [78]. ATLAS used a slightly different definition of the Z, considering it to have mass in the range 66–116 GeV, which reduces the SM expected cross section by 1.6% [79]. Measured cross sections from both experiments are again consistent with SM predictions of  $6.7 \pm 0.2$  pb at 7 TeV and  $8.3 \pm 0.2$  pb at 8 TeV, both calculated at NNNLO in QCD with MATRIX, with factorization and renormalization scales  $\mu_F = \mu_R = m_Z$ .

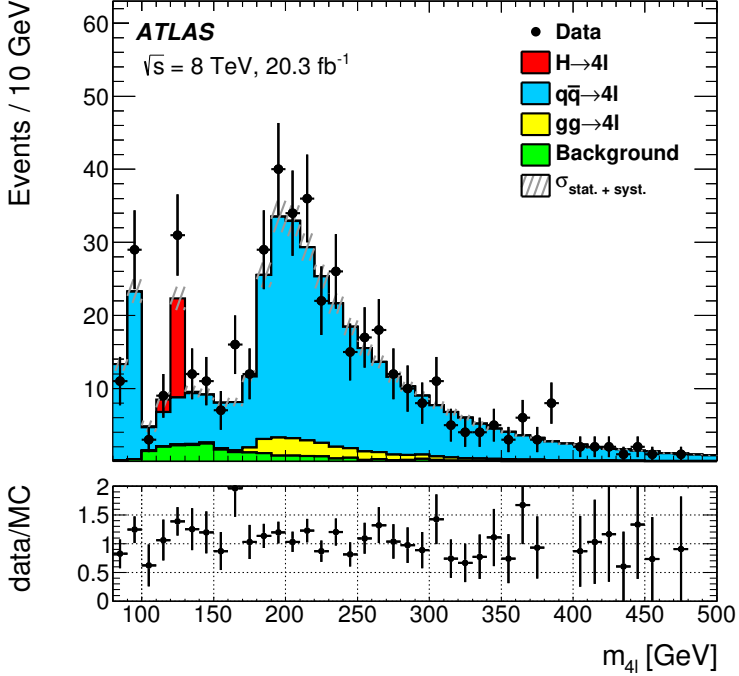


Figure 2.8: Measured  $m_{4\ell}$  distribution from ZZ events collected by ATLAS at  $\sqrt{s} = 8$  TeV, reproduced from Ref. [70]. Points represent data with vertical bars showing statistical uncertainties, while the histograms show the SM expectation.

103     Searches for vector boson scattering were first performed at  $\sqrt{s} = 8$  TeV. The first  
 104   process examined was the low-background same-sign WW process  $pp \rightarrow W^\pm W^\pm jj$   
 105   studied at ATLAS, where evidence for electroweak production was observed at the  
 106   level of a  $3.6\sigma$  standard deviation excess over the null hypothesis [80], and at CMS,  
 107   where a  $2.0\sigma$  excess was found [81]. Subsequent searches for electroweak  $Z\gamma jj$  pro-  
 108   duction found a  $3.0\sigma$  excess above the null hypothesis at CMS [82] and no significant  
 109   excess at ATLAS [83]. A CMS measurement of  $W\gamma jj$  production found a  $2.7\sigma$  ex-  
 110   cess above the null hypothesis consistent with electroweak production [84]. Searches  
 111   for photon-photon VBS were performed as searches for exclusive and quasi-exclusive  
 112    $\gamma\gamma \rightarrow W^+W^-$  production  $pp \rightarrow p^{(*)}W^+W^-p^{(*)}$ , in which the protons do not collide  
 113   but instead both radiate photons, which scatter. CMS found evidence at the level

114 of  $3.4\sigma$  above the null hypothesis [85], and ATLAS saw a  $3.0\sigma$  excess [86]. Roughly  
 115 contemporaneously with this work, electroweak same-sign WW production was ob-  
 116 served at CMS in 13 TeV collisions, with a significance of  $5.5\sigma$  [87]. No searches for  
 117 Electroweak ZZ production had been performed prior to the analysis described in the  
 118 following chapters.

## 119 2.2 Resonant ZZ\*/Z $\gamma^*$ Production

120 Resonant production appears as a sharp peak in the four-lepton invariant mass distri-  
 121 bution over the broad spectrum from nonresonant production. There are two known  
 122 four-lepton resonances: single-Z decays to four leptons around 91 GeV, and Higgs  
 123 decays to ZZ\* around 125 GeV. Another resonance, caused by a new particle, could  
 124 still be discovered at high mass, or at low mass but with a very small cross section.

### 125 2.2.1 Z Boson Decays to Four Leptons

126 A single Z boson may decay to a four-lepton final state when a lepton from a normal  
 127 Z  $\rightarrow \ell^+\ell^-$  decay radiates a virtual photon, as shown in Fig 2.9. In a window around  
 128 the Z mass of  $80 < m_{4\ell} < 100$  GeV, *t*- and *u*-channel production (the diagrams of  
 129 Fig 2.1 with  $\gamma^*$  for both bosons) contribute at the few-percent level (4% at  $\sqrt{s} =$   
 130 13 TeV). Four-fermion decays were studied in detail at LEP [88]. This included  
 131 four-lepton decays, but used all  $\ell^+\ell^- f\bar{f}$  ( $\ell = e, \mu, \tau$ ) final states, where f could be any  
 132 fermion except the neutrinos. Z  $\rightarrow 4\ell$  decays were also observed at 7 and 8 TeV at  
 133 CMS, where the branching fraction was found to be  $\mathcal{B}(Z \rightarrow 4\ell) = 4.2^{+0.9}_{-0.8}$  (stat)  $\pm$   
 134 0.2 (syst)  $\times 10^{-6}$  [89], and at ATLAS, where it was found to be  $3.20 \pm 0.25$  (stat)  $\pm$   
 135 0.13 (syst)  $\times 10^{-6}$  in a slightly different phase space [90]. After correcting for phase  
 136 space differences, the measurements are compatible with each other and with the SM.

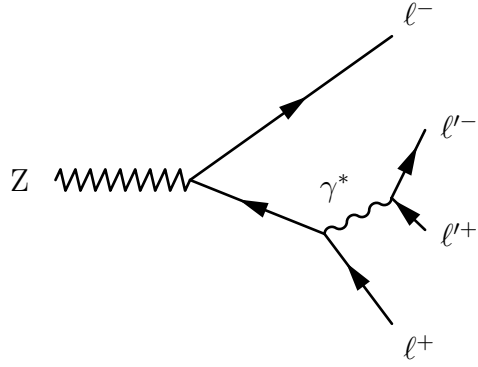


Figure 2.9: Tree-level Feynman diagram for  $Z \rightarrow 4\ell$  production. Either initial lepton may radiate the  $\gamma^*$ .

### <sup>137</sup> 2.2.2 Higgs Boson Production

The primary Higgs production mechanism in multi-TeV hadron collisions is gluon-gluon fusion through a quark loop, because of the gluon's high effective luminosity and the top quark's strong Yukawa coupling. Other mechanisms, in decreasing order by cross section, include vector boson fusion (VBF), vector boson associated production (VH or "Higgsstrahlung"), and top-antitop associated production ( $t\bar{t}H$ ). Tree-level Feynman diagrams for all four are shown in Fig. 2.10. The SM cross sections for the various production mechanisms, and the Higgs branching fractions, are shown as functions of  $m_H$  near the measured mass of 125 GeV in Fig. 2.11. Gluon-gluon fusion has roughly an order of magnitude higher rate than the others. The VBF process contributes to the unitarization of vector boson scattering along with the diagrams in Fig. 2.4. Decays to  $ZZ^*$  are heavily suppressed by the fact that, since  $m_H < 2m_Z$ , energy conservation requires one of the Z bosons to be far off its mass shell. Decays to four charged leptons are further suppressed by the small  $Z \rightarrow \ell^+\ell^-$  branching fraction. However, the distinctive signature of four high-energy charged leptons in a single event is easy to detect with high efficiency and background rejection, and the momentum of electrons and muons can in general be measured with high precision,

allowing the Higgs resonance to be easily seen as a sharp peak over a small, relatively flat background, and  $H \rightarrow 4\ell$  is one of the most attractive channels for Higgs discovery and measurement of its properties.

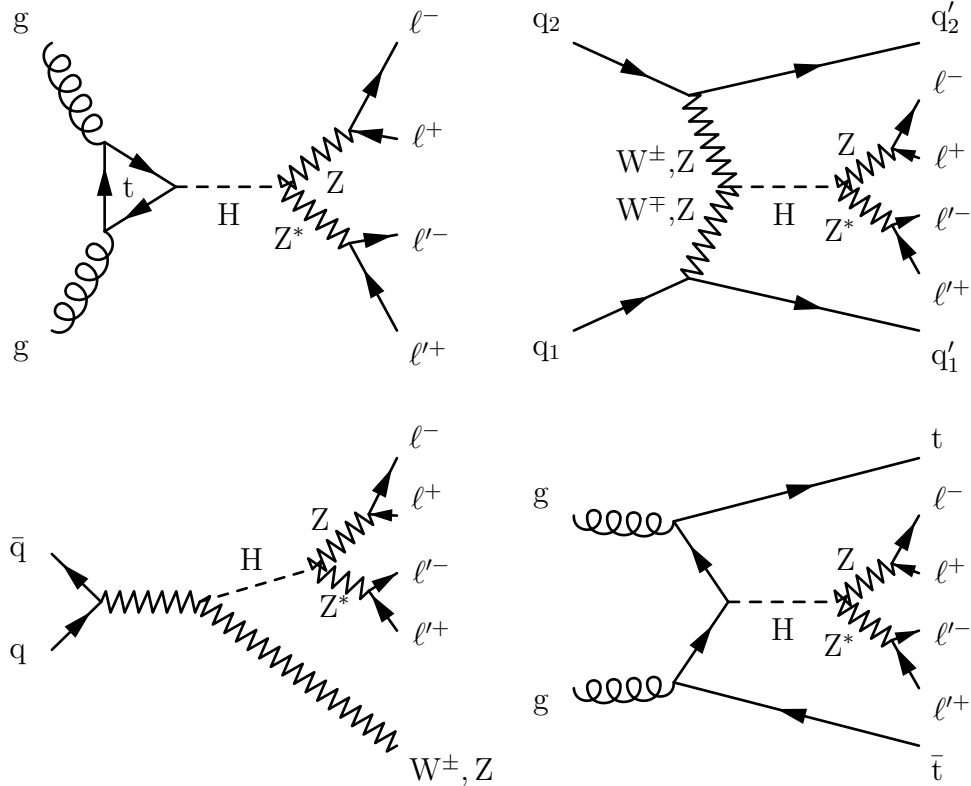


Figure 2.10: Tree-level Higgs production diagrams for gluon-gluon fusion (top left), VBF (top right), VH (bottom left), and  $t\bar{t}H$ , decaying to four leptons.

### 2.2.2.1 Prior Measurements

Higgs boson searches at LEP were for Z-associated production, which has the highest cross section in  $e^+e^-$  collisions. The maximum LEP center-of-mass energy, 209 GeV, was just under the ZH threshold around 216 GeV. The LEP combined 95% confidence level (CL) lower limit on  $m_H$  was 114.4 GeV [92], and a combination of LEP data and electroweak precision measurements set an upper limit of 193 GeV [93]. Searches at the CDF and D0 experiments at the Tevatron were combined to find a

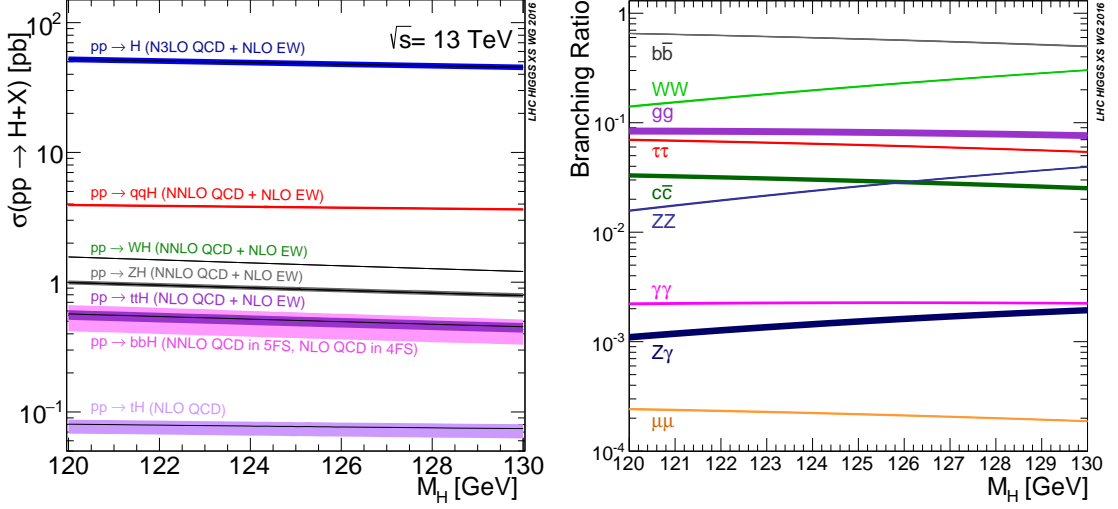


Figure 2.11: The SM cross sections for each Higgs boson production mode (left) and the Higgs branching fraction to several important final states (right), as a function of Higgs mass near the measured mass of 125 GeV. Both plots are reproduced from Ref. [91].

164 3.0 $\sigma$  local excess consistent with  $m_H = 125$  GeV [94], and results from all the Teva-  
 165 tron and LEP measurements and electroweak precision measurements were combined  
 166 to place an upper mass limit of 158 GeV at 95% CL [95]. The Higgs was finally dis-  
 167 covered simultaneously by the CMS and ATLAS collaborations with a combination  
 168 of 7 and 8 TeV data [96, 97]. Its properties were subsequently investigated in detail  
 169 at both experiments. The Higgs mass was found to be

$$m_H = 125.09 \pm 0.21 \text{ (stat)} \pm 0.11 \text{ (syst)} \text{ GeV} \quad (2.7)$$

170 based on a combination of data from the two experiments [98], and SM predictions  
 171 of its properties have been confirmed by a number of measurements [99].

## <sup>172</sup> 2.3 Anomalous Gauge Couplings

173 A primary hallmark of anomalous couplings is an enhanced cross section at center-  
 174 of-mass energies of order 1 TeV [42]. The increase in cross section at high  $m_{4\ell}$  implies  
 175 higher transverse momentum for the outgoing Z bosons and leptons, as shown for two  
 176 example aTGC models in Fig. 2.12. Searches for high-mass ZZ events are attractive  
 177 because SM continuum production cross sections are extremely small above a few  
 178 hundred GeV and all other sources of prompt or nonprompt four-lepton events are  
 179 negligible, so even a handful of events would be an unambiguous sign of new physics.  
 180 The search for nonzero aTGCs is performed using inclusive ZZ events, because the  
 181 aTGC parameters should not have a large effect on jet distributions. The aQGC  
 182 search is performed in ZZjj events because it would specifically enhance the VBS  
 183 cross section at high mass.

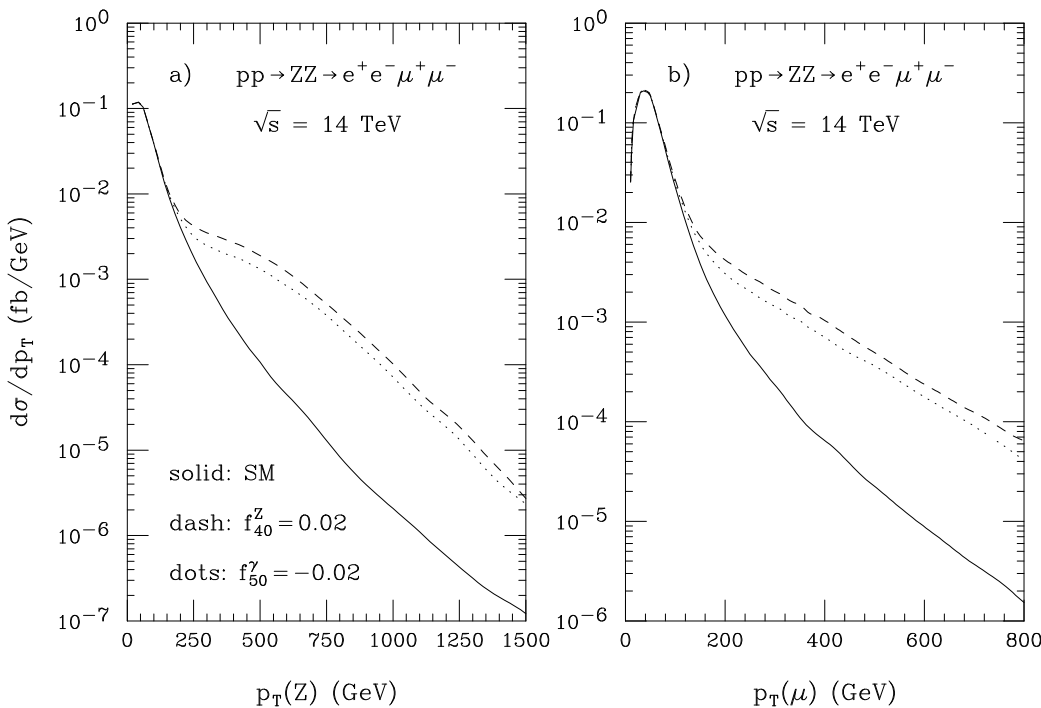


Figure 2.12: Cross section enhancements at high Z and  $\mu$  momenta caused by example nonzero aTGCs. Reproduced from Ref. [42].

184        The neutral aTGC parameters  $f_4^V$  and  $f_5^V$  are expected to have almost identi-  
 185        cal effects at high energy, so the search variables cannot be used to determine the  
 186        relative strengths of the possible anomalous couplings [42]. However, because the  
 187        terms governed by  $f_4^V$  have opposite behavior to the terms governed by  $f_5^Z$  under  
 188        parity transformations, they affect the helicity amplitudes of the Z bosons and al-  
 189        ter the angular distributions of the final-state leptons. Figure 2.13 shows the cross  
 190        section as a function of total angular distance and the azimuthal angular difference  
 191        between muons from the same Z decay for several example nonzero aTGCs and for  
 192        the SM. These distributions could be used to distinguish between the possible aTGC  
 193        parameters and determine the sign of the CP-conserving  $f_5^V$  terms.

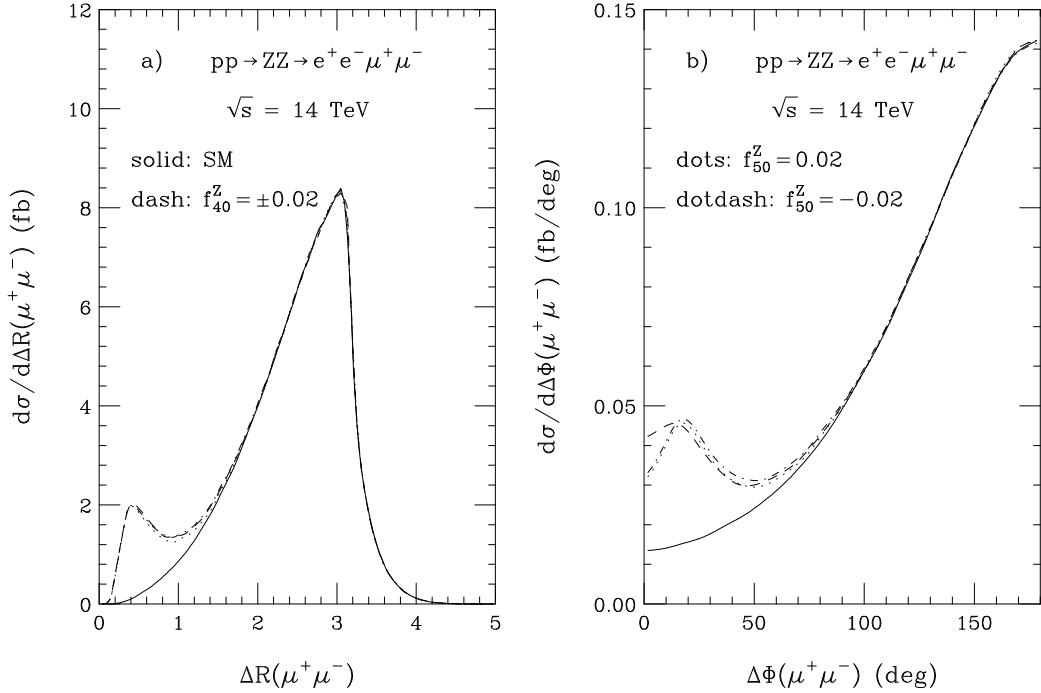


Figure 2.13: Total angular distance and azimuthal angular difference between muons from the same the same Z decay caused by several example nonzero aTGCs. Reproduced from Ref. [42].

### 194 2.3.1 Previous Limits

195 The first neutral aTGC searches were performed at LEP using ZZ and  $Z\gamma$  events [65,  
 196 66, 100, 101]. Depending on the experiment and parameter, 95% CL limits were  
 197 generally  $\mathcal{O}(\pm 1)$ , and the statistical combination set limits around 0.2–0.4 [93]. The  
 198 first searches in hadron collisions were performed at Tevatron by CDF collabora-  
 199 ration, which set symmetric 95% CL limits in the range  $\pm 0.10$ –0.13 for all parame-  
 200 ters [102], and the D0 collaboration, which set symmetric limits around  $\pm 0.20$ –0.31  
 201 for all parameters [103]. Both Tevatron experiments used a unitarity-preserving cut-  
 202 off of  $\Lambda = 1.2$  TeV. CMS and ATLAS set 95% CL limits at 7 TeV at  $\mathcal{O}(\pm 0.1)$  [72,  
 203 76, 104], and  $\mathcal{O}(\pm 0.005)$  at 8 TeV [73, 105]. ATLAS presented limits from 7 TeV data  
 204 with and without a unitarizing form factor; their 8 TeV results, and all CMS results,  
 205 did not use one. Prior to this work, the most stringent limits on all four neutral  
 206 aTGC parameters were set by CMS with a combination of 7 and 8 TeV data [74],

$$\begin{aligned} -0.0022 < f_4^Z < 0.0026, \quad -0.0023 < f_5^Z < 0.0023, \\ -0.0029 < f_4^\gamma < 0.0026, \quad -0.0026 < f_5^\gamma < 0.0027. \end{aligned} \tag{2.8}$$

207 The two-dimensional aTGC limits set by CMS with the 8 TeV dataset are shown in  
 208 Fig. 2.14 [73].

209 No prior aQGC searches were performed using ZZ processes, but both LHC ex-  
 210 periments set limits on the ZZ-sensitive effective field theory operators using other  
 211 channels. The most stringent limits on  $f_{T0}$  were from  $\sqrt{s} = 8$  TeV  $Z\gamma qq$  events at  
 212 ATLAS [83], found to be

$$-3.4 < f_{T0}/\Lambda^4 < 2.9 \text{ TeV}^{-4} \tag{2.9}$$

213 at 95% CL, with similar results produced by CMS [82]. The most stringent limits on  
 214  $f_{T1}$  and  $f_{T2}$  were set by CMS at 8 TeV using same-sign WWqq events [81], and were

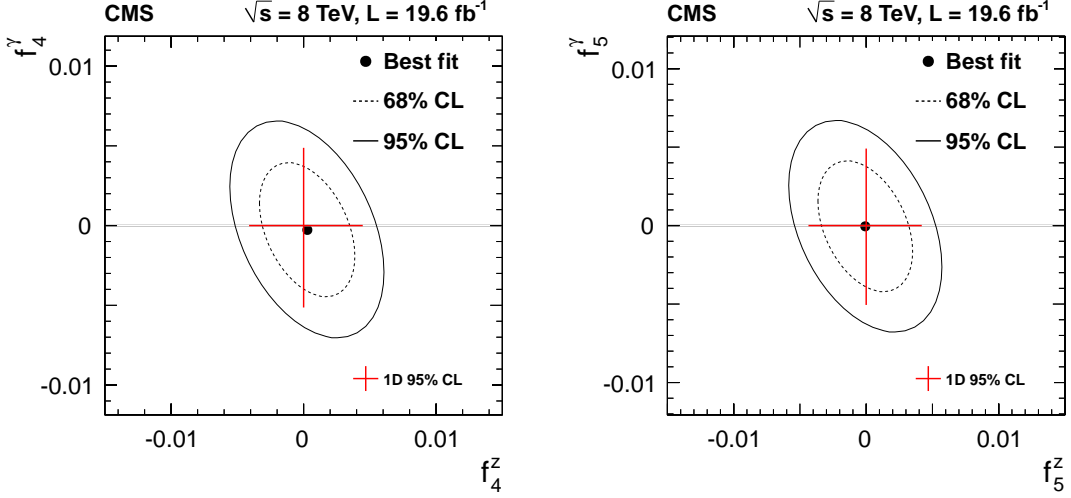


Figure 2.14: Two-dimensional 95% CL aTGC limits set by CMS, reproduced from Ref. [73].

215 found to be

$$-2.1 < f_{\text{T}1}/\Lambda^4 < 2.4 \text{ TeV}^{-4} \quad (2.10)$$

216 and

$$-5.9 < f_{\text{T}2}/\Lambda^4 < 7.1 \text{ TeV}^{-4}. \quad (2.11)$$

217 CMS and ATLAS produced nearly identical limits on  $f_{\text{T}8}$  and  $f_{\text{T}9}$  in the same  $Z\gamma\text{qq}$   
218 searches that set limits on  $f_{\text{T}0}$ ,

$$-1.8 < f_{\text{T}8}/\Lambda^4 < 1.8 \text{ TeV}^{-4} \quad (2.12)$$

219 and

$$-3.9 < f_{\text{T}9}/\Lambda^4 < 3.9 \text{ TeV}^{-4}. \quad (2.13)$$

## 220 2.4 Background Processes

221 Spurious events are categorized as irreducible backgrounds, i.e. those that are ex-  
222 pected to have four prompt leptons, and reducible backgrounds, which have two

or three prompt leptons and another object that is misidentified as a prompt lepton. The only nontrivial irreducible backgrounds to inclusive  $ZZ/Z\gamma^*$  production are WWZ triboson events in which all three bosons decay leptonically, and  $t\bar{t}Z$  events in which both top quarks and the Z all decay leptonically as shown at tree level in Fig. 2.15. The most prominent reducible backgrounds are  $WZ \rightarrow 3\ell\nu$  events in which a jet fragment is misidentified as a prompt lepton,  $Z + \text{jets}$  events in which two jet fragments are misidentified, and leptonic  $t\bar{t}$  events with two misidentified fragments from the secondary b-jets. For the VBS search, the background is real  $ZZ$  events which have two jets, but the jets originate from QCD interactions instead of the fully electroweak processes of Fig. 2.4. An example non-VBS  $ZZ + 2\text{jets}$  diagram is also shown in Fig. 2.15.

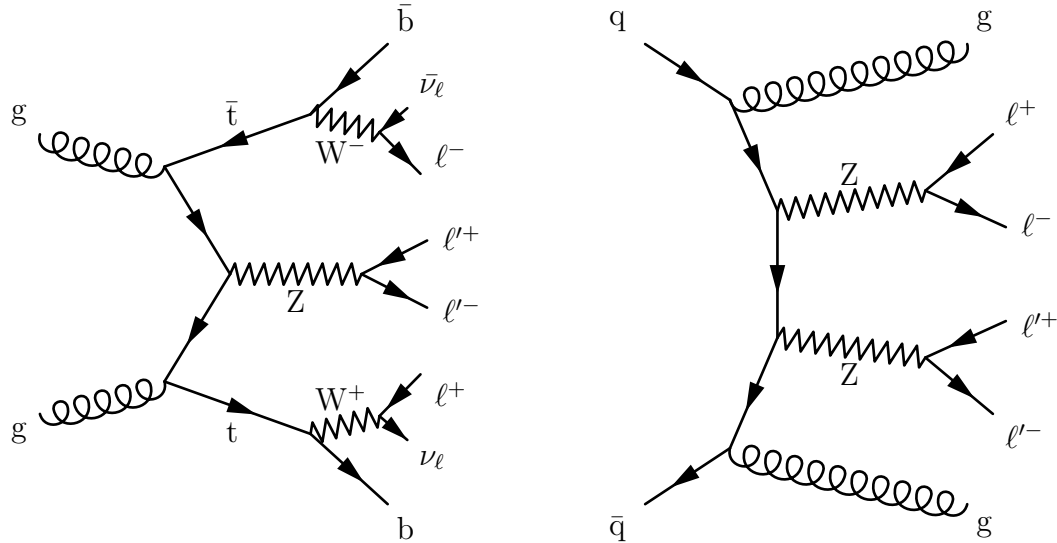


Figure 2.15: An example tree-level  $t\bar{t}Z$  diagram (left), which is an irreducible background for inclusive  $ZZ/Z\gamma^*$  production, and an example non-electroweak  $ZZjj$  diagram (right).

## **0 Chapter 3**

# **1 The CMS Experiment and the 2 CERN LHC**

3 Production of controlled high-energy particle collisions, and detection of particles  
4 created in those collisions, are monumental technical challenges. The apparatus used  
5 to obtain the results presented in this thesis are the result of decades of work by  
6 thousands of scientists and engineers, making use of many techniques developed in  
7 the course of building and operating previous experiments. The LHC [106, 107]  
8 accelerates pairs of charged hadron (proton or lead ion) beams and collides them  
9 to provide a source of high energy particle interactions for several fully independent  
10 detectors, including CMS [108], which collected the data used in the studies presented  
11 here. Detailed descriptions of the LHC and CMS follow.

### **12 3.1 The CERN Large Hadron Collider**

13 The LHC, the most powerful particle accelerator and collider ever built, is a 26.7 km  
14 circumference ring of superconducting magnets running through tunnels roughly

15 100 m below the suburbs and countryside near Geneva, Switzerland. It first produced  
 16 collisions suitable for collecting physics data in 2010 before generating large datasets  
 17 with beam energies of 3.5 TeV in 2011 and 4 TeV in 2012. Following a shutdown  
 18 for upgrades and repairs, it operated in 2015 and 2016 to deliver beam energies of  
 19 6.5 TeV. Beams collide head-on so that the center-of-mass frame of the proton-proton  
 20 system is the rest frame of the detectors, giving proton-proton center-of-mass ener-  
 21 gies of 7, 8, and 13 TeV respectively for collisions in 2010–2011, 2012, and 2015–2016.  
 22 Each successive energy was the highest ever achieved in controlled hadron-hadron  
 23 collisions, giving unprecedented access to extremely high-energy processes at every  
 24 step.

25 In addition to increasing collision energies, the LHC increased its rate of collisions  
 26 with each new machine configuration. The average event rate  $dN/dt$  for a process  
 27 with production cross section  $\sigma$  is determined by the instantaneous luminosity  $\mathcal{L}$  of  
 28 the collider,

$$\frac{dN}{dt} = \mathcal{L}\sigma \quad (3.1)$$

29 so a high instantaneous luminosity enables the observation of rare processes like Higgs  
 30 boson production. The LHC’s unprecedented luminosities have allowed collection of  
 31 the largest physics datasets in history.

32 The desire for high luminosities drove the decision to collide protons with other  
 33 protons instead of with antiprotons as was done at Tevatron, LHC’s predecessor at  
 34 Fermilab in Batavia, IL. Antiprotons simply cannot be produced in sufficient quan-  
 35 tities for a collider on this scale. Tevatron was designed to study many processes  
 36 that are  $q\bar{q}$ -initiated, so it is useful to have valence antiquarks available in the col-  
 37 lisions. The LHC was designed with Higgs boson production in mind, and the two  
 38 most important Higgs production modes are proton/antiproton agnostic. Even for  
 39  $q\bar{q}$ -initiated processes, valence antiquarks are less critical at the LHC because, for the

40 same center of mass energy, the effective  $q\bar{q}$  luminosity is higher for proton-proton  
41 collisions at LHC energies than at Tevatron energies (1.98 TeV center-of-mass energy)  
42 as discussed in Section 1.6.

43 In addition to protons, the LHC can accelerate beams of lead nuclei to 2.51 TeV  
44 per nucleon, also the highest ever achieved. All studies presented in this thesis were  
45 performed on proton-proton collision data, rendering the details of so-called “heavy  
46 ion” beams beyond the scope of this document.

47 Beams are maintained and manipulated with magnets, most of them made of  
48 superconducting niobium-titanium (NbTi) windings cooled to 1.9 K by superfluid  
49 helium. Dipole magnets with fields up to 8.33 T bend the beam around the ring,  
50 interspersed with quadrupoles for focusing. More quadrupoles and higher-moment  
51 magnets keep the beams focused, squeeze them for collisions, and apply a number  
52 of corrections. Superconducting radio frequency (RF) cavities operating at 400 MHz  
53 accelerate the beam, maintain it at its final energy, and maintain bunch shape and  
54 spacing.

### 55 3.1.1 Accelerator Chain, Layout, and Detectors

56 The LHC was built in tunnels originally constructed for the Large Electron-Positron  
57 Collider (LEP), an  $e^+e^-$  collider that operated from 1989 to 2000. Using existing cav-  
58 erns, tunnels, and infrastructure was a substantial cost-saving measure, but imposed  
59 several important constraints on the LHC’s design. In LEP, the electron and positron  
60 beams could be accelerated in opposite directions by the same magnets, because they  
61 are oppositely charged. Conversely, proton beams require opposite magnetic fields for  
62 the two beams. Because the tunnels were not wide enough to accommodate two com-  
63 pletely separate beam lines, most of the magnets in the LHC use a twin-bore design,  
64 shown schematically in Fig. 3.1, in which the pipes and windings for the two beams

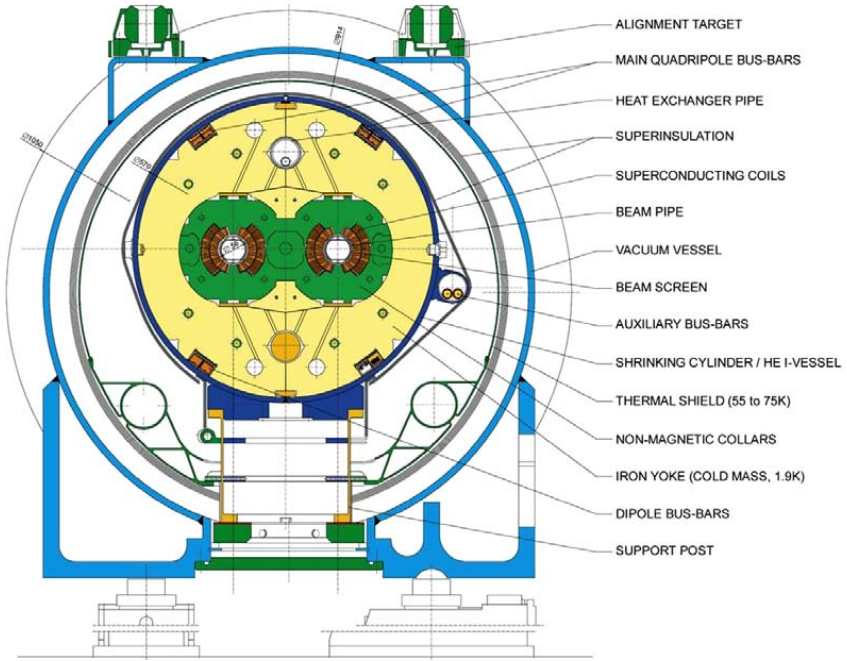


Figure 3.1: Schematic cross section of an LHC dipole and its attendant electrical and cryogenic infrastructure, reproduced from Ref. [106].

65 share a common cryogenic system. The electromagnetic, mechanical, and cryogenic  
66 coupling of the two beamlines represents a significant engineering challenge [106, 107].

67 Because no single accelerator has the dynamic range necessary to take a stationary  
68 proton to TeV-scale energies, a chain of smaller accelerators repurposed from previous  
69 experiments feeds moderate-energy protons into LHC. Protons are obtained by ion-  
70 izing hydrogen atoms, then accelerated to 50 MeV by the Linac 2 linear accelerator  
71 and injected into the Proton Synchrotron Booster (PSB), the first of several circu-  
72 lar accelerators. The PSB feeds 1.4 GeV protons into the Proton Synchrotron (PS),  
73 which in turn injects them into the Super Proton Synchrotron (SPS) at 26 GeV. The  
74 protons are then accelerated to 450 GeV in the SPS before being injected into LHC.

75 A diagram of the entire accelerator chain is shown in Fig. 3.2.

76 The LHC ring is divided into eight sectors, each of which features a 528 m straight  
77 section connected to the adjacent sections by 2.45 km arcs. The straight section length

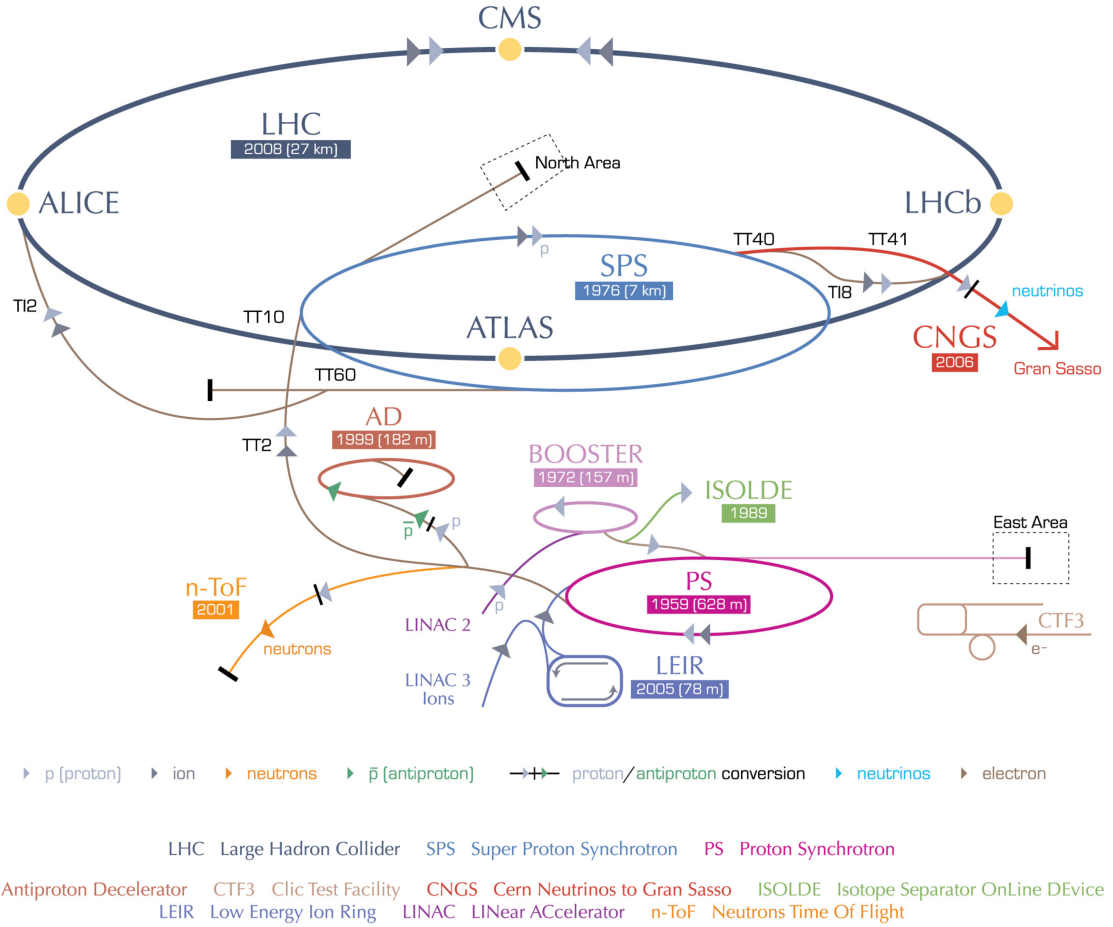


Figure 3.2: A schematic of the LHC accelerator chain and peripheral experiments, reproduced from Ref. [109].

78 was set by the need for RF cavities to accelerate LEP beams to counteract synchrotron  
 79 radiation, which is a primary factor limiting electron and positron beam energy. This  
 80 is not ideal for proton beams; protons' much higher mass means they radiate less and  
 81 need fewer RF cavities. The straight sections feature access points numbered with  
 82 Point 1 at the main CERN site in Meyrin, Switzerland, and the rest numbered 2–8,  
 83 increasing in the clockwise direction when viewed from above. Points 1, 2, 5, and 8  
 84 have beam crossing points and host detectors to study the resulting proton-proton  
 85 collisions. Points 3 and 7 feature collimators to reduce momentum and betatron  
 86 nonuniformities in the beams. The RF cavities are at Point 4 and the beams are

87 dumped after use or in the event of a magnet quench at Point 6. Beams are disbursed  
 88 and deflected into an 8 m long water-cooled graphite absorber by fast kicker magnets  
 89 which activate in a 3  $\mu$ s-long bunch-free region of the beam known as the abort gap.

90 The CMS detector is at Point 5 in Cessy, France, the furthest point on the ring  
 91 from the Meyrin site and Point 1, which houses ATLAS [110], a similar but fully  
 92 independent general-purpose particle detector. CMS and ATLAS use complemen-  
 93 tary detector technology so that any measurement or discovery by one can be made  
 94 concurrently or verified by the other. The other two experimental insertions feature  
 95 specialized detectors studying collisions at lower-luminosity beam interaction points.  
 96 The LHCb detector [111], at Point 8, studies hadronic physics with an emphasis on  
 97 b-hadrons, and ALICE [112] studies heavy ion collisions at Point 2. Three smaller  
 98 experiments share interaction points with the larger detectors, with TOTEM [113]  
 99 studying proton structure and the total proton-proton interaction cross section next  
 100 to CMS; LHCf [114] studying the  $\pi^0$  energy spectrum and multiplicity near ATLAS;  
 101 and MoEDAL [115] searching for magnetic monopoles or other heavy, stable, ionizing  
 102 particles at Point 8 with LHCb.

### 103 3.1.2 Operating Parameters

104 With the beam energy set by the radius of the ring and the strength of available  
 105 magnets, the number of interesting physics events produced in LHC collisions depends  
 106 only on the integrated luminosity

$$\mathcal{L}_{int} = \int \mathcal{L} dt, \quad (3.2)$$

107 where  $\mathcal{L}$  is the instantaneous luminosity defined in Eq. (3.1) and the integral runs  
 108 over the time the machine spends in collisions mode. LHC's availability for colli-  
 109 sions depends on the electrical and mechanical stability of the accelerators and their

110 support systems, including the cryogenics and the vacuum in the beam pipe. The  
 111 instantaneous luminosity while running depends only on the beam parameters. For  
 112 symmetric beams which each have  $n_b$  colliding gaussian bunches of intensity (i.e. num-  
 113 ber of protons in the bunch)  $N_b$ , orbiting the ring with frequency  $f_{rev}$  and relativistic  
 114 factor  $\gamma = E_p/m_p$ , the instantaneous luminosity is give by

$$\mathcal{L} = f_{rev} \frac{n_b N_b^2 \gamma}{4\pi \beta^* \epsilon_N} R, \quad (3.3)$$

115 where  $\beta^*$  is the amplitude of the beams' betatron oscillations around the nominal  
 116 ring path at the interaction point, the normalized emittance  $\epsilon_N$  is a measure of the  
 117 beams' spread in both position and momentum space, and  $R$  is a geometrical factor  
 118 accounting for the beam crossing angle,

$$R = \sqrt{1 + \left( \frac{\theta_c \sigma_z}{2\sigma^*} \right)^2}. \quad (3.4)$$

119 Here  $\theta_c$  is the beams' crossing angle, and  $\sigma_z$  and  $\sigma^*$  are respectively the longitudinal  
 120 and transverse RMS widths of the bunches in the lab frame.

### 121 3.1.2.1 Design

122 The machine parameters in the LHC design specification can be seen in the first col-  
 123 umn of Table 3.1. Machine parameters during data taking have in general been quite  
 124 different, due to both technological advances and technical challenges. In particular,  
 125 beam energy and number of colliding bunches are both lower than designed due to  
 126 commissioning issues with the magnets and their safety systems [116], but increases in  
 127 the number of collisions per bunch crossing (“pileup”) have more than compensated,  
 128 leading to a peak instantaneous luminosity in 2016 that was more than 50% higher  
 129 than designed. Operating parameters have changed frequently during data taking  
 130 and upgrades are always ongoing.

Table 3.1: LHC beam parameters as designed and in practice. As stated in the text,  $n_b$  is the number of colliding bunches,  $N_b$  is the number of protons in each bunch,  $\beta^*$  is the betatron amplitude at the interaction point,  $\epsilon_N$  is the normalized emittance, and  $\mathcal{L}_{(int)}$  is the instantaneous (integrated) luminosity.

Year	Design		Run I		Run II	
		2010	2011	2012	2015	2016
Energy per beam (TeV)	7	3.5	3.5	4	6.5	6.5
Bunch spacing (ns)	25	150	50	50	25	25
$n_b$	2808	348	1331	1368	2232	2208
$N_b (10^{11})$	1.15	1.2	1.5	1.7	1.15	1.25
$\beta^*$ (m)	0.55	3.5	1.0	0.6	0.8	0.4
$\epsilon_N$ (mm mrad)	3.75	2.2	2.3	2.5	3.5	3.0
Peak pileup	FIXME	4	17	37	22	49
Peak $\mathcal{L} (10^{34} \text{cm}^{-2}\text{s}^{-1})$	1	0.02	0.35	0.77	0.52	1.53
$\mathcal{L}_{int} (\text{fb}^{-1})$		0.04	6.1	23.3	4.2	41.1

### 131 3.1.2.2 Run I

132 The LHC came online in 2010 with a beam energy of 3.5 TeV, which was increased  
 133 to 4 TeV in 2012. Bunches were spaced 50 ns apart instead of 25 ns to allow full  
 134 exploitation of excellent injection chain performance [117]. Beams exiting the SPS  
 135 had bunch intensity as much as 50% higher than anticipated in the original LHC  
 136 design and beam emittance as low as 67% of nominal. This allowed the LHC to  
 137 achieve 77% of its design instantaneous luminosity in 2012 despite having roughly  
 138 half as many bunches in each beam.

139 Machine availability was overall good considering the complexity and relative  
 140 newness of the LHC, with about 36% of scheduled time spent in stable beams. In all,  
 141 LHC delivered  $6.1 \text{ fb}^{-1}$  to CMS and ATLAS in 2011 and  $23.3 \text{ fb}^{-1}$  in 2012, enough to  
 142 allow discovery of the Higgs boson. The integrated luminosity for each year of LHC  
 143 operation is shown as a function of calendar month and day in Fig. 3.3.

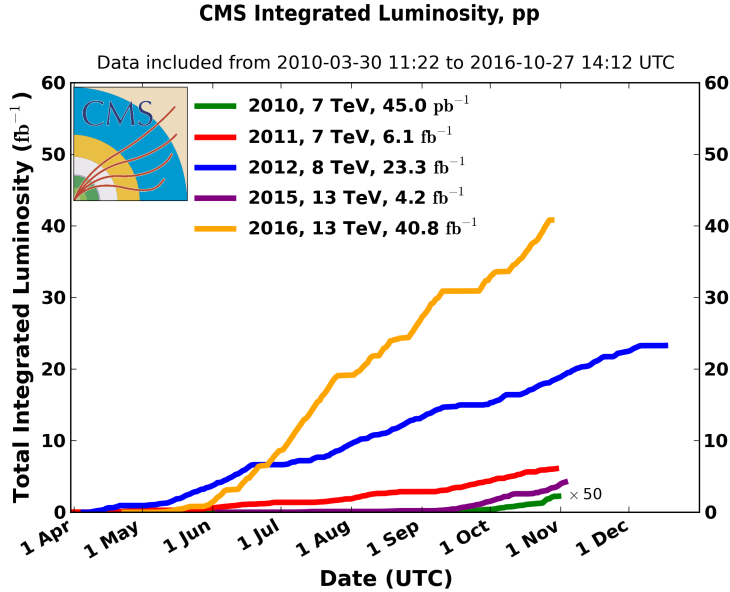


Figure 3.3: The integrated luminosity delivered to CMS in each year of LHC operation, shown as a function of the date within the year.

### 144 3.1.2.3 Run II

145 The LHC shut down for 2013 and 2014 to allow a number of repairs and upgrades,  
 146 including measurements, repairs and upgrades on the electrical connections and cryo-  
 147 genic safety systems. Beam energies were increased to 6.5 TeV, close to the nominal  
 148 7 TeV. The bunch spacing was decreased to 25 ns while maintaining low emittance  
 149 and high bunch intensity with the implementation of the beam compression merging  
 150 and splitting (BCMS) scheme in which bunches are merged in the PS before they  
 151 are split for injection into SPS, allowing higher bunch intensity [118]. This was offset  
 152 by vacuum problems in the SPS beam dump, which limited the total number of col-  
 153 liding bunches to around 2200 [119]. Improvements in collimators and beam optics  
 154 reduced  $\beta^*$  to 40 cm in 2016, lower than the design  $\beta^*$  of 55 cm. Overall instantaneous  
 155 luminosities were substantially higher than originally designed.

156 Machine availability in Run II was excellent, with over 60% of planned time spent  
 157 in stable beams [119]. The world's first 13 TeV collisions in 2015 were the subject of

158 a number of measurements and searches, though the  $4.2 \text{ fb}^{-1}$  integrated luminosity  
 159 delivered to Points 1 and 5 in 2015 was less than planned due to several mechanical is-  
 160 sues. The integrated luminosity achieved in 2016,  $41.1 \text{ fb}^{-1}$ , was far above the roughly  
 161  $25 \text{ fb}^{-1}$  expected and more than all previous runs combined, allowing measurements  
 162 and searches of unprecedented sensitivity and reach, including those presented in this  
 163 Thesis.

## 164 **3.2 The Compact Muon Solenoid Detector**

165 The CMS detector [108] is a general-purpose particle detector located in a cavern  
 166 roughly 100 m below the surface at LHC Point 5. Though designed to do a wide  
 167 range of physics analyses, CMS was designed specifically with Higgs boson discovery  
 168 in mind. Primary design goals include

- 169     • High-efficiency reconstruction of charged particles with precise measurement of  
   170       their trajectories and momenta
- 171     • Good electromagnetic energy resolution, including diphoton and dielectron mass  
   172       resolution
- 173     • Hermetic calorimetry for good missing transverse energy and dijet mass resolu-  
   174       tion
- 175     • Good muon identification, momentum resolution (including dimuon mass reso-  
   176       lution), and charge determination over a broad range of energies

177 To this end, CMS features a silicon tracker, a scintillating crystal electromagnetic  
 178 calorimeter (ECAL), and a hermetic hadronic calorimeter (HCAL) inside a  $3.8 \text{ T}$   
 179 solenoid magnet surrounded by ionized gas muon tracking devices, all of which can

180 be seen as part of the whole detector in Fig. 3.4. Decisions on which events to read  
 181 out are made on-line by a two-level trigger system. Descriptions of these systems  
 182 follow.

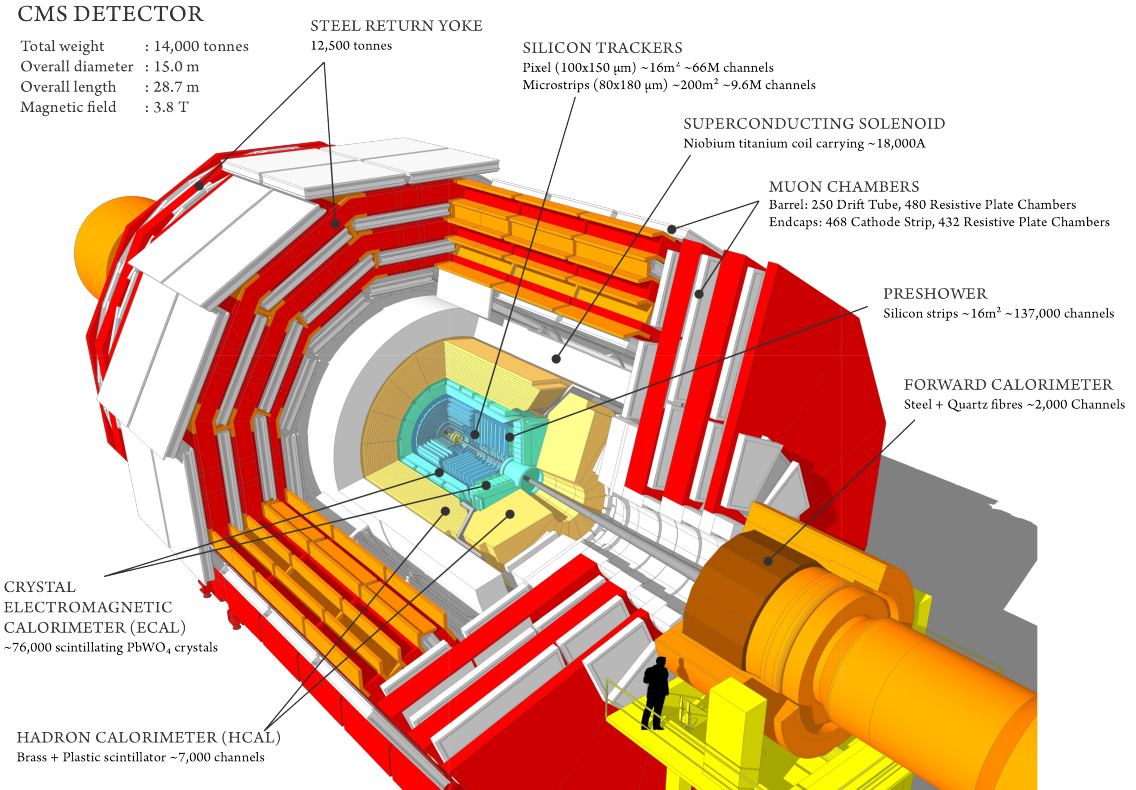


Figure 3.4: Cutout schematic of CMS with all major subdetectors, the beamline, the magnet, and the return yoke visible. Reproduced from Ref. [120].

### 183 3.2.1 Terminology and Geometry

184 The CMS detector systems are arranged in cylindrical layers with the interaction  
 185 point at the center, serving as the origin for the coordinate system. The coordinate  
 186 system is defined with the positive- $x$  direction pointing toward the center of the  
 187 ring, positive- $y$  pointing vertically up, and positive- $z$  pointing parallel to the beam  
 188 in the counterclockwise direction when the LHC ring is viewed from above. Particle

189 momenta are typically expressed in quasicylindrical coordinates  $(p_T, \eta, \phi)$ . Here  $p_T$  is  
 190 the magnitude of the particle's momentum transverse to the beam

$$p_T \equiv \sqrt{p_x^2 + p_y^2}, \quad (3.5)$$

191 and  $\phi$  is the azimuthal angle, i.e. the angle from the  $x$ -axis to the particle's trajectory  
 192 in the  $x$ - $y$  plane. The pseudorapidity  $\eta$  is defined as

$$\eta \equiv -\ln \left[ \tan \left( \frac{\theta}{2} \right) \right] \quad (3.6)$$

193 where  $\theta$  is the polar angle measured from the  $z$ -axis. The relativistic rapidity

$$y \equiv \frac{1}{2} \ln \left( \frac{E + p_z}{E - p_z} \right), \quad (3.7)$$

194 converges to the pseudorapidity in the limit of massless particles. Pseudorapidity  
 195 is preferred to rapidity because it is purely geometrical, with no dependence on the  
 196 particle energy. Both are preferred over  $\theta$  because rapidity differences are invariant  
 197 under longitudinal boosts, and because hadron flux at colliders is roughly constant as  
 198 a function of rapidity. The transverse energy  $E_T$  is the the magnitude of the particle's  
 199 four-momentum transverse to the beam, equal to  $p_T$  in the limit of massless particles.  
 200 Spatial coordinates are expressed as  $(r, \eta, \phi)$ , where  $r$  is the distance from the beam  
 201 in the  $x$ - $y$  plane.

### 202 3.2.2 Magnet and Inner Tracking System

203 A particle of charge  $q$  moving through a uniform magnetic field of strength  $B$  that  
 204 points in the  $z$  direction will travel in a helix of radius  $R$ , given by

$$R = \frac{p_T}{|q|B}, \quad (3.8)$$

205 with the chirality of the helix determined by the sign of  $q$ . Thus one can determine the  
 206 transverse momentum of the particle by measuring its path through the magnetic field

207 and finding the radius of curvature. In practice, all but the lowest-energy particles  
 208 leave too short an arc in the detector for direct measurement of the radius, so the  
 209 sagitta of the arc is used instead, given by

$$s = \frac{qBL^2}{8p_T} \quad (3.9)$$

210 where  $L$  is the length of the chord spanning the arc (typically equal to the radius of  
 211 the tracking system). The transverse momentum resolution varies as

$$\frac{\delta p_T}{p_T} \propto \frac{p_T}{BL^2}, \quad (3.10)$$

212 so a strong field and a large tracking volume are vital to keeping measurements precise  
 213 even at high energies.

214 To this end, CMS contains the world's largest superconducting magnet<sup>1</sup>, a solenoid  
 215 13 m long and 6 m in diameter, which generates a nearly-uniform 3.8 T field in the  
 216 centralmost part of the detector [121]. To measure the paths of charged particles in  
 217 the field, the volume closest to the interaction point contains layers of silicon sensors  
 218 that detect hits from charged particles with high efficiency and excellent position  
 219 resolution, between 4.4 cm and 1.1 m from the beam for 2.7 m on either side of the  
 220 interaction point. This system, called the inner tracker and shown schematically  
 221 in Fig. 3.5, consists of an inner pixel detector surrounded by a larger silicon strip  
 222 detector. Both consist of concentric cylinders of sensors covering the barrel of the  
 223 detector capped by discs covering the high- $\eta$  region, up to  $|\eta| < 2.5$ . With a total of  
 224 roughly 200 m<sup>2</sup> of silicon, the inner tracker is the largest silicon tracker in the world.  
 225 Tracks may be reconstructed with hits in as many as 14 layers. The downside of  
 226 this is that the tracker and its mechanical support structure represent a substantial  
 227 amount of material for electrons and photons to interact with before they reach the

---

<sup>1</sup>Largest in the sense of having the largest stored energy when at constant full field. The largest by size is the ATLAS barrel toroid.

228 calorimeters, with total material budget between 0.4 radiation lengths ( $\eta = 0$ ) and 1.8  
 229 radiation lengths ( $|\eta| \approx 1.4$ ), as shown in Fig. 3.6. The tracker-only  $p_T$  uncertainty  
 230 is around 1.2% at 200 GeV and 15% at 1 TeV. Tracker readout is too slow for it to  
 231 be used in the L1 trigger (see Section 3.2.6.1), the first set of trigger decisions must  
 232 be made using only information from the calorimeters and outer muon system.

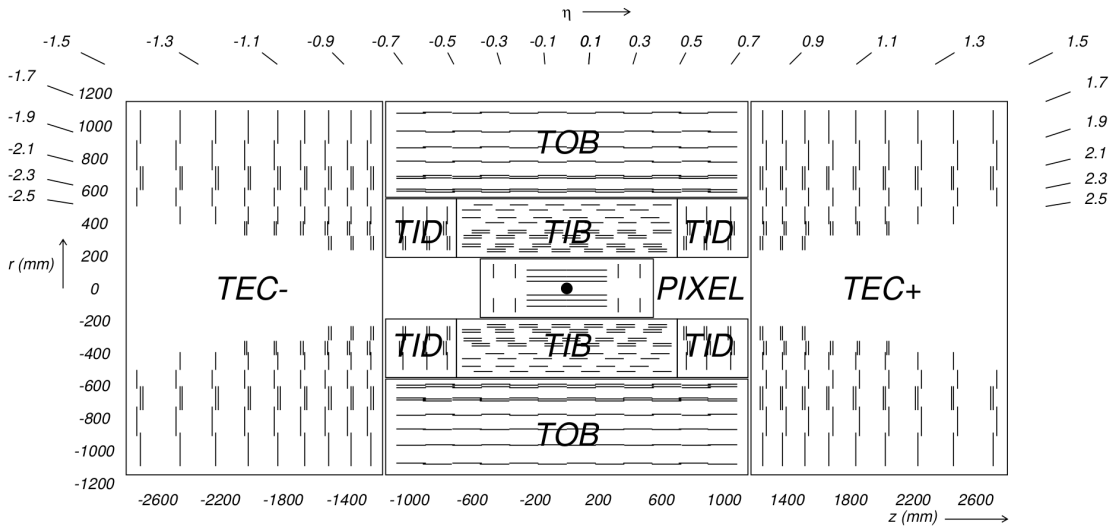


Figure 3.5: Diagram of the inner tracker layout, reproduced from Ref. [108].

233 As the system closest to the interaction point, the inner tracker is subject to  
 234 extremely high radiation doses, equivalent to 840 kGy for the innermost pixel layer  
 235 over an integrated luminosity of  $500 \text{ fb}^{-1}$ , so radiation tolerance is a major design  
 236 constraint for both the sensors and readout electronics [122]. Leakage currents in  
 237 the sensors, which degrade sensor performance, increase linearly with radiation fluence  
 238 and exponentially with temperature. Because leakage currents cause self-heating in  
 239 the silicon, they can create a dangerous positive thermal feedback loop if the sensors  
 240 are not cooled below  $-10^\circ \text{C}$  during operation. Reverse annealing, a process by which  
 241 radiation-induced defects in the silicon can cause further damage months after the  
 242 radiation dose is received, can be mitigated by keeping the sensors below  $0^\circ \text{C}$  at  
 243 all times except for brief maintenance periods [108]. Therefore, to improve tracker

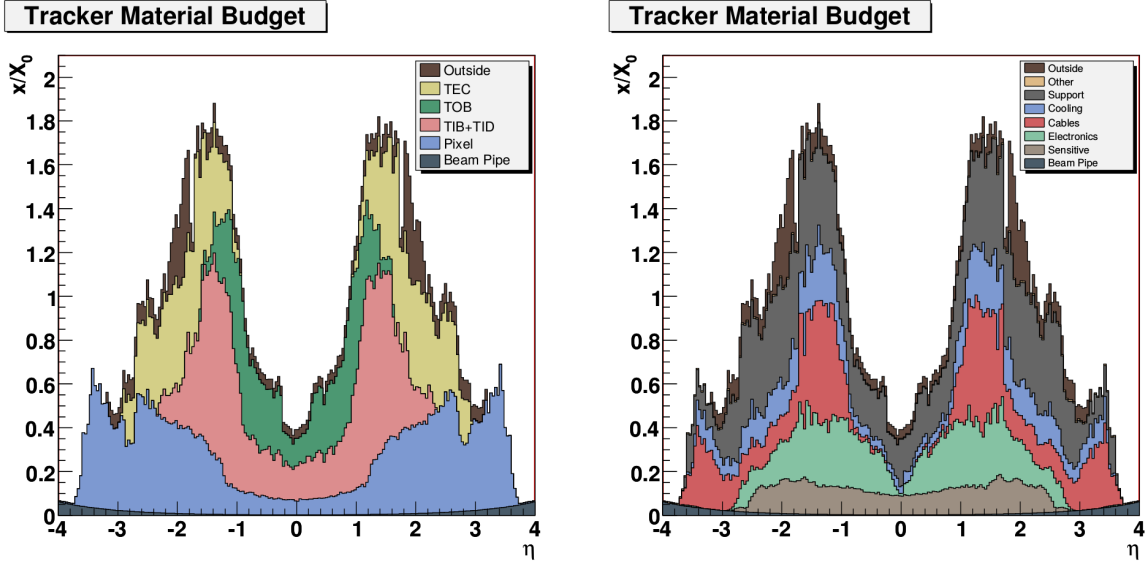


Figure 3.6: Total tracker material budget in units of electromagnetic radiation lengths, as a function of pseudorapidity. At (left) the total is divided by detector subsystem, at (right) by the function of the material. Reproduced from Ref. [108].

244 performance and increase the detectors' lifetimes, a gas cooling system is used to  
 245 keep the strip tracker around  $-15^{\circ}\text{C}$  and the pixel detector around  $-20^{\circ}\text{C}$  during  
 246 operation.

### 247 3.2.2.1 Pixel Detector

248 The pixel detector [122], consisting of three layers in the barrel and two in the endcap,  
 249 is responsible for accurate reconstruction of primary proton-proton interaction ver-  
 250 tices and secondary vertices from decays of b-hadrons or other long-lived particles, as  
 251 well as providing “seed” tracks that may be used in strip tracker reconstruction. As  
 252 the system closest to the interaction point, the pixel system experiences the highest  
 253 charged-particle flux and therefore must have extremely fine granularity to differen-  
 254 tiate between nearby particles. The 66 million pixels in the system have a cell size of  
 255  $100 \times 150 \mu\text{m}^2$ . Interpolation of the analog signals from the individual pixels allows  
 256 a final spatial resolution of  $15 \mu\text{m}$  in each direction. The outermost barrel layer is

257 10.2 cm from the beam, and the second endcap disk is 46.5 cm from the interaction  
 258 point. The sensor modules are arranged such that at least three sensors cover the  
 259 solid angle within the pixel detector's acceptance.

260 **3.2.2.2 Strip Tracker**

261 Outside the pixels is the silicon strip tracker [122], extending out to 1.1 m in the  $r$   
 262 direction and  $\pm 2.8$  m in the  $z$  direction. The tracker is divided into inner and outer  
 263 subdetectors, each of which has both barrel cylinders and endcap discs. In total,  
 264 there are ten layers in the barrel and nine in each of the endcaps. The inner tracker  
 265 uses 320  $\mu\text{m}$ -thick sensors with a typical strip cell size of 10 cm  $\times$  80  $\mu\text{m}$ , leading to  
 266 hit resolutions of 23–35  $\mu\text{m}$ . The outer tracker uses 500  $\mu\text{m}$ -thick sensors with typical  
 267 strip sizes up to 25 cm  $\times$  180  $\mu\text{m}$ , leading to hit resolutions of 35–53  $\mu\text{m}$ .

268 **3.2.3 Electromagnetic Calorimeter**

269 Outside of the tracker is the electromagnetic calorimeter (ECAL), which is designed  
 270 to absorb and measure the energy of electrons and photons. ECAL is made of 68,524  
 271 radiation tolerant lead tungstate ( $\text{PbWO}_4$ ) crystals arranged in a cylindrical barrel  
 272 (EB) covering  $|\eta| < 1.444$  and two endcap discs (EE) covering  $1.566 < |\eta| < 3.0$ .  
 273 The geometry of the ECAL barrel and endcap can be seen in Fig. 3.7; the small  
 274 gap between the barrel and endcap is necessary to accommodate cabling and support  
 275 structures for the tracker.  $\text{PbWO}_4$  crystals scintillate blue-green light and are op-  
 276 tically transparent, so the resulting light can be read out by avalanche photodiodes  
 277 (APDs) in the barrel and vacuum phototriodes (VPTs) in the endcap. ECAL's gran-  
 278 ularity is set by  $\text{PbWO}_4$ 's small Molière radius of 2.2 cm, which is also the size of the  
 279 square front faces of the barrel crystals, which flare out to 2.6 cm at the back, giving

them a truncated pyramid shape covering a roughly  $0.0174 \times 0.174$  area of  $\eta\phi$  space.  
 The endcap crystals go from 2.86 cm squares at the front to 3.0 cm at the back.

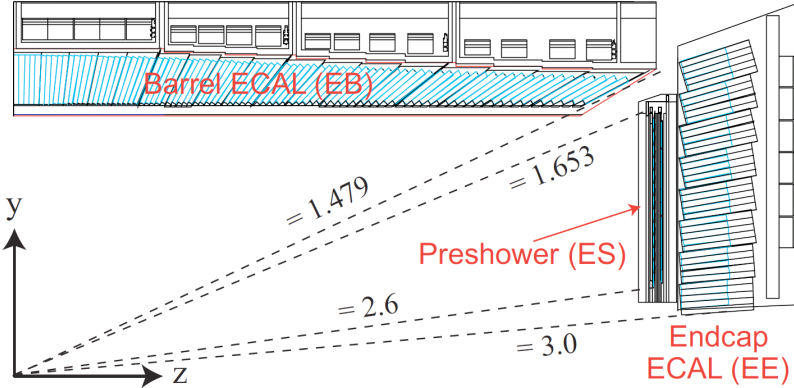


Figure 3.7: Diagram of ECAL geometry, reproduced from Ref. [123].

One of the primary design innovations of CMS—the eponymous compactness—was to place the calorimetry inside the magnet so that tracks can be unambiguously associated with energy deposits in the calorimeters without interference from scattering in the magnet coils. This is possible in part thanks to the high density ( $8.28 \text{ g/cm}^3$ ) and short radiation length (0.89 cm) of  $\text{PbWO}_4$ , which allow ECAL crystals to be only 23 cm long in the barrel and 22 cm long in the endcap while still spanning 25.8 and 24.7 radiation lengths, respectively. This is enough to ensure that few electrons or photons escape ECAL with any appreciable remaining energy.

The total scintillation light yield is relatively low, averaging just 4.5 photons per MeV deposited. This is partially compensated by the fact that virtually all of ECAL is active material and no energy is lost to uninstrumented absorbers, but Poisson fluctuations in the yield are still the largest contribution to ECAL energy resolution for most electron and photon energies. This statistical uncertainty is represented by the first term in the full resolution equation,

$$\left(\frac{\delta E}{E}\right)^2 = \left(\frac{2.8\%}{\sqrt{E/\text{GeV}}}\right)^2 + \left(\frac{0.12}{E/\text{GeV}}\right)^2 + (0.30\%)^2. \quad (3.11)$$

296 The second term comes from electronic noise and noise from pileup, and the last term  
 297 represents intrinsic differences between crystals. The upside to PbWO<sub>4</sub>'s scintillation  
 298 is that it is fast: roughly 80% of the light is emitted in the 25 ns between bunch  
 299 crossings, so energy measurements require integration over only a few bunch crossings.

### 300 3.2.4 Hadronic Calorimeter

301 Between ECAL and the magnet is the hadronic calorimeter (HCAL), responsible for  
 302 measuring the energy of hadronic jets. HCAL is a sampling calorimeter, meaning  
 303 that the hadrons pass through dense, uninstrumented material and the products of  
 304 the resulting interactions deposit energy in scintillators which are used to measure the  
 305 total energy of the original incoming particles. The HCAL barrel (HB,  $|\eta| < 1.305$ )  
 306 and endcap (HE,  $1.305 < |\eta| < 3.0$ ) are made of layers of brass absorber interleaved  
 307 with plastic scintillating tiles. The energy resolution in HB and HE is given by

$$\left(\frac{\delta E}{E}\right)^2 = \left(\frac{90\%}{\sqrt{E/\text{GeV}}}\right)^2 + (4.5\%)^2. \quad (3.12)$$

308 The first term is from the stochastic evolution of hadronic showers in the absorber,  
 309 the second is from calibration uncertainties.

310 The geometry of HB, HE, and HO is shown in Fig. 3.8. The thickness of HB and  
 311 HE is constrained by the size of the magnet, varying from 5.4 nuclear interaction  
 312 lengths in the central barrel to more than 10 in the endcaps. Because HB is not thick  
 313 enough to absorb all hadrons in the barrel, there is an extra outer HCAL component  
 314 (HO) outside of the magnet, consisting of two more layers of scintillator on either  
 315 side of a 20 cm-thick iron “tail catcher” covering  $|\eta| < 1.3$ . With HO and the 1.1  
 316 interaction lengths in ECAL considered, no part of the calorimeter system spans  
 317 fewer than 11.8 interaction lengths except in the gaps between barrel and endcap,  
 318 minimizing the flux of hadronic “punchthrough” interacting with the muon system.

319 The total material budget in front of the layers of the muons systems is shown in  
 320 Fig. 3.9.

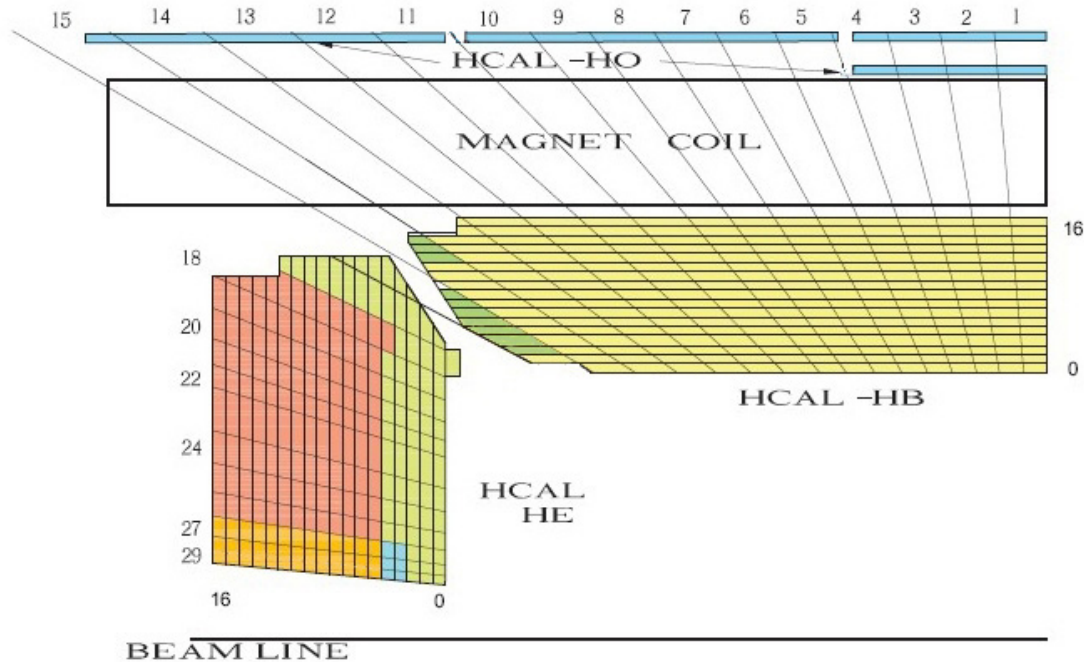


Figure 3.8: Diagram of HCAL geometry, reproduced from Ref. [108].

321 Closer to the beam line on each side, the forward hadronic calorimeter ( $\text{HF}, 3.0 <$   
 322  $|\eta| < 5.2$ ) is made of iron and quartz fibers instead of brass and plastic scintillator to  
 323 maximize radiation hardness. It acts as a Cherenkov detector with the quartz fibers  
 324 as the active detection element. Half the fibers extend the entire depth of HF, while  
 325 the other half start after the hadrons have traversed 22 cm of iron, allowing some  
 326 differentiation between electromagnetic and hadronic energy. The energy resolution  
 327 in HF is given by

$$\left(\frac{\delta E}{E}\right)^2 = \left(\frac{172\%}{\sqrt{E/\text{GeV}}}\right)^2 + (9\%)^2, \quad (3.13)$$

328 where the terms have the same physical interpretation as those in Eq. (3.12). HF  
 329 improves CMS's missing energy resolution by roughly a factor of three.

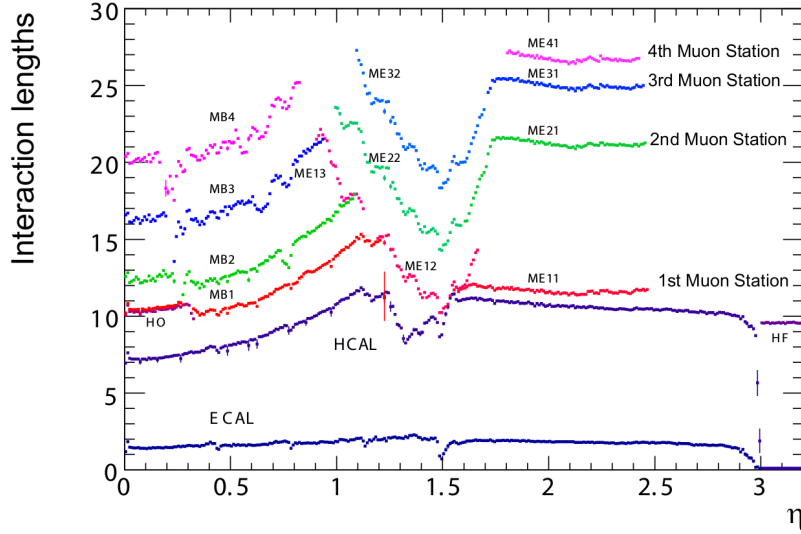


Figure 3.9: Total material budget in units of nuclear interaction lengths, as a function of pseudorapidity, reproduced from Ref. [108].

### 3.2.5 Muon Spectrometer

Many of the most interesting physics processes at the LHC involve high energy muons, so muon identification, triggering, and momentum measurement are important design goals. Muons leave very little energy in the calorimeters, so ECAL and HCAL cannot be used for triggering and identification as they are for electrons, photons and hadrons, or to improve momentum measurements of high- $p_T$  muons whose tracks are too straight to allow good measurements of their curvature. Instead, these functions are provided for muons by three gas-based systems surrounding the rest of the detector [124, 125]. In all three, ionizing gas chambers provide hits which form a track. The magnetic field for this is provided by the return yoke, a set of steel plates interleaved with the muon chambers which confine the solenoid's magnetic return field. The yoke plates weigh a total of 10,000 t and are fully saturated by the solenoid.

Unlike the inner tracker, the muon systems can be read out fast enough to provide triggering. Because muons above 3 GeV generally traverse the muon system while most other measurable particles are stopped in the calorimeters, magnets, or return

345 yoke, the muon system provides high efficiency, low-background muon identification.  
 346 The muon system's momentum measurements are not competitive with the inner  
 347 tracker's at low  $p_T$ , but a combined fit of the inner track and the muon system  
 348 ("standalone") track improves muon  $p_T$  resolution above roughly 200 GeV. The  
 349 geometry of all three muon systems and the return yoke can be seen in Fig. 3.10.

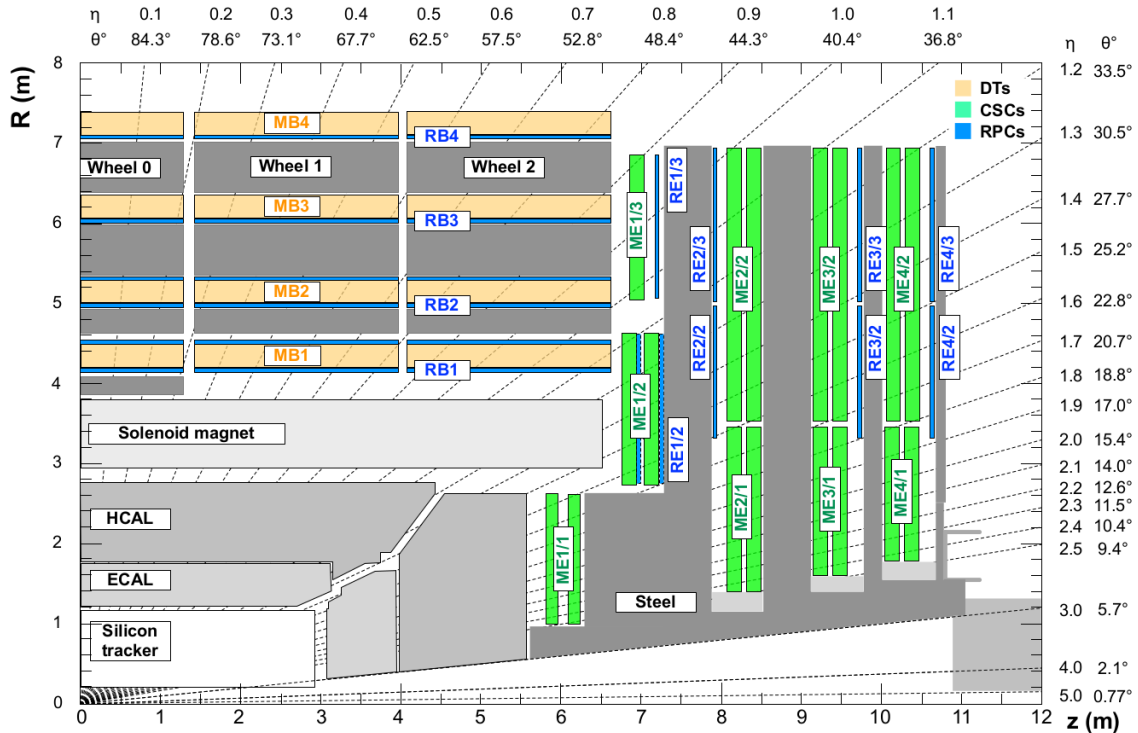


Figure 3.10: Diagram of muon system and return yoke geometry, reproduced from Ref. [125]. The magnet, calorimeters, and inner tracker are also visible.

### 350 3.2.5.1 Drift Tubes

351 In the barrel ( $|\eta| < 1.2$ ), drift tube (DT) chambers are arranged in four "stations"  
 352 separated by the steel layers of the yoke. Stations are made of two or three superlayers  
 353 (SLs) of four layers of rectangular drift cells. Adjacent layers are staggered latterally  
 354 by half a drift cell width to avoid gaps. Each station has two SLs with wires running  
 355 parallel to the beam to measure muon tracks in the  $r\phi$  plane, separated by an

356 aluminum honeycomb lattice to provide mechanical rigidity and act as a spacer. The  
 357 inner three stations contain an extra SL on the outer side of the spacer with wires  
 358 perpendicular to the beam line, to measure muon position along the  $z$ -axis.

359        Each drift cell contains a roughly 2.4 m-long wire in gas (85% Ar, 15% CO<sub>2</sub>). The  
 360 electric field in the cell is provided by aluminum tape glued to the top and bottom  
 361 of the cell and held at +1.8 kV relative to the grounded aluminum plates above and  
 362 below. Aluminum tape cathodes on the side of the cell are held at -1.2 kV, while the  
 363 wires act as +3.6 kV anodes. The width of each cell perpendicular to muon motion,  
 364 42 mm, was chosen for a maximum drift time of 380 ns, sufficient to obviate the need  
 365 for double-hit readout logic in this low-occupancy region of the detector. The height  
 366 of 13 mm set by mechanical and space constraints. Track timing resolution in each  
 367 SL is a few nanoseconds when all cells are allowed to read out all deposited charge.  
 368 The  $r$ - $\phi$  position resolution available for online use in the trigger is about 1.5 mm in  
 369 each SL; offline, for a single wire it is roughly 250  $\mu$ m, leading to an overall offline  
 370 resolution of 100  $\mu$ m at each station.

### 371 3.2.5.2 Cathode Strip Chambers

372 Muons with  $1.2 < |\eta| < 2.4$  are detected by the cathode strip chambers (CSCs).<sup>2</sup>  
 373 The CSC system's trapezoidal chambers are arranged on discs interleaved with the  
 374 endcap yoke in four layers. Chambers close to the beamline each cover 20° sections  
 375 in  $\phi$  while outer chambers cover 10° sections, with overlap to avoid gaps.

376        A CSC chamber is made of seven panels sandwiched together to make six gaps  
 377 filled with a gas mixture (40% Ar, 50% CO<sub>2</sub>, 10% CF<sub>4</sub>). Six of the plates have cathode  
 378 strips milled into one side, varying in pitch from 8.4 mm at the narrow end of the  
 379 trapezoid to 16 mm at the wide end, with 0.5 mm gaps between strips. Three panels

---

<sup>2</sup>Where the CSCs and DTs overlap ( $0.9 < |\eta| < 1.2$ ), tracks are formed from hits in both.

380 are wrapped with anode wires, alternating with the other panels so that every gas  
 381 gap has a plane of wires. Wires are spaced 3.2 mm apart and run azimuthally around  
 382 the detector, except for the innermost chamber closest to the interaction point, which  
 383 are inside the magnet and must have their wires tilted 29° so that charge collected  
 384 by the wires moves parallel to them despite the Lorentz forces from the solenoid.

385 A typical muon will deposit charge in 3–4 cathode strips and a similar number of  
 386 anode wires per gas gap, allowing hit position to be interpolated using all these sig-  
 387 nals as well as timing information. The single-plane spatial resolution can be as good  
 388 as 80  $\mu\text{m}$  but depends strongly on where in the width of the strip the muon hits. The  
 389 strips in alternating planes are therefore offset by half their width. Measurements  
 390 from all six gas gaps in a chamber are combined into a segment with position reso-  
 391 lution in the 30–80  $\mu\text{m}$  range, which depends on the chamber but not where in the  
 392 chamber the muon hit.

393 Anodes and cathodes are held 3.6 kV from each other, leading to a drift time of  
 394 roughly 300 ns. Single anode planes have an RMS timing resolution of around 11 ns,  
 395 insufficient for assigning a hit unambiguously to an individual bunch crossing, as  
 396 required for triggering. However, information from all six anode planes in a chamber  
 397 can be combined to yield a segment timing resolution around 5 ns. Segments are  
 398 therefore the unit of information sent to the trigger. Segment position resolution at  
 399 trigger level is 1–2 mm.

#### 400 3.2.5.3 Resistive Plate Chambers

401 To provide a redundant set of muon momentum measurements, as well as precise  
 402 timing of muon hits, CMS has six layers of resistive plate chambers (RPCs) in the  
 403 barrel and four in the endcap up to  $|\eta| < 1.6$ . RPC chambers consist of two thin  
 404 layers of intert gas (95.2% C<sub>2</sub>H<sub>2</sub>F<sub>4</sub>, 4.5% C<sub>4</sub>H<sub>10</sub>, 0.3% SF<sub>6</sub>) each between a pair of

405 Bakelite electrodes held at 9.3 kV. The two “gas gaps” are placed on either side of  
406 a plane of copper strips. When a passing muon ionizes the gas, the high voltage  
407 causes a fast electron avalanche read out by the strips. The narrow gap allows the  
408 RPCs to have single-hit timing resolution around 1 ns, but the spatial resolution is  
409 limited to about 1 cm by the size of the readout strips. The DTs and CSCs both  
410 have better momentum resolution than the RPCs, but RPCs are a simple, robust  
411 auxiliary system and the timing resolution can be used in conjunction with the other  
412 systems to improve overall muon measurements. The gaps between RPC chambers  
413 do not align with the gaps in the other outer muon systems, increasing the muon  
414 spectrometer’s geometrical acceptance.

### 415 **3.2.6 Data Acquisition and Trigger**

416 With a bunch crossing rate of 40 MHz and over 40 collisions possible in each crossing,  
417 the collision rate can exceed 1.6 GHz. Event sizes on disk of 1–2 MB mean that the  
418 raw data generation rate of CMS could potentially be several PB/s, substantially  
419 more than can be read out, stored or analyzed with current technology. However,  
420 most events consist only of low-energy, well-understood QCD interactions, so the  
421 data rate can be drastically reduced by reading out and storing only events likely to  
422 have interesting physics content. CMS reduces the event rate with a two-level trigger  
423 system.

424 The level-1 (L1) trigger uses custom hardware operating on trigger primitives  
425 (TPs) containing lower-granularity detector information to reduce the event rate to  
426 100 kHz or less. The inner tracker’s readout is too slow for use in the trigger, so only  
427 the calorimeters and muon systems generate TPs. Events accepted at level-1 are fully  
428 read out, digitized, and sent to the high level trigger (HLT), where they are partially  
429 reconstructed in software and filtered further, reducing the final rate of stored events

430 to roughly 1 kHz.

431 **3.2.6.1 Level-1 Trigger**

432 LHC beams collide at too high a rate for trigger decisions to be made in software,  
 433 so the L1 trigger is instead implemented in custom hardware, with processing done  
 434 using field-programmable gate arrays (FPGAs) as much as possible for flexibility, and  
 435 application-specific integrated circuits (ASICs) where required. Hardware limitations  
 436 of other CMS subsystems—in particular, the inner tracker’s readout speed and buffer  
 437 capacity—impose strict constraints on the system. The rate of events passing at  
 438 level-1 cannot exceed 100 kHz and the system’s overall latency cannot exceed roughly  
 439 4.2  $\mu$ s from the proton-proton interaction to data storage at level-1. These goals are  
 440 achieved while maintaining high efficiency for interesting physics events by using low-  
 441 granularity detector information, to reduce the bandwidth needed within the trigger  
 442 system. Information flows through several processing steps, with the data throughput  
 443 reduced at each step. Calorimeter and muon information are processed in parallel  
 444 and combined only in the final step. Optical links between systems provide high-  
 445 bandwidth data transfer and allow flexibility in the overall trigger architecture. The  
 446 calorimeter trigger was upgraded with respect to the Run I configuration in 2015,  
 447 and the whole trigger system was overhauled in 2016 [126]. Both configurations will  
 448 be described here.

449       Calorimeter information is compressed into TPs for use in the trigger by trigger  
 450 primitive generators (TPGs). Each TP represents a “tower” consisting of a  $5 \times 5$   
 451 cluster of barrel or endcap ECAL crystals and the HCAL tower behind them, or a  
 452 section of the HF. The TP contains an 8-bit transverse energy sum and a quality bit  
 453 for each calorimeter, and six bits of error checking and bookkeeping information. In  
 454 2015, TPs were sent to the Regional Calorimeter Trigger (RCT) [127], which processed

455 18 portions of the detector (segmented in  $\phi$  with  $+\eta$  and  $-\eta$  treated separately) in  
 456 parallel in separate crates of electronics, using several ASICs and one FPGA in each  
 457 crate for processing [128]. Each RCT crate summed the TPs with  $|\eta| < 3.0$  into  
 458  $4 \times 4$  tower regions, and found isolated and non-isolated  $2 \times 1$  tower  $e/\gamma$  and  $\tau$   
 459 candidates. These objects were sent to Stage 1 Layer 2, which selected the best  $e/\gamma$   
 460 and  $\tau$  candidates from the entire detector, clustered regions into  $3 \times 3$  region jet  
 461 candidates, and computed global quantities like missing transverse energy and the  
 462 scalar sum of transverse momentum for all particles in the event. Pileup subtraction  
 463 was performed with a lookup table (LUT) based on the number of regions in the  
 464 detector with no energy.

465 In 2016, the whole calorimeter trigger was replaced with a new two-tiered system.  
 466 Stage 2 Layer 1 (“CaloL1”) consists of 18 FPGA-based Calorimeter Trigger Proces-  
 467 sor 7 (CTP7) cards [129], which calibrate and reformat the TPs before forwarding  
 468 them to Stage 2 Layer 2 (“CaloL2”) [128], an FPGA-based time-multiplexed system  
 469 which finds  $e/\gamma$ ,  $\tau$ , and jet candidates and computes global quantities for whole events  
 470 in parallel using tower-level information.

471 In 2015, the DTs and CSCs fed track segments into track finders (DTTF [130] and  
 472 CSCTF [131]) which used pattern recognition algorithms to reconstruct tracks and  
 473 measure their  $p_T$ , sharing information between the track finders to avoid inefficiency  
 474 in the overlap region. The RPCs made their own tracks. Since the 2016 upgrade,  
 475 track finding has been done by geometrical region of the detector rather than detector  
 476 subsystem alone, with separate track finders for the barrel (BMTF,  $|\eta| < 0.85$ ) using  
 477 DT and RPC information [132], the endcap (EMTF,  $1.25 < |\eta| < 2.4$ ) using CSC and  
 478 RPC information [126], and the overlap region (OMTF,  $0.85 < |\eta| < 1.25$ ) using all  
 479 three muon systems [133]. The track finders feed into the Global Muon Trigger (GMT,  
 480 upgraded to  $\mu$ GMT in 2016) [134, 135], which merges and sorts tracks, analyzes their

481 quality and selects the best ones.

482 The calorimeter and muon trigger systems, which have up to this point worked  
 483 entirely in parallel, both send their selected candidates and global quantities to the  
 484 Global Trigger (GT, upgraded to  $\mu$ GT) [136, 137]. The Global Trigger contains the  
 485 trigger menu, the configurable set of algorithms used to determine whether an event  
 486 is accepted or not. These algorithms can use combinations of the objects from the  
 487 calorimeter and muon trigger systems, including imposing topological requirements,  
 488 e.g. requiring a large  $\Delta\eta$  between muons in a pair. The final decision is a logical OR  
 489 of all triggers in the menu, but each trigger may be prescaled, i.e. only included in  
 490 the final decision a fraction of the time in order to reduce its rate. When an event is  
 491 accepted, a level 1 accept (L1A) signal is sent to all CMS subsystems instructing them  
 492 to read out information collected in the accepted event, which is stored in buffers until  
 493 it can be read out or safely discarded. A diagram of the whole 2016 L1 trigger system  
 494 and its information flow is shown in Fig. 3.11.

#### 495 3.2.6.2 High-Level Trigger

496 After an accepted event is read out and digitized, it must undergo another level  
 497 of screening before being stored. The High Level Trigger (HLT) uses full detector  
 498 information reconstructed with versions of the normal CMS reconstruction algorithms  
 499 specially optimized for speed, running on a large farm of commercial computers [138].  
 500 Much of HLT’s power comes from having tracker information, allowing more precise  
 501 momentum measurements, isolation calculations and identification algorithms than  
 502 are available at L1. For example, the pixels can be used to reconstruct vertices and  
 503 tag b-quark jets, and requirements can be placed on the invariant mass of a lepton  
 504 pair. However, track reconstructions is slow, so it is typically only done as one of the  
 505 last steps in the filtering process, allowing the event to be rejected based on more

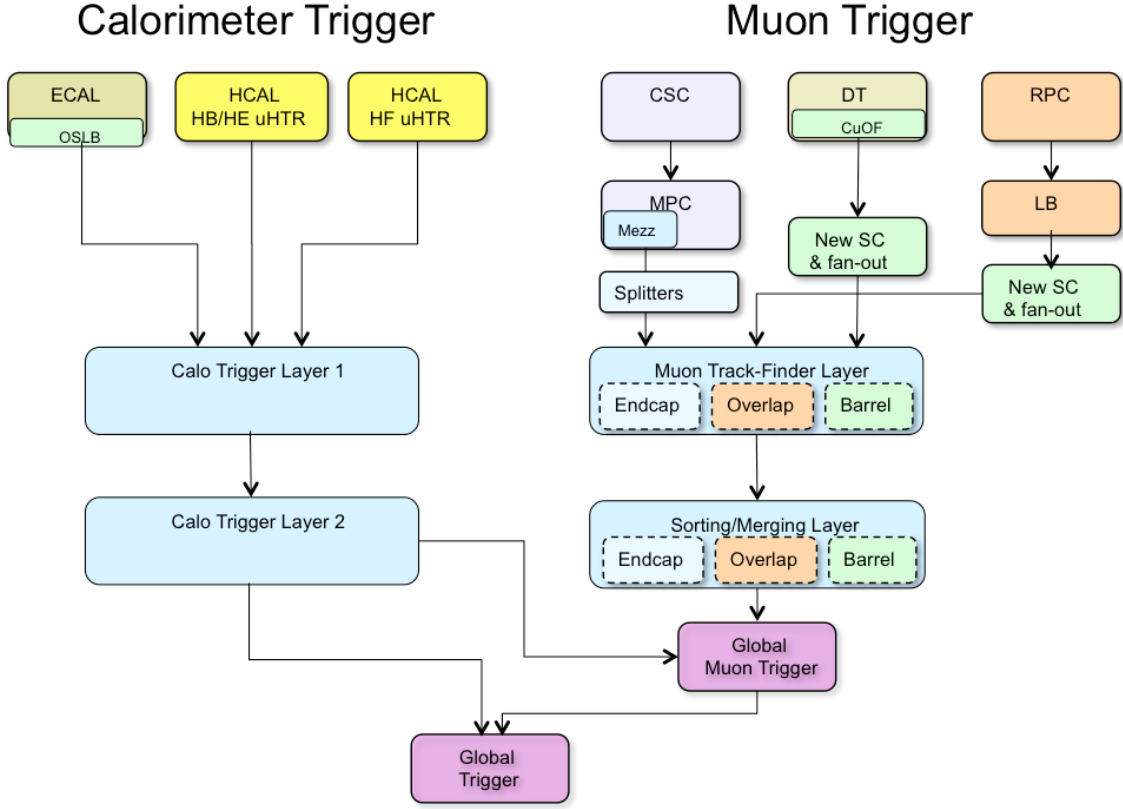


Figure 3.11: Data flow diagram for the CMS L1 trigger after the 2016 overhaul, reproduced from Ref. [126].

506 easily reconstructed objects like tracks in the muon system. Other optimizations  
 507 include only reconstructing tracks near objects passed in by the L1 Global Trigger.  
 508 The final result is that the rate of events saved for later analysis is around 1 kHz.

### 509 3.2.7 Luminosity Determination

510 A precise measurement of the luminosity delivered by the LHC is critical to precisely  
 511 measuring any cross section. The instantaneous luminosity for  $n_b$  colliding bunch  
 512 pairs with intensity  $N_b$  and orbit frequency  $f_{rev}$  is given by

$$\mathcal{L} = \frac{n_b N_b^2 f_{rev}}{A_{\text{eff}}} \quad (3.14)$$

513 where  $A_{\text{eff}}$  is the effective area of the beam-beam overlap. If beam  $i$  has a gaussian  
 514 density profile in the  $u$  direction of width  $\sigma_{i,u}$ , and the beam densities are uncorrelated  
 515 in each direction, then

$$A_{\text{eff}} = 2\pi \sqrt{\sigma_{1,x}^2 + \sigma_{2,x}^2} \sqrt{\sigma_{1,y}^2 + \sigma_{2,y}^2}. \quad (3.15)$$

516 The beam widths  $\sigma_{i,u}$ , the only unknowns in Eq. (3.14), are purely geometrical and  
 517 can be found with the Van de Meer (VdM) scan method [139, 140]. In a VdM scan,  
 518 for which LHC has a special run mode, one beam is held fixed while the position  
 519 of the other is scanned in the  $x$ - $y$  plane, and detector activity is measured as a  
 520 function of beam displacement. Because the width of the interaction rate distribution  
 521 is independent of its overall normalization, the detector activity metric may be any  
 522 quantity linearly proportional to the interaction rate.

523 Over the course of an LHC run,  $n_b$ ,  $N_b$ , and  $A_{\text{eff}}$  are all subject to change, and  
 524 in fact the VdM scans are performed regularly, so in practice the procedure outlined  
 525 above provides a calibration and overall scale for luminosity measurements during  
 526 physics collisions. For a given detector metric labeled  $Q$  with rate  $R^Q$  that peaked  
 527 at  $R_0^Q$  with no beam displacement, the VdM scan yields a visible cross section, the  
 528 constant of proportionality between the rate and the instantaneous luminosity,

$$\sigma_{\text{vis}}^Q \equiv \frac{R^Q}{\mathcal{L}} = \frac{A_{\text{eff}} R_0^Q}{f_{\text{rev}}}. \quad (3.16)$$

529 CMS has several such metrics; the primary one used for measuring integrated lumi-  
 530 nosity is the number of pixel hit clusters [141, 142]. The instantaneous luminosity is  
 531 given by

$$\mathcal{L} = \frac{\langle N_c \rangle f_{\text{rev}}}{\sigma_{\text{vis}}^{\text{PCC}}} = \frac{\langle N_c \rangle f_{\text{rev}}}{A_{\text{eff}} \langle N_c \rangle_0} \quad (3.17)$$

532 where  $\langle N_c \rangle = R^{\text{PCC}} / f_{\text{rev}}$  is the average number of pixel hit clusters at each bunch  
 533 crossing and  $\langle N_c \rangle_0$  is its peak value during the VdM scan.

534 A number of complications must be accounted for or included in systematic un-  
535 certainty estimates. Beam-beam interation effects, correlations between the proton  
536 density distributions in the  $x$  and  $y$  directions, drifts in the beam orbit, and nor-  
537 malization uncertainties on the bunch intensity and absolute distance scale from the  
538 beam spot must all be handled with care. The result is a total integrated luminosity  
539 uncertainty of 2.3% in 2015 [141] and 2.5% in 2016 [142].

## <sup>0</sup> Chapter 4

### <sup>1</sup> Simulation

<sup>2</sup> Comparing data collected by CMS to theoretical predictions is a complex task. The  
<sup>3</sup> theories described in Chapter 1 are understood in great detail, but using this knowl-  
<sup>4</sup> edge to calculate observables is a nontrivial enterprise. Once calculated, observables  
<sup>5</sup> must be compared to data from a detector with finite resolution and subject to a  
<sup>6</sup> number of experimental effects that do not exist in the rarefied world of quantum  
<sup>7</sup> field theory. The general strategy is to employ numerical simulations of individual  
<sup>8</sup> collision events that involve a physics process of interest, and apply accurate simu-  
<sup>9</sup> lations of the detector’s response to these events to obtain samples that are directly  
<sup>10</sup> comparable to data. The success of all steps in this process at a high-luminosity  
<sup>11</sup> hadron collider is one of the triumphs of the LHC era, with many observables in  
<sup>12</sup> interesting processes simulated accurately to the level of a few percent.

#### <sup>13</sup> 4.1 Monte Carlo Event Generation

<sup>14</sup> Even in trivial cases, it would be impossible to integrate over the phase space of hard  
<sup>15</sup> scattering outcomes determined from theory, convolved with matter interactions, de-

16 tector effects, and other experimental factors, to calculate observables analytically.  
 17 Particle interactions are well-understood on a microscopic scale, but it is extremely  
 18 difficult to extrapolate from this first-principles understanding to a description of the  
 19 macroscopic behavior of an ensemble of particles as needed to make predictions about  
 20 fundamentally stochastic processes. Observable spectra are therefore modeled with  
 21 the Monte Carlo (MC) method [11, 143], a numerical integration technique so named  
 22 because, like a casino, it relies heavily on random numbers<sup>1</sup>. The scattering ampli-  
 23 tudes for a process are calculated from theory at a chosen perturbative order, and  
 24 for each simulated event a configuration of final state particles is selected at random  
 25 from this phase space. The final state particles are propagated through decays, radia-  
 26 tion, hadronization, and interaction with other matter—such as the detector—based  
 27 on well-understood physics principles, and the outcome of any stochastic process is  
 28 chosen at random from a realistic set or distribution of possibilities. In the limit of  
 29 a large number of simulated events, the distributions from the simulated detector  
 30 will converge to be directly comparable to aggregated data. Individual steps in this  
 31 process are detailed in the following sections.

### 32 **4.1.1 Matrix Element and Hard Process Generation**

33 Event generator programs start by calculating the scattering amplitudes for a process  
 34 at a chosen order in perturbation theory. For example, the generator **MADGRAPH5-**  
 35 **\_AMC@NLO** [145] generates all the relevant Feynman diagrams up to NLO and  
 36 calculates the matrix elements for them. Others, like **POWHEG** [146–148], **SHER-**  
 37 **PA** [149] and **MCFM** [53, 54, 150], are not fully general but have a broad range of  
 38 physics processes implemented at NLO; **SHERPA** and **MCFM** can do some calculations

---

<sup>1</sup>Pseudorandom numbers are actually used, but there is no difference in practice as long as a good pseudorandom number generator (PRNG) is chosen and seeded properly. The Mersenne Twister algorithm [144] is the modern standard among general-purpose PRNGs in physics and elsewhere.

39 at NNLO [151]. Events are generated across the entire allowed phase space, either  
 40 uniformly or with the specific distribution dictated by one of several “importance  
 41 sampling” techniques [11, 152] which ensure appropriate statistical coverage in regions  
 42 where the distribution has a large slope or value. Each event is assigned a weight  
 43  $w \in (0, 1)$  based on the scattering amplitude in that region of phase space and the  
 44 probability of having an appropriate initial state based on the PDFs discussed in  
 45 Section 1.6. The sample is then “unweighted” to a subset that is directly comparable  
 46 to data by removing events with a probability proportional to  $1 - w$ .

#### 47 4.1.2 Parton Shower, Hadronization, and Underlying Event

48 Processes generated above leading order may have extra radiation, as in the real  
 49 emission diagrams of Fig. 2.2. In the case of calculations at higher orders in QCD, the  
 50 emissions are quarks and gluons which fragment, hadronize, decay, etc. This process is  
 51 handled by a parton shower (PS) MC program such as PYTHIA8 8 [59] (used for most  
 52 simulations used in this analysis), HERWIG [153, 154], or SHERPA [149]. In PYTHIA8,  
 53 parton showering is simulated with the Lund string model [11, 155–157], which treats  
 54 gluons as ropes connecting color charged particles whose tension increases as the  
 55 quarks move apart. When a rope stretches too far, it breaks, producing a quark pair  
 56 at the new rope ends.

57 Parton shower programs also handle radiation of soft gluons from color charged  
 58 particles and photons from electrically charged particles [158]. The emitter may be  
 59 an incoming parton (initial state radiation, ISR), a virtual particle exchanged during  
 60 the interaction, or an outgoing particle (final state radiation, FSR). The distinction  
 61 between “soft” radiation that should be handled by the PSMC and “hard” emission  
 62 present in the matrix element is not well defined, so it is important to avoid double-  
 63 counting regions of phase space at the boundary between the processes. This is done

64 with jet matching [11, 145]. At tree level, matching may be achieved by enforcing  
 65 a jet energy cutoff: partons from the matrix element must have energy  $E > E_{\text{cut}}$ ,  
 66 and the PSMC is responsible for any softer radiation. At NLO, loop diagrams carry  
 67 divergences that must be canceled by divergences of opposite sign in the infrared  
 68 radiation regime, which the cutoff would prevent, so a more sophisticated scheme must  
 69 be used which weights some events negatively to handle destructive interference [145]  
 70 or modifies the shower development algorithm [146, 147].

71 When combining showered samples that have different jet multiplicities at hard  
 72 process level the task becomes even more difficult because the phase space of events  
 73 with  $n$  jets in the matrix element that gain another from the PS overlaps with the  
 74 phase space of events with  $n + 1$  jets at matrix element level. This problem can be  
 75 solved with one of several jet merging algorithms [145, 159–161]. The MLM [162]  
 76 and CKKW [163] algorithms implement merging for tree-level diagrams of different  
 77 jet multiplicities by cutting (MLM) or weighting (CKKW) events based on the prob-  
 78 ability that such an event would originate from the matrix element or PS. The FxFx  
 79 algorithm implements merging when one-loop diagrams are included [164].

80 PSMC programs provide several more features that are vital in obtaining a faith-  
 81 ful reproduction of data, especially in events with only soft hadronic activity. The  
 82 radiation described above affects the  $p_T$  of the hard scatter system, so PSMCs must  
 83 “retroactively” adjust the kinematics generated by the matrix element MC. The un-  
 84 derlying event, further QCD interactions that happen below the regime that can be  
 85 calculated perturbatively, are modeled phenomenologically [11, 59]. This includes soft  
 86 color exchange between fragments of the colliding hadrons that sends proton remnants  
 87 into the detector in the form of extra soft hadrons [165]. There is also a possibility that  
 88 multiple pairs of partons will undergo hard interactions in the same proton-proton  
 89 collision, essentially combining two quasi-independent hard scatters [158, 166].

### 90 4.1.3 Pileup Simulation

91 The high per-bunch luminosity of the LHC causes multiple collisions to occur in each  
 92 bunch crossing. The extra interactions are called pileup. To account for this effect,  
 93 CMS simulations include extra minimum-bias collision events overlaid on top of the  
 94 primary collision [167, 168]. This includes simulated pileup interactions that are time  
 95 evolved to reproduce the effects of “out-of-time” pileup from previous bunch crossings.  
 96 Because MC samples are produced before the pileup profile can be measured in data,  
 97 simulated events are reweighted based on the number of pileup interactions such that  
 98 the distribution of the number of reconstructed vertices becomes similar to that in  
 99 data.

### 100 4.1.4 Samples Used in this Analysis

101 The  $q\bar{q} \rightarrow ZZ$ ,  $qg \rightarrow ZZ$ ,  $gg \rightarrow H \rightarrow ZZ^*$ , and  $q\bar{q} \rightarrow Z \rightarrow 4\ell$  samples are produced  
 102 at NLO with POWHEG [55, 146–148, 169] and scaled to the NNLO total cross section  
 103 with  $K$  factors of 1.7 for the Higgs sample and 1.1 for the others [56]. The non-  
 104 Higgs POWHEG samples include  $ZZ$ ,  $Z/\gamma^*$ , and  $\gamma^*\gamma^*$  production with a generator-level  
 105 constraint of  $m_{\ell\ell} > 4$  GeV for all opposite-charge lepton pairs, to limit the generated  
 106 phase space to only regions of interest and far from infrared divergences. For the  
 107 inclusive cross sections and differential cross sections in fully leptonic observables,  
 108 this POWHEG sample is considered the primary theory prediction. For the differential  
 109 cross sections in jet-related variables, MADGRAPH5\_AMC@NLO is used for the  
 110 nominal sample, because it has an extra jet at matrix-element level, merged with the  
 111 PS jets using the FxFx scheme. Box diagram  $gg \rightarrow ZZ$  samples are generated with  
 112 MCFM at LO [170]; these are scaled to NLO with a  $K$  factor of 1.7 [57].

113 Background WZ events are produced with POWHEG with the same settings as the

114 ZZ sample while  $t\bar{t}Z$  and WWZ samples are generated at LO with MADGRAPH5-  
 115 \_AMC@NLO. Electroweak and non-VBS ZZjj samples are produced with MAD-  
 116 GRAPH5\_AMC@NLO for the VBS and aQGC searches and with PHANTOM for the  
 117 cross section measurements [171]. Samples with nonzero aTGCs are generated at LO  
 118 with SHERPA [149] and scaled such that the total yield from the SM SHERPA sample  
 119 is the same as the yield from the POWHEG ZZ sample. Signal samples for the aQGC  
 120 search are made with MADGRAPH5\_AMC@NLO.

121 All samples use the NNPDF3.0 PDF sets [172]. Parton showing, hadronization,  
 122 and underlying event simulation are done with PYTHIA8 using the CUETP8M1  
 123 tune [173] for all samples except the aTGC samples, for which SHERPA performs  
 124 these tasks.

## 125 4.2 Detector Simulation

126 To incorporate experimental effects into MC samples, the detector and the final state  
 127 particles' interactions with it are simulated with the highest possible level of de-  
 128 tail [167, 168]. The detector geometry and material, including both instrumented  
 129 and non-instrumented components, are modeled with the GEANT4 package [174],  
 130 which describes microscopic particle interactions with matter over a wide range of  
 131 energies and propagates the effects of these interactions to their macroscopic conse-  
 132 quences. Stochastic effects are again implemented with Monte Carlo methods that  
 133 select outcomes at random from realistic distributions of possibilities. The GEANT4  
 134 simulation includes a detailed model of the magnetic field, so particle trajectories are  
 135 calculated correctly, and the generation of secondary particles like  $e^+e^-$  pairs from  
 136 photons interacting with tracker material. Charge deposition in silicon, scintillation  
 137 in clear crystals, hadronic showers from nuclear interactions, and gas ionization are

138 all included, among many other processes, so detector signals are derived from micro-  
139 scopic interactions too, and GEANT4 has signal digitization capabilities which ensure  
140 that the signals coming out of the simulated detector are exactly those that would  
141 be produced by the real detector in the same situation.

142 The simulated signals are fed into the same reconstruction software as is used  
143 for data (see Chapter 5). The same analysis strategy may then be used for MC  
144 samples and data, and comparing the results is meaningful. Though every effort  
145 is made to model the detector accurately, no simulation can incorporate all real  
146 effects with perfect fidelity. Monte Carlo samples must be produced before data are  
147 actually collected, so the final detector alignment and calibration cannot be known  
148 exactly, and conditions may change mid-run if—for example—a subdetector channel  
149 goes dead or LHC beam conditions change. Residual corrections for these small  
150 effects are applied to final physics objects in the final steps of the analysis to make  
151 distributions of interest, such as dilepton mass around the Z resonance or the overall  
152 jet  $p_T$  spectrum, match in aggregate. The overall level of agreement between data  
153 and simulation may be seen in Fig. 4.1, which shows the invariant mass of  $e^+e^-$  events  
154 around the Z resonance for simulated samples and data, and their ratio.

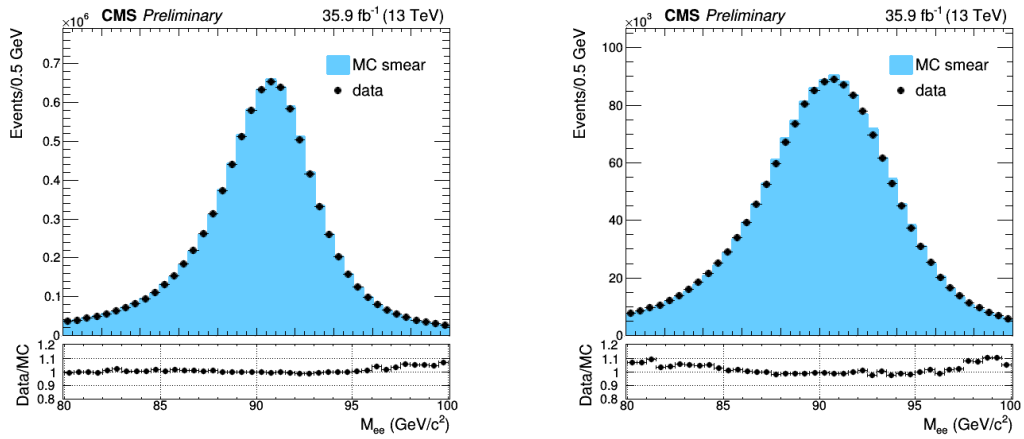


Figure 4.1: The invariant mass of  $e^+e^-$  events with both electrons in the barrel (left) and both electrons in the endcaps (right) in the whole 2016 dataset after all corrections are applied. The lower plots show the ratio of data and simulation to show the level of agreement achieved.

## **0 Chapter 5**

# **1 Object Reconstruction and 2 Selection**

3 The raw detector information stored on disk after an event passes trigger selections  
4 is not yet suitable for physics analysis. Hits in the tracker and muon systems, and  
5 energy deposits in the calorimeters, require significant processing to build physics  
6 objects that are interpretable in terms of the physics of the hard scatter. Patterns in  
7 the tracker and muon system hits are found and used to construct charged particle  
8 and muon tracks, and energy deposits in the calorimeters are grouped into clusters.  
9 Final state particles that interact with CMS are reconstructed from the tracks and  
10 calorimeter clusters, final state particles are clustered into jets, charged particles are  
11 clustered by track origin to find proton-proton collision vertices, and visible particle  
12 momenta are summed to find the transverse momentum imbalance from undetectable  
13 particles (in the SM, neutrinos). The resulting physics objects undergo selection to  
14 determine which represent real particles of interest for the analysis. Selected particles  
15 are used to reconstruct the hard interaction from the collision—in the analyses pre-  
16 sented here, leptons are paired to form  $Z/\gamma^*$  boson candidates which may be paired

17 to form Higgs or Z boson candidates or nonresonant ZZ candidates, and jets are  
 18 used to construct hadronic observables and to distinguish electroweak and QCD ZZ  
 19 production.

20 **5.1 Track Reconstruction and Vertex  
 21 Identification**

22 Tracks are reconstructed in the inner tracker by iterative application of a combina-  
 23 torial Kalman filter algorithm [175–178]. At each iteration, tracks found in the pixel  
 24 detector are used as “seeds”, track segments which serve as the initial trajectories on  
 25 which strip tracker hits from the same particle are expected. The pixel seed supplies  
 26 the initial parameters for the combinatorial Kalman filter. At each tracker layer, the  
 27 algorithm predicts where the particle will hit the next layer based on the track’s cur-  
 28 rent parameters, taking into account the effects of particle interaction with tracker  
 29 material. The extrapolated trajectory is used to find compatible hits in the next layer  
 30 with a  $\chi^2$  test, and if possible the most compatible hit is added to the track and its  
 31 parameters are updated accordingly. If no hits are compatible, a “ghost” hit which  
 32 does not contribute to the track parameters may be added to account for the possibil-  
 33 ity of a missing hit in the corresponding layer. This procedure is repeated recursively  
 34 at each tracker layer, from the innermost layer past the seed to the outermost layer  
 35 of the silicon strip tracker. If two tracks found in an iteration share too many hits,  
 36 they are assumed to be from the same particle and the one with fewer hits is rejected,  
 37 using the total  $\chi^2$  of all hits as a tiebreaker. The first iterations of the track finding  
 38 algorithm searches for high- $p_T$  tracks from primary proton-proton interactions, which  
 39 are easier to find because they are close to straight and originate from the beam line.  
 40 When a track is found, its constituent hits are removed from consideration in future

41 iterations, reducing the computational complexity of finding the more difficult tracks  
 42 from lower- $p_T$  particles and products of b hadron decays which happen away from  
 43 the beam line.

44 Because the Kalman filter obtains the final track parameters only at the out-  
 45 ermost tracker layer, each track is refit and smoothed with further Kalman filters,  
 46 improving track quality and reducing fake rate. Spurious tracks are rejected from the  
 47 final collection with requirements on the number of layers hit, the  $\chi^2$  of the fit, and  
 48 compatibility with a primary vertex.LHC The efficiency for reconstructing tracks of  
 49 all prompt charged particles with  $p_T > 900$  MeV is around 94% in the barrel and  
 50 85% in the endcap; for isolated muons, it is virtually 100% in the whole tracker  
 51 acceptance [178].

52 Electrons lose substantially more energy to interactions with the tracker material  
 53 than other charged particles, often breaking the assumption of Gaussian energy loss  
 54 inherent to the Kalman filter. To mitigate the impact of the resulting poor track  
 55 fits, tracks with many missing hits or a poor  $\chi^2$  are refit using a Gaussian sum filter  
 56 (GSF) [179]. Any Kalman filter or GSF tracks with trajectories that intersect ECAL  
 57 energy clusters (see below) are considered electron track candidates and refit with a  
 58 second, more complicated GSF. This GSF track collection is used as inputs to the  
 59 PF electron reconstruction described below.

60 Proton-proton interaction vertices are found by clustering tracks by minimizing  
 61 the figure of merit

$$\chi^2 = \sum_i \sum_j p_{ij} \frac{(z_j^t - z_i^V)^2}{\sigma_j^2}, \quad (5.1)$$

62 where  $z_i^V$  is the  $z$  position of vertex  $i$ ,  $z_j^t$  is the  $z$  position of track  $j$  at its closest  
 63 point to the beamline, and  $\sigma_j^2$  is its uncertainty. The track-vertex association matrix  
 64  $p_{ij}$  maps tracks to their associated vertices, i.e.  $p_{ij} = 1$  if vertex  $i$  and track  $j$  are  
 65 associated,  $p_{ij} = 0$  if they are not. Rather than minimize Eq. (5.1) directly with an

66 unknown number of vertices, the CMS clustering algorithm [178, 180] uses a tech-  
 67 nique known as deterministic annealing [181], which treats the system as a statistical  
 68 ensemble of associations between the tracks and an unknown number of vertices. The  
 69 association matrix  $p_{ij}$  is then the probability that vertex  $i$  and track  $j$  are associated.  
 70 If every possible set of assignments, for every possible number and arrangement of  
 71 vertices, is considered equally probable, this is analogous to a thermodynamic system  
 72 at high temperature, with  $\chi^2$  playing the role of energy. The system is simulated at  
 73 high “temperature” and the analog of free energy is minimized to determine  $p_{ij}$ . The  
 74 temperature is then lowered in steps, with track-vertex associations deterministic in  
 75 the limit of zero temperature.

76 Among the interaction vertices in an event, the one whose associated charged  
 77 particles have the highest sum of  $p_T^2$  is labeled the primary vertex (PV). A PV must  
 78 be less than 24 cm from the nominal beam spot in the  $z$  direction and less than  
 79 2 cm from it in the  $x$ - $y$  plane. Many commonly-used analysis observables are strongly  
 80 dependent on the number of secondary proton-proton interaction vertices in the event,  
 81 colloquially called the pileup. The pileup distributions used in Monte Carlo samples  
 82 are not the same as the distribution in data, biasing sensitive quantities. Monte  
 83 Carlo events are therefore reweighted based on the number of simulated pileup vertices  
 84 such that the overall  $N_{vtx}$  (number of proton-proton interaction vertices) distributions  
 85 match.

## 86 5.2 Particle Flow Reconstruction

87 The simplest conceivable algorithm would reconstruct each type of particle mostly  
 88 with information from single subsystems: muons with the outer muon system, elec-  
 89 trons and photons with ECAL (using HCAL to differentiate them from hadrons), jets

90 with the calorimeters aided by inner tracker information to handle b jet vertexing, etc.  
91 This approach is sufficient for many analyses and sophisticated versions of the general  
92 principle have performed admirably at a number of experiments, but it is suboptimal.  
93 It fails to exploit the full detector information for many objects—for example, not  
94 using the inner tracker’s precise measurements of low-energy charged hadrons in jets  
95 made by clustering calorimeter deposits—and misses significant correlations between  
96 detector systems. The CMS collaboration takes a different approach, using a particle  
97 flow (PF) algorithm combining subdetector signals for optimal particle reconstruction  
98 and identification [182–184].

99 Several features of CMS facilitate PF reconstruction, as described in Section 3.2.  
100 The most important is that the calorimeters are inside the magnet and close to the  
101 tracker, so charged particles are much less likely to interact with material between  
102 them. The inner tracker’s precise position measurement and ECAL’s fine segmen-  
103 tation thus allow tracks to be associated to calorimeter clusters even for individual  
104 charged hadrons of modest energy.

### 105 5.2.1 PF Candidates

106 The inputs to the PF algorithm are inner tracker tracks, muon system tracks, and  
107 clusters of energy deposits in the calorimeters, all of which are calibrated beforehand.  
108 Calorimeter clusters are built independently for each subsystem, with ECAL and  
109 HCAL barrel and endcaps considered separately. Topological clusters are built by  
110 combining adjacent cells with energy deposits over a threshold, using cells that are  
111 local energy maxima as seeds. Within the topological clusters, the final calorime-  
112 ter clusters are built by fitting the energy deposits with the sum of several two-  
113 dimensional Gaussians, one Gaussian for each seed in the topological cluster.

114 The first step of the PF algorithm is to link tracks and clusters across subdetec-

115 tors. Tracks are linked to calorimeter clusters by extrapolating from the track to the  
 116 calorimeter cells the particle would be expected to hit. To account for bremsstrahlung  
 117 photons from electron interactions with tracker material, GSF tracks are linked with  
 118 ECAL clusters compatible ( $\Delta\eta < 0.05$ ) with a tangent to the track where it hit the  
 119 tracker. Overlapping ECAL and HCAL clusters are linked outside the inner tracker  
 120 acceptance. Inner tracks are linked to muon system tracks if their hits can be propa-  
 121 gated onto a common surface and merged into a single track within the resolution of  
 122 the muon system (see Section 3.3 of Ref. [184]). The groups of linked objects, called  
 123 “PF blocks”, usually originate from one or a few particles and are the basic unit of  
 124 PF reconstruction.

### 125 5.2.1.1 Muons

126 Muon candidates in CMS [185] come in three flavors: “standalone”, “tracker”, and  
 127 “global” muons. Standalone muons use only the track from the muon spectrometer  
 128 (the “standalone track”), built with a fit to track segments made of clusters of hits in  
 129 the DTs, CSCs, and RPCs. Tracker muons use only the inner track, identified as a  
 130 muon because the track is compatible with one or more track segments in the muon  
 131 system within 3 cm transverse to the track direction, or four standard deviations  
 132 of the track’s angular position uncertainty. Global muons use a combined “global  
 133 track” made by fitting the hits in an inner track and a compatible standalone track  
 134 to a common muon trajectory through the whole detector. By construction, global  
 135 muons have corresponding standalone and tracker muons. Tracker muons are merged  
 136 into their corresponding global muons, which use the inner track momentum for  
 137 muons with  $p_T < 200$  GeV and the momentum of the track with the best normalized  
 138  $\chi^2$  otherwise. When a muon candidate is reconstructed, its constituent tracks are  
 139 removed from the PF block and are therefore not used in further reconstruction.

140 **5.2.1.2 Electrons and Prompt Photons**

141 Electron reconstruction uses GSF tracks linked with ECAL clusters [179, 186]. The  
 142 cluster associated with a track and the bremsstrahlung candidate clusters on tangents  
 143 to the track are collectively called the “supercluster”. Prompt photons are recon-  
 144 structed from superclusters without associated tracks except displaced track pairs  
 145 consistent with photon-initiated electron-positron pair production in the tracker ma-  
 146 terial [187]. In both cases, the HCAL energy near the supercluster cannot be more  
 147 than 10% of the supercluster energy. Non-isolated photons, i.e. those with substan-  
 148 tial nearby tracks or calorimeter deposits or a high ratio of HCAL energy to ECAL  
 149 energy, are assumed to be from  $\pi^0$  decays and are described with neutral hadrons in  
 150 the next section. Tracks and clusters used to reconstruct electrons and photons are  
 151 removed from the PF block and are not used in hadron reconstruction.

152 **5.2.1.3 Charged and Neutral Hadrons**

153 With muon, electron, and prompt photon constituents removed, remaining detector  
 154 signals are taken to be from charged and neutral hadrons (including non-prompt  
 155 photons) [182, 184]. Clusters in ECAL without associated tracks are taken to be  
 156 photons from  $\pi^0$  decays, because neutral hadrons deposit very little energy in ECAL.  
 157 Trackless clusters in HCAL are taken to be neutral hadrons. Both are removed from  
 158 the PF blocks, so all that remain are linked clusters and tracks. Paired tracks and  
 159 clusters with compatible energies are taken to be charged hadrons. If the track  $p_T$   
 160 is much less than the calorimeter-measured  $p_T$ , the pair is labeled as overlapping  
 161 charged and neutral hadrons.

162 **5.2.2 Jets**

163 Effective clustering of hadrons, non-prompt photons, and non-prompt leptons into jets  
 164 is critically important for many physics analyses, including the ZZ + jets differential  
 165 cross section measurements and the ZZ VBS search (see Sections 6.5 and 5.4.3).  
 166 Clustering must be efficient, to ensure the tagging jets in VBS events are found,  
 167 but the clustering algorithm should not tag spurious jets, as the number of jets in  
 168 an event is sensitive to higher-order QCD corrections and therefore an interesting  
 169 quantity to compare to theoretical predictions. Similarly, the algorithm should not  
 170 erroneously cluster particles from the same initial parton into multiple jets or merge  
 171 jets from multiple original partons, because the kinematics of the original quarks and  
 172 gluons are also of theoretical interest and the detector-level jet kinematics should  
 173 accurately reflect them. A clustering algorithm is said to be “infrared safe” if the  
 174 presence of low-energy hadrons from soft gluon radiation does not change the number  
 175 of jets or have a qualitatively significant effect on jet shapes and kinematics. This  
 176 fits with the intuition that a single 1 GeV pion should have essentially no effect in  
 177 an event with multiple jets with energies on the order of hundreds of GeV [188].  
 178 An algorithm is said to be “collinear safe” if the jets are not changed substantially  
 179 by splitting one hadron into two nearly collinear hadrons with the same total four-  
 180 momentum. This also fits with physical intuition in that jets deposit energy over  
 181 an area significantly larger than the spatial resolution of the detector, so increasing  
 182 the detector granularity enough to resolve two very close particles (without changing  
 183 their total four-momentum) should have little or no effect on the jet.

184 Infrared and collinear (IRC) safety are critically important for comparing data  
 185 to theoretical predictions [189]. Collinear splittings and soft gluon radiation during  
 186 jet fragmentation should not affect the dynamics of the TeV-scale hard scattering  
 187 processes we wish to probe, but they are nonperturbative and difficult to model

188 (see Section 4.1.2), and experimental analysis can only probe the underlying hard  
 189 interaction if it is insensitive to this kind of mismodeling. Experimental detectors'  
 190 finite resolution and inability to measure arbitrarily soft particles enforces some level  
 191 of IRC safety on any algorithm, but the results of an analysis methods that uses  
 192 an IRC unsafe clustering will depend on the complex, detector-dependent details  
 193 of this partial IRC regularization. In any case, the most meaningful comparisons  
 194 between data and theory should use the same definition of a jet in the experimental  
 195 analysis and the perturbative calculation, and perturbative calculations require IRC  
 196 safe observables to preserve unitarity.

197 These considerations, and the desire for conical jets with a well-defined area in  
 198 the  $\eta$ - $\phi$  plane, lead most CMS analyses (including this one) to use jets clustered with  
 199 the anti- $k_T$  algorithm [190, 191]. The anti- $k_T$  algorithm defines the distance between  
 200 two particles  $i$  and  $j$  as

$$d_{ij} = \min(p_{Ti}^{-2}, p_{Tj}^{-2}) \frac{\Delta_{ij}}{R}, \quad (5.2)$$

201 where  $\Delta_{ij}$  is the distance in the rapidity-polar angle plane,

$$\Delta_{ij}^2 \equiv (y_i - y_j)^2 + (\phi_i - \phi_j)^2, \quad (5.3)$$

202 and  $R$  is a parameter setting the size of the resulting jets. The algorithm proceeds  
 203 iteratively. At each iteration, if the smallest  $d_{ij}$  between any pair of particles in the  
 204 event is smaller than the smallest  $p_T^{-2}$  of any single particle, the particles in the pair  
 205 are merged into a single particle with their total four-momentum. If the minimum  
 206 single-particle  $p_T^{-2}$  is smaller than the minimum  $d_{ij}$ , the single particle is labeled a  
 207 jet and removed from further consideration. Iteration proceeds until all particles are  
 208 part of a jet. In this analysis, the size parameter used is  $R = 0.4$ .

209 Charged hadrons whose tracks originate in pileup interactions are not included in  
 210 jet clustering [192]. The contribution of neutral hadrons from pileup is estimated with

211 a jet area technique [193–195] in which the energy density of neutral hadrons from  
 212 pileup is calculated event-by-event and multiplied by the area of the jet to estimate  
 213 the neutral pileup contribution, which is subtracted from the jet energy. Jets in  
 214 Monte Carlo samples have their energy shifted and stochastically smeared such that  
 215 the overall energy scale and resolution match that of jets in data [193, 196].

### 216 5.2.3 Missing Transverse Energy

217 Neutrinos—or, hypothetically, WIMP dark matter or other new particles that do not  
 218 decay or interact directly with the detector—escape and cannot be directly measured.  
 219 Because the beams have no momentum in the  $x$ - $y$  plane, the transverse momentum  
 220 of the visible particles must balance the transverse momentum of the invisible ones.  
 221 The missing transverse momentum is thus

$$\vec{p}_T^{\text{miss}} = - \sum_{\text{visible}} \vec{p}_T, \quad (5.4)$$

222 where the sum runs over the transverse momenta of all PF candidates in the event.  
 223 The missing transverse energy,  $E_T^{\text{miss}}$ , is its magnitude. The  $E_T^{\text{miss}}$  is calibrated by  
 224 propagating the jet energy scale corrections to the  $E_T^{\text{miss}}$  calculation [197–199]. All  
 225 PF candidates are included in the sum in Eq. (5.4), including those originating from  
 226 pileup interactions, because these soft collisions are very unlikely to produce neutrili-  
 227 nos, so including them biases the measurement less than trying to determine which  
 228 neutral particles should be considered pileup and which should not.

## 229 5.3 Object Identification and Selection

230 The reconstruction algorithms described above are general purpose in the sense that  
 231 they can be used in nearly any analysis, but do not address the specific needs of

any, so further selections are essentially always required to optimize object efficiency and purity for studying a specific physics process. The leptons used in this analysis are required to pass identification requirements on top of those imposed during PF reconstruction, and are required to be isolated from other particles in the event, to reject fake objects from jet fragmentation. Four-lepton processes have low reducible backgrounds, so the selections presented here are generally loose, optimized for high efficiency compared to most CMS analyses.

### 5.3.1 Electrons

Electrons are required to have  $p_T > 7 \text{ GeV}$  and to be in the tracker acceptance,  $|\eta| < 2.5$ . They must be compatible with the PV, with minimum track-PV distance  $d_z < 1 \text{ cm}$  in the  $z$  direction and  $d_{xy} < 5 \text{ mm}$  in the plane transverse to the beam. Each electron's 3-dimensional impact parameter (IP)  $d_{3\text{D}}$  must satisfy a requirement on its significance,

$$\text{SIP}_{3\text{D}} \equiv \frac{d_{3\text{D}}}{\sigma_{d_{3\text{D}}}}, \quad (5.5)$$

where  $\sigma_{d_{3\text{D}}}$  is the uncertainty on the IP. The  $\text{SIP}_{3\text{D}}$  requirement is  $\text{SIP}_{3\text{D}} < 10$  for the ZZ and  $Z \rightarrow 4\ell$  cross section measurements and the aTGC search, and  $\text{SIP}_{3\text{D}} < 4$  for the Higgs boson measurement and the VBS and aQGC searches. To remove fake electrons arising from muon tracks being associated to photons or other incidental ECAL energy clusters, electrons within  $\Delta R < 0.05$  of a muon are vetoed.

To further reduce photon and jet fragment backgrounds while maintaining high prompt electron efficiency, a further selection is applied using a multivariate discriminator made with a boosted decision tree (BDT) [200, 201]. The BDT uses 21 input variables, which fall into three broad categories:

- Track-related observables like the number of hits and normalized  $\chi^2$  of the

255        Kalman and GSF tracks and the energy lost to bremsstrahlung according to  
 256        the GSF fit. These are intended to discriminate between electrons and charged  
 257        hadrons.

- 258        • Calorimetric information including a number of supercluster shape observables  
 259        and the amount of HCAL energy near the supercluster, to discriminate electrons  
 260        from electromagnetically rich jets.
- 261        • Track-cluster observables comparing the positions and momenta of the particles  
 262        seen in the tracker and by ECAL.

263        The BDT training and working point selection are done separately for electron can-  
 264        didates with  $p_T$  above and below 10 GeV and in three bins of  $|\eta|$  (0–0.8, 0.8–1.479,  
 265        and 1.479–2.5). The working points are chosen to correspond to 98% efficiency for  
 266        single signal electrons in each bin.

267        To ensure that electron candidates are not part of a jet, they are required to be  
 268        isolated from other particles in the event. The relative isolation is defined as

$$R_{\text{Iso}} = \left( \sum_{\text{charged}} p_T + \max \left[ 0, \sum_{\text{neutral}} p_T + \sum_{\text{photons}} p_T - p_T^{\text{PU}}(\ell) \right] \right) / p_T^\ell \quad (5.6)$$

269        where the sums run over the  $p_T$  of PF hadrons and photons in a cone of  $\Delta R < 0.3$   
 270        around the electron trajectory. To mitigate the contribution of pileup to the isolation  
 271        calculations, charged hadrons are included only if they originate from the event’s PV.  
 272        The estimated neutral contribution to isolation from pileup,  $p_T^{\text{PU}}(\ell)$ , is defined for  
 273        electrons as

$$p_T^{\text{PU}}(e) \equiv \rho \times A_{\text{eff}}, \quad (5.7)$$

274        where the average transverse-momentum flow density  $\rho$  is calculated in each event  
 275        using the jet area method described above. The effective area  $A_{\text{eff}}$  is the geometric  
 276        area of the isolation cone times an  $\eta$ -dependent correction factor that accounts for

277 the residual dependence of the isolation on pileup. Electrons are considered isolated  
 278 if their relative isolations satisfy  $R_{\text{iso}} < 0.35$ .

279       Efficiencies for GSF track reconstruction, electron reconstruction and identifica-  
 280 tion, and electron isolation criteria, are found with a “tag-and-probe” method [202].  
 281 In this technique, events are selected which contain at least one high- $p_{\text{T}}$  “tag” electron  
 282 passing strict ID and isolation requirements, and a “probe” track with the opposite  
 283 sign that combines with the electron to have an invariant mass close to the Z boson  
 284 mass. The resulting sample is enriched with  $Z \rightarrow e^+e^-$  events, so the track is likely  
 285 to correspond to a real prompt electron. Unlike all background processes,  $Z \rightarrow e^+e^-$   
 286 production forms a distinct resonance peak in the  $m_{\ell\ell}$  distribution, so shape fits can  
 287 be used to find the overall purity of the sample, and thus the number of prompt elec-  
 288 trons among the probes. The selection efficiency is then the number of passing probes  
 289 divided by the total number of prompt probes. This procedure is performed in bins  
 290 of  $p_{\text{T}}$  and  $\eta$  for data and Monte Carlo events, and residual differences in efficiency in  
 291 Monte Carlo samples are corrected to match data by weighting events by the ratio  
 292 of data and Monte Carlo efficiency for each electron candidate. Overall electron effi-  
 293 ciency varies between roughly 85% in the inner endcap ( $|\eta| > 2.0$ ) to around 95% in  
 294 the central barrel ( $|\eta| < 0.8$ ).

### 295 5.3.2 Muons

296 Muon selection is similar to electron selection, but simpler because muon backgrounds  
 297 are much smaller. Candidate muons are required to be tracker or global muons with  
 298  $p_{\text{T}} > 5 \text{ GeV}$  within the muon system acceptance ( $|\eta| < 2.4$ ). They are subject to the  
 299 same PV compatibility criteria as electrons,  $d_z < 1 \text{ cm}$ ,  $d_{xy} < 5 \text{ mm}$ , and  $\text{SIP}_{3D} < 10$   
 300 or 4 depending on the analysis. Muon candidates are further subject to the so-called  
 301 “PF ID” criteria, which require them to be isolated from calorimeter deposits or to

302 have high-quality tracks with good fits [184].

303 Isolation is defined as in Eq. (5.6), the same as for electrons except for the defini-  
 304 tion of the neutral pileup contribution, which for muons is based on using the known  
 305 charged pileup density to estimate the neutral pileup based on the average charge  
 306 composition of pileup jets,

$$p_T^{\text{PU}}(\mu) \equiv 0.5 \sum_{\text{charged}} p_T^{\text{PU}}, \quad (5.8)$$

307 where the sum runs over the charged particles from all pileup vertices. As for elec-  
 308 trons, the radius of the isolation cone is 0.3 in the  $\eta$ - $\phi$  plane and the selection criterion  
 309 is  $R_{\text{iso}} < 0.35$ . Muon efficiencies are measured and corrected with the same tag-and-  
 310 probe technique as used for electrons, and found to be around 97%.

### 311 5.3.3 Final State Photon Radiation

312 Final-state radiation (FSR) photons emitted by muons are not included in the PF  
 313 momentum reconstruction, and some photons emitted by electrons may be missed,  
 314 degrading Z boson reconstruction. Photons are considered FSR candidates if they  
 315 have  $p_T > 2 \text{ GeV}$ ,  $|\eta| < 2.4$ , relative isolation  $R_{\text{iso}} < 1.8$  as defined in Eq. (5.6) (with  
 316 no neutral pileup correction), and  $\Delta R(\ell, \gamma) < 0.5$  with respect to the nearest lepton.  
 317 To avoid double counting, photons in electron superclusters are not considered. Be-  
 318 cause FSR has a higher energy spectrum than photons from pileup and is expected  
 319 to be quasi-collinear with the emitting leptons, a photon is accepted as FSR and  
 320 included in the ZZ final state if  $\Delta R(\ell, \gamma) / E_{T\gamma}^2 < 0.012$ . The performance of this  
 321 algorithm is tuned and evaluated with comparisons to generator-level information in  
 322 MC samples, and is found to have efficiency around 60% for a purity around 80%.  
 323 FSR photons are omitted from the isolation determination for emitting leptons. In

324 the rest of this thesis, the momentum of any FSR photons found is included in  $Z/\gamma^*$   
 325 and ZZ four-momenta unless otherwise stated.

326 **5.3.4 Jets**

327 Jets are considered for analysis if they have  $p_T > 30 \text{ GeV}$  and  $|\eta| < 4.7$ . Loose criteria  
 328 are applied to reject spurious jets by requiring they contain multiple particles, and  
 329 the particles be a mix of charged and neutral consistent with hadronic jets. Jets are  
 330 removed from consideration in the event if a lepton or FSR photon is in its cone  
 331 ( $\Delta R < 0.4$  with respect to the jet’s total momentum vector).

332 **5.3.5 Misidentified Objects**

333 The reducible background estimation method described in Section 6.1 requires the use  
 334 of “loose” lepton candidates which are similar to candidates passing the full selection  
 335 but much more likely to be jet fragments or other non-prompt objects. Loose lepton  
 336 candidates pass the  $p_T$  and  $\eta$  cuts and vertex compatibility criteria, but the other  
 337 identification criteria are reduced. The electron BDT discriminator is not applied to  
 338 loose electrons. Loose muons must still be tracker or global muons, but the PF ID is  
 339 not applied. Isolation requirements are not applied to loose candidates. Depending  
 340 on their use, loose candidates may have no further requirements applied, or may be  
 341 required to fail the tight ID and/or isolation requirements, as detailed in Section 6.1,  
 342 where the fake rates for electrons and muons are shown in Fig. 6.1. Aside from the  
 343 ID and isolation criteria, loose leptons are treated the same as their tight cousins,  
 344 with FSR recovery performed with the same algorithm. Jets near loose leptons are  
 345 only removed if the loose lepton is taken to be one of the four in the ZZ candidate in  
 346 the final event interpretation.

## <sup>347</sup> 5.4 ZZ Candidate and Event Selection

<sup>348</sup> Online event selections used single, double, and triple lepton triggers. The double  
<sup>349</sup> lepton triggers were the primary paths, with single and triple lepton triggers correct-  
<sup>350</sup> ing for residual inefficiencies to bring the overall trigger efficiency above 99%. Exact  
<sup>351</sup> HLT parameters changed over the course of datataking as instantaneous luminosities  
<sup>352</sup> changed and trigger rates rose, so many thresholds are shown here as ranges.

<sup>353</sup> • Single muon  $p_T$  thresholds were between 20 and 24 GeV for isolated muons.  
<sup>354</sup> Nonisolated single muons were required to have  $p_T > 50$  GeV or  $p_T > 45$  GeV  
<sup>355</sup> and  $|\eta| < 2.1$ . Single electron  $p_T$  thresholds were 25 or 27 GeV depending on  
<sup>356</sup> ID criteria applied.

<sup>357</sup> • Leading lepton  $p_T$  thresholds in double lepton paths were 17 or 23 GeV. Trailing  
<sup>358</sup> lepton thresholds were 12 GeV and 8 GeV for electrons and muons, respectively.  
<sup>359</sup> Isolation requirements and requirements on the  $z$ -axis distance between lepton  
<sup>360</sup> track origins were added part way through datataking.

<sup>361</sup> • The  $p_T$  requirements in triple lepton paths varied between 5 and 16 GeV, with  
<sup>362</sup> no isolation or vertex requirements.

<sup>363</sup> An event is considered for the analysis if any of these triggers fires.

<sup>364</sup> Several distinct analyses fall under the four-lepton umbrella, each with different  
<sup>365</sup> requirements and therefore different selection criteria. The sets of selections will be  
<sup>366</sup> listed here with brief descriptions of their uses, and detailed in full below.

<sup>367</sup> • The *full spectrum selection* picks a phase space that encompasses all four-lepton  
<sup>368</sup> events, and all other selection sets yield strict subsets of the full spectrum phase  
<sup>369</sup> space.

- 370        • The *singly resonant* ( $Z \rightarrow 4\ell$ ) *selection* picks events with four-lepton mass  
 371              around the Z boson resonance.
- 372        • The *Higgs selection* is that used for the Higgs boson discovery and properties  
 373              measurements. It is similar to the full spectrum selection but with slightly  
 374              tighter requirements on the second  $Z/\gamma^*$  candidate, because  $Z \rightarrow 4\ell$  events are  
 375              of less interest and some backgrounds may be reduced by excluding events with  
 376              an on-shell Z boson and a low mass lepton pair that could be a decay of an  $\Upsilon$   
 377              or similar meson.
- 378        • The *on-shell* or *doubly resonant* selection requires both Z candidates to be  
 379              compatible with a resonant Z boson. It is used for the ZZ and ZZ + jets cross  
 380              section measurements and the aTGC search.
- 381        • The *dijet* (ZZjj) *selection* uses the on-shell selection for the four-lepton system,  
 382              and additionally requires at least two jets. It is used for the VBS and aQGC  
 383              searches.

### 384 5.4.1 $Z/\gamma^*$ Candidate Selection

385 A  $Z/\gamma^*$  candidate is built from a pair of opposite-sign, same-flavor leptons with  
 386 invariant mass between 4 and 120 GeV. The  $Z/\gamma^*$  candidate with mass closest to the  
 387 nominal Z boson mass is labeled  $Z_1$ , the other is labeled  $Z_2$ . Mass requirements on  
 388 the  $Z/\gamma^*$  candidates are among the primary differences between the various analysis  
 389 selections. The full spectrum,  $Z \rightarrow 4\ell$ , and Higgs selections require  $m_{Z_1} > 40$  GeV.  
 390 The Higgs selection additionally requires  $m_{Z_2} > 12$  GeV. The on-shell and dijet  
 391 selections require both  $Z_1$  and  $Z_2$  to have  $m_{Z_i} > 60$  GeV. The mass range thus  
 392 allowed,  $60 < m_{Z_{1,2}} < 120$  GeV, serves as the definition of an on-shell Z boson for  
 393 purposes of this analysis.

### 394 5.4.2 ZZ Candidate Selection

395 Four-lepton candidates are built from pairs of  $Z/\gamma^*$  candidates. Among the four lep-  
 396 tons in the candidate, all opposite-sign pairs must have invariant mass  $m_{\ell^+\ell'^-} > 4 \text{ GeV}$   
 397 regardless of flavor, to remove events in which decay products of a light, leptонically  
 398 decaying particle like a  $J/\psi$  are erroneously paired with the two leptons from a real  $Z$   
 399 boson to form two false  $Z/\gamma^*$  candidates by chance when paired incorrectly. The re-  
 400 quirement on all pairs does not include FSR photons, because the mesons that would  
 401 cause such a problem are generally found in jets which include photons from  $\pi^0$  decays,  
 402 whcih are likely to be misidentified as FSR. All lepton pairs must have  $\Delta R > 0.02$   
 403 to avoid “ghost” leptons with shared tracks. The leading and lepton among the four  
 404 must have  $p_T > 20 \text{ GeV}$ , and the subleading lepton must have  $p_T > 10 \text{ GeV}$  if it is  
 405 an electron or  $p_T > 12 \text{ GeV}$  if it is an electron. The  $Z \rightarrow 4\ell$  selection requires the  
 406 candidate to have  $80 < m_{4\ell} < 100 \text{ GeV}$ , consistent with resonant single- $Z$  production.

407 All allowed pairings of leptons into  $Z/\gamma^*$  candidates are examined separately, so  
 408 an event with two electrons and two positrons, for example, will yield two possible  
 409 ZZ candidates, with the only difference being how the electrons are paired into  $Z_1$   
 410 and  $Z_2$ . In the case that multiple interpretations of the same event pass the full  
 411 selection, the one with  $Z_1$  closest to the nominal  $Z$  mass is chosen. In the rare case of  
 412 further ambiguity, which may arise in events with five or more leptons,  $Z_2$  is chosen  
 413 to maximize the scalar  $p_T$  sum of the four leptons. This best candidate selection is  
 414 done after the full selection is applied, and the other analysis selections are applied to  
 415 the disambiguated events in the full spectrum phase space. Like the mass cut on all  
 416 opposite-sign lepton pairs, this prevents events with one on-shell  $Z$  and one lower-mass  
 417  $\gamma^*$  from passing the on-shell  $Z$  mass cuts with an erroneous lepton pairing.

418 The total efficiency of all selections is estimated by finding the fraction of events  
 419 in the POWHEG and MCFM ZZ samples which pass both the fiducial cuts at generator

420 level and the full analysis selection after detector simulation and reconstruction. For  
421 the doubly on-shell selection ( $60 < m_{\ell\ell} < 120$  GeV), the efficiency is 54% for 4e events,  
422 65% for 2e2 $\mu$  events, and 78% for 4 $\mu$  events. For  $Z \rightarrow 4\ell$  events, the efficiencies for  
423 the 4e, 2e2 $\mu$ , and 4 $\mu$  channels are, respectively, 24%, 36%, and 73%.

#### 424 5.4.3 Dijet and VBS Signal Selection

425 The dijet selection, used for the VBS and aQGC searches, requires the event to contain  
426 two or more jets. The two highest- $p_T$  jets are called the “tagging jets.” The tagging  
427 dijet system must have  $m_{jj} > 100$  GeV. This criterion is not intended to preferentially  
428 select the EWK signal, which is concentrated at much higher dijet masses, but rather  
429 to provide a minimal selection for the sample on which to perform the multivariate  
430 VBS analysis described in Section 6.5 and the shape-based aQGC analysis described  
431 in Section 6.6. No further selections are applied, and the VBS signal efficiency is  
432 therefore close to 100%.

## <sup>0</sup> Chapter 6

### <sup>1</sup> Analysis Strategy

#### <sup>2</sup> 6.1 Background Estimation

3 Reducible backgrounds for four-lepton events typically have two or three prompt  
 4 leptons and two or one other objects—typically jet fragments, sometimes photons—  
 5 which are misidentified as prompt leptons. The largest source of background contam-  
 6 ination is from events in which a Z boson is produced in association with a photon  
 7 and a jet, a leptonically-decaying W boson and a jet, or two jets. There is also a  
 8 contribution from  $t\bar{t}$  events in which both top quarks decay to a lepton, a neutrino,  
 9 and a b quark jet. For simplicity, the two sets of processes are not treated separately  
 10 in what follows, and are collectively labeled “Z + X” events<sup>1</sup>.

11 The contributions of the reducible backgrounds to the selected four-lepton sig-  
 12 nal samples are evaluated using the tight-to-loose “fake rates” method, described in  
 13 Ref. [203]. In this procedure, the likelihood of a nonprompt (“fake”) object to be  
 14 misidentified as a prompt lepton is estimated and applied to control regions enriched  
 15 with Z + X events to estimate their contribution to the signal region. The lepton

---

<sup>1</sup>This is a bit of a misnomer, as “Z + X” does not accurately describe  $t\bar{t}$  events, but the terminology is retained here for consistency with the CMS papers on these analyses.

16 misidentification rate  $f_\ell(p_T^\ell, \eta^\ell)$  is measured from a sample of  $Z + \ell_{\text{fake}}$  events, where  
 17 the  $Z$  boson candidate is selected as in the signal region but with  $|m_{\ell\ell} - m_Z| < 10 \text{ GeV}$ ,  
 18 and the  $\ell_{\text{fake}}$  object is a lepton candidate that passes relaxed ID requirements as de-  
 19 fined in Section 5.3.5, with no isolation or tight ID requirements applied.

20 The misidentification rate is defined as the fraction of  $\ell_{\text{fake}}$  candidates which pass  
 21 full lepton identification and isolation criteria, in bins of  $p_T$  and  $\eta$ . One should note  
 22 that the misidentification rate cannot be interpreted as a probability in the usual  
 23 sense, and in fact there is no simple physical interpretation of it. Events with three  
 24 prompt leptons can contaminate this control region and bias the misidentification  
 25 rate, because the non- $Z$  lepton is falsely assumed fake. To mitigate this bias, the  
 26  $WZ \rightarrow 3\ell\nu$  yields in the numerator and denominator in each bin are estimated from  
 27 a simulated sample and subtracted before the ratio of yields is taken. Figure 6.1  
 28 shows the misidentification rates for electrons and muons separately as a function of  
 29  $p_T$  and  $\eta$ .

30 To estimate the total reducible background yield, the misidentification rates are  
 31 applied to two  $Z + X$  enriched control samples, each containing a  $Z$  boson candidate  
 32 passing all signal region requirements plus two more lepton candidates which pass the  
 33 relaxed identification criteria and would make a second  $Z$  boson candidate according  
 34 to Section 5.4.1 except that one or both fail the full identification or isolation criteria.  
 35 The sample with one failing lepton, called the “3P1F” sample for “3 prompt 1 fake,”  
 36 covers the contribution from  $WZ$  events, while the sample with both leptons in the  
 37 second  $Z$  boson failing (“2P2F”) covers  $Z + \text{jets}$  and  $t\bar{t}$  events. The fake object transfer  
 38 factor

$$F_\ell(p_T^\ell, \eta^\ell) = \frac{f_\ell(p_T^\ell, \eta^\ell)}{1 - f_\ell(p_T^\ell, \eta^\ell)} \quad (6.1)$$

39 is the ratio of nonprompt objects passing the relaxed and full selection criteria, and  
 40 thus serves as a per-lepton extrapolation factor between control sample yields and

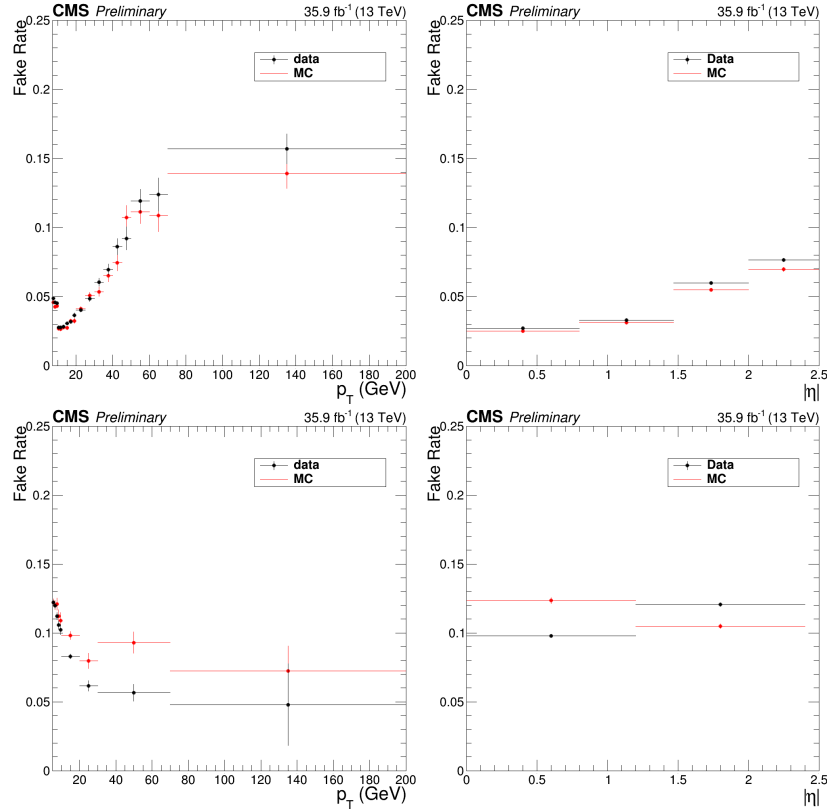


Figure 6.1: Fake rate for electrons (top) and muons (bottom) as a function of  $p_T$  (left) and  $\eta$  (right).

41 signal sample yields.

42 The total reducible background yield is thus

$$N_{\text{bkg}} = \sum_{\ell \in 3\text{P1F}} F_\ell(p_T^\ell, \eta^\ell) - \sum_{\ell_1, \ell_2 \in 2\text{P2F}} F_{\ell_1}(p_T^{\ell_1}, \eta^{\ell_1}) F_{\ell_2}(p_T^{\ell_2}, \eta^{\ell_2}). \quad (6.2)$$

43 The minus sign prevents double-counting of Z+2jets events in which one jet fragment  
 44 is misidentified. The failing lepton candidates in the 3P1F and 2P2F control samples  
 45 are assumed to truly be jet fragments or other nonprompt objects, but selection  
 46 inefficiencies may cause prompt leptons to fail and contaminate the control regions  
 47 with signal events. The yield of such signal events in the background control regions is  
 48 estimated by applying the same fake factors to failing events in the ZZ signal Monte  
 49 Carlo samples, and subtracted from the result of Eq. (6.2).

50 There are also irreducible background contributions from  $t\bar{t}Z$  and  $WWZ$  events,  
 51 which can have four prompt leptons. Expected yields for these processes are taken  
 52 from simulation.

## 53 6.2 Systematic Uncertainties

54 Systematic uncertainties for trigger efficiency are taken to be the difference between  
 55 trigger efficiencies in data and in simulated signal events, found to be around 2%  
 56 of the final event yield. Because leptons in  $Z \rightarrow 4\ell$  events generally have lower  $p_T$ ,  
 57 the uncertainty increases to 4% for  $Z \rightarrow 4e$  events. In both data and simulated  
 58 events, trigger efficiencies are found with a tag-and-probe technique [202], performed  
 59 on four-lepton events.

60 The lepton identification and isolation efficiencies in simulation are corrected with  
 61 scaling factors derived with the tag-and-probe method, performed on  $Z \rightarrow \ell^+\ell^-$  events  
 62 in data and a single-Z Monte Carlo sample. To find the uncertainties associated with  
 63 these corrections, the total yield is recomputed with the scaling factors varied up and  
 64 down by one standard deviation of the uncertainties from the tag-and-probe method,  
 65 treating all bins as correlated. The resulting changes in the  $ZZ \rightarrow 4\ell$  yield, taken to  
 66 be the one sigma variations resulting from lepton efficiency uncertainties, are found  
 67 to be 6% in the 4e final state, 3% in the 2e2 $\mu$  final state, and 2% in the 4 $\mu$  final state.  
 68 Leptons in  $Z \rightarrow 4\ell$  events tend to have lower  $p_T$ , and the tag-and-probe samples  
 69 for leptons with  $p_T$  below about 15 GeV are smaller and more contaminated with  
 70 nonprompt objects, so the uncertainties are larger; they are found to be 10%, 6%,  
 71 and 7% for the 4e, 2e $\mu$ , and 4 $\mu$  final states, respectively.

72 The uncertainty on the integrated luminosity of the data sample is 2.5% [142].

73 The uncertainty on lepton fake rates is 40%, which includes both statistical un-

74 certainty and systematic uncertainties associated with the loosened lepton selections  
 75 defined in Section 5.3.5 and the differences in the underlying physics processes be-  
 76 tween events in the  $Z + \ell_{\text{fake}}$ , 3P1F, and 2P2F control samples [73]. Statistical uncer-  
 77 tainties arising from the limited size of the  $Z + X$  control samples are also included  
 78 as a systematic uncertainty on the background yield. The total uncertainty on the  
 79 background yield varies by channel but is below 1% of the expected total yield.

80 Uncertainties due to the effect of QCD scale on the  $ZZ \rightarrow 4\ell$  acceptance are  
 81 evaluated with POWHEG and MCFM, by varying the QCD scales up and down by a  
 82 factor of two with respect to the default  $\mu_R = \mu_F = m_{ZZ}$ . Parametric uncertainties  
 83 ( $\text{PDF} + \alpha_s$ ) are evaluated according to the PDF4LHC prescription in the acceptance  
 84 calculation [204], and with NNPDF3.0 in the cross section calculations. An additional  
 85 theoretical uncertainty arises from scaling the  $q\bar{q} \rightarrow ZZ$  and  $gg \rightarrow ZZ$  simulated  
 86 samples to their NNLO and NLO predicted cross sections, respectively, with the  
 87  $K$  factors described in Section 4.1.4. The corresponding change in the acceptance,  
 88 1.1%, is added to the previous theoretical errors in quadrature.

89 Systematic uncertainties on expected signal yield are summarized in Table 6.1. To  
 90 obtain uncertainties in the inclusive cross sections, each uncertainty source is treated  
 91 as a nuisance parameter in the fits described in Section 6.3.1. For differential cross  
 92 section and other shape uncertainties, the calculation is fully redone for each uncer-  
 93 tainty source, with the inputs shifted by one standard deviation in each direction.  
 94 Variations across bins are taken to be fully correlated for each uncertainty source.  
 95 Lepton and jet momentum scale and resolution uncertainties are taken to be trivial  
 96 for the overall yield, but they are considered among the shape uncertainties.

Table 6.1: The contributions of each source of signal systematic uncertainty in the total yields. The integrated luminosity uncertainty and the PDF and scale uncertainties are considered separately. All other uncertainties are added in quadrature into a single systematic uncertainty. Uncertainties that vary by decay channel are listed as a range.

Uncertainty	$Z \rightarrow 4\ell$	$ZZ \rightarrow 4\ell$
Lepton efficiency	6–10%	2–6%
Trigger efficiency	2–4%	2%
MC statistics	1–2%	0.5%
Background	0.6–1.3%	0.5–1%
Pileup	1–2%	1%
PDF	1%	1%
QCD Scales	1%	1%
Integrated luminosity	2.5%	2.5%

### 97 6.3 Fiducial and Total Cross Section Calculation

98 Inclusive cross section measurements can be treated as simple binned counting experiments,  
99 where the bins are the three decay channels ( $4e$ ,  $2e2\mu$ , and  $4\mu$ ). If  $\nu$  events are  
100 expected in a given bin, the probability of observing  $n$  events is given by the Poisson  
101 distribution,

$$f(n; \nu) = e^{-\nu} \frac{\nu^n}{n!}. \quad (6.3)$$

102 In a particle physics analysis like this one,  $\nu$  takes the form

$$\nu = \nu_s(\vec{\theta}_s) + \nu_b(\vec{\theta}_b) = \mu(\vec{\theta}_s) \mathcal{L}_{int} \sigma_{SM} \epsilon + \nu_b(\vec{\theta}_b) \quad (6.4)$$

103 where  $\nu_s$  and  $\nu_b$  are respectively the expected signal and background yields,  $\sigma_{SM}$  is  
104 the standard model expectation for the cross section of the signal process and  $\epsilon$  is our  
105 efficiency for detecting and identifying its events. The signal and background nuisance  
106 parameter vectors  $\vec{\theta}_s$  and  $\vec{\theta}_b$  represent hidden quantities that we do not measure  
107 directly but which affect our yields, i.e. systematic effects. The signal strength  $\mu$

108 compares our expectation to what we actually measure:

$$\mu = \frac{\sigma_{meas}}{\sigma_{SM}}. \quad (6.5)$$

109 Of the variables in Eqs. (6.3) and (6.4),  $\sigma_{SM}$  is known from theoretical calculations,  
 110 and  $\epsilon$  is determined from simulation. The CMS detector is designed to measure  $n$   
 111 and  $\mathcal{L}_{int}$ ,  $\nu_b$  is estimated from data or simulation, and inferring  $\sigma_{meas}$  is a matter of  
 112 finding the most likely value of the signal strength  $\mu$  given the observed data. Then  
 113 the measured cross section is simply

$$\sigma_{meas} = \mu\sigma_{SM}. \quad (6.6)$$

114 One interesting feature of this method is that  $\sigma_{SM}$  is used in the calculation of  $\mu$   
 115 (Eq. (6.4)) and in the final cross section (Eq. (6.6)) in such a way that it cancels out,  
 116 and in fact anything proportional to the true cross section may be used. In practice,  
 117 this means that the order at which  $\sigma_{SM}$  is calculated does not matter to the extent  
 118 that higher order corrections to the kinematics of the events do not affect  $\epsilon$ .

119 Typically,  $\sigma_{meas}$  in Eq. (6.6) is the fiducial cross section, the cross section for the  
 120 process in a phase space similar to (typically, slightly larger than) the phase space  
 121 in which the experimental analysis can in principle detect events. In the four-lepton  
 122 case, the fiducial phase space is a space of  $2\ell 2\ell'$  ( $\ell, \ell' \in e, \mu$ ) events defined by criteria  
 123 on lepton kinematics, dilepton invariant masses, and four-lepton mass. Table 6.2  
 124 shows the fiducial definitions for both the  $Z \rightarrow 4\ell$  and  $ZZ \rightarrow 4\ell$  cross section mea-  
 125 surements. Lepton kinematic requirements and an invariant mass requirement on  
 126 all opposite-sign, same-flavor lepton pairs in the event are common to both mea-  
 127 surements; requirements on the invariant masses of  $Z/\gamma^*$  boson candidates and the  
 128 four-lepton system are different.

129 The total  $ZZ$  cross section is defined subject to no constraints except the require-  
 130 ment that  $m_{Z_1}$  and  $m_{Z_2}$  be between 60 and 120 GeV, which serves as the definition

131 of a Z boson. The fiducial cross section is related to the total cross section by the  
 132 branching fraction  $\mathcal{B}$  to the final state in question—here, two factors of the  $Z/\gamma^*$   
 133 branching ratio to electron and muon pairs—and an acceptance factor  $\mathcal{A}$  which is the  
 134 fraction of events falling in the fiducial phase space,

$$\sigma_{fid} = \mathcal{A}\sigma_{tot} (\mathcal{B}(Z \rightarrow 2\ell))^2. \quad (6.7)$$

135 The acceptance factor  $\mathcal{A}$  is determined entirely from theory, and is well known [11], so  
 136 it is straightforward to calculate the total cross section once the fiducial cross section  
 137 is known. Calculating both fiducial and total cross sections is interesting because  
 138 it effectively factorizes experimental and theoretical uncertainties. The experimental  
 139 uncertainties are contained entirely in the uncertainties on  $\epsilon$ ,  $\mathcal{L}_{int}$ , and  $\nu_b$  in Eq. (6.4),  
 140 which have little or no dependence on theory, while the theoretical uncertainties are  
 141 contained entirely in the uncertainty on  $\mathcal{A}$ , which is determined with no experimental  
 142 input. Thus the uncertainty on  $\sigma_{fid}$  is entirely experimental, and the theoretical  
 143 uncertainties enter only in the uncertainty on  $\sigma_{tot}$ .

Table 6.2: Fiducial phase space definitions for the  $Z \rightarrow 4\ell$  and  $ZZ \rightarrow 4\ell$  cross section measurements. The common requirements apply to both. The  $m_{\ell^+\ell'^-}$  criterion is applied to all opposite-sign same-flavor lepton pairs in the event.

Measurement	Fiducial requirements
Common	$p_T^{\ell_1} > 20 \text{ GeV}$ , $p_T^{\ell_2} > 10 \text{ GeV}$ , $p_T^{\ell_{3,4}} > 5 \text{ GeV}$ , $ \eta^\ell  < 2.5$ , $m_{\ell^+\ell'^-} > 4 \text{ GeV}$
$Z \rightarrow 4\ell$	$m_{Z_1} > 40 \text{ GeV}$ , $80 < m_{4\ell} < 100 \text{ GeV}$
$ZZ \rightarrow 4\ell$	$60 < m_{Z_1}, m_{Z_2} < 120 \text{ GeV}$

<sup>144</sup> **6.3.1 Signal Strength Extraction**

<sup>145</sup> The signal strength is found by the method of maximum likelihood [11, 205]. The  
<sup>146</sup> likelihood function is the product of the probability distributions across all bins,

$$L \left( \vec{\theta}_s, \vec{\theta}_b \right) = \prod_{bins} f \left( n; \nu \left( \vec{\theta}_s, \vec{\theta}_b \right) \right). \quad (6.8)$$

<sup>147</sup> The most likely value of  $\nu$  is the one that maximizes  $L$ . In practice,  $\log L$  is typically  
<sup>148</sup> maximized instead because it is easier to work with,

$$\frac{\partial^2 \log L}{\partial \vec{\theta}_s \partial \vec{\theta}_b} = 0. \quad (6.9)$$

<sup>149</sup> This maximization is performed simultaneously for all bins, yielding a single signal  
<sup>150</sup> strength across all channels. Systematic uncertainties enter as log-normal constraints  
<sup>151</sup> imposed on the fit, encoded in  $\vec{\theta}_s$  and  $\vec{\theta}_b$ . The fit is performed numerically.

<sup>152</sup> **6.3.2  $Z \rightarrow 4\ell$  Branching Fraction**

<sup>153</sup> The total  $Z$  cross section can be calculated from the  $Z \rightarrow 4\ell$  fiducial cross section  
<sup>154</sup> with Eq. (6.7), but it is better measured in the  $2\ell$  channel, where the larger branching  
<sup>155</sup> fraction yields samples several orders of magnitude larger than the  $Z \rightarrow 4\ell$  sample  
<sup>156</sup> used here. It is therefore more interesting to use  $\sigma_{fid}(Z \rightarrow 4\ell)$  for a measurement of the  
<sup>157</sup> four-lepton branching fraction  $\mathcal{B}(Z \rightarrow 4\ell)$ . After applying the acceptance correction  
<sup>158</sup> to obtain  $\sigma_{tot}(Z \rightarrow 4\ell) = \sigma_{fid}(Z \rightarrow 4\ell) / \mathcal{A}$ , the four-lepton branching fraction is given  
<sup>159</sup> by

$$\mathcal{B}(Z \rightarrow 4\ell) = \frac{\sigma_{tot}(Z \rightarrow 4\ell)}{\mathcal{C}_{80-100}^{60-120} \sigma(Z \rightarrow 2\ell)} \mathcal{B}(Z \rightarrow 2\ell), \quad (6.10)$$

<sup>160</sup> where  $\sigma(Z \rightarrow 2\ell)$  is the dileptonic  $Z$  cross section in the 60–120 GeV mass range and  
<sup>161</sup>  $\mathcal{C}_{80-100}^{60-120}$  corrects for the fact that  $\sigma(Z \rightarrow 4\ell)$  is found in a mass range of 80–100 GeV.

## 162 6.4 Differential Cross Sections

163 Measurement of a differential fiducial cross section is also a problem of finding the  
164 most likely true distribution given observed yields in multiple bins, estimated back-  
165 ground yields, and detector effects understood through simulation. Unlike the inclu-  
166 sive cross section, however, finite detector resolution leads to “smearing” effects that  
167 cause events to migrate across bins, in addition to the same inefficiencies. The mean  
168 detector-level distribution  $\vec{\delta}$  is related to the true distribution  $\vec{\theta}$  by a response matrix  
169  $\mathbf{R}$ :

$$\vec{\delta} = \mathbf{R}\vec{\theta}. \quad (6.11)$$

170 The observed distribution in data  $\vec{d}$  is sampled from the Poisson distribution with  
171 mean  $\vec{\delta}$  independently in each bin. CMS simulation software is sufficiently sophis-  
172 ticated to give a good estimate of  $R$ , reproducing the real detector’s resolution and  
173 smearing effects at the level of a few per cent or better for all distributions of interest.

174 If  $\mathbf{R}$  is square and invertible, the maximum likelihood estimate (MLE) of the true  
175 distribution,  $\hat{\vec{\theta}}$ , is given by

$$\hat{\vec{\theta}} = \mathbf{R}^{-1}\vec{d}. \quad (6.12)$$

176 Even when  $\mathbf{R}$  is invertible, however, it is frequently ill-conditioned, giving  $\hat{\vec{\theta}}$  unphysical  
177 features like large bin-by-bin fluctuations or even negative bins as a consequence of the  
178 stochastic nature of  $\vec{d}$ . It is therefore necessary to use a more sophisticated procedure  
179 to ensure the differential cross section distributions obey physics-inspired constraints.

180 The variables used for differential cross sections in this analysis are in general well-  
181 measured, so bin-to-bin fluctuations are small and the response matrices are nearly  
182 diagonal, but some bins have low occupancy which can still cause pathologies.

183 **6.4.1 Unfolding**

184 The technique used here is an iterative frequentist method developed in high energy  
 185 physics by D'Agostini [206] and independently in other fields [207–210], as imple-  
 186 mented in ROOUNFOLD [211]. At iteration  $k$ , bin  $j$  of the predicted true distribution  
 187 is set based on its expected contribution to all other bins, weighted by the observed  
 188 data yield in each:

$$\begin{aligned}\theta_j^{(k+1)} &= \sum_i \mathbf{R}_{ij} \theta_j^{(k)} \frac{d_i}{\delta_i} \\ &= \sum_i \mathbf{R}_{ij} \theta_j^{(k)} \frac{d_i}{\sum_m \mathbf{R}_{im} \theta_m^{(k)}}.\end{aligned}\tag{6.13}$$

189 After several iterations,  $\vec{\theta}^{(k)}$  depends only weakly on the ansatz  $\vec{\theta}^{(0)}$ .

190 The sequence will converge to the MLE for any non-pathological choice of  $\vec{\theta}^{(0)}$  [212]  
 191 but again the MLE often displays unphysical behavior. If  $\vec{\theta}^{(0)}$  is strictly positive,  $\vec{\theta}^{(k)}$   
 192 will be strictly positive for all  $k$ , and in this case  $\hat{\vec{\theta}}$  (as defined in Eq. (6.12)) will be  
 193 the asymptotic unfolded distribution as long as it is also strictly positive. Choosing a  
 194 smooth function for  $\vec{\theta}^{(0)}$  will generally lead to smooth  $\vec{\theta}^{(k)}$  for small  $k$ ; typical choices  
 195 include a flat initial distribution and the truth-level distribution used to construct  $\mathbf{R}$   
 196 (used in this analysis). What constitutes “small”  $k$  depends on the condition of  $\mathbf{R}$ ,  
 197 but for most physics distributions of interest, including all those used in this analysis,  
 198 nonphysical fluctuations do not arise until after  $\vec{\theta}^{(k)}$  is close to convergence. Full  
 199 regularization is therefore imposed by ceasing iteration early. For all distributions  
 200 shown here, stopping after four iterations was found to obtain a result close to the  
 201 asymptotic distribution without artificially increasing the bin-to-bin variance.

202 **6.4.2 Uncertainties**

203 The largest uncertainties in the unfolded distributions arise from the unfolding pro-  
 204 cedure itself, which can inflate statistical uncertainties present in the detector-level  
 205 distributions. The correlation matrix which gives the full uncertainty—considered  
 206 the statistical uncertainty of the unfolded distribution—does not have a closed form  
 207 due to the nonlinearity of the method. The covariance matrix is therefore estimated  
 208 by propagating the statistical error of the inputs at each iteration of the method, as  
 209 laid out in Ref. [206] and improved in Ref. [211]. This procedure does not account for  
 210 the bias introduced by regularization, but this is expected to be negligible relative to  
 211 other systematic uncertainties for the well-modeled processes studied here.

212 Most systematic uncertainties are propagated through unfolding by recomputing  
 213 the response matrix with the training sample shifted or reweighted to reflect a  $1\sigma$   
 214 shift in the quantity in question. The uncertainty related to that quantity is taken  
 215 to be the resulting shape difference in the final unfolded distribution. Systematic  
 216 uncertainties are negligible compared to statistical uncertainties in most bins.

217 **6.5 VBS Signal Extraction**

218 The VBS signal search considers events passing the selections described in Sec-  
 219 tion 5.4.3. The electroweak yield is insufficient to have sensitivity at  $35.9 \text{ fb}^{-1}$ , even  
 220 with further cut optimization, so a gradient-boosted decision tree (GBDT), imple-  
 221 mented with the SCIKIT-LEARN package [213], is used to extract the signal. Hyper-  
 222 parameters of the GBDT are optimized with a grid search. Each Monte Carlo sample  
 223 used in the VBS search (see Section 4.1.4) is split into a “training” subsample, used to  
 224 train the GBDT, and a “test” subsample used to evaluate its performance and make  
 225 templates for use in the statistical analysis. The GBDT performance is nearly the

226 same for the test and training samples, a sign that the algorithm is not overtrained.

227 A number of observables have been proposed to discriminate VBS events from  
 228 background [58], of which  $m_{jj}$  and  $\Delta\eta_{jj}$  are the most powerful. Other commonly-used  
 229 variables include  $m_{4\ell}$ ,  $\eta^{j_1} \times \eta^{j_2}$ ,  $\Delta\phi_{Z_1 Z_2}$ , and the so-called Zeppenfeld variables, defined  
 230 as

$$\eta_P^* = \eta_P - \frac{\eta_{j_1} - \eta_{j_2}}{2}, \quad (6.14)$$

231 where  $P$  may stand for  $Z_1$ ,  $Z_2$ , or  $j_3$ , the highest- $p_T$  untagged jet in the event. In ad-  
 232 dition to these “traditional” quantities, several other groups of observables have been  
 233 examined, including production angles, decay angles, measures of total hadronic ac-  
 234 tivity in the event, properties of individual leptons and jets and of the ZZjj system, and  
 235 a discriminator designed to distinguish jets originating from quarks and gluons [214].

236 The hadronic activity and quark-gluon tagging variables have some discriminating  
 237 power, but they differ significantly depending on the Monte Carlo generator used  
 238 and were therefore considered too poorly-modeled to use. New GBDTs were trained,  
 239 each with the traditional observables and one other group of observables, and the  
 240 groups that improved the GBDT discrimination power significantly were retained.  
 241 This procedure yielded 17 observables, including the hard process relative transverse  
 242 momentum, defined as the ratio of the  $p_T$  of the ZZjj system to the scalar sum of the  
 243  $p_T$  of each object,

$$p_T^{rel. hard} = \frac{p_T^{ZZjj}}{\sum_{Z_1, Z_2, j_1, j_2} p_T}, \quad (6.15)$$

244 and the dijet relative transverse momentum,

$$p_T^{rel. jj} = \frac{p_T^{jj}}{\sum_{j_1, j_2} p_T}. \quad (6.16)$$

245 The list of observables was further optimized by retraining the GBDT once with  
 246 each variable dropped and eliminating the one with the least discriminating power.  
 247 This pruning was repeated until seven observables remained, namely  $m_{jj}$ ,  $\Delta\eta_{jj}$ ,  $m_{4\ell}$ ,

248  $\eta_{Z_1}^*$ ,  $\eta_{Z_2}^*$ ,  $p_T^{rel.\ hard}$ , and  $p_T^{rel.\ jj}$ . The resulting GBDT performs only marginally worse  
 249 (0.2 $\sigma$  less expected significance on the VBS signal) than a version with all observables  
 250 included, and is faster and easier to train, simpler, and less susceptible to biases and  
 251 systematic uncertainties from mismodeling.

252 The signal and background yields are extracted from the GBDT output spectrum  
 253 with a binned maximum likelihood fit to templates from the test Monte Carlo samples.  
 254 To obtain templates with better fit convergence properties, the GBDT output is  
 255 mapped to the range [0, 1] with the logistic transformation

$$x \rightarrow \frac{1}{1 - e^{-x}}. \quad (6.17)$$

256 This provides better separation between signal and background and allows uniform  
 257 binning in the templates.

## 258 6.6 Anomalous Gauge Coupling Searches

259 The new physics represented by aGCs would generally manifest as an increase in  
 260 events with high invariant mass, so it is natural to use the shape of the  $m_{4\ell}$  distribution  
 261 for the search. For the aTGC search, the doubly on-shell ZZ selection is used, while  
 262 the aQGC search is performed with the ZZjj selection described in Section 5.4.3.

263 Monte Carlo samples with nonzero aTGCs are generated at grids of points in the  
 264  $f_4^Z-f_4^\gamma$  and  $f_5^Z-f_5^\gamma$  planes. In each bin of the  $m_{4\ell}$  distribution, the yields at the various  
 265 working points are fit to a function of the form

$$y(f^Z, f^\gamma) = x_0 + x_1 f^Z + x_2 f^\gamma + x_3 f^Z f^\gamma + x_4 (f^Z)^2 + x_5 (f^\gamma)^2 \quad (6.18)$$

266 where  $y(f^Z, f^\gamma)$  is the yield in the bin,  $f^V$  can be  $f_4^Z$  and  $f_4^\gamma$  or  $f_5^Z$  and  $f_5^\gamma$ , and  $x_i$   
 267 are the parameters to be fit.

268 A similar procedure is performed for the aQGC search. Rather than simulating a  
 269 full sample for each working point, which is computationally expensive, events from  
 270 `MADGRAPH5_AMC` produced at LO are used to obtain samples for nonzero values  
 271 of  $f_{T0}/\Lambda^4$ ,  $f_{T1}/\Lambda^4$ ,  $f_{T2}/\Lambda^4$ ,  $f_{T8}/\Lambda^4$ , and  $f_{T9}/\Lambda^4$  by matrix element reweighting [145].  
 272 The yields in each  $m_{4\ell}$  bin are fit to parabolas as a function of the five aQGC param-  
 273 eters separately.

274 A binned profile likelihood method [11] is used to derive the limits. Systematic  
 275 uncertainties are taken into account by varying the number of signal and background  
 276 events within their uncertainties. Exclusion limits are found by comparing the p-  
 277 values of the signal hypothesis and the background only hypothesis

$$CL_s = \frac{p_{s+b}}{1 - p_b} \quad (6.19)$$

278 to set thresholds. Further details on the method can be found in Ref. [215]. The  
 279 software for setting limits, implemented with `RooStats`, has been validated and  
 280 used extensively by the CMS and ATLAS collaborations [216].

## <sup>0</sup> Chapter 7

## <sup>1</sup> Results

2 A number of measurements and analyses fall under the umbrella of four-lepton  
3 physics, and results presented in this thesis were originally made public in several  
4 journal articles and Physics Analysis Summary documents released by the CMS col-  
5 laboration. The first CMS measurement of the ZZ inclusive cross section at 13 TeV  
6 used roughly half the 2015 dataset ( $1.34 \text{ fb}^{-1}$ ) and was made public in Ref. [217] in  
7 December 2015 as one of the first measurements done on 13 TeV collision data. That  
8 analysis was expanded to use the whole  $2.6 \text{ fb}^{-1}$  collected in 2015, and to include  
9 the  $Z \rightarrow 4\ell$  branching fraction measurement, as reported in Ref. [218], submitted in  
10 July 2016 and published the following December. With the full 2016 dataset, the ZZ  
11 cross section and  $Z \rightarrow 4\ell$  branching ratio were measured again to greater precision in  
12 Ref. [79], which also included differential cross section measurements and aTGC lim-  
13 its, made public in March 2017. A new paper including these measurements [OUR  
14 PAPER] also includes a combination of the 2015 and 2016 inclusive cross section  
15 measurements. Differential cross sections with respect to jet-related observables, and  
16 searches for EWK ZZ production and aTGCs, were reported in May 2017 in Ref. [219],  
17 with a paper on only the VBS and aQGC searches following [220]. The Higgs boson

18 was studied in the four-lepton final state in Refs. [221–223]. In the following, results  
 19 for each topic are only shown for 2016 data, which significantly exceed the accuracy  
 20 of the results from 2015 data.

## 21 **7.1 Four-Lepton Yield and Distributions**

### 22 **7.1.1 Full Spectrum**

23 The full four-lepton invariant mass spectrum is shown in Fig. 7.1. The single-Z  
 24 resonance can be seen below 100 GeV, the Higgs resonance is visible—though it is  
 25 not sharply resolved with this binning—in the  $Z/\gamma^*$  region below  $2m_Z$ , where doubly  
 26 resonant ZZ continuum production begins. The dilepton invariant mass spectrum is  
 27 shown for both  $Z/\gamma^*$  candidates in Fig. 7.2 and for the  $Z/\gamma^*$  candidate closest to the  
 28 nominal Z boson mass ( $Z_1$ ) in Fig. 7.3. Figure 7.4 shows  $m_{Z_2}$  plotted against  $m_{Z_1}$   
 29 for data events representative of all four-lepton production. Clusters of events with  
 30 zero ( $Z \rightarrow 4\ell$  and nonresonant  $\gamma^*\gamma^*$  production), one ( $H \rightarrow ZZ^*$  and nonresonant  $Z\gamma^*$   
 31 production), and two (nonresonant ZZ production) on-shell Z bosons can be clearly  
 32 seen.

### 33 **7.1.2 $Z \rightarrow 4\ell$ Resonance**

34 Expected and observed yields for events satisfying the  $Z \rightarrow 4\ell$  selection criteria  
 35 ( $80 < m_{4\ell} < 100$  GeV) are shown in Table 7.1. The invariant mass distribution of  
 36 these events is shown in Fig. 7.5. Figure 7.6 shows  $m_{Z_2}$  plotted against  $m_{Z_1}$  for  
 37 all data events consistent with  $Z \rightarrow 4\ell$  production. Predictions from Monte Carlo  
 38 samples generally agree well with the data.

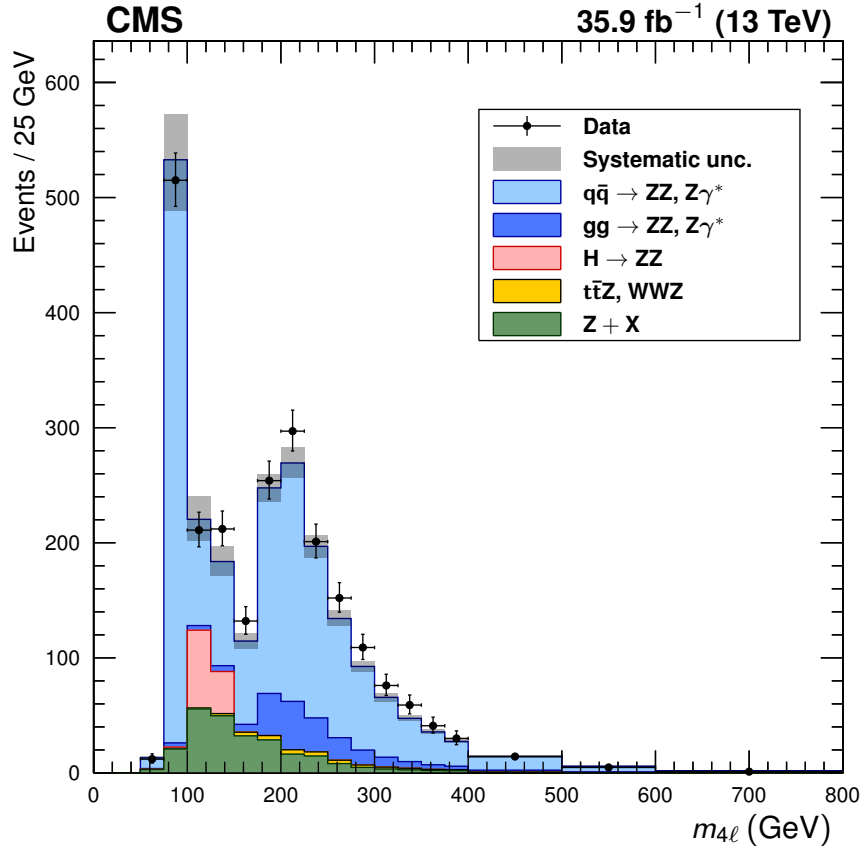


Figure 7.1: Distribution of the four-lepton invariant mass  $m_{4\ell}$  of all events in the full spectrum selection. Points represent data, with statistical uncertainty bars. The stack of filled histograms represents the SM signal prediction and background estimate, with a grey band showing the sum in quadrature of the statistical and systematic uncertainties on the total expected yield.

Table 7.1: Observed and expected yields of  $Z \rightarrow 4\ell$  events, including expected background yields, shown for each final state and summed to the total. Uncertainties are statistical, then systematic, not including the integrated luminosity uncertainty.

Final state	Expected $N_{4\ell}$	Background	Total expected	Observed
$4\mu$	$224 \pm 1 \pm 16$	$7 \pm 1 \pm 2$	$231 \pm 2 \pm 17$	225
$2e2\mu$	$207 \pm 1 \pm 14$	$9 \pm 1 \pm 2$	$216 \pm 2 \pm 14$	206
4e	$68 \pm 1 \pm 8$	$4 \pm 1 \pm 2$	$72 \pm 1 \pm 8$	78
Total	$499 \pm 2 \pm 32$	$19 \pm 2 \pm 5$	$518 \pm 3 \pm 33$	509

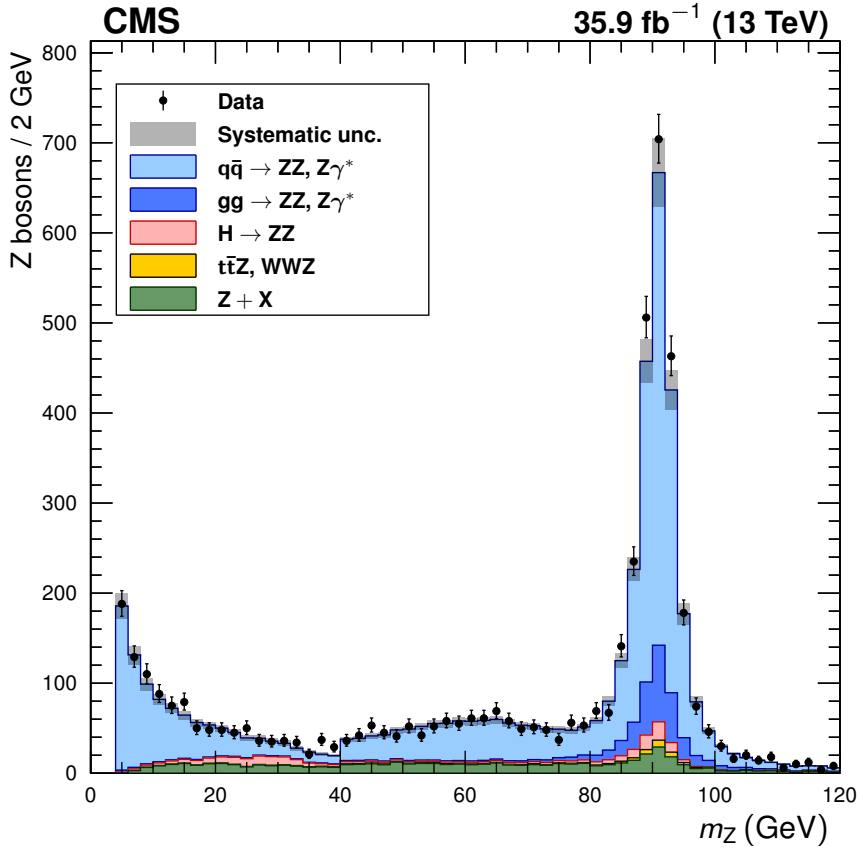


Figure 7.2: Distribution of the dilepton invariant mass of  $Z/\gamma^*$  candidates in all events in the full spectrum selection, regardless of whether the lepton pair is labeled  $Z_1$  or  $Z_2$ . Points represent data, with statistical uncertainty bars. The stack of filled histograms represents the SM signal prediction and background estimate, with a grey band showing the sum in quadrature of the statistical and systematic uncertainties on the total expected yield.

### <sup>39</sup> 7.1.3 Higgs Resonance

<sup>40</sup> Figure 7.7 shows the four-lepton invariant mass around the Higgs resonance, which  
<sup>41</sup> can be clearly seen above the SM continuum background, for events passing the Higgs  
<sup>42</sup> selection ( $m_{Z_2} > 12 \text{ GeV}$ ,  $SIP_{3D} < 4$  for all leptons). Table 7.2 shows the observed  
<sup>43</sup> and expected yields in the mass range  $118 < m_{4\ell} < 130 \text{ GeV}$ . Here, SM continuum  
<sup>44</sup> production—considered signal in all other parts of this analysis—is considered back-  
<sup>45</sup> ground. Figures 7.8–7.10 show the  $Z_1$  mass, the  $Z_2$  mass, and the scatter plot of

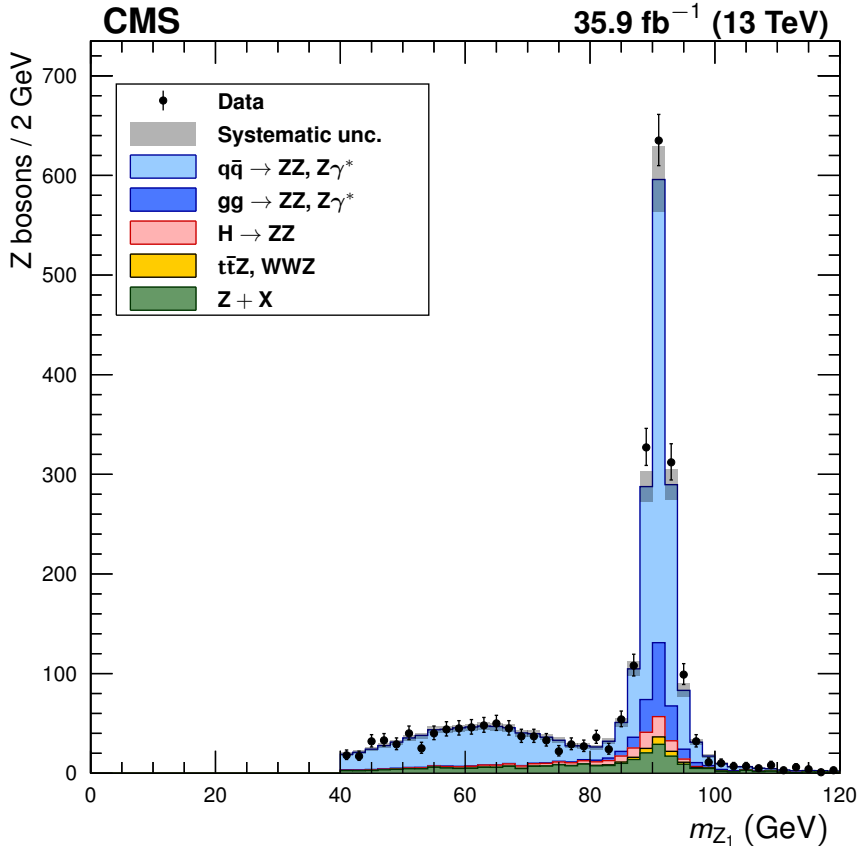


Figure 7.3: Distribution of the dilepton invariant mass of  $Z_1$ , the  $Z/\gamma^*$  candidate in each event closest to the nominal  $m_Z$ , in the full spectrum selection. Points represent data, with statistical uncertainty bars. The stack of filled histograms represents the SM signal prediction and background estimate, with a grey band showing the sum in quadrature of the statistical and systematic uncertainties on the total expected yield.

46  $m_{Z_2}$  against  $m_{Z_1}$ , for events in the same four-lepton mass region around the Higgs  
 47 resonance. Agreement between predictions and data is again good. Measurements of  
 48 Higgs boson properties, couplings, and production rates are beyond the scope of this  
 49 thesis, but were reported in Ref. [223].

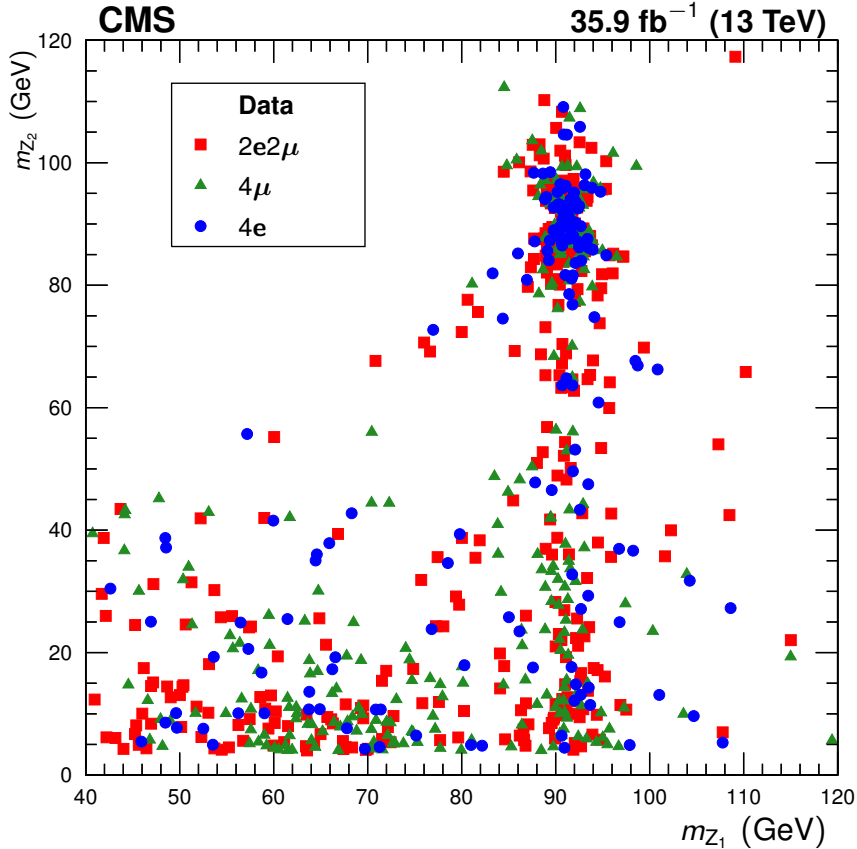


Figure 7.4: The reconstructed  $m_{Z_2}$  plotted against the reconstructed  $m_{Z_1}$  for data events in the full spectrum selection, with distinctive markers for each final state. For readability, only every fourth event is drawn. Clusters of events from different production modes are visible, as discussed in the text.

Table 7.2: Observed and expected yields of  $H \rightarrow ZZ^* \rightarrow 4\ell$  events, including expected background yields, for events passing the Higgs selection in the mass range  $118 < m_{4\ell} < 130$  GeV, shown for each final state and summed to the total. Uncertainties are statistical and systematic combined.

Final state	Expected $N_H$	SM continuum background	$Z + X$	Total expected	Observed
$4\mu$	$21.6 \pm 1.9$	$9.4^{+0.6}_{-0.7}$	$4.7^{+2.0}_{-1.8}$	$35.8 \pm 2.9$	34
$2e2\mu$	$26.5 \pm 2.3$	$11.0^{+0.7}_{-0.8}$	$6.9^{+3.1}_{-2.9}$	$44.4^{+3.7}_{-3.6}$	41
$4e$	$10.2 \pm 1.1$	$3.6 \pm 0.3$	$1.9^{+0.8}_{-1.0}$	$15.8 \pm 1.6$	19
Total	$58.3 \pm 5.0$	$24.1^{+1.5}_{-1.6}$	$13.5^{+3.7}_{-3.5}$	$96.0 \pm 6.7$	94

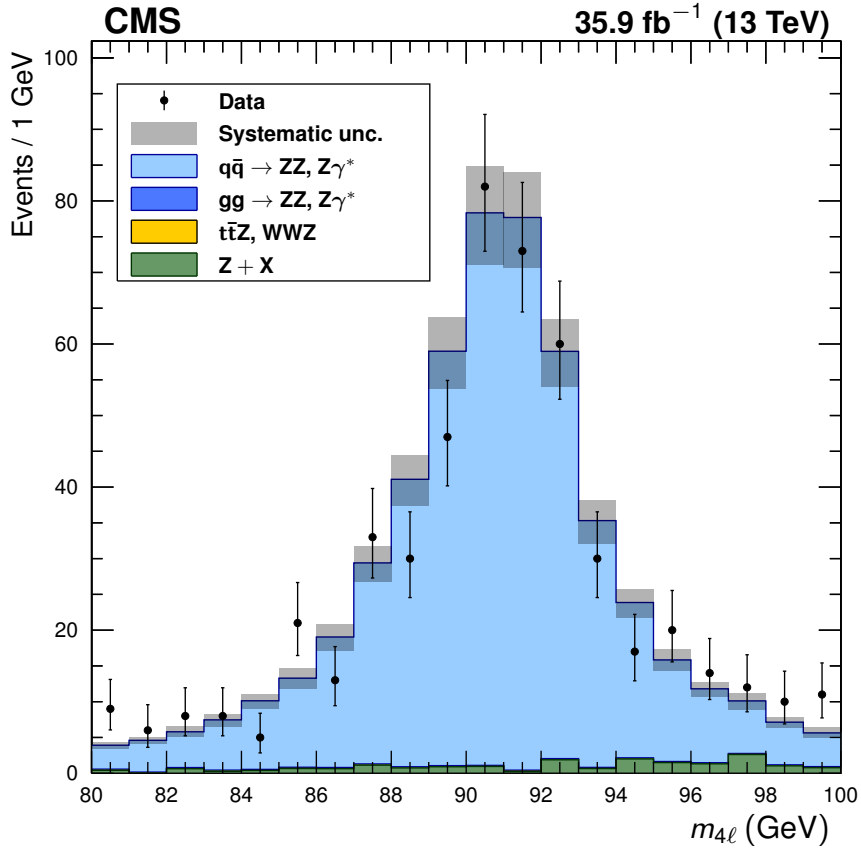


Figure 7.5: Distribution of the four-lepton invariant mass  $m_{4\ell}$  of all events in the mass range  $80 < m_{4\ell} < 100$  GeV, the  $Z \rightarrow 4\ell$  selection. Points represent data, with statistical uncertainty bars. The stack of filled histograms represents the SM signal prediction and background estimate, with a grey band showing the sum in quadrature of the statistical and systematic uncertainties on the total expected yield.

### 50 7.1.4 ZZ Production

51 Expected and observed yields for on-shell ZZ events are shown in Table 7.3. The corre-  
 52 sponding four-lepton and Z boson candidate invariant masses are shown in Figs. 7.11  
 53 and 7.12, respectively. Figure 7.13 shows the distribution of the number of jets ( $N_{\text{jets}}$ )  
 54 in these events. The leading and subleading jet  $p_T$  are shown separately in Fig. 7.14,  
 55 and the leading and subleading jet  $|\eta|$  are shown separately in Fig. 7.15, for all events  
 56 with at least one (leading) or two (subleading) jets. Figures 7.16 and 7.17 show the

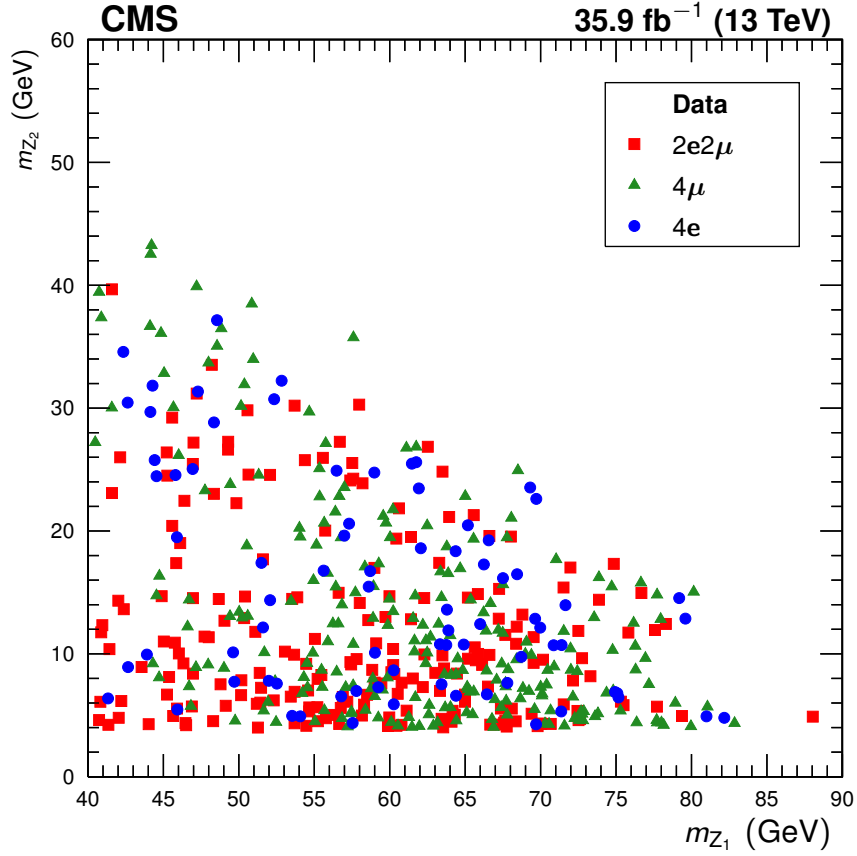


Figure 7.6: The reconstructed  $m_{Z_2}$  plotted against the reconstructed  $m_{Z_1}$  for all data events with  $80 < m_{4\ell} < 100$  GeV, with distinctive markers for each final state.

57  $m_{jj}$  and  $|\Delta\eta_{jj}|$  distributions for tagging jet pairs in the dijet selection. Agreement is,  
 58 again, overall good.

## 59 7.2 ZZ Fiducial and Total Cross Section

60 The yields shown in Table 7.3 and the systematic uncertainties of Table 6.1 are used  
 61 as inputs to the maximum likelihood method described in Section 6.3.1 to obtain the  
 62 on-shell ZZ signal strength across all four-lepton final states,

$$\mu = 1.040^{+0.033}_{-0.032} \text{ (stat)}^{+0.037}_{-0.035} \text{ (syst)} \pm 0.026 \text{ (lumi)}, \quad (7.1)$$

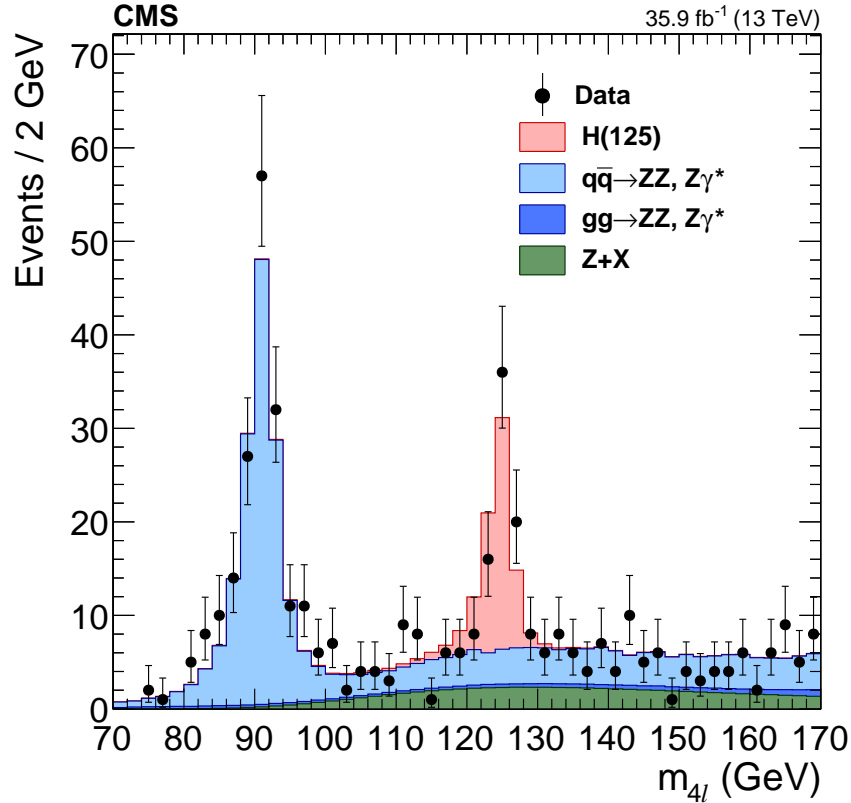


Figure 7.7: Distribution of the four-lepton invariant mass  $m_{4\ell}$  for events in the Higgs selection. Points represent data, with statistical uncertainty bars. The stack of filled histograms represents the signal and SM background predictions and the reducible background estimate.

Table 7.3: Observed and expected yields of ZZ events, including expected background yields, in the on-shell selection, shown for each final state and summed to the total. Uncertainties are statistical, then systematic, not including the integrated luminosity uncertainty.

Final state	Expected $N_{ZZ}$	Background	Total expected	Observed
$4\mu$	$301 \pm 2 \pm 9$	$10 \pm 1 \pm 2$	$311 \pm 2 \pm 9$	335
$2e2\mu$	$503 \pm 2 \pm 19$	$31 \pm 2 \pm 4$	$534 \pm 3 \pm 20$	543
$4e$	$205 \pm 1 \pm 12$	$20 \pm 2 \pm 2$	$225 \pm 2 \pm 13$	220
Total	$1009 \pm 3 \pm 36$	$60 \pm 3 \pm 8$	$1070 \pm 4 \pm 37$	1098

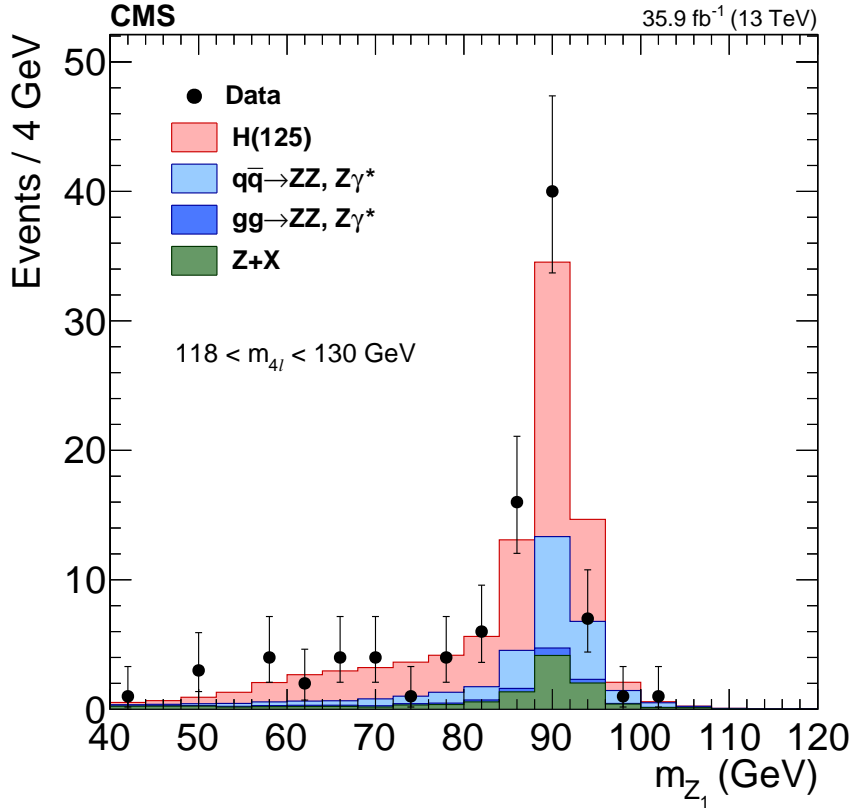


Figure 7.8: Distribution of the dilepton invariant mass of  $Z_1$ , the dilepton candidate in each event closest to the nominal  $m_Z$ , in events in the Higgs selection with  $118 < m_{4\ell} < 130 \text{ GeV}$ . Points represent data, with statistical uncertainty bars. The stack of filled histograms represents the signal and SM background predictions and the reducible background estimate.

63 which gives a fiducial cross section

$$\sigma_{\text{fid}}(\text{pp} \rightarrow \text{ZZ} \rightarrow 4\ell) = 40.9 \pm 1.3 \text{ (stat)} \pm 1.4 \text{ (syst)} \pm 1.0 \text{ (lumi)} \text{ fb}, \quad (7.2)$$

64 in the  $\text{ZZ} \rightarrow 4\ell$  fiducial phase space of Table 6.2. The corresponding total cross

65 section is

$$\sigma(\text{pp} \rightarrow \text{ZZ}) = 17.5^{+0.6}_{-0.5} \text{ (stat)} \pm 0.6 \text{ (syst)} \pm 0.4 \text{ (theo)} \pm 0.4 \text{ (lumi)} \text{ pb}. \quad (7.3)$$

66 This measurement, on 2016 data, agrees with the result of the 2015 measure-

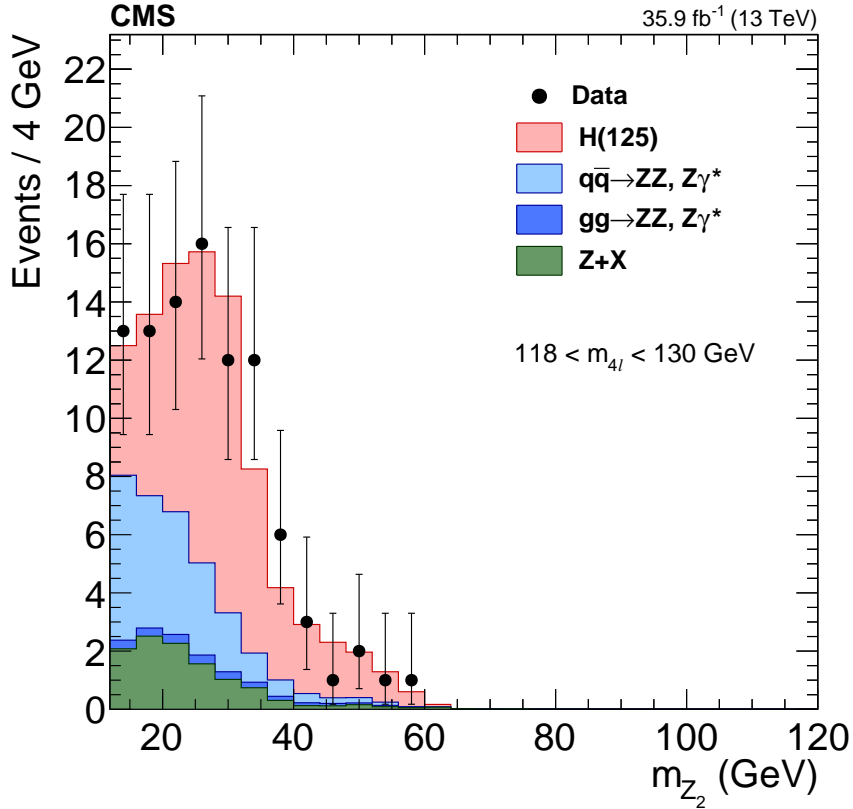


Figure 7.9: Distribution of the dilepton invariant mass of  $Z_2$ , the dilepton candidate in each event farther from the nominal  $m_Z$ , in events in the Higgs selection with  $118 < m_{4\ell} < 130 \text{ GeV}$ . Points represent data, with statistical uncertainty bars. The stack of filled histograms represents the signal and SM background predictions and the reducible background estimate.

67 ment [218],

$$\sigma(\text{pp} \rightarrow \text{ZZ}) = 14.6^{+1.9}_{-1.8} (\text{stat})^{+0.3}_{-0.5} (\text{syst}) \pm 0.2 (\text{theo}) \pm 0.4 (\text{lumi}) \text{ pb.} \quad (7.4)$$

68 One may combine the measurements by doing a six-bin simultaneous fit with the bins  
 69 representing the same final state in 2015 and 2016 considered separately. The degree  
 70 of correlation between the systematic uncertainties in the 2015 and 2016 runs is not  
 71 known, but the 2015 contribution is small enough that the systematic uncertainties  
 72 are dominated by those in the 2016 dataset, and the degree of correlation will have  
 73 only a small effect on the measurement. We therefore do the fit twice, once treating

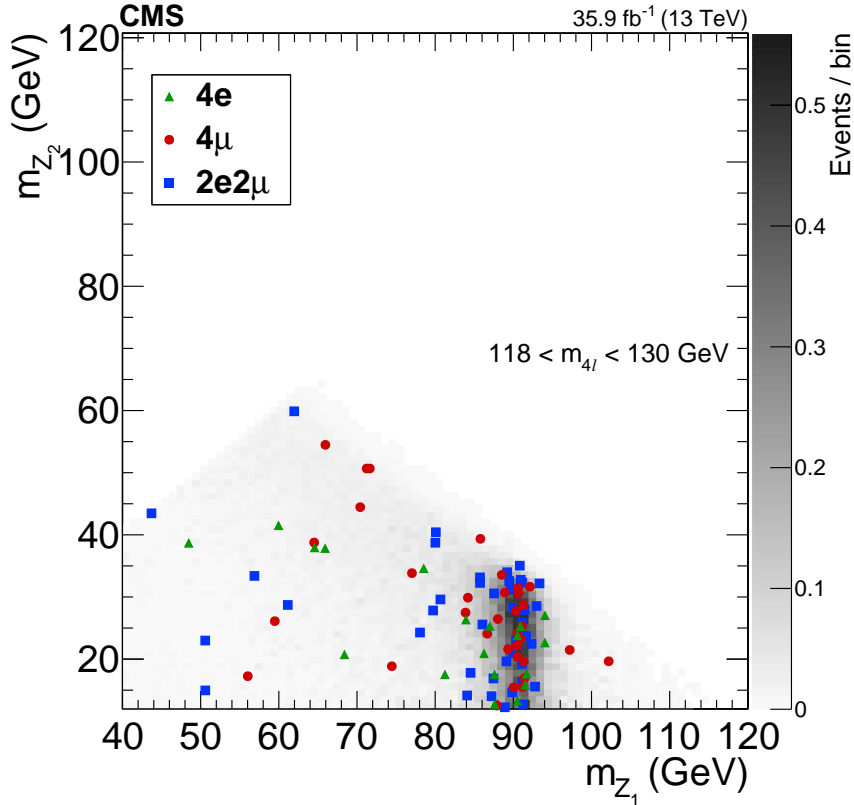


Figure 7.10: The reconstructed  $m_{Z_2}$  mass plotted against the reconstructed  $m_{Z_1}$  for data events in the Higgs selection with  $118 < m_{4\ell} < 130$  GeV, with distinctive markers for each final state. The shading represents the expected number of events in the bin.

74 the experimental uncertainties as fully correlated between the datasets, and again  
 75 treating them as fully uncorrelated. The small difference in the central value obtained  
 76 is added linearly to the systematic error of the result. After the full combination, the  
 77 “2015 + 2016” total cross section is found to be

$$\sigma(pp \rightarrow ZZ) = 17.2 \pm 0.5 \text{ (stat)} \pm 0.7 \text{ (syst)} \pm 0.4 \text{ (theo)} \pm 0.4 \text{ (lumi)} \text{ pb.} \quad (7.5)$$

78 These results can be compared to the MATRIX v1.0.0\_beta4 prediction of  $16.2^{+0.6}_{-0.4}$  pb,  
 79 computed at NNLO in QCD, or the MCFM v7.0 prediction of  $15.0^{+0.7}_{-0.6} \pm 0.2$  pb, cal-  
 80 culated at NLO in QCD with LO  $gg \rightarrow ZZ$  diagrams included. Both predictions use  
 81 the NNPDF3.0 PDF sets and fixed scales  $\mu_F = \mu_R = m_Z$ .

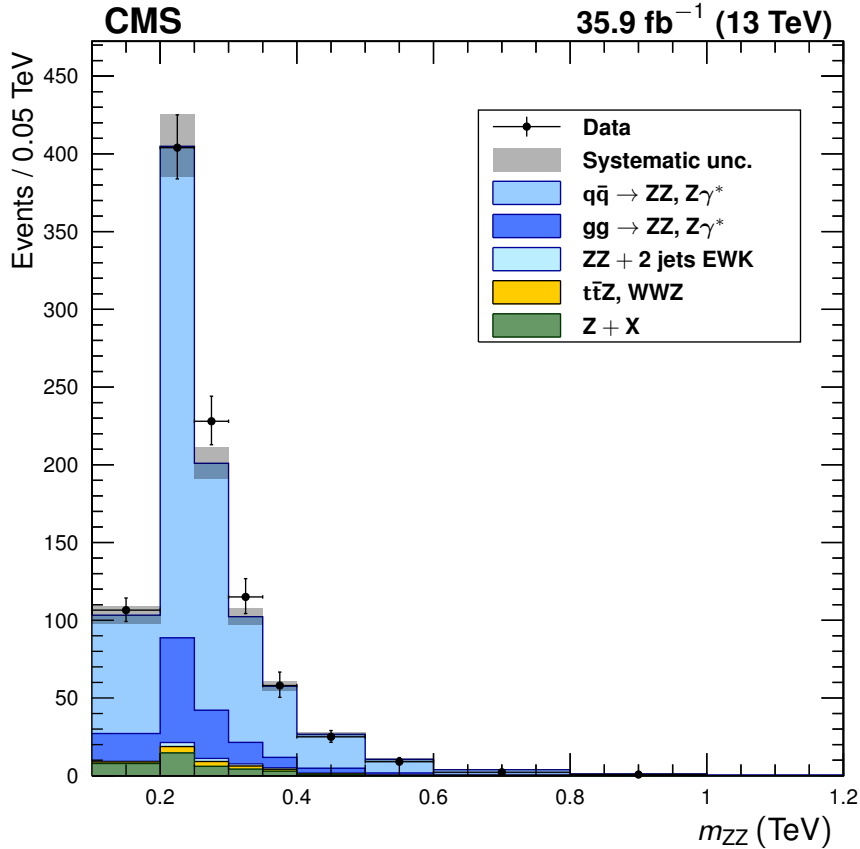


Figure 7.11: Distribution of the four-lepton invariant mass  $m_{ZZ}$  of all events in the on-shell selection. Points represent data, with statistical uncertainty bars. The stack of filled histograms represents the SM signal prediction and background estimate, with a grey band showing the sum in quadrature of the statistical and systematic uncertainties on the total expected yield.

82        The total cross section is shown as a function of  $\sqrt{s}$  in Fig. 7.18. Measurements from CMS [72–74, 218] and ATLAS [76, 77, 105] are compared to NLO predictions made with MCFM (with contributions from leading order gluon-gluon fusion diagrams), and NNLO predictions made with MATRIX. Results from both experiments agree with the predictions, verifying this aspect of the SM to within the measurements’ uncertainties.

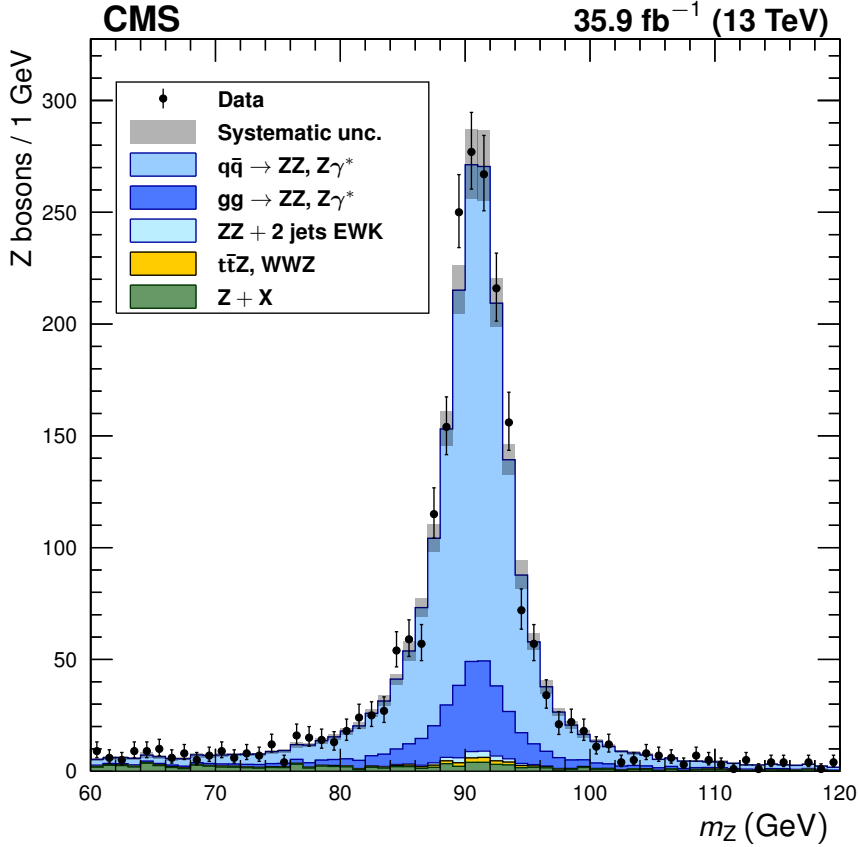


Figure 7.12: Distribution of the dilepton invariant mass of Z candidates in all events in the on-shell selection, regardless of whether the lepton pair is labeled  $Z_1$  or  $Z_2$ . Points represent data, with statistical uncertainty bars. The stack of filled histograms represents the SM signal prediction and background estimate, with a grey band showing the sum in quadrature of the statistical and systematic uncertainties on the total expected yield.

### 88 7.2.1 $Z \rightarrow 4\ell$ Branching Fraction

89 The signal strength in the  $Z \rightarrow 4\ell$  selection is

$$\mu = 0.980^{+0.046}_{-0.044} \text{ (stat)}^{+0.065}_{-0.059} \text{ (syst)} \pm 0.025 \text{ (lumi)}, \quad (7.6)$$

90 yielding a fiducial cross section

$$\sigma_{\text{fid}} (\text{pp} \rightarrow Z \rightarrow 4\ell) = 31.2^{+1.5}_{-1.4} \text{ (stat)}^{+2.1}_{-1.9} \text{ (syst)} \pm 0.8 \text{ (lumi)} \text{ fb}. \quad (7.7)$$

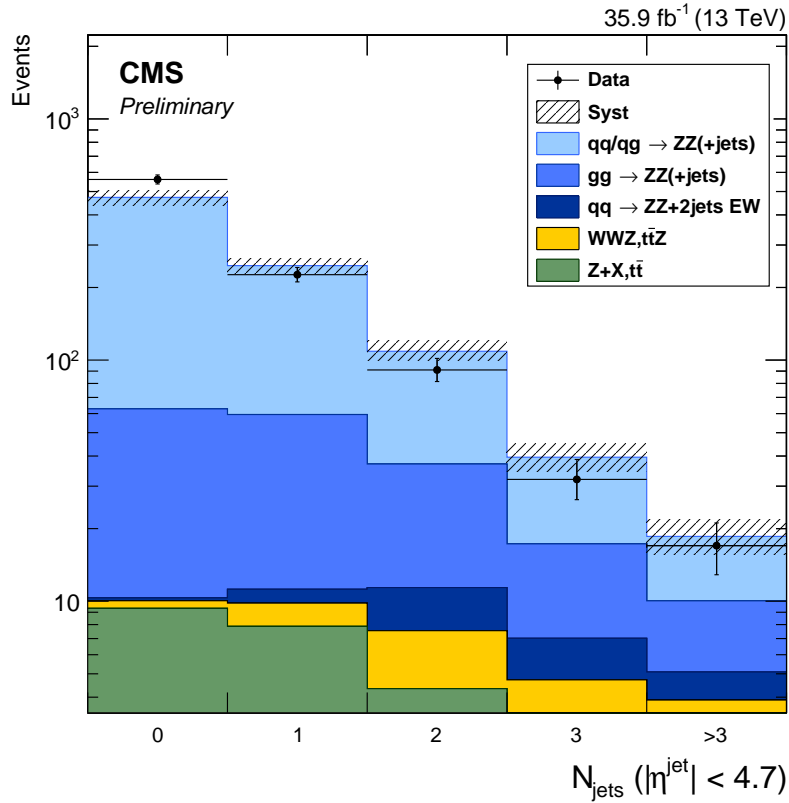


Figure 7.13: Distribution of jet multiplicity in ZZ events. Points represent data, with statistical uncertainty bars. The stack of filled histograms represents the SM signal prediction and background estimate, with a hatched band showing the sum in quadrature of the statistical and systematic uncertainties on the total expected yield.

91 This is scaled by an acceptance correction factor  $\mathcal{A} = 0.125 \pm 0.002$ , estimated with  
 92 POWHEG v2.0, to the total  $Z \rightarrow 4\ell$  cross section times branching ratio,

$$\sigma(pp \rightarrow Z) \times \mathcal{B}(Z \rightarrow 4\ell) = 249 \pm 8 \text{ (stat)}^{+9}_{-8} \text{ (syst)} \pm 4 \text{ (theo)} \pm 6 \text{ (lumi)} \text{ fb.} \quad (7.8)$$

93 Equation (6.10) is used to calculate the branching fraction. The Z cross section  
 94 times dilepton branching ratio is calculated with FEWZ v2.0 [224] at NNLO in QCD  
 95 to be  $\sigma(Z \rightarrow 2\ell) = 1870^{+50}_{-40}$  pb. The Z mass window correction factor is calculated  
 96 with POWHEG and found to be  $\mathcal{C}_{80-100}^{60-120} = 0.926 \pm 0.001$ . Its uncertainty includes  
 97 scale and PDF variations [204]. The nominal Z to dilepton branching fraction is

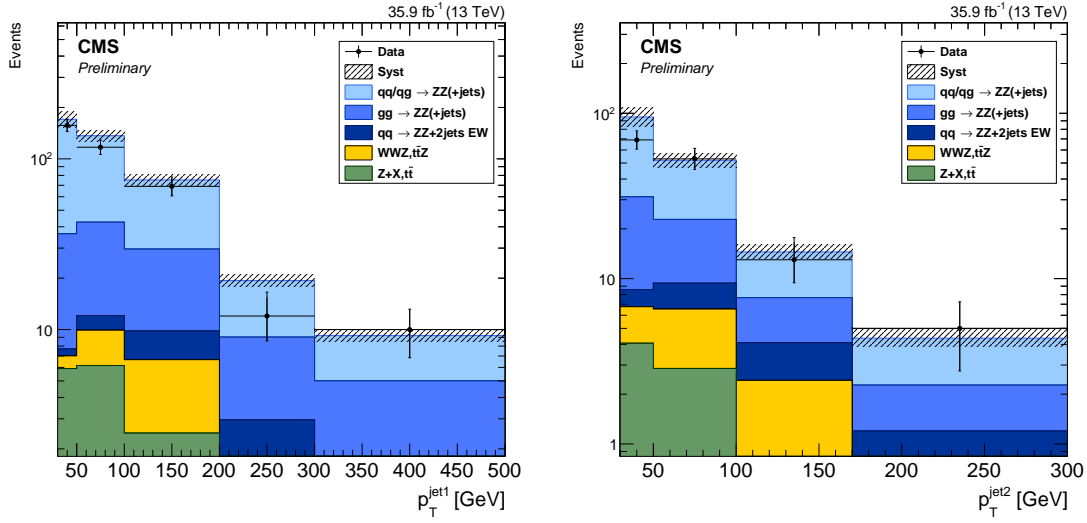


Figure 7.14: Distribution of leading (left) and subleading (right) jet  $p_T$  for all ZZ events with at least one jet and at least two jets, respectively. Points represent data, with statistical uncertainty bars. The stack of filled histograms represents the SM signal prediction and background estimate, with a hatched band showing the sum in quadrature of the statistical and systematic uncertainties on the total expected yield.

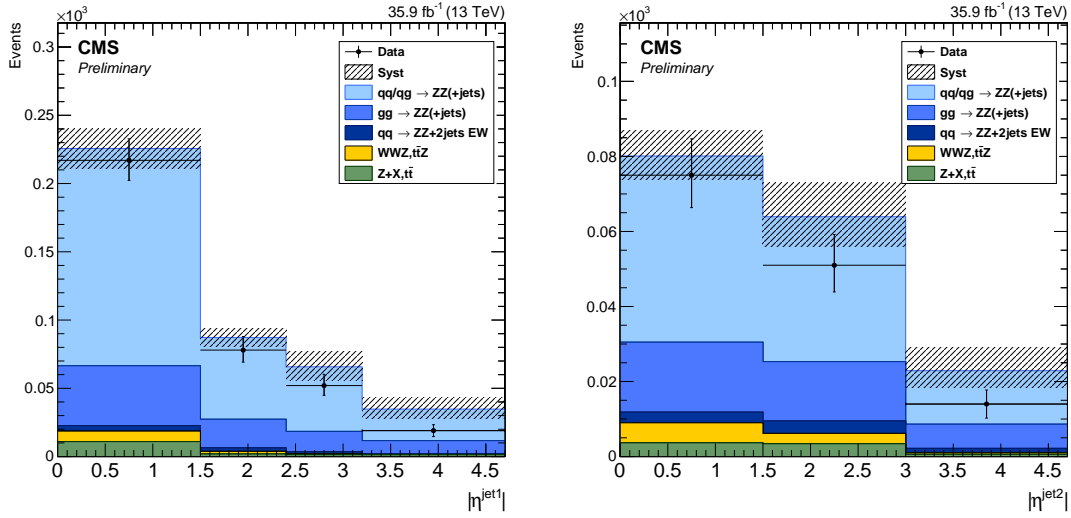


Figure 7.15: Distribution of leading (left) and subleading (right) jet  $|\eta|$  for all ZZ events with at least one jet and at least two jets, respectively. Points represent data, with statistical uncertainty bars. The stack of filled histograms represents the SM signal prediction and background estimate, with a hatched band showing the sum in quadrature of the statistical and systematic uncertainties on the total expected yield.

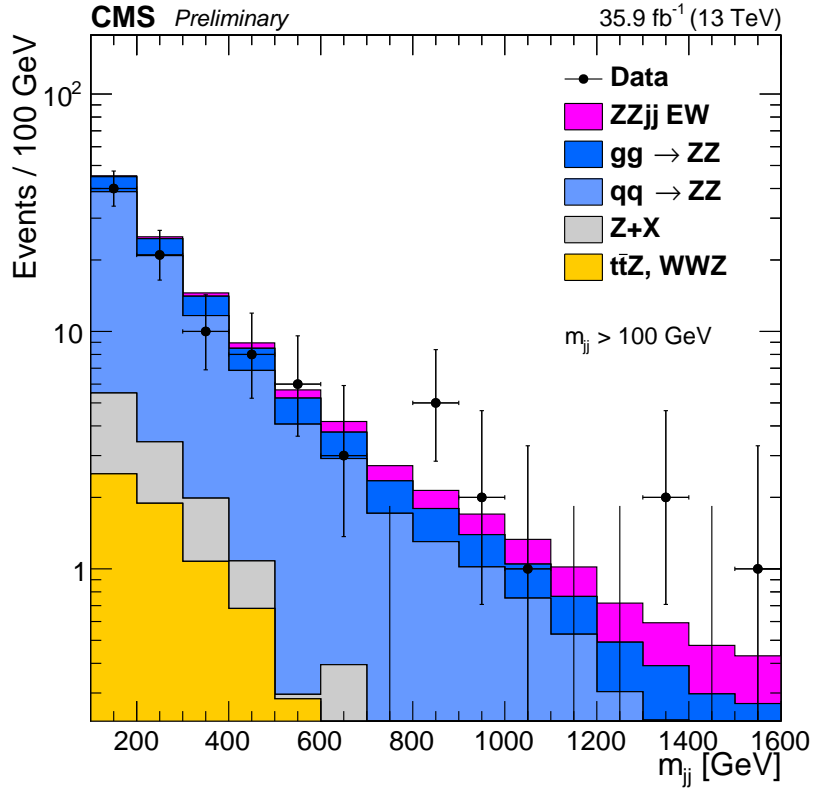


Figure 7.16: Dijet invariant mass  $m_{jj}$  of the tag jets in ZZ events passing the dijet selection ( $m_{jj} > 100$  GeV). Points represent data, with statistical uncertainty bars. The stack of filled histograms represents the SM signal prediction, including EWK production, and background estimate.

98     $\mathcal{B}(Z \rightarrow 2\ell) = 0.03366$  [11]. The four-lepton branching fraction is measured to be

$$\mathcal{B}(Z \rightarrow 4\ell) = 4.8 \pm 0.2 \text{ (stat)} \pm 0.2 \text{ (syst)} \pm 0.1 \text{ (theo)} \pm 0.1 \text{ (lumi)} \times 10^{-6}. \quad (7.9)$$

99    This value is consistent with the theoretical value of  $4.6 \times 10^{-6}$ , calculated with  
100    MADGRAPH5\_AMC@NLO v2.3.3, and with previous measurements from CMS and  
101    ATLAS [89, 90, 218], which had uncertainties 2–4 times larger.

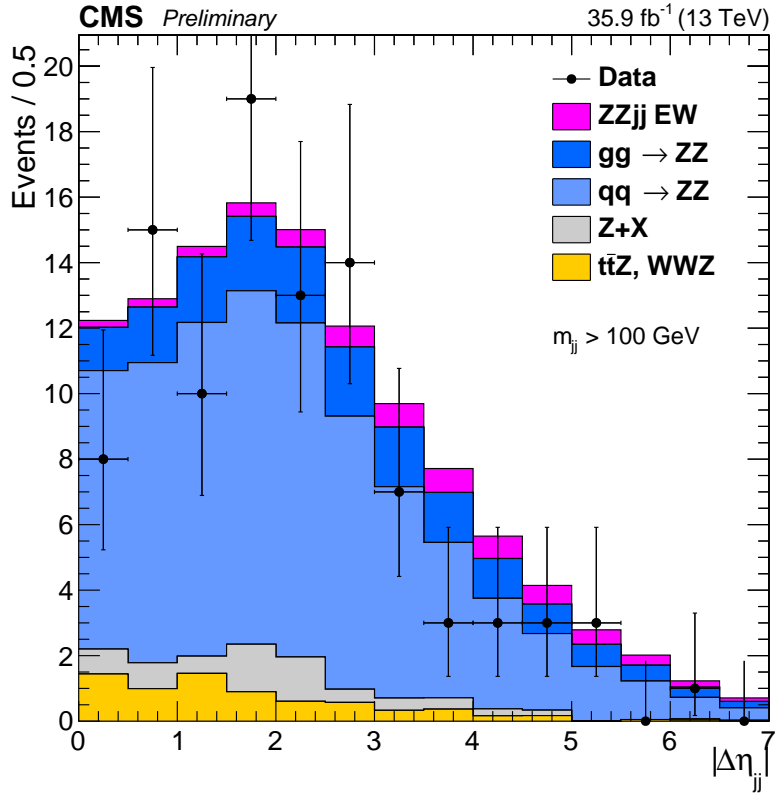


Figure 7.17: Pseudorapidity separation  $|\Delta\eta_{jj}|$  of tag jets in ZZ events passing the dijet selection ( $m_{jj} > 100 \text{ GeV}$ ). Points represent data, with statistical uncertainty bars. The stack of filled histograms represents the SM signal prediction, including EWK production, and background estimate.

### <sup>102</sup> 7.3 Differential Cross Sections

<sup>103</sup> Detector-level distributions are unfolded to calculate differential cross sections as de-  
<sup>104</sup> scribed in Section 6.4. Figures 7.19–7.30 show measured differential cross sections  
<sup>105</sup> and corresponding theory predictions, as functions of different observables. All dis-  
<sup>106</sup> tributions are normalized to the inclusive fiducial cross section, such that the integral  
<sup>107</sup> of each is unity, including overflow bins (not shown). The observables in Figs. 7.19–  
<sup>108</sup> 7.24 consider only the four-lepton system. For the calculation of these distributions,  
<sup>109</sup> as well as the differential cross section as a function of  $N_{\text{jets}}$  (Fig. 7.25), all events

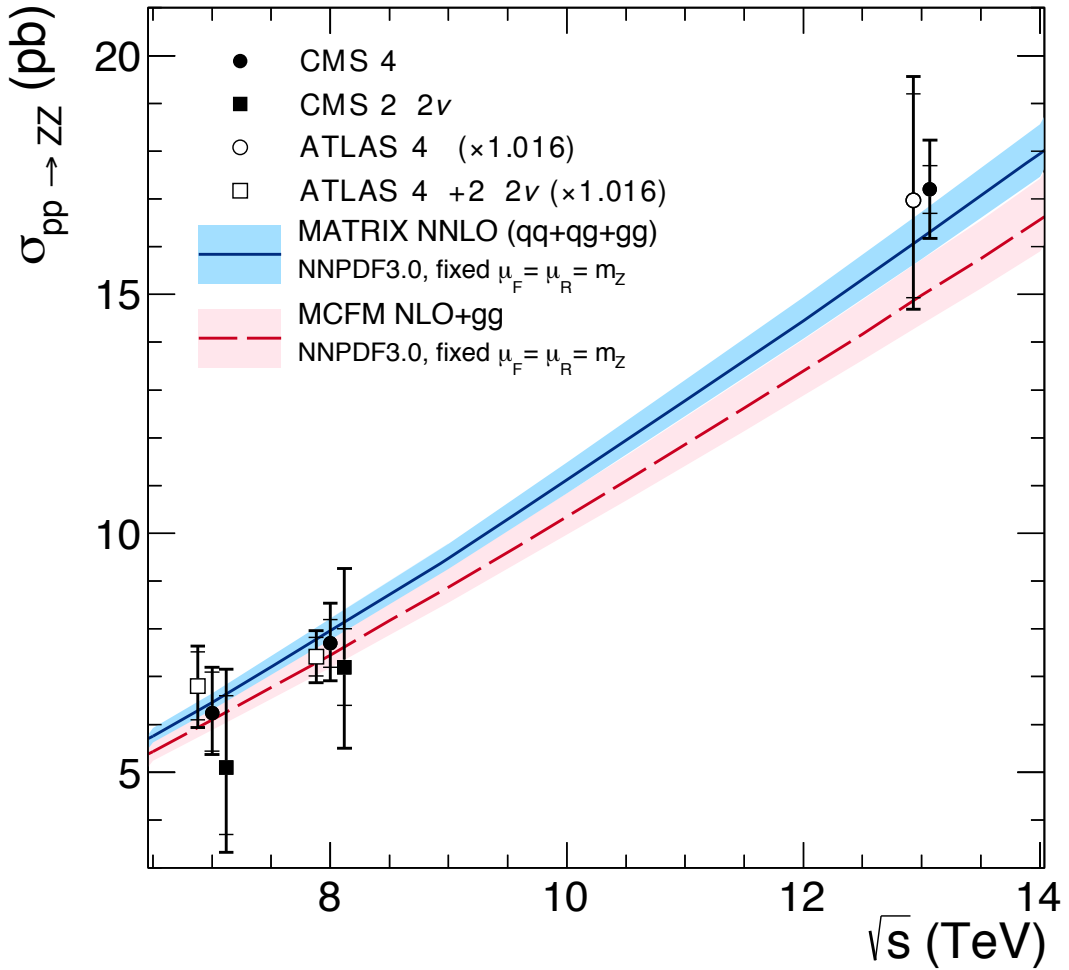


Figure 7.18: The total ZZ cross section is shown as a function of  $\sqrt{s}$ . Measurements from CMS and ATLAS are both shown, with the ATLAS numbers adjusted upward by 1.6% to account for differences in Z mass window choice. Points at the same center-of-mass energy are shifted slightly in the horizontal direction for clarity. Experimental measurements are compared to predictions from MCFM at NLO in QCD with additional contributions from LO gluon-gluon fusion diagrams, and MATRIX at NNLO in QCD. Both sets of predictions use the NNPDF3.0 PDF sets and fixed scales  $\mu_F = \mu_R = m_Z$ .

passing the on-shell selection of Table 6.2 are used. Figures 7.26 and 7.27 show  $m_{jj}$  and  $|\Delta\eta_{jj}|$  for all ZZ events with at least two jets, while Figs 7.28 and 7.29 show  $p_T$  and  $\eta$ , respectively, for the leading jet in events with  $N_{jets} \geq 1$  on the left and the subleading jet in events with  $N_{jets} \geq 2$  on the right. In Fig. 7.30, the phase space is expanded to the full spectrum selection of Table 6.2 at both detector and true level, to show the four-lepton differential cross section through all production modes as a function of  $m_{4\ell}$ . Measured cross sections overall agree with the theoretical predictions within their uncertainties, which are dominated by statistical uncertainties in all bins.

## 7.4 Vector Boson Scattering

Figure 7.31 shows the output of the GBDT discussed in Section 6.5 for events in the dijet selection. The search procedure finds a modest excess of events compatible with VBS ZZjj signal, at the level of 2.7 standard deviations over the null hypothesis of the SM without VBS ZZ production. The expected significance is 1.6 standard deviations. This corresponds to a VBS fiducial cross section of

$$\sigma_{fid}(pp \rightarrow ZZjj(EWK) \rightarrow 4\ell jj) = 0.40^{+0.21}_{-0.16} (\text{stat})^{+0.13}_{-0.09} (\text{syst}) \text{ fb}, \quad (7.10)$$

which is consistent with the SM prediction of  $0.29^{+0.02}_{-0.03}$  fb.

## 7.5 Anomalous Coupling Limits

The ZZ invariant mass is shown in Fig. 7.32 for all events in the on-shell selection, with two example distributions shown for potential scenarios with nonzero aTGCs, one of which sets  $f_5^\gamma = 0.0019$  and  $f_5^Z = 0.0015$ , and the other  $f_4^\gamma = 0.0019$  and  $f_4^Z = 0.0015$ . The limit setting procedure described in Section 6.6 is applied to each aTGC parameter, with all other couplings fixed to their SM values, to yield

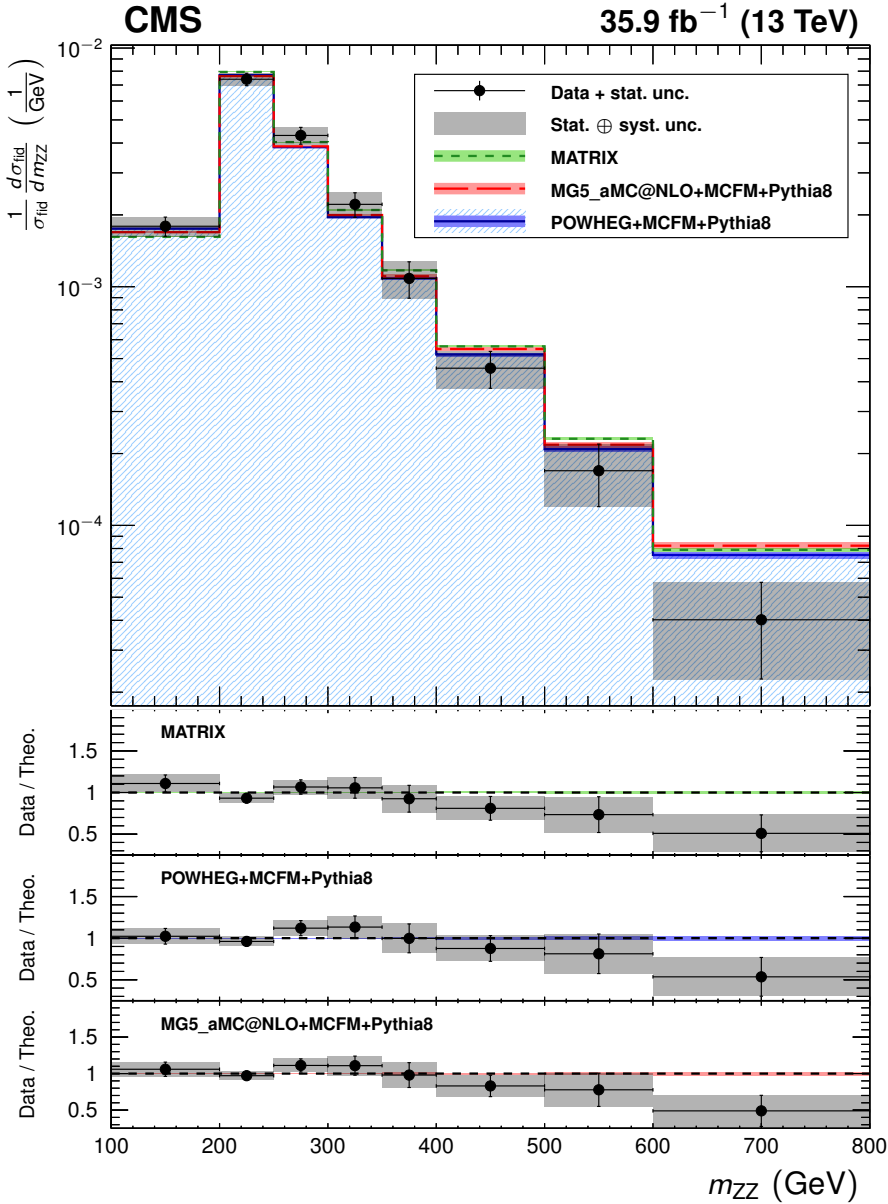


Figure 7.19: The ZZ differential cross section as a function of  $m_{ZZ}$ , normalized to the inclusive fiducial cross section. Points represent the unfolded data, with vertical bars showing the statistical uncertainty and a grey band showing the sum in quadrature of the statistical and systematic uncertainties. Blue, red, and green histograms represent the POWHEG+MCFM, MADGRAPH5\_AMC@NLO+MCFM, and MATRIX predictions, respectively, with bands around each which represent their combined statistical, scale, and PDF uncertainties. The lower sections of the plot represents the ratio of the measured cross section to each of the predictions.

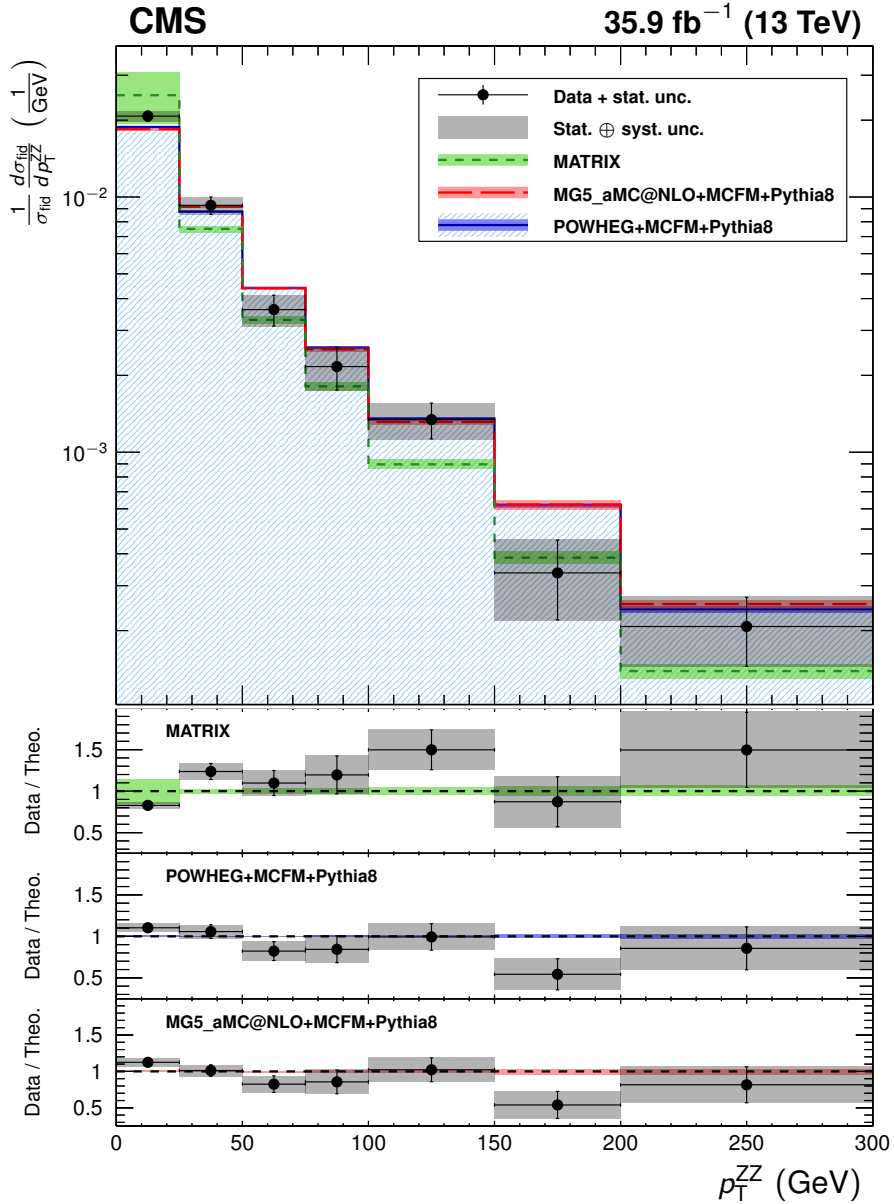


Figure 7.20: The ZZ differential cross section as a function of the four-lepton  $p_T$ , normalized to the inclusive fiducial cross section. Points represent the unfolded data, with vertical bars showing the statistical uncertainty and a grey band showing the sum in quadrature of the statistical and systematic uncertainties. Blue, red, and green histograms represent the POWHEG+MCFM, MADGRAPH5\_AMC@NLO+MCFM, and MATRIX predictions, respectively, with bands around each which represent their combined statistical, scale, and PDF uncertainties. The lower sections of the plot represents the ratio of the measured cross section to each of the predictions.

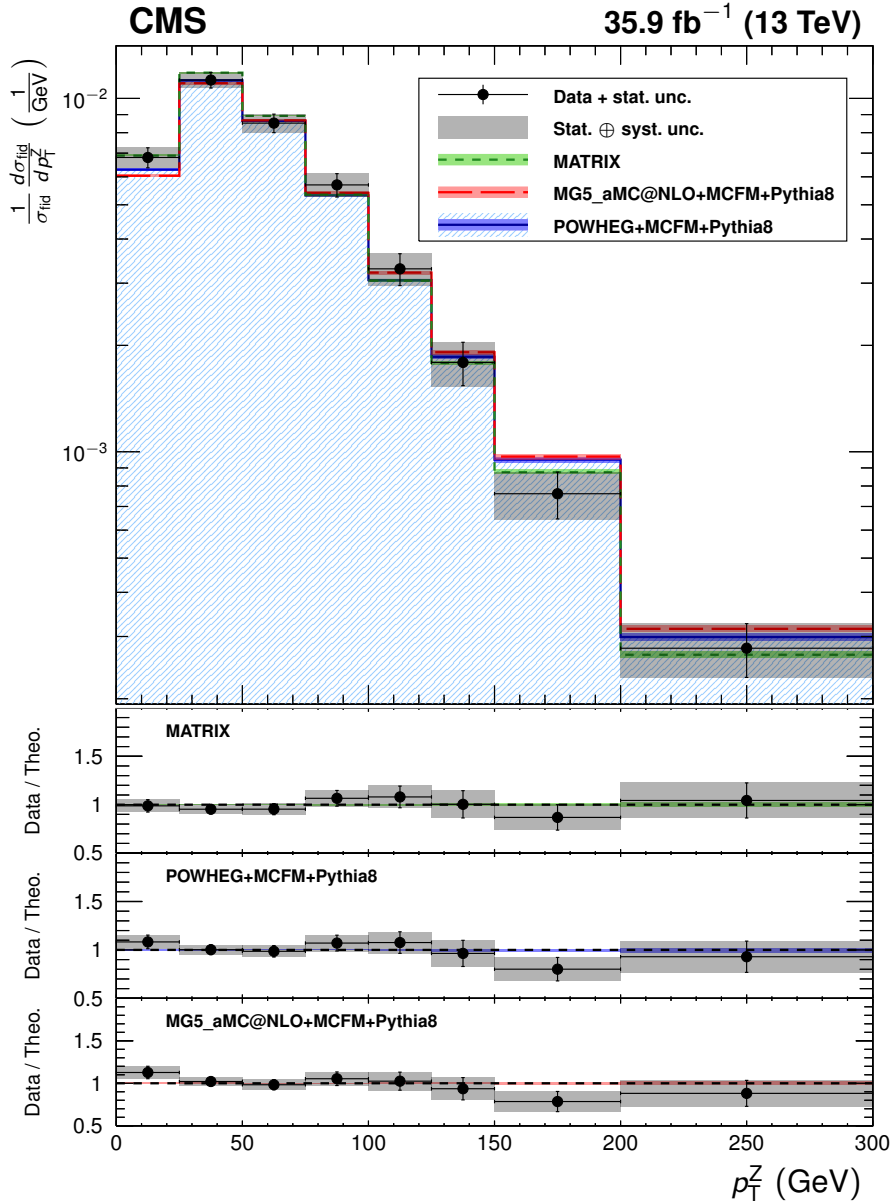


Figure 7.21: The ZZ differential cross section as a function of the  $p_T$  of both Z boson candidates, regardless of which one is  $Z_1$  and which is  $Z_2$ , normalized to the inclusive fiducial cross section. Points represent the unfolded data, with vertical bars showing the statistical uncertainty and a grey band showing the sum in quadrature of the statistical and systematic uncertainties. Blue, red, and green histograms represent the POWHEG+MCFM, MADGRAPH5\_AMC@NLO+MCFM, and MATRIX predictions, respectively, with bands around each which represent their combined statistical, scale, and PDF uncertainties. The lower sections of the plot represents the ratio of the measured cross section to each of the predictions.

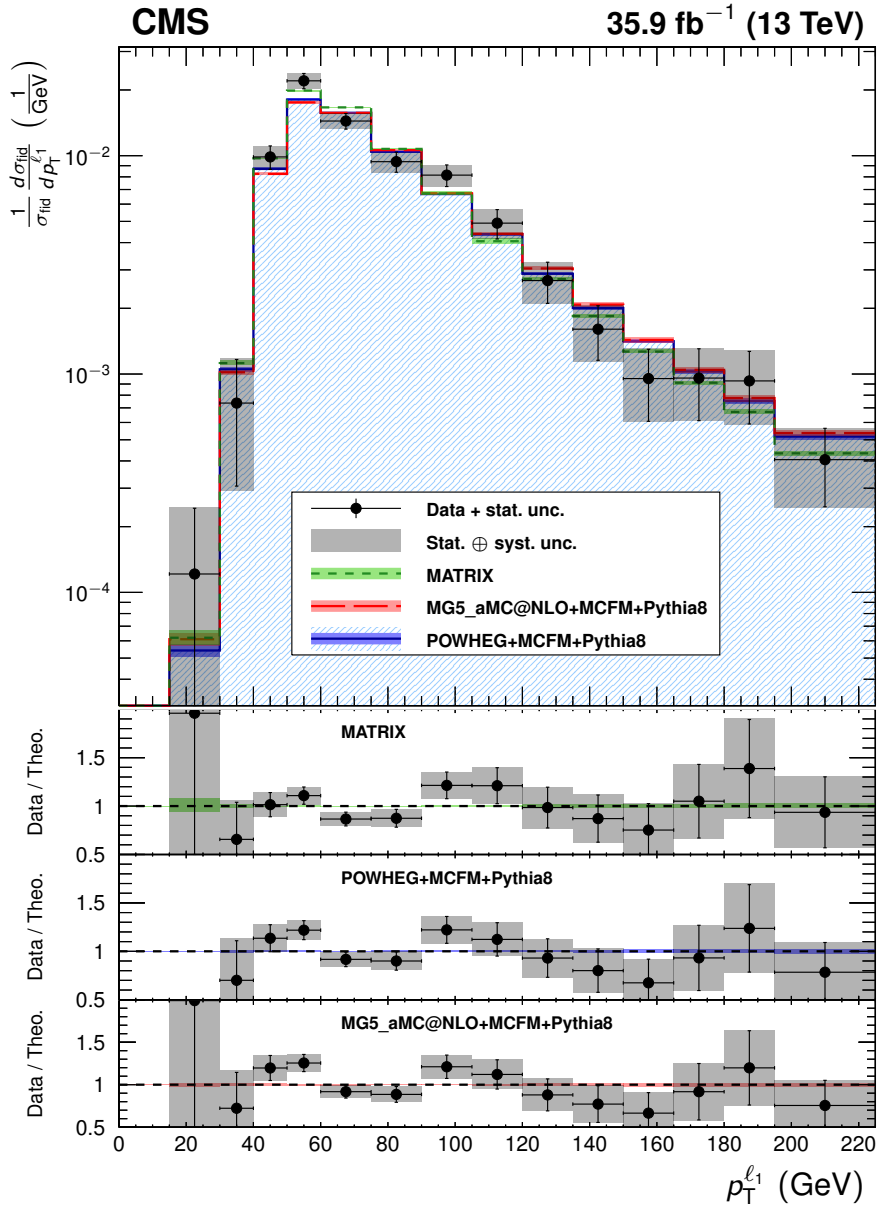


Figure 7.22: The ZZ differential cross section as a function of leading lepton  $p_T$ , normalized to the inclusive fiducial cross section. Points represent the unfolded data, with vertical bars showing the statistical uncertainty and a grey band showing the sum in quadrature of the statistical and systematic uncertainties. Blue, red, and green histograms represent the POWHEG+MCFM, MADGRAPH5\_AMC@NLO+MCFM, and MATRIX predictions, respectively, with bands around each which represent their combined statistical, scale, and PDF uncertainties. The lower sections of the plot represents the ratio of the measured cross section to each of the predictions.

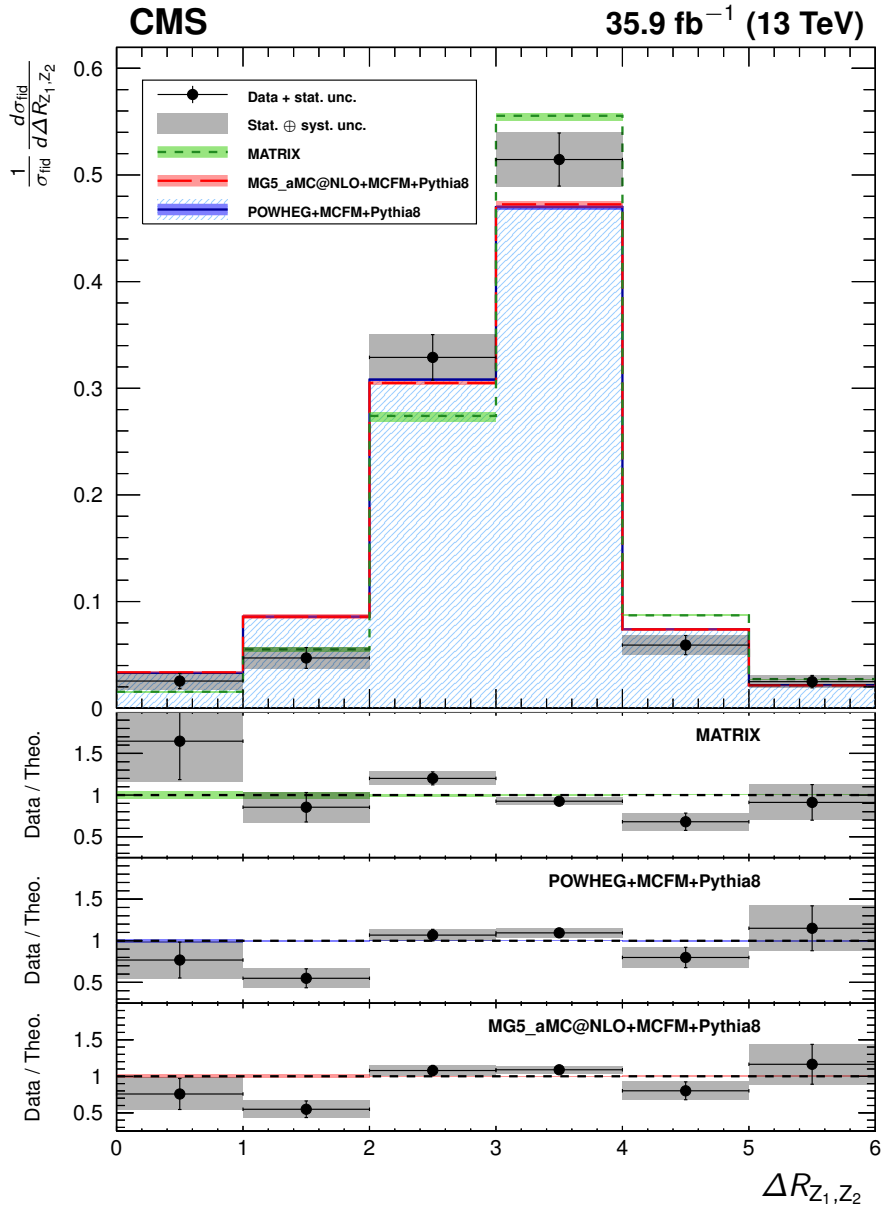


Figure 7.23: The ZZ differential cross section as a function of  $\Delta R$  between the two Z bosons, normalized to the inclusive fiducial cross section. Points represent the unfolded data, with vertical bars showing the statistical uncertainty and a grey band showing the sum in quadrature of the statistical and systematic uncertainties. Blue, red, and green histograms represent the POWHEG+MCFM, MADGRAPH5\_AMC@-NLO+MCFM, and MATRIX predictions, respectively, with bands around each which represent their combined statistical, scale, and PDF uncertainties. The lower sections of the plot represents the ratio of the measured cross section to each of the predictions.

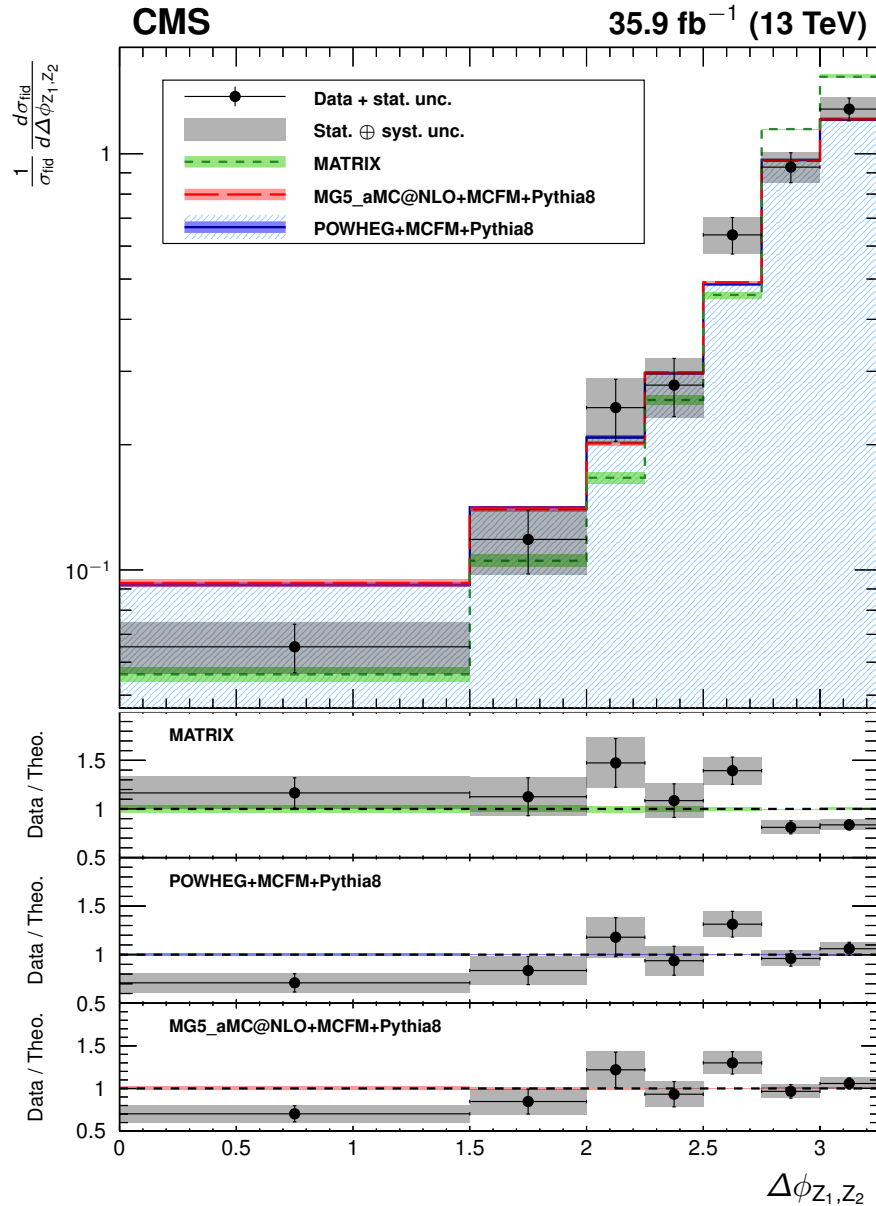


Figure 7.24: The ZZ differential cross section as a function of  $\Delta\phi$  between the two Z bosons, normalized to the inclusive fiducial cross section. Points represent the unfolded data, with vertical bars showing the statistical uncertainty and a grey band showing the sum in quadrature of the statistical and systematic uncertainties. Blue, red, and green histograms represent the POWHEG+MCFM, MADGRAPH5\_AMC@-NLO+MCFM, and MATRIX predictions, respectively, with bands around each which represent their combined statistical, scale, and PDF uncertainties. The lower sections of the plot represents the ratio of the measured cross section to each of the predictions.

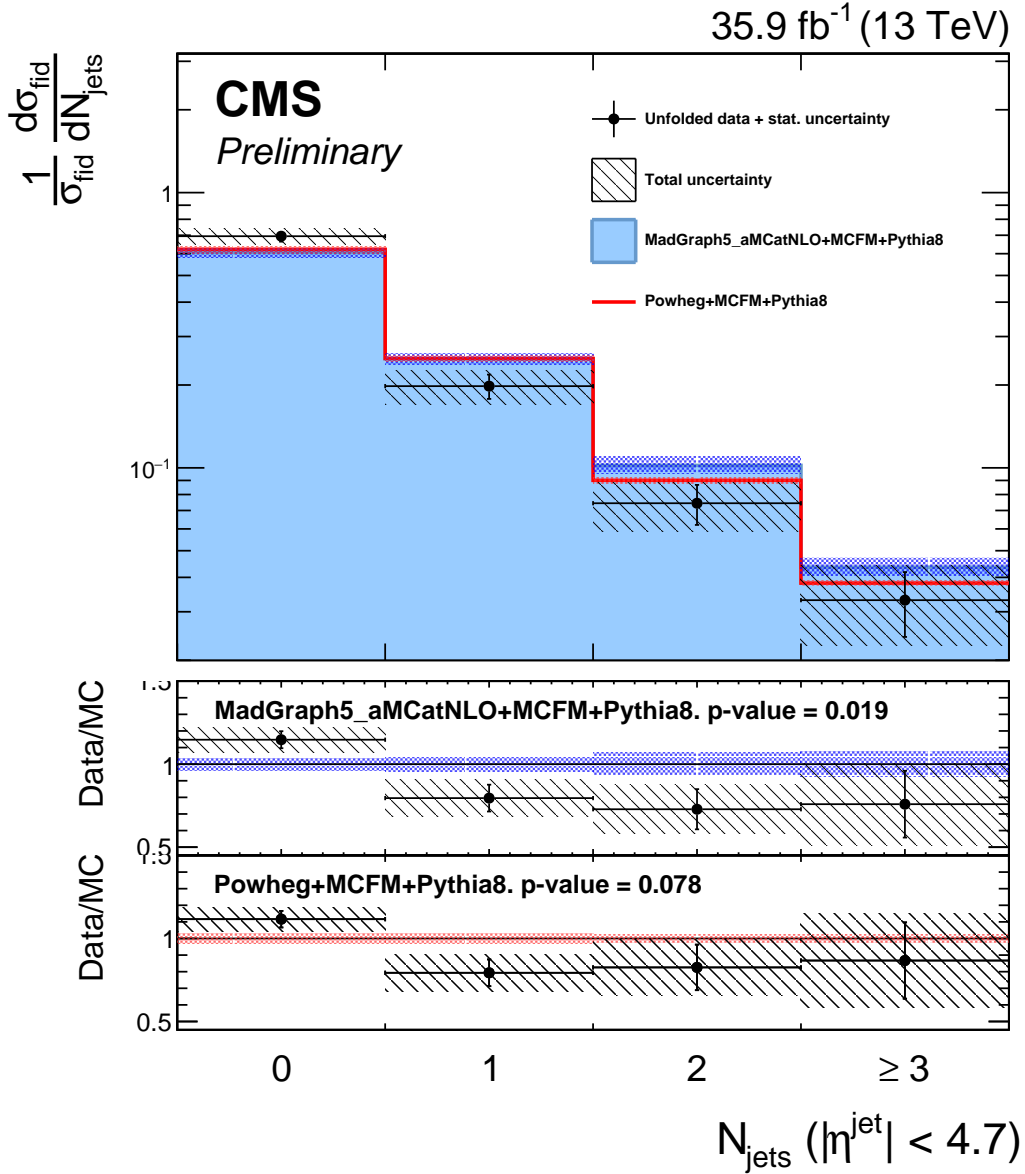


Figure 7.25: The ZZ differential cross section as a function of the jet multiplicity  $N_{\text{jets}}$ , normalized to the inclusive fiducial cross section. Points represent the unfolded data, with vertical bars showing the statistical uncertainty and a hatched band showing the sum in quadrature of the statistical and systematic uncertainties. Red and blue histograms represent the POWHEG+MCFM and MADGRAPH5\_AMC@NLO+MCFM predictions, respectively, with bands around each which represent their combined statistical, scale, and PDF uncertainties. The lower sections of the plot represents the ratio of the measured cross section to each of the predictions.

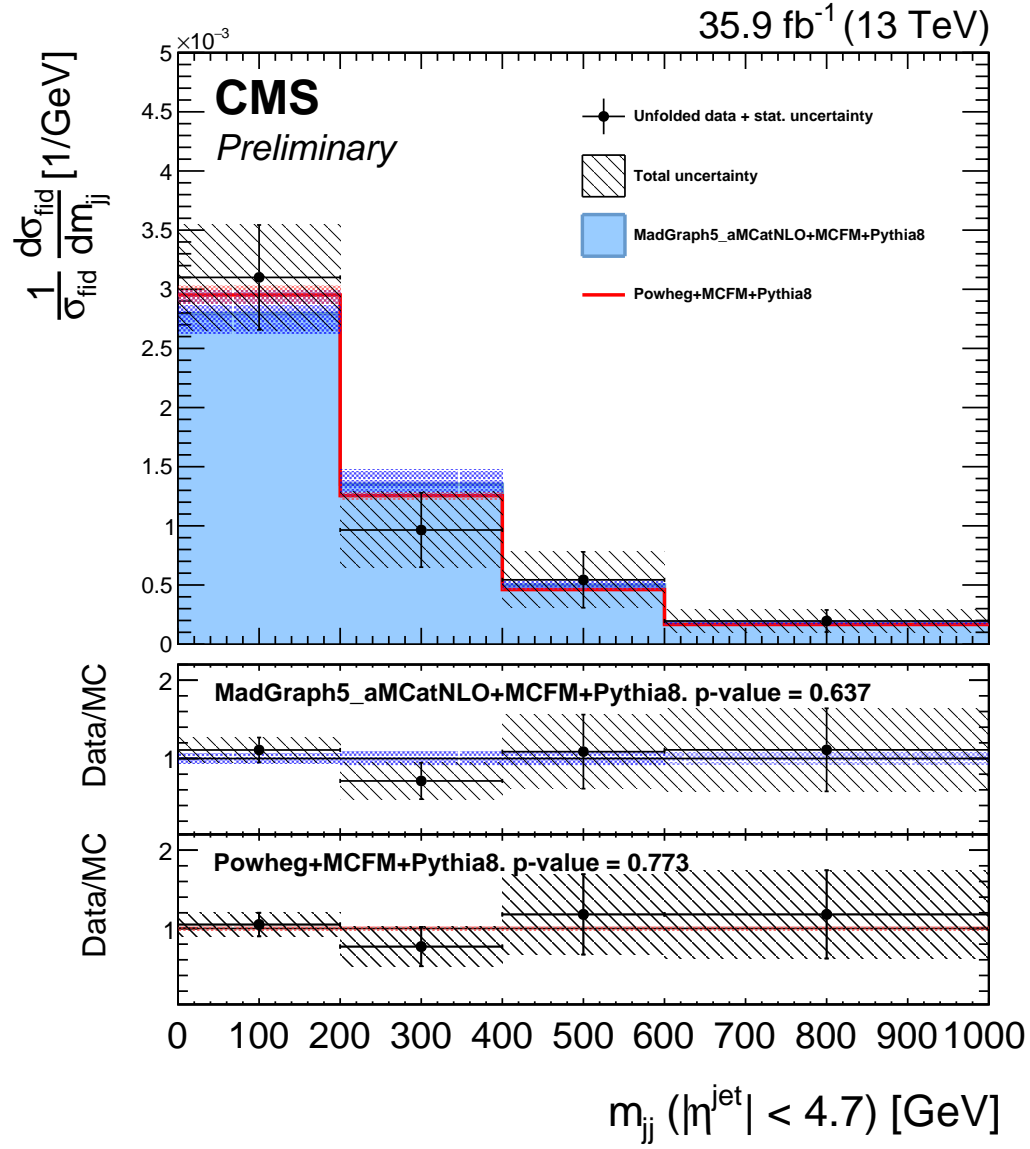


Figure 7.26: The ZZ differential cross section as a function of the invariant mass of the two highest- $p_T$  jets  $m_{jj}$ , including all ZZ events with at least two jets, normalized to the inclusive fiducial cross section. Points represent the unfolded data, with vertical bars showing the statistical uncertainty and a hatched band showing the sum in quadrature of the statistical and systematic uncertainties. Red and blue histograms represent the POWHEG+MCFM and MADGRAPH5\_AMC@NLO+MCFM predictions, respectively, with bands around each which represent their combined statistical, scale, and PDF uncertainties. The lower sections of the plot represents the ratio of the measured cross section to each of the predictions.

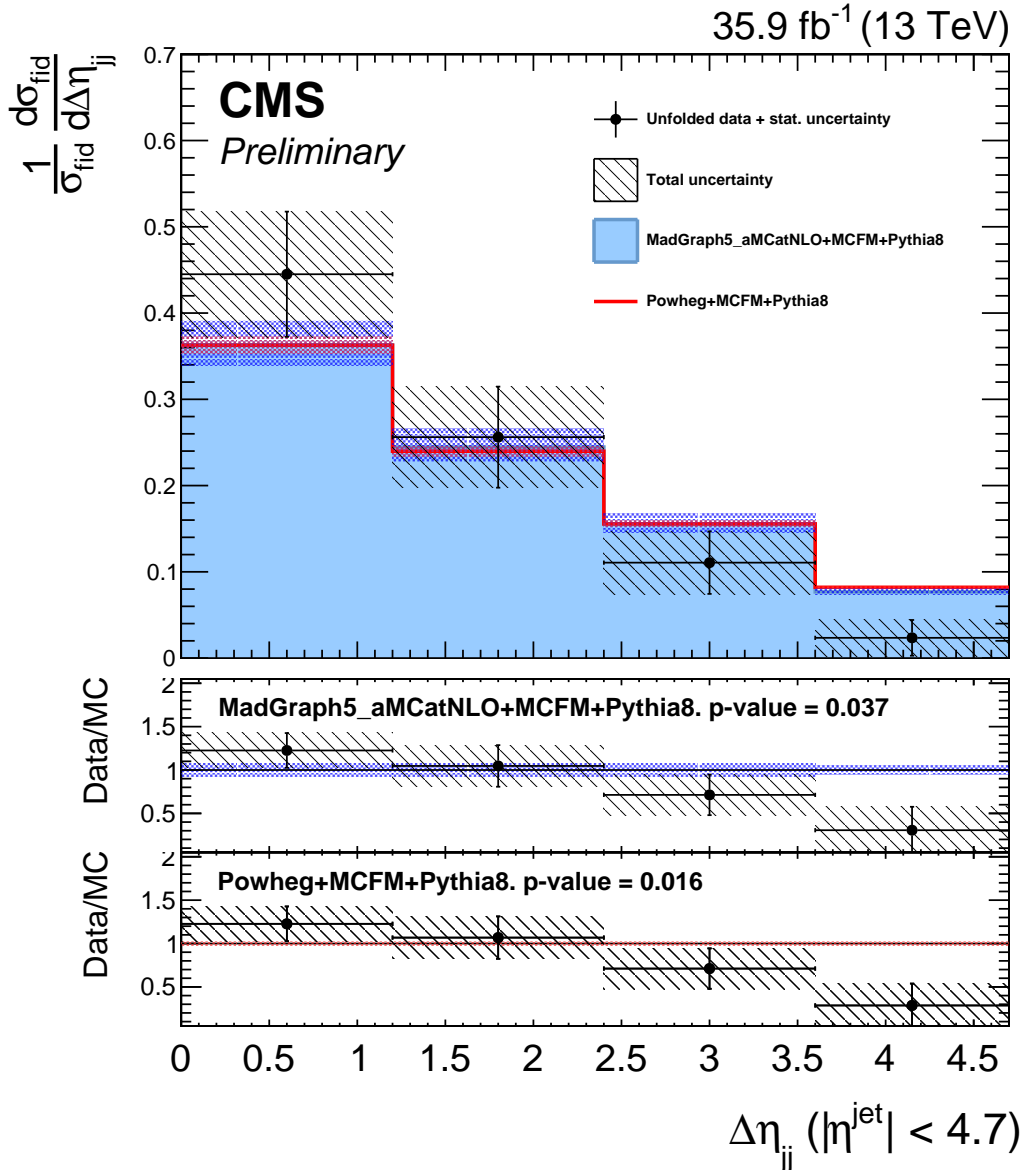


Figure 7.27: The ZZ differential cross section as a function of the absolute pseudo-rapidity separation of the two highest- $p_T$  jets  $|\Delta\eta_{jj}|$ , including all ZZ events with at least two jets, normalized to the inclusive fiducial cross section. Points represent the unfolded data, with vertical bars showing the statistical uncertainty and a hatched band showing the sum in quadrature of the statistical and systematic uncertainties. Red and blue histograms represent the POWHEG+MCFM and MADGRAPH5\_AMC@-NLO+MCFM predictions, respectively, with bands around each which represent their combined statistical, scale, and PDF uncertainties. The lower sections of the plot represents the ratio of the measured cross section to each of the predictions.

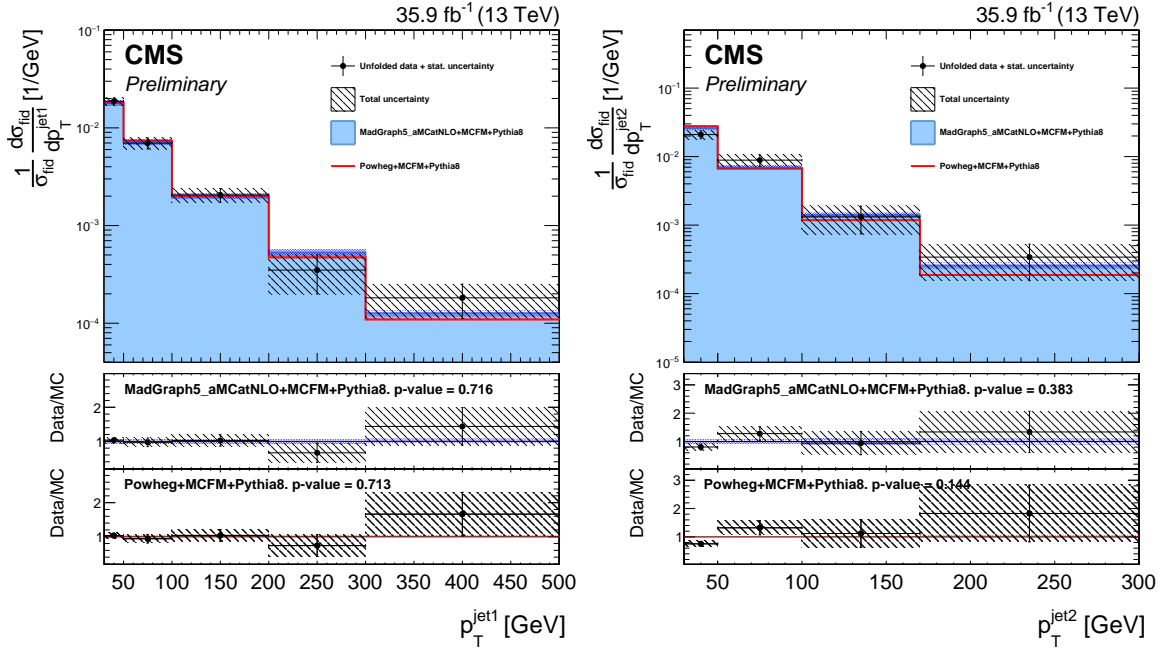


Figure 7.28: The ZZ differential cross section as a function of the leading (left) and subleading (right) jet  $p_T$ , in ZZ events with at least one jet and at least two jets respectively, normalized to the inclusive fiducial cross section. Points represent the unfolded data, with vertical bars showing the statistical uncertainty and a hatched band showing the sum in quadrature of the statistical and systematic uncertainties. Red and blue histograms represent the POWHEG+MCFM and MADGRAPH5\_AMC@NLO+MCFM predictions, respectively, with bands around each which represent their combined statistical, scale, and PDF uncertainties. The lower sections of the plots represent the ratio of the measured cross section to each of the predictions.

131 one-dimensional 95% CL limits,

$$\begin{aligned} -0.0012 < f_4^Z < 0.0010, \quad -0.0010 < f_5^Z < 0.0013, \\ -0.0012 < f_4^\gamma < 0.0013, \quad -0.0012 < f_5^\gamma < 0.0013. \end{aligned} \tag{7.11}$$

132 These results improve the previous CMS limits, which were the most stringent set  
 133 previously, by factors of 2–3 [74] and are the most stringent limits to date on the  
 134 parameters in question. Recent preliminary limits from ATLAS using 13 TeV data  
 135 are 50–80% looser [225]. Two-dimensional limits are set in the  $f_4^\gamma$ - $f_4^Z$  and  $f_5^\gamma$ - $f_5^Z$   
 136 planes, holding all other parameters to the SM values in each calculation. One- and

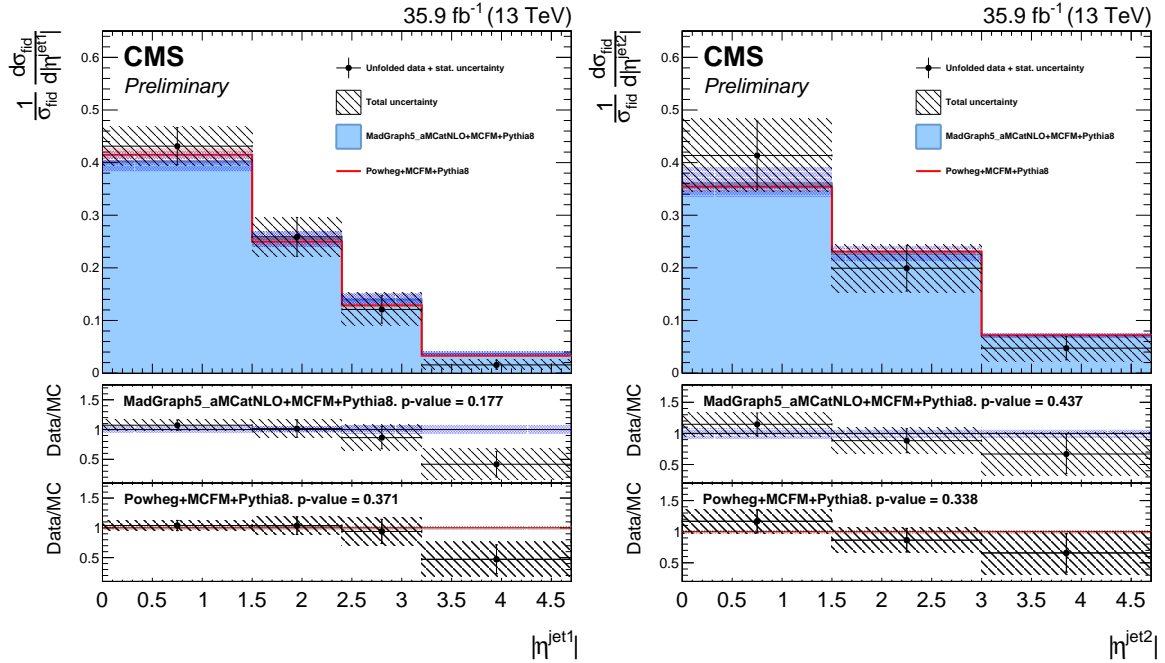


Figure 7.29: The ZZ differential cross section as a function of the leading (left) and subleading (right) jet  $\eta$ , in ZZ events with at least one jet and at least two jets respectively, normalized to the inclusive fiducial cross section. Points represent the unfolded data, with vertical bars showing the statistical uncertainty and a hatched band showing the sum in quadrature of the statistical and systematic uncertainties. Red and blue histograms represent the POWHEG+MCFM and MADGRAPH5\_AMC@-NLO+MCFM predictions, respectively, with bands around each which represent their combined statistical, scale, and PDF uncertainties. The lower sections of the plots represent the ratio of the measured cross section to each of the predictions.

137 two-dimensional 95% CL limits are shown in Fig. 7.33.

138 No unitarizing form factor (c.f. Section 1.5.1) is applied when calculating the  
 139 limits of Eq. (7.11). One way to enforce unitarity without a form factor would be  
 140 to restrict the maximum ZZ invariant mass used, and set the limits considering only  
 141 events with  $m_{ZZ}$  below some cutoff. The limits would then depend on the cutoff  
 142 chosen, converging to the nonunitary limits when the cutoff is larger than the energies  
 143 accessible in the experiment. The limit computations are repeated with multiple  
 144 cutoff values, and the resulting expected and observed limits are shown in Fig. 7.34

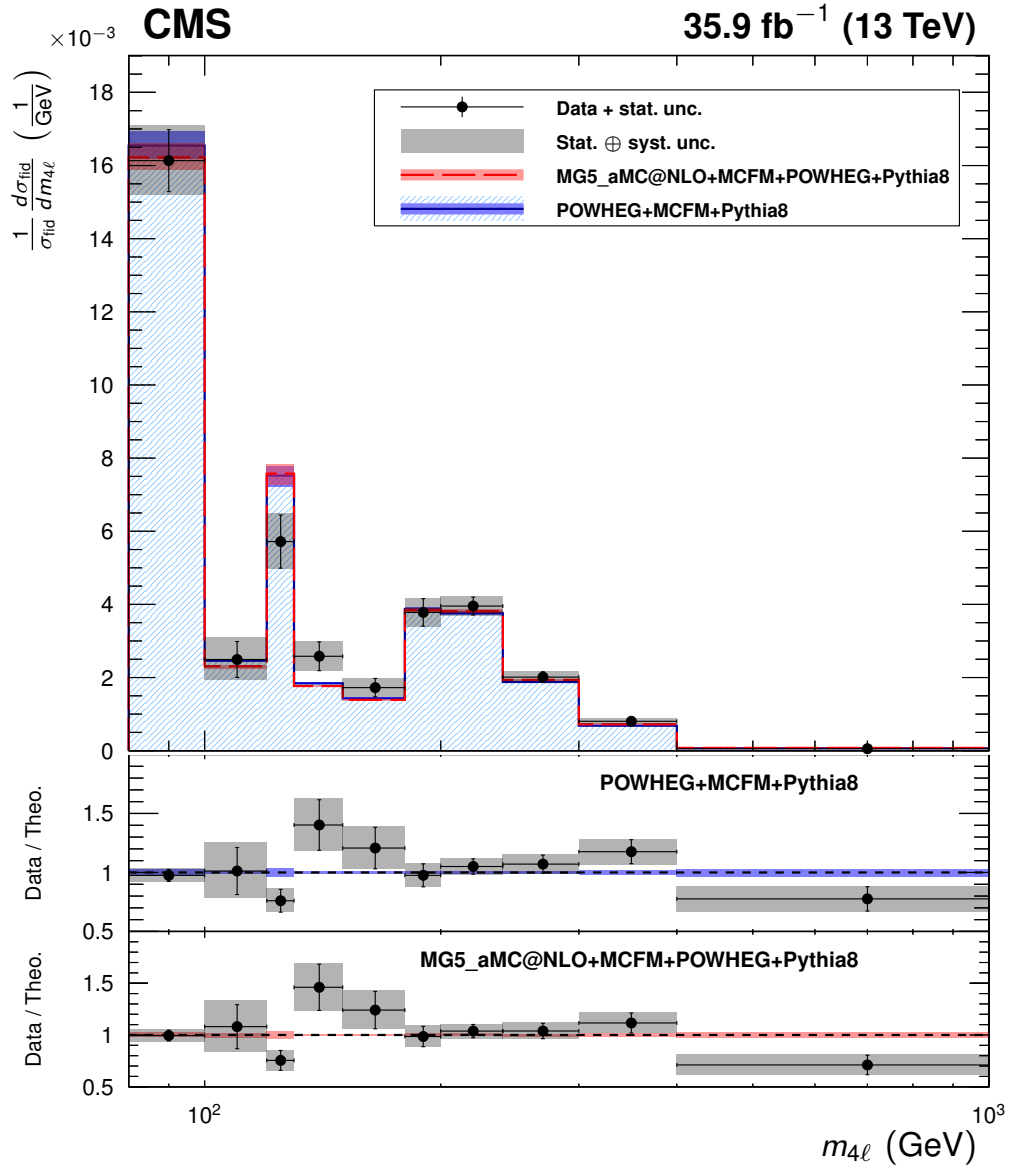


Figure 7.30: The four-lepton differential cross section as a function of  $m_{4\ell}$  under the full spectrum selections, normalized to the inclusive fiducial cross section. Points represent the unfolded data, with vertical bars showing the statistical uncertainty and a grey band showing the sum in quadrature of the statistical and systematic uncertainties. Blue and red histograms represent the POWHEG+MCFM and MADGRAPH5-AMC@NLO+MCFM predictions, respectively, with bands around each which represent their combined statistical, scale, and PDF uncertainties. The lower sections of the plot represents the ratio of the measured cross section to each of the predictions.

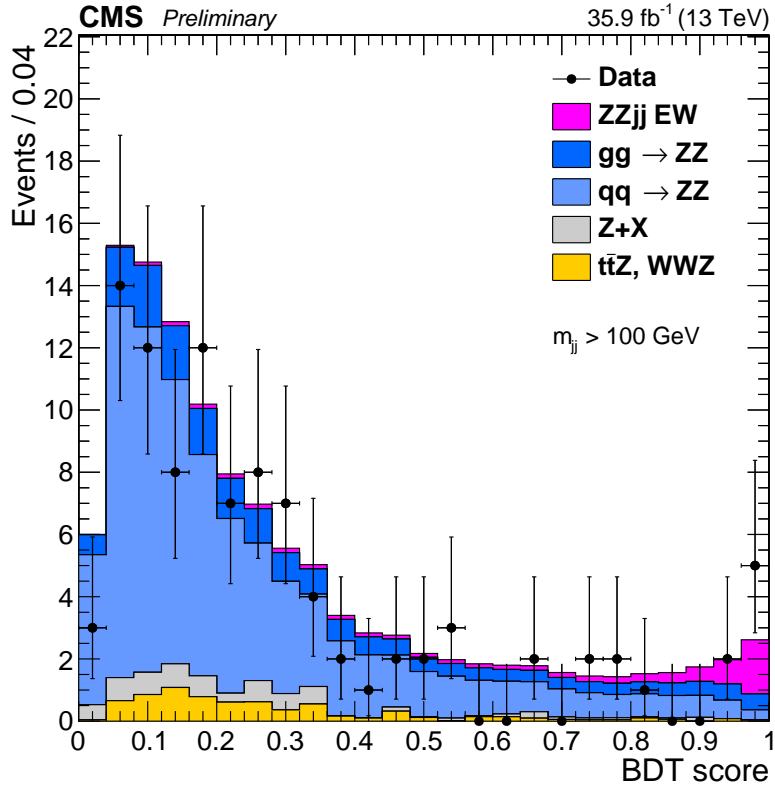


Figure 7.31: Output distribution of the VBS signal extraction GBDT, for events in the dijet selection. Points represent data, with statistical uncertainty bars. The stack of filled histograms represents the SM signal prediction and background estimate.

145 as a function of the maximum  $m_{ZZ}$  used.

146 The aQGC search proceeds the same way, but using events in the dijet selection.

147 The observable used for limit setting is again  $m_{ZZ}$ , which is shown for these events

148 in Fig. 7.35 along with two example distributions for scenarios with nonzero aQGCs,

149 one with  $f_{T8}/\Lambda^4 = 1 \text{TeV}^{-4}$ , the other with  $f_{T9}/\Lambda^4 = 2 \text{TeV}^{-4}$ . In the aQGC search, a

150 unitarity bound is imposed, chosen with VBFNLO [226] to be the value of  $m_{ZZ}$  at which

151 the scattering amplitude would violate unitarity if the aQGC parameter in question

152 were set to its 95% CL limit value. While limits are set for each parameter, all other

153 parameters and their unitarity bounds are set to zero. The observed 95% CL limits

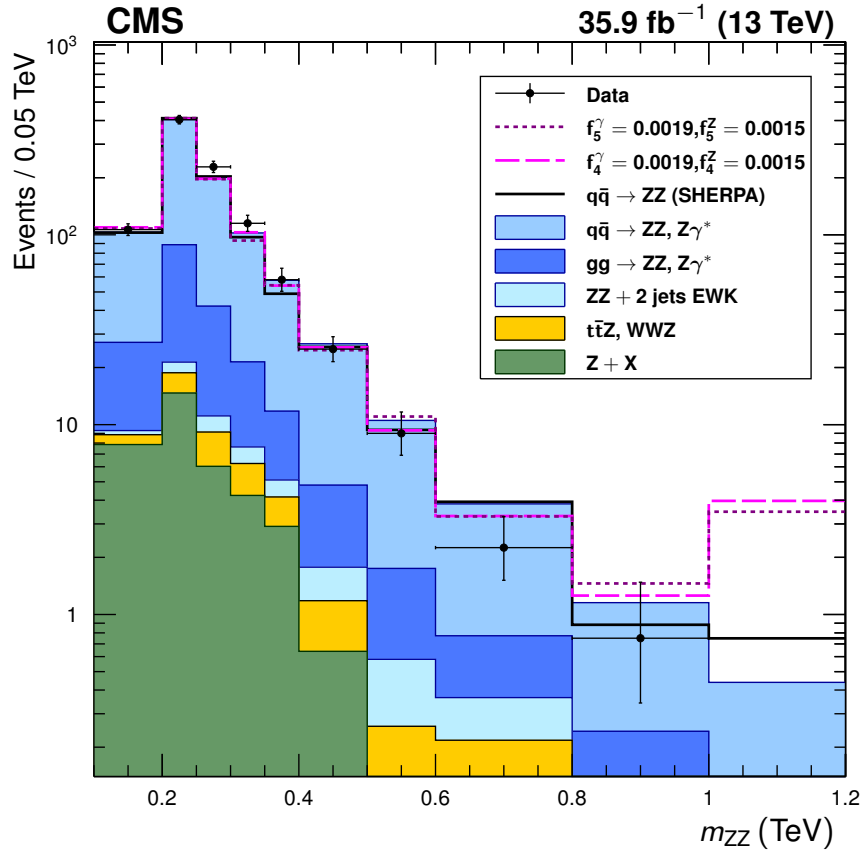


Figure 7.32: Distribution of ZZ invariant mass for all events in the on-shell selection. Points represent data, with statistical uncertainty bars. The stack of filled histograms represents the SM signal prediction and background estimate. The unfilled histograms represent two example SHERPA predictions for nonzero aTGC hypotheses (dashed) and the SHERPA SM prediction (solid), included to illustrate the shape differences between the SHERPA and POWHEG+MCFM SM predictions. The SHERPA distributions are normalized such that the SM prediction's total yield matches that of the other generators. The last bin includes the overflow contributions from events at masses above 1.2 TeV.

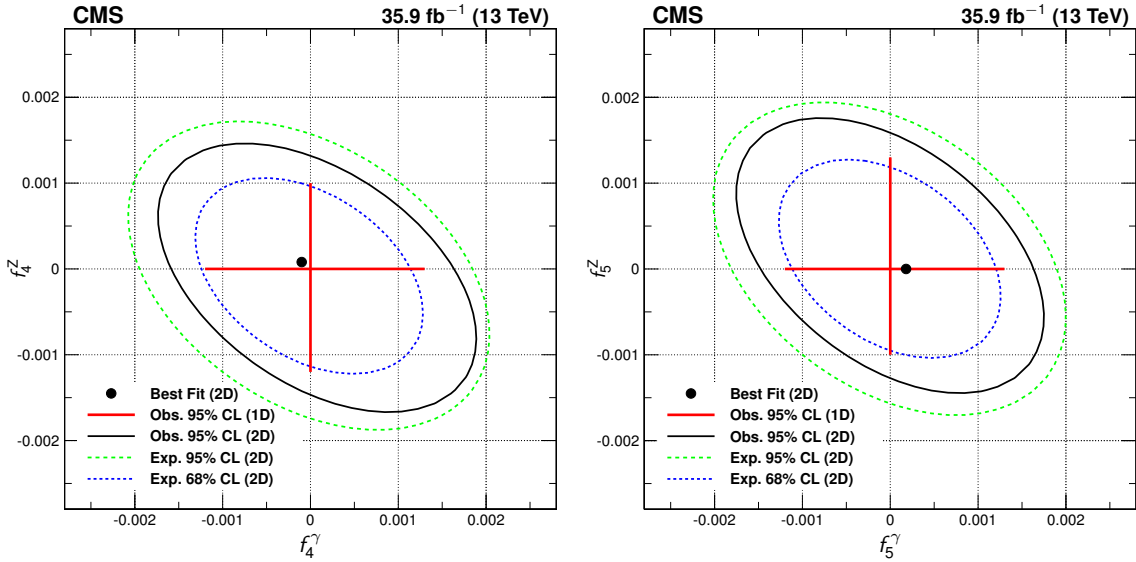


Figure 7.33: Two-dimensional observed 95% CL limits (solid contour) and expected 68 and 95% CL limits (dashed contours) in the  $f_4^\gamma$ - $f_4^Z$  (left) and  $f_5^\gamma$ - $f_5^Z$  (right) planes. The regions outside the contours are excluded at the corresponding confidence level. The dot is the point of maximum likelihood in the two-dimensional fits. Solid, straight lines at the center show the observed one-dimensional 95% CL limits for  $f_{4,5}^\gamma$  (horizontal) and  $f_{4,5}^Z$  (vertical). No form factor is used.

154 on the coefficients of the effective field theory operators covering ZZjj production  
155 are

$$\begin{aligned}
 -0.46 &< f_{T0}/\Lambda^4 < 0.44 \text{ TeV}^{-4}, \\
 -0.61 &< f_{T1}/\Lambda^4 < 0.61 \text{ TeV}^{-4}, \\
 -1.2 &< f_{T2}/\Lambda^4 < 1.2 \text{ TeV}^{-4}, \\
 -0.84 &< f_{T8}/\Lambda^4 < 0.84 \text{ TeV}^{-4}, \\
 -1.8 &< f_{T9}/\Lambda^4 < 1.8 \text{ TeV}^{-4}.
 \end{aligned} \tag{7.12}$$

156 These are the most stringent constraints to date on all five parameters, improving on  
157 the previous best by factors of 2–8 (see Section 2.3.1). This is the first time any of  
158 them have been measured in the ZZjj channel.

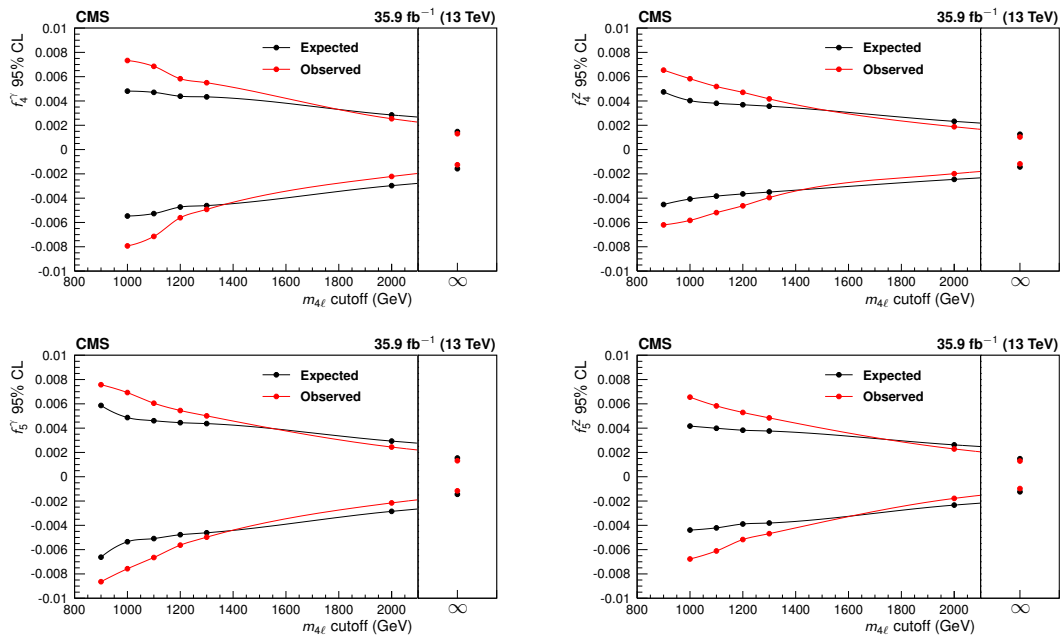


Figure 7.34: Expected and observed one-dimensional limits on the four aTGC parameters, as functions of the  $m_{ZZ}$  cutoff used to enforce unitarity. No form factor is used.

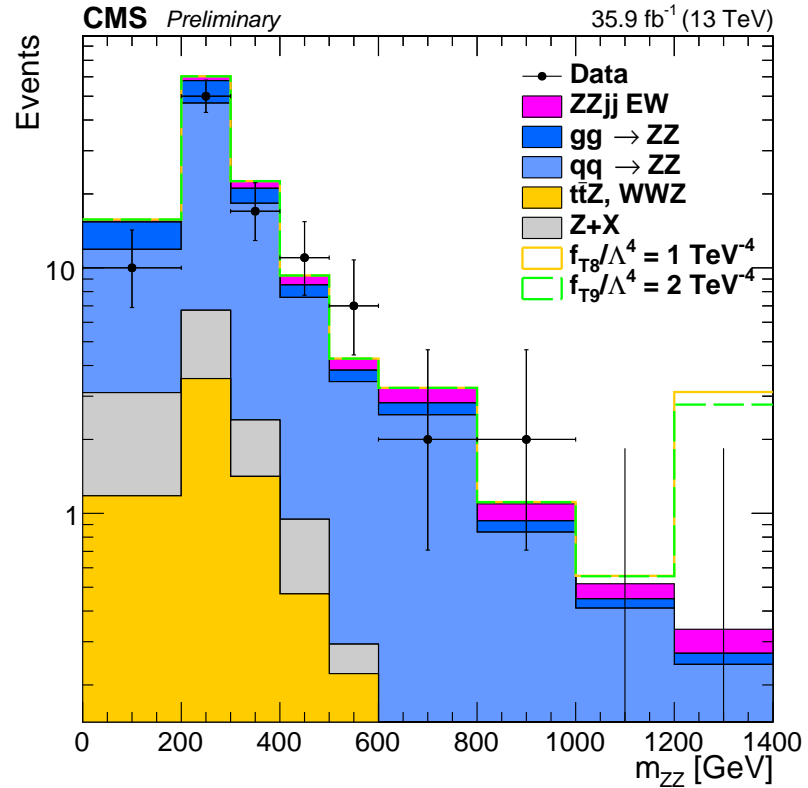


Figure 7.35: Distribution of ZZ invariant mass for events in the dijet selection. Points represent data, with statistical uncertainty bars. The stack of filled histograms represents the SM signal prediction and background estimate. The unfilled histograms represent two example MADGRAPH5\_AMC@NLO distributions for nonzero aQGC hypotheses. The last bin includes the overflow contributions from events at masses above 1.4 TeV.

## **0 Chapter 8**

# **1 Conclusions**

## **2 8.1 Summary**

3 Diboson studies in high-energy particle collisions are important probes of the elec-  
4 troweak sector of the standard model. In particular, measurements of  $ZZ$ ,  $ZZ^*$ ,  $Z\gamma^*$ ,  
5 and  $\gamma^*\gamma^*$  production shed light on the couplings between the neutral gauge bosons  
6 and on the details of electroweak symmetry breaking. Decays to four charged leptons  
7 (electrons or muons) are rare, but they can be easily identified and fully reconstructed,  
8 and they represent a clean channel with low backgrounds. The LHC at CERN has  
9 generated proton-proton collisions with a center-of-mass energy of 13 TeV at record-  
10 breaking luminosities, providing an unprecedented opportunity to study such pro-  
11 cesses. The CMS detector is well designed for these measurements and collected a  
12 high-quality dataset corresponding to an integrated luminosity of  $35.9 \text{ fb}^{-1}$ . Several  
13 studies of four-lepton production were performed with this dataset and reported here.

14 Because the four-lepton channel is so clean, event selections are loose and effi-  
15 ciencies are high. Most backgrounds are estimated from data. The full four-lepton  
16 spectrum includes resonant single-Z decays ( $\text{pp} \rightarrow Z \rightarrow \ell^+\ell^-\gamma^* \rightarrow 4\ell$ ), resonant Higgs

17 boson decays ( $\text{pp} \rightarrow \text{H} \rightarrow \text{ZZ}^* \rightarrow 4\ell$ ), continuum production of a single Z boson and a  
 18 nonresonant lepton pair ( $\text{pp} \rightarrow \text{Z}\gamma^* \rightarrow 4\ell$ ), and continuum production of two on-shell  
 19 ( $60 < m_{\ell\ell} < 120 \text{ GeV}$ ) Z bosons ( $\text{pp} \rightarrow \text{ZZ} \rightarrow 4\ell$ ).

20 Both inclusive and differential ZZ cross sections were measured. Inclusive cross  
 21 sections were measured with a signal strength found by a maximum likelihood fit.  
 22 The measured fiducial ZZ cross section, subject to the requirements of Table 6.2, is

$$\sigma_{\text{fid}}(\text{pp} \rightarrow \text{ZZ} \rightarrow 4\ell) = 40.9 \pm 1.3 \text{ (stat)} \pm 1.4 \text{ (syst)} \pm 1.0 \text{ (lumi)} \text{ fb}. \quad (8.1)$$

23 The total ZZ cross section, subject only to the constraint that both Z bosons be on-  
 24 shell, was extrapolated with an acceptance correction and combined with the smaller  
 25 ( $2.9 \text{ fb}^{-1}$ ) dataset collected in 2015. Its measured value is

$$\sigma(\text{pp} \rightarrow \text{ZZ}) = 17.2 \pm 0.5 \text{ (stat)} \pm 0.7 \text{ (syst)} \pm 0.4 \text{ (theo)} \pm 0.4 \text{ (lumi)} \text{ pb}. \quad (8.2)$$

26 The  $Z \rightarrow 4\ell$  branching fraction was measured for events with  $80 < m_{4\ell} < 100 \text{ GeV}$   
 27 and a requirement of  $m_{\ell\ell} > 4 \text{ GeV}$  for all opposite-sign, same-flavor lepton pairs, and  
 28 found to be

$$\mathcal{B}(Z \rightarrow 4\ell) = 4.8 \pm 0.2 \text{ (stat)} \pm 0.2 \text{ (syst)} \pm 0.1 \text{ (theo)} \pm 0.1 \text{ (lumi)} \times 10^{-6}. \quad (8.3)$$

29 Differential cross sections were measured as functions of a number of observables  
 30 including fully leptonic kinematic variables and quantities related to the production  
 31 of associated jets. All results are in agreement with SM predictions.

32 A search was performed for fully electroweak ZZjj production using a gradient-  
 33 boosted decision tree. An excess consistent with VBS was found at the level of 2.7  
 34 standard deviations above the null hypothesis ( $1.6\sigma$  expected). This corresponds to  
 35 a measured electroweak fiducial cross section of

$$\sigma_{\text{fid}}(\text{pp} \rightarrow \text{ZZjj(EWK)} \rightarrow 4\ell\text{jj}) = 0.40^{+0.21}_{-0.16} \text{ (stat)}^{+0.13}_{-0.09} \text{ (syst)} \text{ fb}, \quad (8.4)$$

36 consistent with SM predictions.

37 Searches were performed for anomalous triple and quartic gauge couplings. The  
 38 aTGC search, considered in an effective lagrangian framework, used the invariant  
 39 mass of inclusive ZZ events to set the most stringent 95% CL limits to date on ZZZ  
 40 and ZZ $\gamma$  couplings,

$$\begin{aligned} -0.0012 < f_4^Z < 0.0010, \quad -0.0010 < f_5^Z < 0.0013, \\ -0.0012 < f_4^\gamma < 0.0013, \quad -0.0012 < f_5^\gamma < 0.0013. \end{aligned} \tag{8.5}$$

41 Two-dimensional limits were also set. The aQGC search, performed in an effective  
 42 field theory parameterization with ZZjj events, set the most stringent 95% CL limits  
 43 to date on several dimension-8 operators which govern quartic gauge couplings,

$$\begin{aligned} -0.46 &< f_{T0}/\Lambda^4 &< 0.44 \text{ TeV}^{-4}, \\ -0.61 &< f_{T1}/\Lambda^4 &< 0.61 \text{ TeV}^{-4}, \\ -1.2 &< f_{T2}/\Lambda^4 &< 1.2 \text{ TeV}^{-4}, \\ -0.84 &< f_{T8}/\Lambda^4 &< 0.84 \text{ TeV}^{-4}, \\ -1.8 &< f_{T9}/\Lambda^4 &< 1.8 \text{ TeV}^{-4}. \end{aligned} \tag{8.6}$$

## 44 8.2 Outlook

45 Diboson measurements have great potential to shed further light on the SM or find  
 46 deviations from it. In the long term, cross section measurements at higher center-  
 47 of-mass energies are of great interest because new physics should be most obvious at  
 48 high  $\sqrt{s}$ . With no new colliders expected in the near future<sup>1</sup>, progress will first come  
 49 in the form of precision measurements of processes that are in principle accessible  
 50 now. The statistical uncertainties of the measured inclusive cross sections are now

---

<sup>1</sup>The LHC may operate at  $\sqrt{s} = 14$  TeV in the near future, which would be useful but only marginally more likely to reveal new physics, in line with the marginal increase in energy.

51 comparable to or smaller than the systematic uncertainties, and systematics should  
52 dominate after the inclusion of data collected in 2017, even if new techniques are  
53 developed which reduce lepton efficiency and trigger uncertainties somewhat. Un-  
54 certainty reductions that can be expected in the short term will make the inclusive  
55 measurements somewhat more useful—experimental uncertainties will be comparable  
56 to or smaller than theoretical uncertainties, allowing further theoretical improvements  
57 to be of interest—but the improvements will overall be limited by the difficulty of  
58 reducing systematics in the highly active environments envisioned for future LHC  
59 runs.

60 Differential cross sections and searches, however, will be statistically limited for  
61 some time and will benefit greatly from additional luminosity at  $\sqrt{s} = 13$  TeV. Sta-  
62 tistical uncertainties dominate in almost all bins in the differential cross sections.  
63 Assuming no deviations from the SM, data collected in 2017 will likely be enough to  
64 allow  $3\sigma$  evidence for VBS, when added to the 2016 data presented here. The statisti-  
65 cal power for the aGC searches comes largely from the highest-mass bins, where very  
66 few events have been observed—only three above 800 GeV and none above 1 TeV,  
67 even in the inclusive selection. Further data collection will improve these limits sub-  
68 stantially and place stringent restrictions on BSM neutral gauge boson couplings—or  
69 discover them.

# 70 Bibliography

- 71 [1] D. J. Griffiths, *Introduction to elementary particles; 2nd rev. version*, ser.  
72 Physics textbook. New York, NY: Wiley, 2008.
- 73 [2] F. Halzen and A. Martin, *Quarks & Leptons: An introductory course in*  
74 *modern particle physics*. New York, USA: John Wiley & Sons, 1984.
- 75 [3] V. Barger and R. Phillips, *Collider Physics*, ser. Frontiers in physics. Avalon  
76 Publishing, 1997, ISBN: 9780201149456.
- 77 [4] M. E. Peskin and D. V. Schroeder, *An Introduction to quantum field theory*.  
78 Reading, USA: Addison-Wesley, 1995, ISBN: 9780201503975, 0201503972.
- 79 [5] J. F. Donoghue, E. Golowich, and B. R. Holstein, *Dynamics of the Standard*  
80 *Model*, ser. Cambridge monographs on particle physics, nuclear physics, and  
81 cosmology. Cambridge: Cambridge Univ. Press, 1992.
- 82 [6] O. W. Greenberg, “Spin and unitary-spin independence in a paraquark  
83 model of baryons and mesons,” *Phys. Rev. Lett.*, vol. 13, p. 598, 20 1964.  
84 DOI: 10.1103/PhysRevLett.13.598. <https://link.aps.org/doi/10.1103/PhysRevLett.13.598>.
- 86 [7] S. L. Glashow, “Quarks with color and flavor,” *Scientific American*, vol. 233,  
87 p. 38, 1975. <http://www.jstor.org/stable/24949915>.
- 88 [8] Super-Kamiokande Collaboration, “Evidence for oscillation of atmospheric  
89 neutrinos,” *Phys. Rev. Lett.*, vol. 81, pp. 1562–1567, 1998. DOI: 10.1103/  
90 PhysRevLett.81.1562. arXiv: [hep-ex/9807003](https://arxiv.org/abs/hep-ex/9807003) [hep-ex].
- 91 [9] SNO Collaboration, “Measurement of the rate of  $\nu_e + d \rightarrow p + p + e^-$  interac-  
92 tions produced by  $^8B$  solar neutrinos at the Sudbury Neutrino Observatory,”  
93 *Phys. Rev. Lett.*, vol. 87, p. 071301, 2001. DOI: 10.1103/PhysRevLett.87.  
94 071301. arXiv: [nucl-ex/0106015](https://arxiv.org/abs/nucl-ex/0106015) [nucl-ex].

- 95 [10] SNO Collaboration, “Direct evidence for neutrino flavor transformation from  
96 neutral current interactions in the Sudbury Neutrino Observatory,” *Phys. Rev.*  
97 *Lett.*, vol. 89, p. 011301, 2002. DOI: 10.1103/PhysRevLett.89.011301. arXiv:  
98 nucl-ex/0204008 [nucl-ex].
- 99 [11] Particle Data Group, C. Patrignani, *et al.*, “Review of particle physics,”  
100 *Chin. Phys. C*, vol. 40, no. 10, p. 100001, 2016. DOI: 10.1088/1674-1137/  
101 40/10/100001.
- 102 [12] N. Cabibbo, “Unitary symmetry and leptonic decays,” *Phys. Rev. Lett.*, vol.  
103 10, p. 531, 1963. DOI: 10.1103/PhysRevLett.10.531.
- 104 [13] M. Kobayashi and T. Maskawa, “CP-violation in the renormalizable theory  
105 of weak interaction,” *Progress of Theoretical Physics*, vol. 49, no. 2, p. 652,  
106 1973. DOI: 10.1143/PTP.49.652.
- 107 [14] J. H. Christenson, J. W. Cronin, V. L. Fitch, and R. Turlay, “Evidence for  
108 the  $2\pi$  decay of the  $K_2^0$  meson,” *Phys. Rev. Lett.*, vol. 13, p. 138, 4 Jul. 1964.  
109 DOI: 10.1103/PhysRevLett.13.138.
- 110 [15] KTeV Collaboration, “Observation of direct CP violation in  $K_{S,L} \rightarrow \pi\pi$   
111 decays,” *Phys. Rev. Lett.*, vol. 83, p. 22, 1999. DOI: 10.1103/PhysRevLett.  
112 83.22. arXiv: hep-ex/9905060 [hep-ex].
- 113 [16] NA48 Collaboration, “A new measurement of direct CP violation in two  
114 pion decays of the neutral kaon,” *Phys. Lett. B*, vol. 465, p. 335, 1999. DOI:  
115 10.1016/S0370-2693(99)01030-8. arXiv: hep-ex/9909022 [hep-ex].
- 116 [17] BaBar Collaboration, “Measurement of CP violating asymmetries in  $B^0$   
117 decays to CP eigenstates,” *Phys. Rev. Lett.*, vol. 86, p. 2515, 2001. DOI: 10.  
118 1103/PhysRevLett.86.2515. arXiv: hep-ex/0102030 [hep-ex].
- 119 [18] Belle Collaboration, “Observation of large CP violation in the neutral  $B$   
120 meson system,” *Phys. Rev. Lett.*, vol. 87, p. 091802, 2001. DOI: 10.1103/  
121 PhysRevLett.87.091802. arXiv: hep-ex/0107061 [hep-ex].
- 122 [19] LHCb Collaboration, “Observation of CP violation in  $B^\pm \rightarrow D K^\pm$  de-  
123 cays,” *Phys. Lett. B*, vol. 712, p. 203, 2012, [Corrigendum: DOI: 110.1016/j.  
124 physletb.2012.05.060]. DOI: 10.1016/j.physletb.2012.04.060. arXiv:  
125 1203.3662 [hep-ex].

- 126 [20] LHCb Collaboration, “First observation of CP violation in the decays of  $B_s^0$   
127 mesons,” *Phys. Rev. Lett.*, vol. 110, no. 22, p. 221601, 2013. DOI: 10.1103/  
128 PhysRevLett.110.221601. arXiv: 1304.6173 [hep-ex].
- 129 [21] E. Noether, “Invariant variation problems,” trans. by M. A. Tavel, *Gott.  
130 Nachr.*, p. 235, 1918, [*Transp. Theory Statist. Phys.*, vol. 1, p. 186, 1971]. DOI:  
131 10.1080/00411457108231446. arXiv: physics/0503066 [physics].
- 132 [22] M. Srednicki, *Quantum Field Theory*. Cambridge: Cambridge Univ. Press,  
133 2007.
- 134 [23] S. L. Glashow, “Partial symmetries of weak interactions,” *Nucl. Phys.*, vol.  
135 22, p. 579, 1961. DOI: 10.1016/0029-5582(61)90469-2.
- 136 [24] S. Weinberg, “A model of leptons,” *Phys. Rev. Lett.*, vol. 19, p. 1264, 1967.  
137 DOI: 10.1103/PhysRevLett.19.1264.
- 138 [25] A. Salam, “Weak and electromagnetic interactions,” *Conf. Proc.*, vol. C680-  
139 519, p. 367, 1968.
- 140 [26] F. Englert and R. Brout, “Broken symmetry and the mass of gauge vec-  
141 tor mesons,” *Phys. Rev. Lett.*, vol. 13, p. 321, 9 Aug. 1964. DOI: 10.1103/  
142 PhysRevLett.13.321. <https://link.aps.org/doi/10.1103/PhysRevLett.13.321>.
- 144 [27] P. W. Higgs, “Broken symmetries and the masses of gauge bosons,” *Phys.  
145 Rev. Lett.*, vol. 13, p. 508, 16 Oct. 1964. DOI: 10.1103/PhysRevLett.13.508.  
146 <https://link.aps.org/doi/10.1103/PhysRevLett.13.508>.
- 147 [28] G. S. Guralnik, C. R. Hagen, and T. W. B. Kibble, “Global conservation  
148 laws and massless particles,” *Phys. Rev. Lett.*, vol. 13, p. 585, 20 Nov. 1964.  
149 DOI: 10.1103/PhysRevLett.13.585. <https://link.aps.org/doi/10.1103/PhysRevLett.13.585>.
- 151 [29] A. Alboteanu, W. Kilian, and J. Reuter, “Resonances and unitarity in weak  
152 boson scattering at the LHC,” *JHEP*, vol. 11, p. 010, 2008. DOI: 10.1088/  
153 1126-6708/2008/11/010. arXiv: 0806.4145 [hep-ph].
- 154 [30] V. C. Rubin, “Dark matter in spiral galaxies,” *Scientific American*, vol. 248,  
155 p. 96, 1983. DOI: 10.1038/scientificamerican0683-96.
- 156 [31] K. Garrett and G. Duda, “Dark matter: a primer,” *Adv. Astron.*, vol. 2011,  
157 p. 968283, 2011. DOI: 10.1155/2011/968283. arXiv: 1006.2483 [hep-ph].

- 158 [32] J. Ellis, “Searching for particle physics beyond the standard model at the  
159 LHC and elsewhere,” *AIP Conf. Proc.*, vol. 1446, p. 9, 2012. DOI: 10.1063/  
160 1.4727987. arXiv: 1102.5009 [hep-ph].
- 161 [33] H. Georgi, H. R. Quinn, and S. Weinberg, “Hierarchy of interactions in  
162 unified gauge theories,” *Phys. Rev. Lett.*, vol. 33, p. 451, 1974. DOI: 10.1103/  
163 PhysRevLett.33.451.
- 164 [34] E. Gildener, “Gauge symmetry hierarchies,” *Phys. Rev. D*, vol. 14, p. 1667,  
165 1976. DOI: 10.1103/PhysRevD.14.1667.
- 166 [35] A. J. Buras, J. R. Ellis, M. K. Gaillard, and D. V. Nanopoulos, “Aspects of  
167 the grand unification of strong, weak and electromagnetic interactions,” *Nucl.  
168 Phys. B*, vol. 135, p. 66, 1978. DOI: 10.1016/0550-3213(78)90214-6.
- 169 [36] S. Mele, “The measurement of the number of light neutrino species at LEP,”  
170 *Adv. Ser. Direct. High Energy Phys.*, vol. 23, p. 89, 2015. DOI: 10.1142/  
171 9789814644150\_0004. <http://cds.cern.ch/record/2103251>.
- 172 [37] S. P. Martin, “A supersymmetry primer,” in *Perspectives on Supersymmetry  
173 II*. DOI: 10.1142/9789814307505\_0001. arXiv: hep-ph/9709356 [hep-ph].
- 174 [38] C. Autermann, “Experimental status of supersymmetry after the LHC run-  
175 I,” *Prog. Part. Nucl. Phys.*, vol. 90, p. 125, 2016. DOI: 10.1016/j.ppnp.2016.  
176 06.001. arXiv: 1609.01686 [hep-ex].
- 177 [39] H. Georgi and S. L. Glashow, “Unity of all elementary particle forces,” *Phys.  
178 Rev. Lett.*, vol. 32, p. 438, 1974. DOI: 10.1103/PhysRevLett.32.438.
- 179 [40] K. Hagiwara, R. D. Peccei, D. Zeppenfeld, and K. Hikasa, “Probing the weak  
180 boson sector in  $e^+e^- \rightarrow W^+W^-$ ,” *Nucl. Phys. B*, vol. 282, p. 253, 1987. DOI:  
181 10.1016/0550-3213(87)90685-7.
- 182 [41] G. J. Gounaris, J. Layssac, and F. M. Renard, “New and standard physics  
183 contributions to anomalous Z and  $\gamma$  self-couplings,” *Phys. Rev. D*, vol. 62,  
184 p. 073013, 2000. DOI: 10.1103/PhysRevD.62.073013. arXiv: hep-ph/  
185 0003143 [hep-ph].
- 186 [42] U. Baur and D. L. Rainwater, “Probing neutral gauge boson self-interactions  
187 in ZZ production at hadron colliders,” *Phys. Rev. D*, vol. 62, p. 113011, 2000.  
188 DOI: 10.1103/PhysRevD.62.113011. arXiv: hep-ph/0008063 [hep-ph].

- 189 [43] U. Baur and E. L. Berger, “Probing the weak boson sector in  $Z\gamma$  production  
 190 at hadron colliders,” *Phys. Rev. D*, vol. 47, p. 4889, 1993. DOI: 10.1103/  
 191 PhysRevD.47.4889.
- 192 [44] C. Degrande, N. Greiner, W. Kilian, O. Mattelaer, H. Mebane, T. Stelzer,  
 193 S. Willenbrock, and C. Zhang, “Effective field theory: a modern approach to  
 194 anomalous couplings,” *Annals Phys.*, vol. 335, p. 21, 2013. DOI: 10.1016/j.  
 195 aop.2013.04.016. arXiv: 1205.4231 [hep-ph].
- 196 [45] O. J. P. Éboli, M. C. Gonzalez-Garcia, and J. K. Mizukoshi, “ $pp \rightarrow jj e^\pm \mu^\pm \nu\nu$   
 197 and  $jje^\pm \mu^\mp \nu\nu$  at  $\mathcal{O}(\alpha_{em}^6)$  and  $\mathcal{O}(\alpha_{em}^4 \alpha_s^2)$  for the study of the quartic electroweak  
 198 gauge boson vertex at LHC,” *Phys. Rev. D*, vol. 74, p. 073005, 2006. DOI:  
 199 10.1103/PhysRevD.74.073005. arXiv: hep-ph/0606118 [hep-ph].
- 200 [46] NNPDF Collaboration, “Parton distributions from high-precision collider  
 201 data,” 2017. arXiv: 1706.00428 [hep-ph].
- 202 [47] A. Lazopoulos, K. Melnikov, and F. Petriello, “QCD corrections to tri-boson  
 203 production,” *Phys. Rev. D*, vol. 76, p. 014001, 2007. DOI: 10.1103/PhysRevD.  
 204 76.014001. arXiv: hep-ph/0703273 [hep-ph].
- 205 [48] T. Binoth, G. Ossola, C. G. Papadopoulos, and R. Pittau, “NLO QCD  
 206 corrections to tri-boson production,” *JHEP*, vol. 06, p. 082, 2008. DOI: 10.  
 207 1088/1126-6708/2008/06/082. arXiv: 0804.0350 [hep-ph].
- 208 [49] V. Hankele and D. Zeppenfeld, “QCD corrections to hadronic  $wwz$  production  
 209 with leptonic decays,” *Phys. Lett. B*, vol. 661, p. 103, 2008. DOI: 10.1016/j.  
 210 physletb.2008.02.014. arXiv: 0712.3544 [hep-ph].
- 211 [50] F. J. Hasert *et al.*, “Search for elastic  $\nu_\mu$  electron scattering,” *Phys. Lett. B*,  
 212 vol. 46, p. 121, 1973. DOI: 10.1016/0370-2693(73)90494-2.
- 213 [51] UA1 Collaboration, “Experimental observation of lepton pairs of invariant  
 214 mass around  $95 \text{ GeV}/c^2$  at the CERN SPS collider,” *Phys. Lett. B*, vol. 126,  
 215 p. 398, 1983. DOI: 10.1016/0370-2693(83)90188-0.
- 216 [52] SLD Electroweak Group, DELPHI Collaboration, ALEPH Collaboration,  
 217 SLD Collaboration, SLD Heavy Flavour Group, OPAL Collaboration, LEP  
 218 Electroweak Working Group, L3 Collaboration, “Precision electroweak mea-  
 219 surements on the  $Z$  resonance,” *Phys. Rept.*, vol. 427, p. 257, 2006. DOI: 10.  
 220 1016/j.physrep.2005.12.006. arXiv: hep-ex/0509008 [hep-ex].

- 221 [53] J. M. Campbell and R. K. Ellis, “An update on vector boson pair production  
222 at hadron colliders,” *Phys. Rev. D*, vol. 60, p. 113 006, 1999. DOI: 10.1103/  
223 PhysRevD.60.113006. arXiv: hep-ph/9905386 [hep-ph].
- 224 [54] J. M. Campbell, R. K. Ellis, and C. Williams, “Vector boson pair production  
225 at the LHC,” *JHEP*, vol. 07, p. 018, 2011. DOI: 10.1007/JHEP07(2011)018.  
226 arXiv: 1105.0020 [hep-ph].
- 227 [55] T. Melia, P. Nason, R. Röntsch, and G. Zanderighi, “ $W^+W^-$ ,  $WZ$  and  $ZZ$   
228 production in the POWHEG BOX,” *JHEP*, vol. 11, p. 078, 2011. DOI: 10.1007/  
229 JHEP11(2011)078. arXiv: 1107.5051 [hep-ph].
- 230 [56] F. Cascioli, T. Gehrmann, M. Grazzini, S. Kallweit, P. Maierhöfer, A. von  
231 Manteuffel, S. Pozzorini, D. Rathlev, L. Tancredi, and E. Weihs, “ $ZZ$  produc-  
232 tion at hadron colliders in NNLO QCD,” *Phys. Lett. B*, vol. 735, p. 311, 2014.  
233 DOI: 10.1016/j.physletb.2014.06.056. arXiv: 1405.2219 [hep-ph].
- 234 [57] F. Caola, K. Melnikov, R. Röntsch, and L. Tancredi, “QCD corrections to  
235  $ZZ$  production in gluon fusion at the LHC,” *Phys. Rev. D*, vol. 92, p. 094 028,  
236 2015. DOI: 10.1103/PhysRevD.92.094028. arXiv: 1509.06734 [hep-ph].
- 237 [58] D. Rainwater, R. Szalapski, and D. Zeppenfeld, “Probing color-singlet ex-  
238 change in  $Z + 2$ -jet events at the CERN LHC,” *Phys. Rev. D*, vol. 54, p. 6680,  
239 11 Dec. 1996. DOI: 10.1103/PhysRevD.54.6680.
- 240 [59] Sjöstrand, Torbjörn and Ask, Stefan and Christiansen, Jesper R. and Corke,  
241 Richard and Desai, Nishita and Ilten, Philip and Mrenna, Stephen and Prestel,  
242 Stefan and Rasmussen, Christine O. and Skands, Peter Z., “An introduction  
243 to PYTHIA 8.2,” *Comput. Phys. Commun.*, vol. 191, p. 159, 2015. DOI: 10.  
244 1016/j.cpc.2015.01.024. arXiv: 1410.3012 [hep-ph].
- 245 [60] C. Bierlich and J. R. Christiansen, “Effects of color reconnection on hadron  
246 flavor observables,” *Phys. Rev. D*, vol. 92, p. 094 010, 2015. DOI: 10.1103/  
247 PhysRevD.92.094010. arXiv: 1507.02091 [hep-ph].
- 248 [61] ALEPH Collaboration, “Measurement of the  $e^+e^- \rightarrow ZZ$  production cross-  
249 section at center-of-mass energies of 183 GeV and 189 GeV,” *Phys. Lett. B*,  
250 vol. 469, p. 287, 1999. DOI: 10.1016/S0370-2693(99)01288-5. arXiv: hep-  
251 ex/9911003 [hep-ex].
- 252 [62] OPAL Collaboration, “ $Z$  boson pair production in  $e^+e^-$  collisions at  $\sqrt{s} =$   
253 183 GeV and 189 GeV,” *Phys. Lett. B*, vol. 476, p. 256, 2000. DOI: 10.1016/  
254 S0370-2693(00)00197-0. arXiv: hep-ex/0003016 [hep-ex].

- 255 [63] L3 Collaboration, “Z boson pair production at LEP,” *Phys. Lett. B*, vol.  
256 572, p. 133, 2003. DOI: [10.1016/j.physletb.2003.08.023](https://doi.org/10.1016/j.physletb.2003.08.023). arXiv: [hep-ex/0308013](https://arxiv.org/abs/hep-ex/0308013) [hep-ex].
- 258 [64] DELPHI Collaboration, “ZZ production in  $e^+e^-$  interactions at  $\sqrt{s} = 183 - 209$  GeV,” *Eur. Phys. J. C*, vol. 30, p. 447, 2003. DOI: [10.1140/epjc/s2003-01287-0](https://doi.org/10.1140/epjc/s2003-01287-0). arXiv: [hep-ex/0307050](https://arxiv.org/abs/hep-ex/0307050) [hep-ex].
- 261 [65] OPAL Collaboration, “Study of Z pair production and anomalous couplings  
262 in  $e^+e^-$  collisions at  $\sqrt{s}$  between 190 GeV and 209 GeV,” *Eur. Phys. J. c*, vol.  
263 32, p. 303, 2003. DOI: [10.1140/epjc/s2003-01467-x](https://doi.org/10.1140/epjc/s2003-01467-x). arXiv: [hep-ex/0310013](https://arxiv.org/abs/hep-ex/0310013)  
264 [hep-ex].
- 265 [66] ALEPH Collaboration, “Measurement of Z-pair production in  $e^+e^-$  collisions  
266 and constraints on anomalous neutral gauge couplings,” *JHEP*, vol. 04, p. 124,  
267 2009. DOI: [10.1088/1126-6708/2009/04/124](https://doi.org/10.1088/1126-6708/2009/04/124).
- 268 [67] CDF Collaboration, “First measurement of ZZ production in  $\bar{p}p$  collisions at  
269  $\sqrt{s} = 1.96$  TeV,” *Phys. Rev. Lett.*, vol. 100, p. 201801, 2008. DOI: [10.1103/PhysRevLett.100.201801](https://doi.org/10.1103/PhysRevLett.100.201801). arXiv: [0801.4806](https://arxiv.org/abs/0801.4806) [hep-ex].
- 271 [68] D0 Collaboration, “ $ZZ \rightarrow \ell^+\ell^-\nu\bar{\nu}$  production in  $p\bar{p}$  collisions at  $\sqrt{s} =$   
272  $1.96$  TeV,” *Phys. Rev. D*, vol. 78, p. 072002, 2008. DOI: [10.1103/PhysRevD.78.072002](https://doi.org/10.1103/PhysRevD.78.072002). arXiv: [0808.0269](https://arxiv.org/abs/0808.0269) [hep-ex].
- 274 [69] D0 Collaboration, “Observation of ZZ production in  $p\bar{p}$  collisions at  $\sqrt{s} =$   
275  $1.96$  TeV,” *Phys. Rev. Lett.*, vol. 101, p. 171803, 2008, DOI: [10.1103/PhysRevLett.101.171803](https://doi.org/10.1103/PhysRevLett.101.171803). arXiv: [0808.0703](https://arxiv.org/abs/0808.0703) [hep-ex].
- 277 [70] D0 Collaboration, “Measurement of the ZZ production cross section in  $p\bar{p}$   
278 collisions at  $\sqrt{s} = 1.96$  TeV,” *Phys. Rev. D*, vol. 84, p. 011103, 2011. DOI:  
279 [10.1103/PhysRevD.84.011103](https://doi.org/10.1103/PhysRevD.84.011103). arXiv: [1104.3078](https://arxiv.org/abs/1104.3078) [hep-ex].
- 280 [71] CDF Collaboration, “Measurement of ZZ production in leptonic final states  
281 at  $\sqrt{s}$  of 1.96 TeV at CDF,” *Phys. Rev. Lett.*, vol. 108, p. 101801, 2012. DOI:  
282 [10.1103/PhysRevLett.108.101801](https://doi.org/10.1103/PhysRevLett.108.101801). arXiv: [1112.2978](https://arxiv.org/abs/1112.2978) [hep-ex].
- 283 [72] CMS Collaboration, “Measurement of the ZZ production cross section and  
284 search for anomalous couplings in  $2\ell 2\ell'$  final states in pp collisions at  $\sqrt{s} =$   
285  $7$  TeV,” *JHEP*, vol. 01, p. 063, 2013. DOI: [10.1007/JHEP01\(2013\)063](https://doi.org/10.1007/JHEP01(2013)063). arXiv:  
286 [1211.4890](https://arxiv.org/abs/1211.4890) [hep-ex].

- 287 [73] CMS Collaboration, “Measurement of the  $\text{pp} \rightarrow \text{ZZ}$  production cross section  
288 and constraints on anomalous triple gauge couplings in four-lepton final states  
289 at  $\sqrt{s} = 8 \text{ TeV}$ ,” *Phys. Lett. B*, vol. 740, p. 250, 2015, [Corrigendum: DOI: 10.  
290 1016/j.physletb.2016.04.010]. DOI: 10.1016/j.physletb.2014.11.059.  
291 arXiv: 1406.0113 [hep-ex].
- 292 [74] CMS Collaboration, “Measurements of the ZZ production cross sections in the  
293  $2\ell 2\nu$  channel in proton–proton collisions at  $\sqrt{s} = 7$  and 8 TeV and combined  
294 constraints on triple gauge couplings,” *Eur. Phys. J. C*, vol. 75, no. 10, p. 511,  
295 2015. DOI: 10.1140/epjc/s10052-015-3706-0. arXiv: 1503.05467 [hep-ex].
- 296 [75] CMS Collaboration Collaboration, “Measurement of the differential cross  
297 sections for pairs of Z bosons produced in association with jets in pp collisions  
298 at  $\sqrt{s} = 8 \text{ TeV}$ ,” CERN, Geneva, Tech. Rep. CMS-PAS-SMP-15-012, 2016.  
299 <https://cds.cern.ch/record/2209215>.
- 300 [76] ATLAS Collaboration, “Measurement of ZZ production in pp collisions at  
301  $\sqrt{s} = 7 \text{ TeV}$  and limits on anomalous zzz and ZZ $\gamma$  couplings with the ATLAS  
302 detector,” *JHEP*, vol. 03, p. 128, 2013. DOI: 10.1007/JHEP03(2013)128.  
303 arXiv: 1211.6096 [hep-ex].
- 304 [77] ATLAS Collaboration, “Measurements of four-lepton production in pp colli-  
305 sions at  $\sqrt{s} = 8 \text{ TeV}$  with the ATLAS detector,” *Phys. Lett. B*, vol. 753, p. 552,  
306 2016. DOI: 10.1016/j.physletb.2015.12.048. arXiv: 1509.07844 [hep-ex].
- 307 [78] ATLAS Collaboration, “Measurement of the ZZ production cross section  
308 in proton-proton collisions at  $\sqrt{s} = 8 \text{ TeV}$  using the  $\text{ZZ} \rightarrow \ell^-\ell^+\ell^-\ell^+$  and  
309  $\text{ZZ} \rightarrow \ell^-\ell^+\nu\bar{\nu}$  channels with the ATLAS detector,” *JHEP*, vol. 01, p. 099,  
310 2017. DOI: 10.1007/JHEP01(2017)099. arXiv: 1610.07585 [hep-ex].
- 311 [79] CMS Collaboration, “Measurement of the  $\text{pp} \rightarrow \text{ZZ}$  production cross section,  
312  $Z \rightarrow 4\ell$  branching fraction and constraints on anomalous triple gauge couplings  
313 at  $\sqrt{s} = 13 \text{ TeV}$ ,” 2017. <https://cds.cern.ch/record/2256100>.
- 314 [80] ATLAS Collaboration, “Evidence for electroweak production of  $\text{W}^\pm\text{W}^\pm\text{jj}$  in  
315 pp collisions at  $\sqrt{s} = 8 \text{ TeV}$  with the ATLAS detector,” *Phys. Rev. Lett.*, vol.  
316 113, no. 14, p. 141803, 2014. DOI: 10.1103/PhysRevLett.113.141803. arXiv:  
317 1405.6241 [hep-ex].
- 318 [81] CMS Collaboration, “Study of vector boson scattering and search for new  
319 physics in events with two same-sign leptons and two jets,” *Phys. Rev. Lett.*,  
320 vol. 114, no. 5, p. 051801, 2015. DOI: 10.1103/PhysRevLett.114.051801.  
321 arXiv: 1410.6315 [hep-ex].

- 322 [82] CMS Collaboration, “Measurement of the cross section for electroweak pro-  
323 duction of  $Z\gamma$  in association with two jets and constraints on anomalous qua-  
324 ratic gauge couplings in proton–proton collisions at  $\sqrt{s} = 8$  TeV,” *Phys. Lett.*  
325 *B*, vol. 770, p. 380, 2017. DOI: 10.1016/j.physletb.2017.04.071. arXiv:  
326 1702.03025 [hep-ex].
- 327 [83] ATLAS Collaboration, “Studies of  $Z\gamma$  production in association with a high-  
328 mass dijet system in pp collisions at  $\sqrt{s} = 8$  TeV with the ATLAS detector,”  
329 *JHEP*, vol. 07, p. 107, 2017. DOI: 10.1007/JHEP07(2017)107. arXiv: 1705.  
330 01966 [hep-ex].
- 331 [84] CMS Collaboration, “Measurement of electroweak-induced production of  
332  $W\gamma$  with two jets in pp collisions at  $\sqrt{s} = 8$  TeV and constraints on anom-  
333 alous quartic gauge couplings,” *JHEP*, vol. 06, p. 106, 2017. DOI: 10.1007/  
334 JHEP06(2017)106. arXiv: 1612.09256 [hep-ex].
- 335 [85] CMS Collaboration, “Evidence for exclusive  $\gamma\gamma \rightarrow W^+W^-$  production and  
336 constraints on anomalous quartic gauge couplings in pp collisions at  $\sqrt{s} = 7$   
337 and 8 TeV,” *JHEP*, vol. 08, p. 119, 2016. DOI: 10.1007/JHEP08(2016)119.  
338 arXiv: 1604.04464 [hep-ex].
- 339 [86] ATLAS Collaboration, “Measurement of exclusive  $\gamma\gamma \rightarrow W^+W^-$  production  
340 and search for exclusive Higgs boson production in pp collisions at  $\sqrt{s} = 8$  TeV  
341 using the ATLAS detector,” *Phys. Rev. D*, vol. 94, no. 3, p. 032011, 2016. DOI:  
342 10.1103/PhysRevD.94.032011. arXiv: 1607.03745 [hep-ex].
- 343 [87] CMS Collaboration Collaboration, “Observation of electroweak production  
344 of same-sign W boson pairs in the two jet and two same-sign lepton final state  
345 in proton-proton collisions at 13 TeV,” CERN, Geneva, Tech. Rep. CMS-PAS-  
346 SMP-17-004, 2017. <https://cds.cern.ch/record/2264525>.
- 347 [88] ALEPH Collaboration, “Study of the four fermion final state at the Z reso-  
348 nance,” *Z. Phys. C*, vol. 66, p. 3, 1995. DOI: 10.1007/BF01496576.
- 349 [89] CMS Collaboration, “Observation of Z decays to four leptons with the  
350 CMS detector at the LHC,” *JHEP*, vol. 12, p. 034, 2012. DOI: 10.1007/  
351 JHEP12(2012)034. arXiv: 1210.3844 [hep-ex].
- 352 [90] ATLAS Collaboration, “Measurements of four-lepton production at the Z  
353 resonance in pp collisions at  $\sqrt{s} = 7$  and 8 TeV with ATLAS,” *Phys. Rev. Lett.*,  
354 vol. 112, no. 23, p. 231806, 2014. DOI: 10.1103/PhysRevLett.112.231806.  
355 arXiv: 1403.5657 [hep-ex].

- 356 [91] LHC Higgs Cross Section Working Group Collaboration, “Handbook of LHC  
357 Higgs cross sections: 4. deciphering the nature of the Higgs sector,” 2016. DOI:  
358 10.23731/CYRM-2017-002. arXiv: 1610.07922 [hep-ph].
- 359 [92] OPAL Collaboration, DELPHI Collaboration, LEP Working Group for Higgs  
360 boson searches, ALEPH Collaboration, L3 Collaboration, “Search for the stan-  
361 dard model Higgs boson at LEP,” *Phys. Lett. B*, vol. 565, p. 61, 2003. DOI:  
362 10.1016/S0370-2693(03)00614-2. arXiv: hep-ex/0306033 [hep-ex].
- 363 [93] DELPHI Collaboration, OPAL Collaboration, ALEPH Collaboration, LEP  
364 Electroweak Working Group, L3 Collaboration, “A combination of prelimi-  
365 nary electroweak measurements and constraints on the standard model,” 2006.  
366 arXiv: hep-ex/0612034 [hep-ex].
- 367 [94] CDF Collaboration, D0 Collaboration, “Higgs boson studies at the Teva-  
368 tron,” *Phys. Rev. D*, vol. 88, no. 5, p. 052014, 2013. DOI: 10.1103/PhysRevD.  
369 88.052014. arXiv: 1303.6346 [hep-ex].
- 370 [95] Tevatron Electroweak Working Group, CDF Collaboration, DELPHI Collab-  
371 oration, SLD Electroweak and Heavy Flavour Groups, ALEPH Collaboration,  
372 LEP Electroweak Working Group, SLD Collaboration, OPAL Collaboration,  
373 D0 Collaboration, L3 Collaboration, “Precision electroweak measurements and  
374 constraints on the standard model,” 2010. arXiv: 1012.2367 [hep-ex].
- 375 [96] CMS Collaboration, “Observation of a new boson at a mass of 125 GeV with  
376 the CMS experiment at the LHC,” *Phys. Lett. B*, vol. 716, p. 30, 2012. DOI:  
377 10.1016/j.physletb.2012.08.021. arXiv: 1207.7235 [hep-ex].
- 378 [97] ATLAS Collaboration, “Observation of a new particle in the search for the  
379 standard model Higgs boson with the ATLAS detector at the LHC,” *Phys.*  
380 *Lett. B*, vol. 716, p. 1, 2012. DOI: 10.1016/j.physletb.2012.08.020. arXiv:  
381 1207.7214 [hep-ex].
- 382 [98] ATLAS Collaboration, CMS Collaboration, “Combined measurement of the  
383 Higgs boson mass in pp collisions at  $\sqrt{s} = 7$  and 8 TeV with the ATLAS and  
384 CMS experiments,” *Phys. Rev. Lett.*, vol. 114, p. 191803, 2015. DOI: 10.1103/  
385 PhysRevLett.114.191803. arXiv: 1503.07589 [hep-ex].
- 386 [99] ATLAS Collaboration, CMS Collaboration, “Measurements of the Higgs  
387 boson production and decay rates and constraints on its couplings from a  
388 combined ATLAS and CMS analysis of the LHC pp collision data at  $\sqrt{s} = 7$   
389 and 8 TeV,” *JHEP*, vol. 08, p. 045, 2016. DOI: 10.1007/JHEP08(2016)045.  
390 arXiv: 1606.02266 [hep-ex].

- 391 [100] I. Ots, H. Uibo, H. Liivat, R. Saar, and R. K. Loide, “Possible anomalous  $ZZ\gamma$   
392 and  $Z\gamma\gamma$  couplings and Z boson spin orientation in  $e^+e^- \rightarrow Z\gamma$ ,” *Nucl. Phys.*,  
393 vol. B702, pp. 346–356, 2004. DOI: 10.1016/j.nuclphysb.2004.09.019.
- 394 [101] DELPHI Collaboration, “Study of triple-gauge-boson couplings  $zzz$ ,  $ZZ\gamma$  and  
395  $Z\gamma\gamma$  at LEP,” *Eur. Phys. J. C*, vol. 51, p. 525, 2007. DOI: 10.1140/epjc/s10052-007-0345-0. arXiv: 0706.2741 [hep-ex].
- 397 [102] CDF Collaboration, D0 Collaboration, “Diboson physics at the Tevatron,”  
398 *EPJ Web Conf.*, vol. 28, p. 06001, 2012. DOI: 10.1051/epjconf/20122806001.  
399 arXiv: 1201.4771 [hep-ex].
- 400 [103] D0 Collaboration, “Search for  $ZZ$  and  $Z\gamma^*$  production in  $p\bar{p}$  collisions at  
401  $\sqrt{s} = 1.96$  TeV and limits on anomalous  $ZZZ$  and  $ZZ\gamma^*$  couplings,” *Phys. Rev. Lett.*,  
402 vol. 100, p. 131801, 2008. DOI: 10.1103/PhysRevLett.100.131801.  
403 arXiv: 0712.0599 [hep-ex].
- 404 [104] ATLAS Collaboration, “Measurement of the  $ZZ$  production cross section  
405 and limits on anomalous neutral triple gauge couplings in proton-proton col-  
406 lisions at  $\sqrt{s} = 7$  TeV with the ATLAS detector,” *Phys. Rev. Lett.*, vol. 108,  
407 p. 041804, 2012. DOI: 10.1103/PhysRevLett.108.041804. arXiv: 1110.5016  
408 [hep-ex].
- 409 [105] ATLAS Collaboration, “Measurement of the  $ZZ$  production cross section in  
410 pp collisions at  $\sqrt{s} = 13$  TeV with the ATLAS detector,” *Phys. Rev. Lett.*, vol.  
411 116, no. 10, p. 101801, 2016. DOI: 10.1103/PhysRevLett.116.101801. arXiv:  
412 1512.05314 [hep-ex].
- 413 [106] L. Evans and P. Bryant, “LHC machine,” *JINST*, vol. 3, S08001, 2008. DOI:  
414 10.1088/1748-0221/3/08/S08001.
- 415 [107] O. Brüning, H. Burkhardt, and S. Myers, “The Large Hadron Collider,” *Prog.  
416 Part. Nucl. Phys.*, vol. 67, no. 3, p. 7054, 2012, ISSN: 0146-6410. DOI: <https://doi.org/10.1016/j.ppnp.2012.03.001>. <http://www.sciencedirect.com/science/article/pii/S0146641012000695>.
- 419 [108] CMS Collaboration, “The CMS experiment at the CERN LHC,” *JINST*, vol.  
420 3, S08004, 2008. DOI: 10.1088/1748-0221/3/08/S08004.
- 421 [109] C. Lefèvre, “The CERN accelerator complex. complexe des accélérateurs du  
422 CERN,” Dec. 2008, <https://cds.cern.ch/record/1260465>.

- 423 [110] ATLAS Collaboration, “The ATLAS experiment at the CERN Large Hadron  
424 Collider,” *JINST*, vol. 3, S08003, 2008. DOI: 10.1088/1748-0221/3/08/  
425 S08003.
- 426 [111] LHCb Collaboration, “The LHCb detector at the LHC,” *JINST*, vol. 3,  
427 S08005, 2008. DOI: 10.1088/1748-0221/3/08/S08005.
- 428 [112] ALICE Collaboration, “The ALICE experiment at the CERN LHC,” *JINST*,  
429 vol. 3, S08002, 2008. DOI: 10.1088/1748-0221/3/08/S08002.
- 430 [113] TOTEM Collaboration, “The TOTEM experiment at the CERN Large  
431 Hadron Collider,” *JINST*, vol. 3, S08007, 2008. DOI: 10.1088/1748-0221/3/  
432 08/S08007.
- 433 [114] LHCf Collaboration, “The LHCf detector at the CERN Large Hadron Col-  
434 linder,” *JINST*, vol. 3, S08006, 2008. DOI: 10.1088/1748-0221/3/08/S08006.
- 435 [115] MoEDAL Collaboration, “The physics programme of the MoEDAL exper-  
436 iment at the LHC,” *Int. J. Mod. Phys.*, vol. A29, p. 1430050, 2014. DOI:  
437 10.1142/S0217751X14300506. arXiv: 1405.7662 [hep-ph].
- 438 [116] M. Bajko *et al.*, “Report of the task force on the incident of 19th September  
439 2008 at the LHC,” CERN, Geneva, Tech. Rep. LHC-PROJECT-Report-1168.  
440 CERN-LHC-PROJECT-Report-1168, Mar. 2009. [http://cds.cern.ch/](http://cds.cern.ch/record/1168025)  
441 record/1168025.
- 442 [117] M. Lamont, “Status of the LHC,” *Journal of Physics: Conference Series*,  
443 vol. 455, no. 1, p. 012001, 2013. [http://stacks.iop.org/1742-6596/455/  
444 i=1/a=012001](http://stacks.iop.org/1742-6596/455/i=1/a=012001).
- 445 [118] Y. Papaphilippou, H. Bartosik, G. Rumolo, and D. Manglunki, “Operational  
446 beams for the LHC,” 2014. arXiv: 1412.7857 [physics.acc-ph].
- 447 [119] F. Bordry and C. Pralavorio, “LHC smashes targets for 2016 run,” Nov.  
448 2016. <http://cds.cern.ch/record/2235979>.
- 449 [120] T. Sakuma and T. McCauley, “Detector and event visualization with Sketch-  
450 Up at the CMS experiment,” CERN, Geneva, Tech. Rep. CMS-CR-2013-379,  
451 Oct. 2013. arXiv: 1311.4942. <https://cds.cern.ch/record/1626816>.
- 452 [121] CMS Collaboration, “The magnet project: technical design report,” 1997.  
453 <https://cds.cern.ch/record/331056>.

- 454 [122] CMS Collaboration, “The CMS tracker system project: technical design  
455 report,” 1997. <http://cds.cern.ch/record/368412>.
- 456 [123] B. Isildak, “Measurement of the differential dijet production cross section  
457 in proton-proton collisions at  $\sqrt{s} = 7 \text{ TeV}$ ,” PhD thesis, Bogazici U., 2011.  
458 arXiv: 1308.6064 [hep-ex]. <https://inspirehep.net/record/1251416/files/arXiv:1308.6064.pdf>.
- 460 [124] “The CMS muon project: technical design report,” 1997. <http://cds.cern.ch/record/343814>.
- 462 [125] CMS Collaboration, “The CMS muon system in Run2: preparation, status  
463 and first results,” *PoS*, vol. EPS-HEP2015, p. 237, 2015. arXiv: 1510.05424  
464 [physics.ins-det].
- 465 [126] CMS Collaboration, “CMS technical design report for the level-1 trigger up-  
466 grade,” Tech. Rep. CERN-LHCC-2013-011. CMS-TDR-12, Jun. 2013. <https://cds.cern.ch/record/1556311>.
- 468 [127] P. R. K. Chumney, S. Dasu, J. Lackey, M. Jaworski, P. Robl, and W. H.  
469 Smith, “Level-1 regional calorimeter trigger system for CMS,” *EConf*, vol.  
470 C0303241, THHT003, 2003. arXiv: [hep-ex/0305047](https://arxiv.org/abs/hep-ex/0305047) [hep-ex].
- 471 [128] B. Kreis and others, “Run 2 upgrades to the CMS level-1 calorimeter trigger,”  
472 *JINST*, vol. 11, no. 01, p. C01051, 2016. DOI: [10.1088/1748-0221/11/01/C01051](https://doi.org/10.1088/1748-0221/11/01/C01051). arXiv: 1511.05855 [physics.ins-det].
- 474 [129] A. Svetek, M. Blake, M. Cepeda Hermida, S. Dasu, L. Dodd, R. Fobes, B.  
475 Gomber, T. Gorski, Z. Guo, P. Klabbers, A. Levine, I. Ojalvo, T. Ruggles, N.  
476 Smith, W. Smith, J. Tikalsky, M. Vicente, and N. Woods, “The calorimeter  
477 trigger processor card: the next generation of high speed algorithmic data  
478 processing at CMS,” *JINST*, vol. 11, p. C02011, 2016. DOI: [10.1088/1748-0221/11/02/C02011](https://doi.org/10.1088/1748-0221/11/02/C02011).
- 480 [130] J. Ero *et al.*, “The CMS drift tube trigger track finder,” *JINST*, vol. 3,  
481 P08006, 2008. DOI: [10.1088/1748-0221/3/08/P08006](https://doi.org/10.1088/1748-0221/3/08/P08006).
- 482 [131] D. Acosta, A. Atamanchuk, V. Golovtsov, A. Madorsky, B. Razmyslovich,  
483 B. Scurlock, and S. Wang, “The track-finding processor for the level-1 trigger  
484 of the CMS endcap muon system,” 1999.
- 485 [132] J. Ero *et al.*, “The CMS level-1 trigger barrel track finder,” *JINST*, vol. 11,  
486 no. 03, p. C03038, 2016. DOI: [10.1088/1748-0221/11/03/C03038](https://doi.org/10.1088/1748-0221/11/03/C03038).

- 487 [133] W. M. Zabolotny and A. Byszuk, “Algorithm and implementation of muon  
488 trigger and data transmission system for barrel-endcap overlap region of the  
489 CMS detector,” *JINST*, vol. 11, no. 03, p. C03004, 2016. DOI: 10.1088/1748-  
490 0221/11/03/C03004.
- 491 [134] H. Sakulin and A. Taurok, “The level-1 global muon trigger for the CMS ex-  
492 periment,” CERN, Geneva, Tech. Rep. CMS-CR-2003-040, Oct. 2003. <https://cds.cern.ch/record/687846>.
- 494 [135] M. Jeitler, J. Lingemann, D. Rabady, H. Sakulin, and A. Stahl, “Upgrade  
495 of the CMS global muon trigger,” *IEEE Trans. Nucl. Sci.*, vol. 62, no. 3,  
496 pp. 1104–1109, 2015. DOI: 10.1109/TNS.2015.2435060.
- 497 [136] M. Jeitler *et al.*, “The level-1 global trigger for the CMS experiment at LHC,”  
498 *JINST*, vol. 2, P01006, 2007. DOI: 10.1088/1748-0221/2/01/P01006.
- 499 [137] J. Wittmann, B. Arnold, H. Bergauer, M. Jeitler, T. Matsushita, D. Rabady,  
500 B. Rahbaran, and C.-E. Wulz, “The upgrade of the CMS global trigger,”  
501 *JINST*, vol. 11, no. 02, p. C02029, 2016. <http://stacks.iop.org/1748-0221/11/i=02/a=C02029>.
- 503 [138] CMS Collaboration, “The CMS high level trigger,” *Eur. Phys. J. C*, vol. 46,  
504 p. 605, 2006. DOI: 10.1140/epjc/s2006-02495-8. arXiv: [hep-ex/0512077](https://arxiv.org/abs/hep-ex/0512077)  
505 [hep-ex].
- 506 [139] S. Van der Meer, “Calibration of the effective beam height in the ISR,” 1968.
- 507 [140] CMS Collaboration, “Beams scan based absolute normalization of the CMS  
508 luminosity measurement. CMS 2010 luminosity determination,” 2011. <https://cds.cern.ch/record/1357856>.
- 510 [141] CMS Collaboration, “CMS luminosity measurement for the 2015 data-taking  
511 period,” CERN, Geneva, Tech. Rep. CMS-PAS-LUM-15-001, 2017. <http://cds.cern.ch/record/2138682>.
- 513 [142] CMS Collaboration Collaboration, “CMS luminosity measurements for the  
514 2016 data taking period,” CERN, Geneva, Tech. Rep. CMS-PAS-LUM-17-001,  
515 2017. <http://cds.cern.ch/record/2257069>.
- 516 [143] N. Metropolis and S. Ulam, “The Monte Carlo method,” *Journal of the  
517 American Statistical Association*, vol. 44, p. 335, 1949. DOI: 10.2307/2280232.  
518 <http://www.jstor.org/stable/2280232>.

- 519 [144] M. Matsumoto and T. Nishimura, “Mersenne Twister: A 623-dimensional-  
520 ly equidistributed uniform pseudo-random number generator,” *ACM Trans.*  
521 *Model. Comput. Simul.*, vol. 8, p. 3, 1998. DOI: 10.1145/272991.272995.  
522 <http://doi.acm.org/10.1145/272991.272995>.
- 523 [145] J. Alwall, R. Frederix, S. Frixione, V. Hirschi, F. Maltoni, O. Mattelaer,  
524 H.-S. Shao, T. Stelzer, P. Torrielli, and M. Zaro, “The automated computation  
525 of tree-level and next-to-leading order differential cross sections, and their  
526 matching to parton shower simulations,” *JHEP*, vol. 07, p. 079, 2014. DOI:  
527 10.1007/JHEP07(2014)079. arXiv: 1405.0301 [hep-ph].
- 528 [146] P. Nason, “A new method for combining NLO QCD with shower Monte  
529 Carlo algorithms,” *JHEP*, vol. 11, p. 040, 2004. DOI: 10.1088/1126-6708/  
530 2004/11/040. arXiv: hep-ph/0409146 [hep-ph].
- 531 [147] S. Frixione, P. Nason, and C. Oleari, “Matching NLO QCD computations  
532 with parton shower simulations: the POWHEG method,” *JHEP*, vol. 11, p. 070,  
533 2007. DOI: 10.1088/1126-6708/2007/11/070. arXiv: 0709.2092 [hep-ph].
- 534 [148] S. Alioli, P. Nason, C. Oleari, and E. Re, “A general framework for im-  
535 plementing NLO calculations in shower Monte Carlo programs: the POWHEG  
536 BOX,” *JHEP*, vol. 06, p. 043, 2010. DOI: 10.1007/JHEP06(2010)043. arXiv:  
537 1002.2581 [hep-ph].
- 538 [149] T. Gleisberg, S. Hoeche, F. Krauss, M. Schonherr, S. Schumann, F. Siegert,  
539 and J. Winter, “Event generation with SHERPA 1.1,” *JHEP*, vol. 02, p. 007,  
540 2009. DOI: 10.1088/1126-6708/2009/02/007. arXiv: 0811.4622 [hep-ph].
- 541 [150] J. M. Campbell, R. K. Ellis, and W. T. Giele, “A multi-threaded version of  
542 MCFM,” *Eur. Phys. J. C*, vol. 75, p. 246, 2015. DOI: 10.1140/epjc/s10052-  
543 015-3461-2. arXiv: 1503.06182 [physics.comp-ph].
- 544 [151] R. Boughezal, J. M. Campbell, R. K. Ellis, C. Focke, W. Giele, X. Liu, F.  
545 Petriello, and C. Williams, “Color singlet production at NNLO in MCFM,”  
546 *Eur. Phys. J. C*, vol. 77, p. 7, 2017. DOI: 10.1140/epjc/s10052-016-4558-y.  
547 arXiv: 1605.08011 [hep-ph].
- 548 [152] G. P. Lepage, “A new algorithm for adaptive multidimensional integration,”  
549 *J. Comput. Phys.*, vol. 27, p. 192, 1978. DOI: 10.1016/0021-9991(78)90004-  
550 9.

- 551 [153] M. Bahr *et al.*, “Herwig++ physics and manual,” *Eur. Phys. J. C*, vol. 58,  
552 p. 639, 2008. DOI: 10.1140/epjc/s10052-008-0798-9. arXiv: 0803.0883  
553 [hep-ph].
- 554 [154] J. Bellm *et al.*, “Herwig 7.0/Herwig++ 3.0 release note,” *Eur. Phys. J. C*,  
555 vol. 76, no. 4, p. 196, 2016. DOI: 10.1140/epjc/s10052-016-4018-8. arXiv:  
556 1512.01178 [hep-ph].
- 557 [155] B. Andersson, G. Gustafson, and C. Peterson, “A semiclassical model for  
558 quark jet fragmentation,” *Z. Phys. C*, vol. 1, p. 105, 1979. DOI: 10.1007/  
559 BF01450386.
- 560 [156] B. Andersson, G. Gustafson, and B. Soderberg, “A general model for jet  
561 fragmentation,” *Z. Phys. C*, vol. 20, p. 317, 1983. DOI: 10.1007/BF01407824.
- 562 [157] B. Andersson, S. Mohanty, and F. Soderberg, “The lund fragmentation  
563 process for a multigluon string according to the area law,” *Eur. Phys. J. C*,  
564 vol. 21, p. 631, 2001. DOI: 10.1007/s100520100757. arXiv: hep-ph/0106185  
565 [hep-ph].
- 566 [158] Sjöstrand, T. and Skands, Peter Z., “Transverse-momentum-ordered showers  
567 and interleaved multiple interactions,” *Eur. Phys. J. C*, vol. 39, p. 129, 2005.  
568 DOI: 10.1140/epjc/s2004-02084-y. arXiv: hep-ph/0408302 [hep-ph].
- 569 [159] J. Alwall *et al.*, “Comparative study of various algorithms for the merging  
570 of parton showers and matrix elements in hadronic collisions,” *Eur. Phys. J.*  
571 *C*, vol. 53, p. 473, 2008. DOI: 10.1140/epjc/s10052-007-0490-5. arXiv:  
572 0706.2569 [hep-ph].
- 573 [160] J. Alwall, S. de Visscher, and F. Maltoni, “QCD radiation in the production  
574 of heavy colored particles at the LHC,” *JHEP*, vol. 02, p. 017, 2009. DOI:  
575 10.1088/1126-6708/2009/02/017. arXiv: 0810.5350 [hep-ph].
- 576 [161] M. Rauch, “Vector-boson fusion and vector-boson scattering,” 2016. arXiv:  
577 1610.08420 [hep-ph].
- 578 [162] M. L. Mangano, M. Moretti, F. Piccinini, and M. Treccani, “Matching ma-  
579 trix elements and shower evolution for top-quark production in hadronic col-  
580 lisions,” *JHEP*, vol. 01, p. 013, 2007. DOI: 10.1088/1126-6708/2007/01/013.  
581 arXiv: hep-ph/0611129 [hep-ph].

- 582 [163] S. Catani, F. Krauss, R. Kuhn, and B. R. Webber, “QCD matrix elements  
583 + parton showers,” *JHEP*, vol. 11, p. 063, 2001. DOI: 10.1088/1126-6708/  
584 2001/11/063. arXiv: hep-ph/0109231 [hep-ph].
- 585 [164] R. Frederix and S. Frixione, “Merging meets matching in MC@NLO,” *JHEP*,  
586 vol. 12, p. 061, 2012. DOI: 10.1007/JHEP12(2012)061. arXiv: 1209.6215 [hep-  
587 ph].
- 588 [165] Sjöstrand, T. and Skands, Peter Z., “Multiple interactions and the structure  
589 of beam remnants,” *JHEP*, vol. 03, p. 053, 2004. DOI: 10.1088/1126-6708/  
590 2004/03/053. arXiv: hep-ph/0402078 [hep-ph].
- 591 [166] A. V. Manohar and W. J. Waalewijn, “A QCD analysis of double parton  
592 scattering: color correlations, interference effects and evolution,” *Phys. Rev.*  
593 *D*, vol. 85, p. 114009, 2012. DOI: 10.1103/PhysRevD.85.114009. arXiv:  
594 1202.3794 [hep-ph].
- 595 [167] S Banerjee, “CMS simulation software,” *Journal of Physics: Conference Series*,  
596 vol. 396, p. 022003, 2012. %7Bhttp://stacks.iop.org/1742-6596/  
597 396/i=2/a=022003%7D.
- 598 [168] M Hildreth and V N Ivanchenko and D J Lange and M J Kortelainen, “CMS  
599 full simulation for run-2,” *Journal of Physics: Conference Series*, vol. 664,  
600 p. 072022, 2015. %7Bhttp://stacks.iop.org/1742-6596/664/i=7/a=  
601 072022%7D.
- 602 [169] S. Alioli, P. Nason, C. Oleari, and E. Re, “NLO vector-boson production  
603 matched with shower in POWHEG,” *JHEP*, vol. 07, p. 060, 2008. DOI: 10.  
604 1088/1126-6708/2008/07/060. arXiv: 0805.4802 [hep-ph].
- 605 [170] J. M. Campbell and R. K. Ellis, “MCFM for the Tevatron and the LHC,”  
606 *Nucl. Phys. Proc. Suppl.*, vol. 205, p. 10, 2010. DOI: 10.1016/j.nuclphysbps.  
607 2010.08.011. arXiv: 1007.3492 [hep-ph].
- 608 [171] A. Ballestrero, A. Belhouari, G. Bevilacqua, V. Kashkan, and E. Maina,  
609 “PHANTOM : a Monte Carlo event generator for six parton final states at  
610 high energy colliders,” *Comput. Phys. Commun.*, vol. 180, p. 401, 2009. DOI:  
611 10.1016/j.cpc.2008.10.005. arXiv: 0801.3359 [hep-ph].
- 612 [172] NNPDF Collaboration, “Parton distributions for the LHC Run II,” *JHEP*,  
613 vol. 04, p. 040, 2015. DOI: 10.1007/JHEP04(2015)040. arXiv: 1410.8849  
614 [hep-ph].

- 615 [173] CMS Collaboration, “Event generator tunes obtained from underlying event  
616 and multiparton scattering measurements,” *Eur. Phys. J. C*, vol. 76, p. 155,  
617 2016. DOI: 10.1140/epjc/s10052-016-3988-x. arXiv: 1512.00815 [hep-ex].
- 618 [174] GEANT4 Collaboration, “GEANT4: a simulation toolkit,” *Nucl. Instrum.  
619 Meth. A*, vol. 506, p. 250, 2003. DOI: 10.1016/S0168-9002(03)01368-8.
- 620 [175] R. Frühwirth, “Application of Kalman filtering to track and vertex fitting,”  
621 *Nucl. Instrum. Meth. A*, vol. 262, p. 444, 1987. DOI: 10.1016/0168-9002(87)  
622 90887-4.
- 623 [176] P. Billoir and S. Qian, “Simultaneous pattern recognition and track fitting  
624 by the Kalman filtering method,” *Nucl. Instrum. Meth. A*, vol. 294, p. 219,  
625 1990. DOI: 10.1016/0168-9002(90)91835-Y.
- 626 [177] W. Adam, B. Mangano, T. Speer, and T. Todorov, “Track reconstruction in  
627 the CMS tracker,” 2005.
- 628 [178] CMS Collaboration, “Description and performance of track and primary-  
629 vertex reconstruction with the CMS tracker,” *JINST*, vol. 9, no. 10, P10009,  
630 2014. DOI: 10.1088/1748-0221/9/10/P10009. arXiv: 1405.6569 [physics.ins-  
631 det].
- 632 [179] W. Adam, R. Frühwirth, A. Strandlie, and T. Todor, “Reconstruction of  
633 electrons with the Gaussian-sum filter in the CMS tracker at the LHC,” 2005.
- 634 [180] T. Speer, K. Prokofiev, R. Frühwirth, W. Waltenberger, and P. Vanlaer,  
635 “Vertex fitting in the CMS tracker,” 2006.
- 636 [181] K. Rose, “Deterministic annealing for clustering, compression, classification,  
637 regression, and related optimization problems,” *Proceedings of the IEEE*, vol.  
638 86, no. 11, p. 2210, Nov. 1998, ISSN: 0018-9219. DOI: 10.1109/5.726788.
- 639 [182] CMS Collaboration, “Particle-flow event reconstruction in CMS and perfor-  
640 mance for jets, taus, and MET,” CERN, Geneva, Tech. Rep. CMS-PAS-PFT-  
641 09-001, Apr. 2009. <https://cds.cern.ch/record/1194487>.
- 642 [183] CMS Collaboration, “Commissioning of the particle-flow event reconstruction  
643 with the first LHC collisions recorded in the CMS detector,” Tech. Rep. CMS-  
644 PAS-PFT-10-001, 2010. <https://cds.cern.ch/record/1247373>.

- 645 [184] CMS Collaboration, “Particle-flow reconstruction and global event descrip-  
646 tion with the CMS detector,” 2017, Accepted by *JINST*. arXiv: 1706.04965  
647 [physics.ins-det].
- 648 [185] CMS Collaboration, “Performance of CMS muon reconstruction in pp colli-  
649 sion events at  $\sqrt{s} = 7 \text{ TeV}$ ,” *JINST*, vol. 7, P10002, 2012. DOI: 10.1088/1748-  
650 0221/7/10/P10002. arXiv: 1206.4071 [physics.ins-det].
- 651 [186] S. Baffioni, C. Charlot, F. Ferri, D. Futyan, P. Meridiani, I. Puljak, C. Rovelli,  
652 R. Salerno, and Y. Sirois, “Electron reconstruction in CMS,” *Eur. Phys. J. C*,  
653 vol. 49, p. 1099, 2007. DOI: 10.1140/epjc/s10052-006-0175-5.
- 654 [187] CMS Collaboration, “Performance of photon reconstruction and identifi-  
655 cation with the CMS detector in proton-proton collisions at  $\sqrt{s} = 8 \text{ TeV}$ ,”  
656 *JINST*, vol. 10, no. 08, P08010, 2015. DOI: 10.1088/1748-0221/10/08/  
657 P08010. arXiv: 1502.02702 [physics.ins-det].
- 658 [188] G. P. Salam and G. Soyez, “A practical seedless infrared-safe cone jet algo-  
659 rithm,” *JHEP*, vol. 05, p. 086, 2007. DOI: 10.1088/1126-6708/2007/05/086.  
660 arXiv: 0704.0292 [hep-ph].
- 661 [189] G. P. Salam, “Towards jetography,” *Eur. Phys. J. C*, vol. 67, p. 637, 2010.  
662 DOI: 10.1140/epjc/s10052-010-1314-6. arXiv: 0906.1833 [hep-ph].
- 663 [190] M. Cacciari, G. P. Salam, and G. Soyez, “The anti- $k_T$  jet clustering algo-  
664 rithm,” *JHEP*, vol. 04, p. 063, 2008. DOI: 10.1088/1126-6708/2008/04/063.  
665 arXiv: 0802.1189 [hep-ph].
- 666 [191] M. Cacciari, G. P. Salam, and G. Soyez, “FastJet user manual,” *Eur. Phys.  
667 J. C*, vol. 72, p. 1896, 2012. DOI: 10.1140/epjc/s10052-012-1896-2. arXiv:  
668 1111.6097 [hep-ph].
- 669 [192] CMS Collaboration, “Study of pileup removal algorithms for jets,” 2014.
- 670 [193] CMS Collaboration, “Jet energy scale and resolution in the CMS experiment  
671 in pp collisions at 8 TeV,” *JINST*, vol. 12, no. 02, P02014, 2017. DOI: 10.1088/  
672 1748-0221/12/02/P02014. arXiv: 1607.03663 [hep-ex].
- 673 [194] M. Cacciari, G. P. Salam, and G. Soyez, “The catchment area of jets,”  
674 *JHEP*, vol. 04, p. 005, 2008. DOI: 10.1088/1126-6708/2008/04/005. arXiv:  
675 0802.1188 [hep-ph].

- 676 [195] M. Cacciari and G. P. Salam, “Pileup subtraction using jet areas,” *Phys.  
677 Lett. B*, vol. 659, p. 119, 2008. DOI: 10.1016/j.physletb.2007.09.077.  
678 arXiv: 0707.1378 [hep-ph].
- 679 [196] CMS Collaboration, “Determination of jet energy calibration and transverse  
680 momentum resolution in CMS,” *JINST*, vol. 6, P11002, 2011. DOI: 10.1088/  
681 1748-0221/6/11/P11002. arXiv: 1107.4277 [physics.ins-det].
- 682 [197] CMS Collaboration, “Missing transverse energy performance of the CMS  
683 detector,” *JINST*, vol. 6, P09001, 2011. DOI: 10.1088/1748-0221/6/09/  
684 P09001. arXiv: 1106.5048 [physics.ins-det].
- 685 [198] CMS Collaboration, “Performance of the CMS missing transverse momen-  
686 tumb reconstruction in pp data at  $\sqrt{s} = 8\text{ TeV}$ ,” *JINST*, vol. 10, no. 02,  
687 P02006, 2015. DOI: 10.1088/1748-0221/10/02/P02006. arXiv: 1411.0511  
688 [physics.ins-det].
- 689 [199] CMS Collaboration, “Performance of missing energy reconstruction in 13 TeV  
690 pp collision data using the CMS detector,” CERN, Geneva, Tech. Rep. CMS-  
691 PAS-JME-16-004, 2016. <http://cds.cern.ch/record/2205284>.
- 692 [200] CMS Collaboration, “Electron reconstruction and identification at  $\sqrt{s} =$   
693 7 TeV,” CERN, Geneva, Tech. Rep. CMS-PAS-EGM-10-004, 2010. <https://cds.cern.ch/record/1299116>.
- 695 [201] CMS Collaboration, “Performance of electron reconstruction and selection  
696 with the CMS detector in proton-proton collisions at  $\sqrt{s} = 8\text{ TeV}$ ,” *JINST*,  
697 vol. 10, no. 06, P06005, 2015. DOI: 10.1088/1748-0221/10/06/P06005.  
698 arXiv: 1502.02701 [physics.ins-det].
- 699 [202] CMS Collaboration, “Measurement of the inclusive W and Z production  
700 cross sections in pp collisions at  $\sqrt{s} = 7\text{ TeV}$ ,” *JHEP*, vol. 10, p. 132, 2011.  
701 DOI: 10.1007/JHEP10(2011)132. arXiv: 1107.4789 [hep-ex].
- 702 [203] CMS Collaboration, “Measurement of the properties of a Higgs boson in the  
703 four-lepton final state,” *Phys. Rev. D*, vol. 89, no. 9, p. 092007, 2014. DOI:  
704 10.1103/PhysRevD.89.092007. arXiv: 1312.5353 [hep-ex].
- 705 [204] J. Butterworth *et al.*, “PDF4LHC recommendations for LHC Run II,” *J.  
706 Phys. G*, vol. 43, p. 023001, 2016. DOI: 10.1088/0954-3899/43/2/023001.  
707 arXiv: 1510.03865 [hep-ph].

- 708 [205] G. Bohm and G. Zech, *Introduction to statistics and data analysis for physi-  
709 cists*. DESY, 2010, ISBN: 9783935702416. [https://books.google.ch/books?  
710 id=aQBHcgAACAAJ](https://books.google.ch/books?id=aQBHcgAACAAJ).
- 711 [206] G. D'Agostini, "A multidimensional unfolding method based on Bayes' the-  
712 oreum," *Nucl. Instrum. Meth. A*, vol. 362, p. 487, 1995. DOI: 10.1016/0168-  
713 9002(95)00274-X.
- 714 [207] A. P. Dempster, N. M. Laird, and D. B. Rubin, "Maximum likelihood from  
715 incomplete data via the EM algorithm," *J. R. Stat. Soc. B*, vol. 39, p. 1, 1977,  
716 ISSN: 00359246. <http://www.jstor.org/stable/2984875>.
- 717 [208] L. B. Lucy, "An iterative technique for the rectification of observed distri-  
718 butions," *Astron. J.*, vol. 79, p. 745, Jun. 1974. DOI: 10.1086/111605.
- 719 [209] W. H. Richardson, "Bayesian-based iterative method of image restoration,"  
720 *J. Opt. Soc. Am.*, vol. 62, p. 55, Jan. 1972. DOI: 10.1364/JOSA.62.000055.  
721 <http://www.osapublishing.org/abstract.cfm?URI=josa-62-1-55>.
- 722 [210] L. A. Shepp and Y. Vardi, "Maximum likelihood reconstruction for emission  
723 tomography," *IEEE Transactions on Medical Imaging*, vol. 1, no. 2, p. 113,  
724 Oct. 1982, ISSN: 0278-0062. DOI: 10.1109/TMI.1982.4307558.
- 725 [211] T. Adye, "Unfolding algorithms and tests using RooUnfold," in *Proceedings,  
726 PHYSTAT 2011 Workshop on Statistical Issues Related to Discovery Claims  
727 in Search Experiments and Unfolding*, CERN, Geneva, Switzerland 17–20 January  
728 2011, CERN, Geneva: CERN, 2011, p. 313. DOI: 10.5170/CERN-2011-  
729 006.313. arXiv: 1105.1160 [physics.data-an]. [https://inspirehep.net/  
record/898599/files/arXiv:1105.1160.pdf](https://inspirehep.net/<br/>730 record/898599/files/arXiv:1105.1160.pdf).
- 731 [212] Y. Vardi, "Empirical distributions in selection bias models," *Ann. Statist.*,  
732 vol. 13, p. 178, Mar. 1985. DOI: 10.1214/aos/1176346585. [http://dx.doi.org/10.1214/aos/1176346585](http://dx.doi.<br/>733 org/10.1214/aos/1176346585).
- 734 [213] F. Pedregosa, G. Varoquaux, A. Gramfort, V. Michel, B. Thirion, O. Grisel,  
735 M. Blondel, P. Prettenhofer, R. Weiss, V. Dubourg, J. Vanderplas, A. Pas-  
736 soss, D. Cournapeau, M. Brucher, M. Perrot, and E. Duchesnay, "Scikit-learn:  
737 Machine learning in Python," *J. Mach. Learn. Res.*, vol. 12, p. 2825, 2011.
- 738 [214] CMS Collaboration Collaboration, "Performance of quark/gluon discrimina-  
739 tion in 8 TeV pp data," CERN, Geneva, Tech. Rep. CMS-PAS-JME-13-002,  
740 2013. <https://cds.cern.ch/record/1599732>.

- 741 [215] G. Cowan, K. Cranmer, E. Gross, and O. Vitells, “Asymptotic formulae for  
742 likelihood-based tests of new physics,” *Eur. Phys. J. C*, vol. 71, p. 1554, 2011,  
743 [Erratum: DOI: 10.1140/epjc/s10052-013-2501-z]. DOI: 10.1140/epjc/  
744 s10052-011-1554-0. arXiv: 1007.1727 [physics.data-an].
- 745 [216] CMS Collaboration and ATLAS Collaboration, “Combination of results from  
746 the ATLAS and CMS experiments on anomalous triple gauge couplings in ZZ  
747 production from pp collisions at a centre-of-mass energy of 7 TeV at the LHC,”  
748 CERN, Geneva, Tech. Rep. CMS-PAS-SMP-15-001. ATLAS-CONF-2016-036,  
749 2016. <https://cds.cern.ch/record/2202807>.
- 750 [217] CMS Collaboration, “Measurement of the ZZ production cross section in  
751  $\ell\ell\ell'\ell'$  decays in pp collisions at  $\sqrt{s} = 13$  TeV,” 2015. <https://cds.cern.ch/record/2114822>.
- 753 [218] CMS Collaboration, “Measurement of the ZZ production cross section and  
754  $Z \rightarrow \ell^+\ell^-\ell'^+\ell'^-$  branching fraction in pp collisions at  $\sqrt{s} = 13$  TeV,” *Phys.*  
755 *Lett. B*, vol. 763, p. 280, 2016. DOI: 10.1016/j.physletb.2016.10.054.  
756 arXiv: 1607.08834 [hep-ex].
- 757 [219] CMS Collaboration, “Measurements of differential cross sections and search  
758 for the electroweak production of two Z bosons produced in association with  
759 jets,” 2017. <https://cds.cern.ch/record/2264556>.
- 760 [220] CMS Collaboration, “Measurement of vector boson scattering and constraints  
761 on anomalous quartic couplings from events with four leptons and two jets in  
762 proton-proton collisions at  $\sqrt{s} = 13$  TeV,” 2017, Submitted to *Phys. Lett. B*.  
763 arXiv: 1708.02812 [hep-ex].
- 764 [221] CMS Collaboration, “Studies of Higgs boson production in the four-lepton  
765 final state at  $\sqrt{s} = 13$  TeV,” 2016. <https://cds.cern.ch/record/2139978>.
- 766 [222] CMS Collaboration, “Measurements of properties of the Higgs boson and  
767 search for an additional resonance in the four-lepton final state at  $\sqrt{s} =$   
768 13 TeV,” 2016. <https://cds.cern.ch/record/2204926>.
- 769 [223] CMS Collaboration, “Measurements of properties of the Higgs boson decay-  
770 ing into the four-lepton final state in pp collisions at  $\sqrt{s} = 13$  TeV,” 2017,  
771 Submitted to *JHEP*. arXiv: 1706.09936 [hep-ex].
- 772 [224] R. Gavin, Y. Li, F. Petriello, and S. Quackenbush, “FEWZ 2.0: a code  
773 for hadronic Z production at next-to-next-to-leading order,” *Comput. Phys.*

- 774           *Commun.*, vol. 182, p. 2388, 2011. DOI: 10.1016/j.cpc.2011.06.008. arXiv:  
775           1011.3540 [hep-ph].
- 776 [225]       ATLAS Collaboration, “ $ZZ \rightarrow \ell^+ \ell^- \ell'^+ \ell'^-$  cross-section measurements and  
777           aTGC search in 13 TeV pp collisions with the ATLAS detector,” 2017. <http://cds.cern.ch/record/2263045>.
- 779 [226]       K. Arnold *et al.*, “VBFNLO: a parton level Monte Carlo for processes with  
780           electroweak bosons,” *Comput. Phys. Commun.*, vol. 180, pp. 1661–1670, 2009.  
781           DOI: 10.1016/j.cpc.2009.03.006. arXiv: 0811.4559 [hep-ph].